Chem Soc Rev

REVIEW ARTICLE

View Article Online
View Journal

Check for updates

Cite this: DOI: 10.1039/d5cs01418b

Emerging deposition–dissolution chemistry for next-generation metal-based hybrid flow batteries: progress and perspectives

Jie Wei,[a] Jingjie Sun,[c] Sijia Bai,[ad] Liuxin Ding,[ad] Pengbo Zhang,[c] Yixing Wang,[a] Yuzhu Liu,[e] Kang Huang,*[ad] Zhong Jin *[c] and Zhi Xu *[b]

As fossil fuels deplete and environmental pollution intensifies, the effective utilization of intermittent renewables calls for large-scale long-duration energy storage technologies. Metal-based hybrid flow batteries (MBHFBs) have considerable potential in energy density and cost efficiency, attributed to unique deposition–dissolution chemistry and abundant metal resources. However, the deployment and understanding of MBHFBs remain in their infancy. Moreover, the variation among metals leads to distinct challenges across various MBHFBs. To systematically address these challenges, this review adopts deposition–dissolution chemistry as a central theme and provides a comprehensive analysis of MBHFBs from an all-round perspective. Horizontally, MBHFBs are categorized into two groups based on non-aqueous/aqueous electrolyte, and further subdivided into eleven subcategories according to the anodic metals, evaluated in terms of principles, architectures, advantages, challenges, and corresponding strategies. Vertically, the advances and limitations of four core components (electrolytes, electrodes, membranes, and bipolar plates) are examined, aiming to reveal underlying interconnections and synergistic effects. Finally, we propose ten promising future research directions for MBHFBs. This review aims to improve the understanding of design principles and optimization strategies for MBHFBs, support the establishment of a unified theoretical framework for deposition–dissolution chemistry, and offer relevant insights for developing next-generation low-cost and high-energy-density energy storage technologies.

Received 26th December 2025

DOI: 10.1039/d5cs01418b

rsc.li/chem-soc-rev

1. Introduction

With the continuous development of human society and economy, the supply of fossil fuels has gradually decreased, resulting in an increasingly urgent energy shortage problem. At the same time, with the improvement of human production capacity and the surge in demand for products, the burning of a large number of traditional fuels has led to increasingly serious environmental pollution problems. The energy crisis and environmental problems have a negative effect on global economic growth, creating a vicious spiral.[1–4] Therefore, developing clean, renewable energy and building a low-carbon society is an inevitable trend that aligns with the common interests of all humanity. However, renewable energy sources such as wind and solar power exhibit inherent variability, randomness, and intermittency in their electricity output, which cannot be readily adjusted by human intervention to improve generation efficiency. The non-steady characteristics of renewable energy sources result in a temporal and spatial mismatch between energy generation and energy consumption. Large-scale and long-duration energy storage technologies can effectively smooth power output and peak shaving and valley filling, enabling the optimal temporal and spatial allocation of energy resources.[5,6] Therefore, it is necessary to further promote the development of low-cost, large-scale and long-duration energy storage technologies to ensure the compatibility of renewable energy with smart grid.

Redox flow batteries (RFBs) are a promising large-scale long-duration energy storage technology. As illustrated in Fig. 1a,

---

[a] *Energy and Environmental Materials Research Department, Suzhou Laboratory, Suzhou 215124, China. E-mail: kanghuang@njtech.edu.cn*
[b] *State Key Laboratory of Chemical Engineering, School of Chemical Engineering, East China University of Science and Technology, Shanghai 200237, China. E-mail: zhixu@ecust.edu.cn*
[c] *State Key Laboratory of Coordination Chemistry, MOE Key Laboratory of Mesoscopic Chemistry, MOE Key Laboratory of High Performance Polymer Materials and Technology, Jiangsu Key Laboratory of Clean Energy Catalysis and Intelligent Green Chemical Engineering, Suzhou Key Laboratory of Green Intelligent Manufacturing of New Energy Materials and Devices, Tianchang New Materials and Energy Technologies Research Center, Institute of Green Chemistry and Engineering, School of Chemistry and Chemical Engineering, Nanjing University, Nanjing, Jiangsu 210023, P. R. China. E-mail: zhongjin@nju.edu.cn*
[d] *State Key Laboratory of Materials-Oriented Chemical Engineering, College of Chemical Engineering, Nanjing Tech University, Nanjing 211816, China*
[e] *School of Materials Science and Engineering, Nanyang Technological University, 50 Nanyang Avenue, Singapore 639798, Singapore*

conventional flow batteries, or called all-soluble flow batteries (ASFBs), utilize redox-active species dissolved in the electrolyte to form redox couples and facilitate reversible redox reactions on carbon felts by circulating the electrolyte between external storage tanks and within the batteries. Redox flow batteries enable the reversible conversion of electrical and chemical energy, offering advantages such as high safety, decoupling of capacity and power.[7,8] Furthermore, RFBs have potential advantages for smart grid energy storage, as their lifespan and cost can directly impact the price of zero-carbon electricity fed into the grid.[9,10] All-vanadium redox flow batteries (VRFBs) and Fe–Cr RFBs, as the main representatives of ASFBs, currently face challenges such as high system costs, relatively low energy density, and narrow operating temperature range (as shown in Table 1).[11–15] The relatively low energy density of ASFBs necessitates the use of a larger volume of electrolyte, which in turn leads to increased costs. Therefore, developing low-cost, high-energy density flow batteries is currently a key focus of research in the field of flow batteries. Metal-based hybrid flow batteries (MBHFBs) have emerged as an ideal solution for large-scale energy storage and renewable energy integration, owing to their low cost, scalability, rapid response, high energy density, wide temperature range, environmental friendliness, and adaptability.[16–26]

MBHFBs constitute an emerging class of rechargeable flow batteries that harness the deposition and dissolution of metals within redox reactions as the mechanism for energy storage and release.[3,4] Typically, MBHFBs involve phase-conversion reactions of metals in the one side electrolyte, alongside redox reactions of dissolved active materials in the other side electrolyte (Fig. 1b). Similar to conventional ASFBs, the redox reaction of MBHFBs occurs only at the electrolyte–electrode interface within the reactor. The 1970s witnessed the advent of the first authentic and practical MBHFBs, featuring the zinc–bromine ($Zn–Br_2$) flow batteries as their primary prototype. Since then, a diverse range of metal ion/metal redox couples have been proven to be fundamentally applicable in MBHFBs (as shown in Table 1), forming a clear main trunk of development vein for

Jie Wei

Jie Wei received his BS from Hunan University, P. R. China (2018) and PhD from Nanjing University, P. R. China (2023) under the supervision of Prof. Zhong Jin. He is currently a postdoctoral scholar at Suzhou Laboratory, P. R. China. His current research interests primarily focus on safe aqueous flow batteries with scale energy storage potential, including electrolyte optimization for aqueous metal-based hybrid flow batteries, redox active materials synthesis for aqueous organic flow batteries, principal design and verification for new types of aqueous flow batteries.

Kang Huang

Kang Huang is a professor at the College of Chemical Engineering at Nanjing Tech University. He received his PhD at Nanjing Tech University under the supervision of Prof. Wanqin Jin and then joined Nanjing Tech University. From 2016–2019, he was a postdoc of Prof. Kang Li at Imperial College London. His research focuses on ion conductive membranes for ion separation and energy storage.

Zhong Jin

Zhong Jin received his BS (2003) and PhD (2008) in chemistry from Peking University, P. R. China. He worked as a postdoctoral scholar at Rice University (2008–2010) and Massachusetts Institute of Technology (2010–2014). Now he is a professor and the Dean of the Institute of Green Chemistry and Engineering at Nanjing University. He leads a research group working on functional nanomaterials and devices for clean energy conversion and storage applications.

Zhi Xu

Zhi Xu is a professor and the Dean of the School of Chemical Engineering at East China University of Science and Technology. His research focuses on the development of membranes and catalysts related to separation and energy fields. He also serves as an editorial board member for "Advances in Chemical Engineering" and "Membrane Science and Technology" and as a young editorial board member for "Engineering" and "Advanced Membranes".

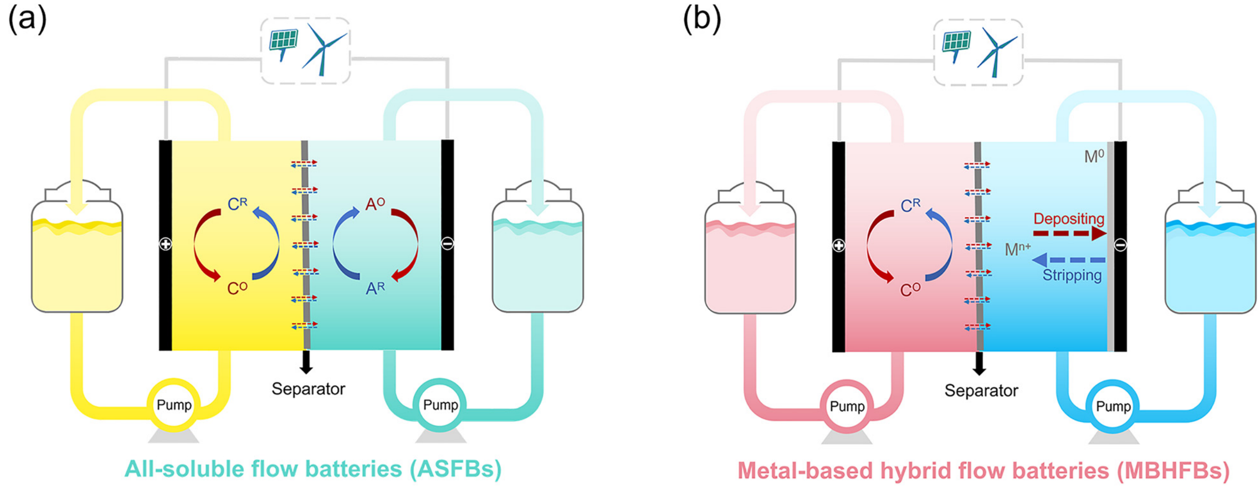

Fig. 1 Schematic of (a) conventional all-soluble flow batteries and (b) metal-based hybrid flow batteries.

Table 1 Comparison of typical ASFBs (*e.g.*, VRFBs and Fe–Cr RFBs) and MBHFBs (recorded as X-based HFBs)[11–47]

Types	Operating voltage[a] (V)	Energy density[a] (Wh L^{-1})	Cycle numbers	Major challenges	Cost (\$ kWh^{-1})	Maturity	Ref.
VRFBs	1.2–1.5	15–35	>2000	Cost, solubility, temperature range	280–440	High	11–13
Fe–Cr RFBs	1.0–1.2	10–20	>1000	H_2 evolution, toxicity, kinetics	250–300	Moderate	14 and 15
Li-based HFBs	2.0–4.7	300–1000	>1000	Dendrite, flammability, toxicity	400–500	Low	16–18
Na-based HFBs	1.8–3.0	50–200	<100	Dendrite, flammability, toxicity	100–200	Low	19–22
K-based HFBs	3.1–3.4	20–170	<100	Dendrite, flammability, toxicity	—	Low	23
Mg-based HFBs	1.7–2.5	40–120	<500	Flammability, toxicity, dendrite	—	Low	24–26
Al-based HFBs	1.0–2.0	100–200	<100	Dendrite, passivation, polarization	—	Low	27 and 28
Zn-based HFBs	1.0–2.0	40–210	>2000	Dendrite, H_2 evolution, corrosion	200–250	Moderate	29–32
Fe-based HFBs	0.8–1.2	20–40	<800	Dendrite, H_2 evolution, hydrolysis	125–200	Moderate	33–36
Cd-based HFBs	0.8–2.0	20–250	>1000	Toxicity, dendrite, corrosion	100–210	Low	37–39
Sn-based HFBs	0.7–1.4	30–150	<600	"Dead Sn", powdering, dendrite	220–300	Low	40–43
Cu-based HFBs	0.5–1.3	20–75	<100	Dendrite, H_2 evolution, self-discharge	170–230	Low	44 and 45
Pb-based HFBs	0.7–1.8	20–100	>2000	Toxicity, dendrite, powdering	100–150	Moderate	46 and 47

[a] The wide data range is caused by the use of different cathodic active materials.

MBHFBs.[16–47] Overall, MBHFBs generally exhibit significant benefits, such as high voltage, substantial energy density, and cost-efficiency, attributed to their employment of low working potential, high gravimetric/volumetric capacity, and low-cost metals facilitating multielectron redox reactions (Fig. 2a and b). Based on the differing solvents employed, MBHFBs can be categorized into aqueous MBHFBs and non-aqueous MBHFBs. The use of water as a solvent in aqueous MBHFBs offers several advantages, including high ionic conductivity, environmental benignity, and extremely low cost.[29,30] However, the operational voltage window of aqueous MBHFBs is constrained by the decomposition potential of water, thereby imparting limitations on both the attainable energy density and the selection of metal-based active materials. In contrast, non-aqueous MBHFBs employ solvents other than water, such as organic solvents or ionic liquids. These solvents offer wider operational voltage windows compared to aqueous electrolytes, enabling the use of a broader range of metal-based active materials. However, in comparison to aqueous MBHFBs, non-aqueous MBHFBs pose potential safety risks, environmental concerns, and cost implications.[16,17,23,27,28] Amidst the burgeoning interest in metal deposition–dissolution chemistry within the realm of secondary batteries, as exemplified by the advancements in lithium-ion and zinc-ion batteries, MBHFBs leveraging this chemistry are also experiencing renewed developmental prospects. We have witnessed an astounding increase in publications regarding MBHFBs, especially after 2018 (Fig. 2c). This growth is attributable to their considerable cost-effectiveness and their possession of higher specific capacities, making them highly attractive for a range of energy storage applications.

While we have witnessed a remarkable surge in publications on MBHFBs in recent years, it is undeniable that both the application and development of these batteries, along with the underlying deposition–dissolution chemistry, remain in their nascent stages. This is primarily due to our incomplete understanding of emerging deposition–dissolution chemistry strategies and the various MBHFBs that utilize these strategies: (1) the variety of metals that can be used in MBHFBs is abundant. Key properties such as the redox potential, specific capacity, corrosion resistance, and dendritic growth propensity vary among different metals, leading to distinct challenges faced by various types of MBHFBs. (2) The metal deposition–dissolution process

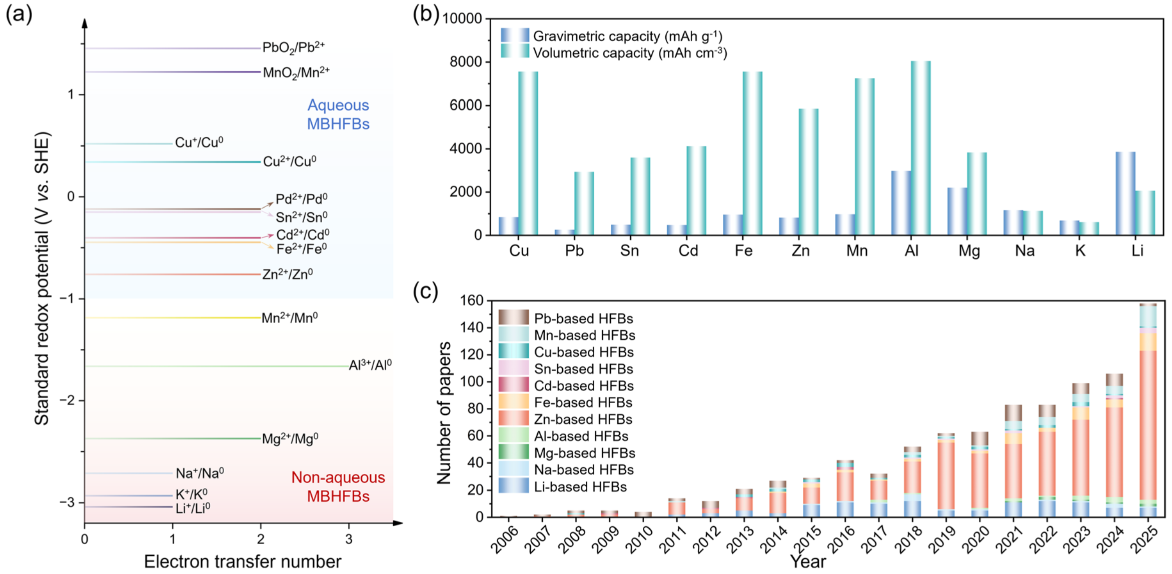

Fig. 2 (a) The standard redox potential and electron transfer number of redox pairs typically employed in MBHFBs. (b) Comparisons of theoretical specific capacity and volumetric capacity among metals and metal oxides typically employed in MBHFBs. (c) Number of publications devoted to different MBHFBs. Data were collected from January 2006 to December 2025 on Web of Science.

exhibits a complex phase transformation phenomenon, characterized by intricate interactions between solid and liquid phases coupled with complicate behavior at the solid–liquid interface. The metal the deposition–dissolution behavior is significantly influenced by multiple factors and interferences, and the current understanding remains insufficient to establish a unified theoretical framework for deposition–dissolution chemistry. Furthermore, to the best of our knowledge, existing review articles on MBHFBs have predominantly focused on specific categories or individual battery systems, such as zinc-based HFBs or zinc–bromine flow batteries, rather than providing a comprehensive overview of the entire field. Within the broader research scope of MBHFBs, conducting a comprehensive and holistic review with deposition–dissolution chemistry as the throughline is a feasible and rational approach, which also helps present readers with a more complete panorama of this field. Various types of MBHFBs possess inherent similarities, and different systems are highly consistent in terms of working principles (all centered on deposition–dissolution chemistry), common challenges (interfacial instability, dendrite growth, side reactions, *etc.*) and core research strategies (design and optimization of key materials, *etc.*), so the corresponding research and development ideas as well as successful strategies are inherently universal. Moreover, the intrinsic correlations between these systems can be rationally utilized: effective technical schemes and mature methods developed for a kind of specific MBHFBs can provide important lessons and insightful references for the research of other MBHFBs, and relevant research achievements and technical paths can also be conveniently inspired and transferred across different systems. Therefore, to facilitate a deeper understanding of the implementation and mechanistic principles of emerging deposition–dissolution chemistry in next-generation flow battery systems, the subsequent sections will focus on establishing a fundamental comprehension of various MBHFBs, encompassing their working principles, inherent advantages, technical challenges, corresponding solution strategies, and future development prospects. This review adopts a historical development perspective to conduct a critical analysis of key issues and existing strategies across different MBHFBs systems, rather than merely compiling the latest research findings. We aim to form a holistic understanding of the entire MBHFBs field, systematically elucidate potential interconnections, and provide comprehensive strategic insights. Furthermore, given that the large-scale application of MBHFBs is still not sufficiently mature, it is both opportune and significant to propose design principles and practical recommendations for the development of reliable next-generation MBHFBs systems. A comprehensive and in-depth analysis of deposition–dissolution chemistry strategies for next-generation MBHFBs is expected to advance the future progress and wider application of large-scale, high-energy-density, low-cost energy storage technologies.

2. Current core issues and challenges

The core advantage of MBHFBs resides in their innovative "hybrid" architecture, which skillfully integrates the high-capacity, depositable/dissolvable metal negative electrode characteristic of traditional batteries with the power/energy decoupling and flowable electrolyte features inherent to flow battery systems. This design confers dual advantages of high energy and power density (surpassing traditional ASFBs), while simultaneously enabling scalable energy storage capacity, simplified system maintenance, and eco-friendly material selection. It thus presents a highly viable pathway for large-scale, long-duration energy storage applications. However, the dual-edged nature of innovation is exemplified by this unique ''hybrid'' architecture: while conferring significant performance enhancements to MBHFBs, it concurrently introduces a series of underlying scientific puzzles and technical challenges that demand systematic investigation (as displayed in Table 1).

(1) The reversible, uniform, and dense deposition of metals on electrodes constitutes one of the core challenges for MBHFBs. By facilitating the repetitive and reversible electrochemical deposition/dissolution of metallic species at electrode, MBHFBs achieve sustained energy storage and release. The reversibility of metal plating/stripping processes critically governs the fraction of active metal that undergoes irreversible inactivation, resulting in the formation of electrically isolated ''dead metal'' after each electrochemical cycle.[40] Consequently, suboptimal reversibility emerges as the primary root cause of accelerated capacity degradation and diminished cycle lifespan in MBHFBs. Non-uniform metal deposition serves as a critical trigger for systemic collapse in battery performance and safety, rather than being confined to a morphological issue. Non-uniform metal deposition, characterized by spatial heterogeneity in metallic deposition, induces inhomogeneous electric field distribution and localized electrochemical gradients. Under operational stresses such as high current densities and prolonged cycling, it initiates a cascade of adverse outcomes including dendritic growth (for the vast majority of metals), accelerated localized metal corrosion, and parasitic side reactions. These processes collectively undermine battery functionality and result in short circuits by creating a vicious cycle.[29,31] The density of metal deposition determines the actual utilization rate of the anode. Loose and porous deposition structures will result in a decrease in areal capacity and an increase in interfacial resistance. Meanwhile, such loose deposition structures are relatively fragile, and the porous deposition structures provide a larger area for parasitic reactions. During the electrolyte circulation process, metals are more prone to partial detachment, leading to flow channel blockage and irreversible capacity loss.[36] While a series of improvement strategies are carried out, including modifications to electrolytes, electrodes, membranes, and flow channels to enable the reversible, uniform, and dense deposition of metals, the outcomes turn out to be significantly different. This difference mainly arises from the inherent fundamental property contrasts among various metal species.

(2) Electrolyte decomposition and interfacial parasitic reactions during electrochemical cycling emerge as a critical technical bottleneck for MBHFB, significantly degrading their cycling performance and energy retention capabilities. The chemical and electrochemical stability of electrolytes is subjected to rigorous scrutiny under the combined influence of elevated redox potentials and high metal reactivity. Non-aqueous electrolytes, despite possessing a comparatively broad electrochemical window, are still plagued by the issue of decomposition under high voltage.[16] In contrast, aqueous electrolytes, characterized by an even narrower electrochemical window, are more susceptible to hydrogen evolution reactions.[34] Beyond electrochemical stability, the persistent contact between the electrolyte and active metals is also prone to parasitic reactions, which result in the irreversible and continuous depletion of both active metals and electrolytes, along with an increase in interfacial impedance.[24,27] These cumulative effects ultimately manifest as a decline in battery capacity and efficiency. While a variety of strategies involving electrolyte or electrode modification have been implemented to alleviate electrolyte decomposition and interfacial parasitic reactions, these approaches merely offer symptomatic relief rather than a root-cause solution.

(3) The ion crossover-induced contamination and solvent migration between catholyte and anolyte during electrochemical cycling also represent critical challenges that significantly compromise the operational stability and energy efficiency of MBHFBs. The ionic cross-contamination and solvent migration (especially water migration) of MBHFBs stem from the inherent and ineliminable concentration gradients and potential differences during battery operation, which drive the directional migration of different species through the membrane. Although the ionic strengths of the catholyte and anolyte are pre-equilibrated prior to the initiation of battery charge–discharge cycling, the ionic concentration undergoes substantial fluctuations during charging and discharging processes owing to the solid–liquid phase transition occurring at the metal deposition side. This induces a significant overall ionic concentration gradient and osmotic pressure across the membrane, which act as the intrinsic driving force for the diffusion of ions from the high-concentration region to the low-concentration region. Concurrently, solvent molecules migrate across the membrane from the side with low ionic concentration toward the side with high ionic concentration. Furthermore, as a result of electromigration, charged ions and the solvent molecules within their solvation shells exhibit continuous migration in response to the reversible change in the direction of the electric field during charge–discharge cycles. Consequently, the combined effects of the ionic concentration gradient, osmotic pressure, and electromigration drive the persistent transmembrane transport of ions and solvents in the electrolyte to achieve equilibrium, thereby leading to the occurrences of ionic cross-membrane contamination and solvent migration.[29] Notably, the unique solid–liquid phase transition inherent to MBHFBs further exacerbates these issues, which significantly compromises the actual service life of the battery. The severity of these two issues is directly dependent on the performance of the membrane, which has consequently attracted substantial research efforts. Currently, the core focus of relevant studies lies in the development of highly selective ion-exchange membranes or porous membranes. Nevertheless, achieving high performance and low cost simultaneously remains a significant challenge for the design and fabrication of such membranes.

The aforementioned three scientific issues represent the most prominent challenges in MBHFBs. Nevertheless, owing to the extensive diversity of metal species and the distinctiveness of their respective physicochemical properties, the challenges confronting different MBHFBs are rendered far more intricate. For instance, Li and Zn are more susceptible to dendrite formation compared to Mg and Sn. Beyond the metal anode side, the adoption of distinct cathodic active materials may also give rise to new challenges for MBHFBs. To facilitate a more comprehensive, in-depth, and meticulous analysis of these scientific issues and challenges, this review will elaborate on them in subsequent chapters, incorporating various types of representative MBHFBs.

3. Non-aqueous metal-based hybrid flow batteries

Given the urgent demand for energy storage technologies with higher energy density, non-aqueous MBHFBs have emerged as a critical approach to overcoming the performance bottlenecks of traditional flow batteries, owing to their distinctive electrolyte systems and deposition–dissolution chemistry. By adopting organic solvents or ionic liquids as electrolytes, these MBHFBs remarkably widen the electrochemical window (>4 V), thereby enabling the employment of high-potential cathodes and low-potential metal anodes (*e.g.*, lithium, sodium, potassium, magnesium, aluminum). Theoretically, non-aqueous MBHFBs can achieve an energy density several times higher than that of aqueous systems. Depending on the differences in composition and reaction mechanisms, the cathodic materials of non-aqueous MBHFBs can be classified into solid-suspended cathodes, soluble cathodes, and redox-targeting medium cathodes, reflecting the diversity of material design strategies. Nevertheless, their development is still plagued by critical challenges, including the flammability and high cost of organic solvents, uneven deposition and dendrite growth during the metal deposition/dissolution processes, as well as interfacial side reactions under long-term cycling conditions. A comprehensive review of the research progress on five typical non-aqueous MBHFBs, represented by lithium, sodium, potassium, magnesium, and aluminum, is conducive to facilitating researchers in advancing the innovation of next-generation non-aqueous MBHFBs technologies.

3.1. Lithium (Li)-based hybrid flow batteries

Lithium (Li) metal batteries are recognized as potential high-energy-density power sources, owing to their high theoretical capacity (3860 mAh g^{-1} or 2061 mAh cm^{-3}) and low redox electrochemical potential (-3.04 V *vs.* standard hydrogen electrode, SHE).[48] To facilitate large-scale energy storage, Li-based HFBs have emerged as a potential battery technology that integrates the functional principles of lithium metal batteries with non-aqueous electrolytes, while operating in a manner of redox flow batteries.[49,50] Based on the diverse designs and principles of the cathode, Li-HFBs can be divided into four categories: Li-slurry HFBs, Li–O_2 HFBs, Li-soluble HFBs, and Li-targeting HFBs (Fig. 3). However, the anode side of these Li-HFBs often faces the problem of uneven Li deposition, and more seriously, dendrites may form. Li dendrite growth-induced battery short circuits are one of the most critical factors affecting the long-term use of Li-HFBs. Common irregular deposition morphologies in lithium batteries mainly include whisker-like dendrites, mossy dendrites, tree-like dendrites, and random spheres (Fig. 4).[51] How to promote uniform metal deposition and inhibit dendrite growth is one of the core issues in lithium battery research, and it is obvious that these hidden dangers now also plague the development of Li-HFBs. Dendrite growth results from uneven metal electro-deposition and uncontrolled crystal growth. To address this, researchers should deeply understand the scope and boundary conditions of classical electrodeposition theories, and clarify the intrinsic and extrinsic factors affecting dendrite growth.

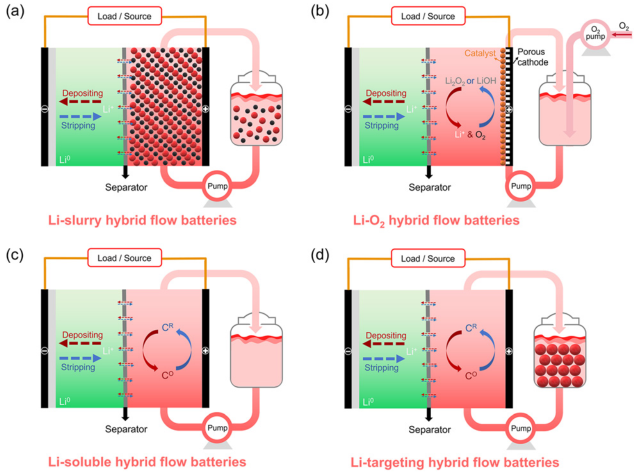

Fig. 3 Configurations of four important Li-based HFBs. (a) A typical configuration of Li-slurry HFBs featuring a lithium metal anode, alongside solid active materials and conducting agents suspended within the cathodic electrolyte. (b) A standard design of Li–O_2 HFBs comprising a lithium metal anode, with oxygen (O_2) circulating within the cathodic electrolyte. (c) A representative schematic depiction of Li-soluble HFBs featuring a lithium metal anode, accompanied by soluble redox-active materials in the cathodic electrolyte. (d) A typical arrangement of Li-targeting HFBs comprising a lithium metal anode, coupled with solid redox-targeting active materials dispersed within the cathodic energy storage tanks.

3.1.1. Electrodeposition behaviors and theories. A typical electrodeposition process of metal ions generally includes (Fig. 4): (i) diffusion of metal ions through the bulk electrolyte; (ii) de-solvation of metal ions and dissociation from coordinating anions; (iii) adsorption of metal ions onto the electrode surface followed by reduction to atomic species; (iv) self-diffusion of adsorbed atoms across the electrode surface and subsequent nucleation; (v) crystal growth from nuclei *via* electro-crystallization. The time-voltage curve of uniform electrodeposition for conventional metal typically comprises three stages: nucleation, growth, and steady-state; whereas in highly reactive metal systems such as lithium and zinc, an undesired stage characterized by uncontrolled dendritic growth appears.[52,53] With respect to achieving uniform electrodeposition, two predominant theories currently hold sway within the electrochemical community: diffusion limited theory and nucleation theory. In diffusion limited theory, the electrochemical reaction rate and diffusion rate are considered as the two determining factors affecting the electrodeposition morphology. Diffusion rates encompass both the transport of metal ions within the electrolyte and the self-diffusion of metal atoms at the electrode surface. The diffusion limited theory posits that Sand's time (τ_{stand}) and limited current (i_L) serve as the critical parameters governing

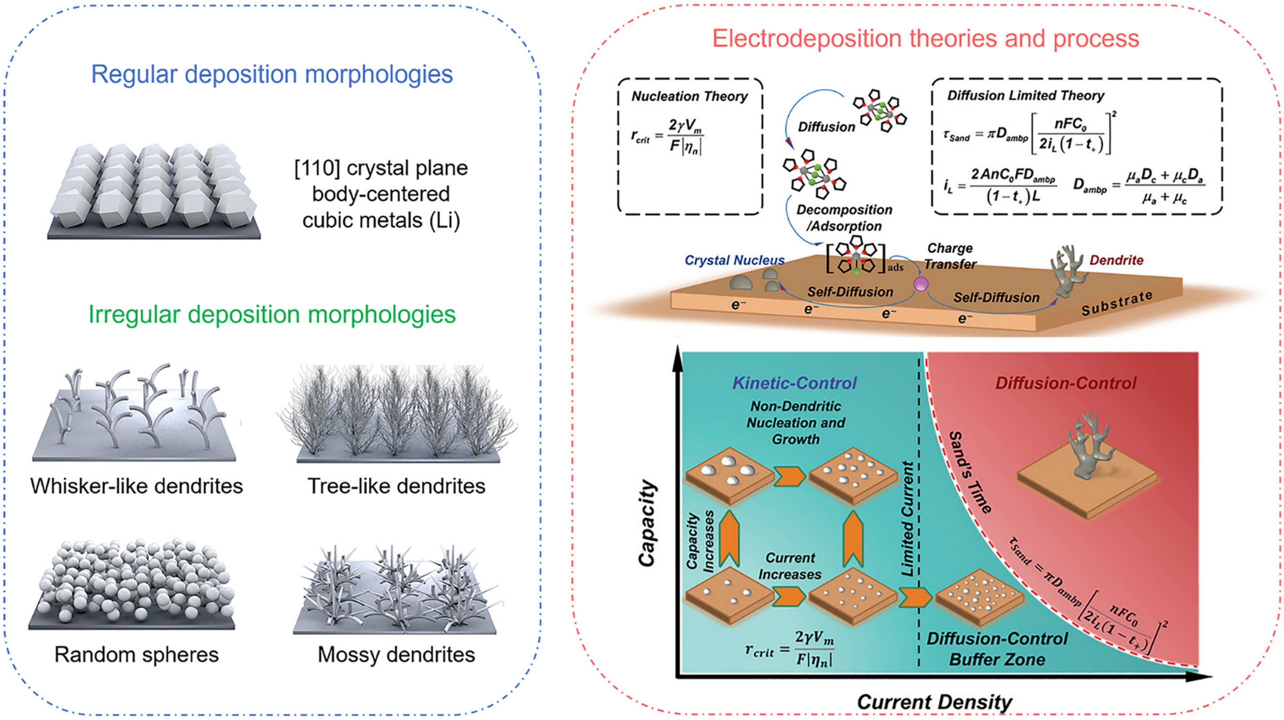

Fig. 4 Left: Schematic diagrams of ideal regular deposition morphologies and common irregular deposition morphologies for lithium batteries. Reproduced from ref. 51 with permission from American Association for the Advancement of Science, copyright 2025. Right: Schematic diagram of the electrodeposition process, electrodeposition theories and their boundary conditions. Reproduced from ref. 57 with permission from Wiley-VCH, copyright 2023.

the maximum allowable current density and deposition duration for safe electrodeposition practices.[54] These variables define the kinetic boundary between uniform plating and dendritic instability, with τ_{stand} reflecting mass transport limitations and i_L delineating the onset of diffusion-controlled growth regimes. In other words, when the applied current density exceeds i_L, dendritic deposits initiate after a critical timescale (τ_{stand}), commencing with a tip-growth mode. This threshold demarcates the transition from stable plating to morphologically unstable growth, where mass transport limitations override kinetic stabilization mechanisms. In nucleation theory, the applied current density governs electro-crystallization by modulating both the reduction rate of metal ions at the electrode surface and the critical nucleus size for crystallization. This nucleation theory can be interpreted as: small overpotential (η) facilitates the growth of existing crystals, while large overpotential (η) induces the nucleation of small new crystals. According to the equation, the critical spherical crystal nucleation radius (r_{crit}) is inversely proportional to the η, while the nucleation density is directly proportional to the cube of the η.[55] And the applied current density is directly proportional to both the nucleation overpotential (η_n) and the nucleation-growth overpotential (η_g).[56] Therefore, under the nucleation theory, the uniformity of electrodeposition requires small crystals, which can be achieved by increasing polarization (*i.e.*, high overpotential or high current density). The recommendations from diffusion limited theory and nucleation theory for avoiding dendritic growth and achieving uniform electrodeposition appear to diverge. This discrepancy primarily arises because the two theories apply to distinct boundary conditions: the former is relevant under diffusion-rate-limited regimes, while the latter operates within electrochemical-kinetics-limited regimes. To reconcile these theories, Cui and colleagues introduced the concept of a "diffusion-controlled buffer regime", which bridges the kinetic transition between mass transport limitations and surface reaction dynamics.[57] Within this buffer regime, uniform and dense deposition is achieved even when the applied current density exceeds the i_L, yet the deposition duration remains below the τ_{stand}. It is important to note that while the aforementioned theories have been well-validated in metal batteries (*e.g.*, lithium, zinc, and magnesium batteries), their direct applicability to MBHFBs remains to be thoroughly verified. This limitation stems from fundamental differences in operational conditions: MBHFBs employ continuously circulating rather than static electrolytes, and utilize porous carbon felt substrates instead of dense metal foils for electrodeposition. Therefore, the electrodeposition behavior of metals in MBHFBs and the underlying theories involved may be more complex.

Once the boundary conditions are exceeded, uniform electrodeposition becomes unattainable. The apical deposits experience elevated current densities, triggering self-accelerating tip growth. This self-accelerating tip growth, coupled with the formation of an ion-depleted layer adjacent to the electrode, is named as dendritic growth. The boundary conditions for dendritic growth vary across metals, primarily due to the interplay of intrinsic factors (*e.g.*, thermodynamic properties, reaction kinetics) and extrinsic factors (*e.g.*, local current distribution,

ion diffusion). Thermodynamic properties of metals are critical factors determining deposition morphology. The nucleation/growth processes of different metals are constrained by crystal planes with varying orientations. When crystals exhibit anisotropy, their growth rates differ across crystal planes: crystal planes with the lowest surface energy are preferentially exposed, exhibit slower growth rates, and are more prone to nucleate, ultimately forming metal crystals with thermodynamically equilibrium structures.[58] However, researchers can employ effective strategies to expose more dominant facets (with strong corrosion resistance), regulate electro-crystallization orientations, and optimize grain boundaries, thereby improving deposition morphology. For external causes, under high current density, the superposition of activation polarization and concentration polarization forms an electrochemical-mass transfer coupled polarization, which drives the rapid growth of dendrites. Due to the non-uniform environment on the electrode surface, the current density distribution is also uneven. In local areas such as electrode edges or defects, the current density becomes excessively high, causing the ionic reduction rate to far exceed the diffusion rate. This triggers the "tip effect", further accelerating dendrite growth. The charge transfer resistance varies across different regions of the electrode surface. Areas with lower resistance exhibit faster charge transfer rates, leading to more rapid ion reduction and deposition, which preferentially forms dendrite nuclei. Therefore, by rationally designing the electrode geometry, it is possible to achieve smaller local currents under larger apparent currents, thereby inducing uniform deposition morphology. Additionally, when the ion migration rate in the electrolyte is lower than the electrochemical reaction rate, the ion concentration at the electrode surface decreases, forming a concentration gradient. In low-concentration regions (due to insufficient ion supply), the deposition rate slows down, while in high-concentration regions (such as dendrite tips), deposition accelerates, exacerbating dendrite growth. Therefore, how to utilize favorable flow to reduce this concentration polarization is worth considering for suppressing dendrite growth, especially since this is a unique advantage of flow batteries. Besides the electric field and ion concentration field, the stress field and temperature also affect dendrite growth. Stress can be divided into internal stress and external stress. Internal stress arises from drastic volume changes during electrodeposition, attributed to atomic migration through grain boundaries under non-equilibrium growth conditions.[59] Under internal stress, metal deposits may evolve into dendrites of various morphologies. External stress, generated by compressive stress from adjacent solid interfaces (*e.g.*, SEI and separator), can suppress dendrite growth when appropriately applied.[60] Operating temperature can regulate the distribution of nucleation sites, and the temperature-dependent nucleation process can be described by the classical heterogeneous nucleation theory. Only by thoroughly grasping the intrinsic and extrinsic causes of dendrite formation of different metal ions can researchers better develop strategies to suppress dendrite growth.

3.1.2. Li-slurry HFBs. The Li-slurry HFBs boast remarkable energy density, stemming from its Li anode featuring an ultra-low potential and a slurry cathode offering exceptionally high capacity. It is worth noting that employing active materials in slurry form within the flow battery reaction allows for the circumvention of solubility limitations imposed on active materials in electrolytes. Nonetheless, this approach imposes stricter criteria for the rheological characteristics and electrical conductivity of the slurry. As depicted in Table 2 and Fig. 5a, Chiang's group first completed a proof of concept for Li-slurry HFBs in 2011, using $LiCoO_2$ (LCO), $LiNi_{0.5}Mn_{1.5}O_4$, and $Li_4Ti_5O_{12}$ (LTO) slurries as cathode.[61] More detailly, these slurries are meticulously prepared through a sonication technique, ensuring a homogeneous dispersion of the cathodic active materials, conductive agents (specifically, Ketjen black), and $LiPF_6$, uniformly blended within an alkyl carbonate or dioxolane (DOL) electrolyte. The researchers tested the rheological properties and ionic conductivity of $LiCO_2$-based slurry, and emphasized the crucial role of conductive agents in slurries by visually depicting the dense conductive network formed by Ketjen black through a wet scanning electron microscopy (SEM) image. Despite the relatively rudimentary nature of the research conducted at that time, it still offers a foundational paradigm for the preparation and investigation of slurries available for Li-HFBs. Subsequently, a variety of mature electrode materials, previously utilized in lithium-ion batteries (LIBs), have progressively been adopted as active materials for the cathodic slurries in Li-HFBs. As seasoned cathodic materials in the realm of commercial LIBs, LCO,[61,62] $LiFePO_4$ (LFP),[63–66] $LiNi_xCo_xM_xO_2$ (LNCM),[67–69] and $LiMn_2O_4$ (LMO),[70] have naturally transitioned into applications within Li-HFBs. Some other custom-synthesized cathodic active materials of LIBs (such as $LiMn_{0.7}Fe_{0.3}PO_4$) have also exhibited impressive performance.[71] Moreover, as anodic materials of commercial LIBs, LTO,[61,72,73] graphite,[68] silicon,[74–76] and oxide (such as SiO_x,[77,78] Nb_2O_5,[79] SnO_2@$ZnCo_2O_4$,[80] MnO,[81] *etc.*), have also been studied in Li-HFBs.

Generally, the assessment of the most crucial performance indicators (conductivity, fluidity, and stability) for slurries is comprehensively demonstrated through a combination of electronic conductivity test curves (Fig. 5b), ionic conductivity test curves (Fig. 5c), viscosity test curves (Fig. 5d), and static experiment assessment (Fig. 5e). To improve the conductivity, fluidity, and stability of slurries comprising solid active materials, thereby enhancing the performance of Li-slurry HFBs, the incorporation of suitable and optimally metered quantities of conductive additives represents a crucial approach. Commonly utilized conductive agents primarily encompass carbon black (Fig. 5f, such as Ketjen black [KB], Super-P, acetylene black, *etc.*), carbon nanotubes (Fig. 5g, including single-walled carbon nanotubes [SWCNTs] and multi-walled carbon nanotubes [MWCNTs]), and graphene (Fig. 5h).[82] Among them, KB is the most prevalently employed in lithium-slurry HFBs, owing to its distinctive branched chain structure and good conductivity, thereby facilitating the formation of a dense and efficient conductive network. It is worth noting that while the incorporation of the conductive agents facilitates an enhancement in the electronic conductivity of the slurry, it concurrently leads to an inevitable augmentation in its viscosity. Thereby, the researchers conducted an array of

Table 2 Various key materials utilized in Li-slurry HFBs, including active materials, conducting agents, electrolyte solvents, salt, current collector and separator[61–81]

Active materials	Conducting agents	Electrolyte solvents	Salt	Current collector	Separator	Ref.
$LiCoO_2$ (LCO), $LiNi_{0.5}Mn_{1.5}O_4$, $Li_4Ti_5O_{12}$ (LTO)	Ketjen black (KB)	Alkyl carbonate, dioxolane (DOL)	$LiPF_6$	Al@Au plate	Celgard 2500, Tonen	61
LCO	None	Ethylene carbonate (EC) : ethyl methyl carbonate (EMC) (3 : 7 v/v)	$LiPF_6$	Al foil	Polypropylene/polyethylene/polypropylene	62
Carbon-coated $LiFePO_4$ (LFP)	KB	EC : dimethyl carbonate (DMC) (1 : 1 w/w)	$LiPF_6$	Al foam	Celgard 2500	63
LFP	None	EC/diethyl carbonate (DEC)	$LiPF_6$	Carbon felt/cloth/paper	Glass fiber	64
LFP	—	—	LiTFSI	—	Celgard||Nafion/PVDF/	
$Li_{6.4}La_3Zr_{1.4}Ta_{0.6}O_{12}$||Celgard	65					
LFP	KB	EC : DMC (1 : 1 w/w)	LiTFSI	Al plate	Celgard 2325	66
$LiNi_{1/3}Co_{1/3}Mn_{1/3}O_2$ (LNCM111)	KB	EC : DMC (1 : 1 w/w)	$LiPF_6$	Al/Ti plate	Celgard 2500	67
$LiNi_{0.8}Co_{0.1}Mn_{0.1}O_2$ (LNCM811), carbon coated LFP, carbon coated LTO, graphite	KB	EC : DMC (3 : 7 w/w)	$LiPF_6$, LiTFSI	—	—	68
$LiNi_{0.6}Co_{0.2}Mn_{0.2}O_2$ (LNCM622)	KB: multi-walled carbon nanotubes (MWCNTs) (1 : 1 w/w)	EC : DMC (3 : 7 w/w)	$LiPF_6$	—	Celgard 2325	69
$LiMn_2O_4$ (LMO), LMO-Fe_3O_4-CNT	KB	EC : DMC : DEC (1 : 1 : 1 v/v/v)	$LiPF_6$	Al plate	Celgard 2400	70
$LiMn_{0.7}Fe_{0.3}PO_4$	KB, MWCNTs, graphene nanoplatelets (GNPs)	EC : DMC (3 : 7 w/w)	$LiPF_6$	Al plate	Homemade separator (NPE)	71
LTO	KB, C-NERGY™ Super C45	Propylene carbonate (PC)	LiTFSI	Steel	Glass-fiber separators (Whatman GF/D)	72
LTO	None	EC : EMC (3 : 7 v/v)	$LiPF_6$	Al wire	Polypropylene/polyethylene/polypropylene	73
Silicon (Si)	KB	EC : DMC (1 : 1 w/w)	$LiPF_6$	Cu foam	Celgard 2500	74
Si@C nanocomposite	KB	EC : DEC (1 : 1 v/v)	$LiPF_6$	Cu foil	Celgard 2325	75
Nanosilicon	KB	EC : DMC (3 : 7 v/v)	$LiPF_6$	Ni foam	Double-sided ceramic	76
Micro-sized SiO_x@C	KB, single-walled carbon nanotubes (SWCNTs)	EC : DMC (3 : 7 w/w)	LiTFSI	Ni foam	Celgard 2325	77
SiO_x@lithiated polymer laye/SWCNT-COOH	SWCNTs	EC : DMC (3 : 7 w/w) + 10 wt% fluoroethylene carbonate (FEC)	LiTFSI	Ni foam	Celgard 2325	78
T-Nb_2O_5@C/CNTs	KB	EC : DMC (3 : 7 w/w)	LiTFSI	Ni foam	Celgard 2325	79
SnO_2@$ZnCo_2O_4$	Acetylene black	EC : DEC : DMC (1 : 1 : 1 v/v/v)	$LiPF_6$	Cu plate	Polypropylene	80
MnO@C/CNTs	None	EC : DMC (3 : 7 w/w)	LiTFSI	Cu plate	Celgard	81

meticulous tests aimed at determining the optimum usage amount of the conductive agents. However, discrepancies in kinds and mixing methods (such as ball milling or ultrasonic treatment) of solid active materials, conductive agents and electrolytes, coupled with inconsistent testing conditions for electronic/ionic conductivity and viscosity of slurries, pose challenges in determining precise and uniform optimum usage amount of the conductive agents. Another method to enhance the conductivity of the slurry is to pre-composite the solid active materials with conductive materials (as depicted in Fig. 5i), thereby eliminating the need for adding additional conductive agents, ultimately maximizing the utilization efficiency of the conductive materials and minimizing the adverse impact on the viscosity of slurry. More profoundly, the electric and force fields within the battery, the transport of ions and electrons, as well as the rheological properties of the slurry, are simulated and thoroughly discussed with the aid of computational science.[66]

Typically, the chosen lithium salt is lithium hexafluorophosphate ($LiPF_6$), lithium bis(trifluoromethanesulfonyl)imide (LiTFSI), and lithium perchlorate ($LiClO_4$), respectively. The prevalent solvent utilized in the electrolytes is a mixed solvent comprising carbonate. The chosen separator is Celgard, glass fiber, Nafion/PVDF membrane, and ceramic membrane, *etc*. The current collectors utilized in Li-slurry HFBs typically comprise aluminum (Al), titanium (Ti), steel, copper (Cu), and nickel (Ni), respectively, in the forms of plates, foils, or foams. The residence thickness of the slurries on the electrode has a direct bearing on the battery's performance, and the dynamic equilibrium between the flow resistance and motive force of the slurries on the electrode facilitates a nuanced balance between power output and auxiliary pumping. Therefore, it is particularly noteworthy to emphasize that the designs of the current collectors and the flow field frames hold paramount importance for Li-slurry HFBs.[50] On the one hand, for slurry transport, carbon felts with a three-dimensional porous structure are preferred as current collectors due to their ability to provide more efficient and stable pathways for electron transfer.[64] On the other hand, flow channel designs with a larger surface area, such as serpentine flow channels, can offer enhanced flow quantity for the slurry and facilitate more thorough and stable contact between

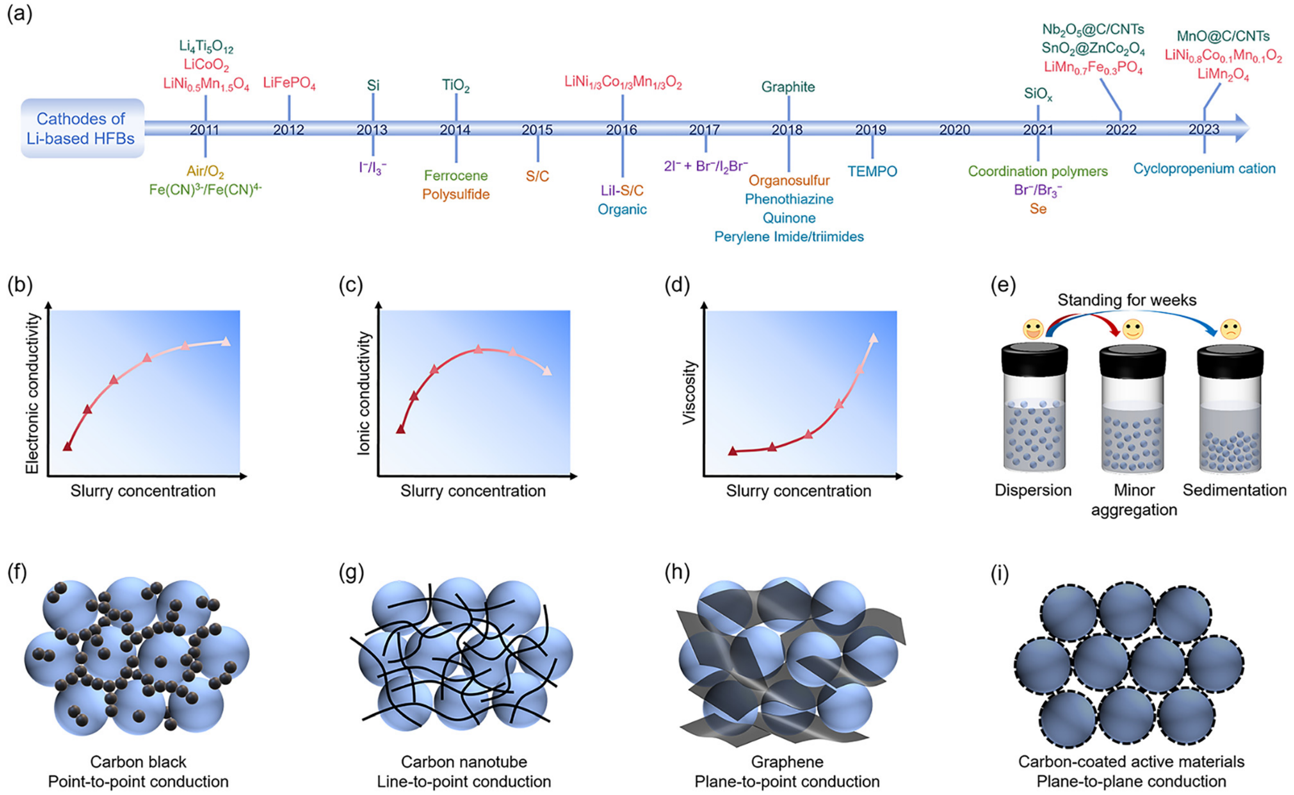

Fig. 5 (a) The timeline of cathodes for Li-based HFBs over recent decades. (b–e) Key performance indicators evaluation of slurries: (b) electronic conductivity test curves, (c) ionic conductivity test curves, (d) viscosity test curves, and (e) static experiment assessment. Methods for improving the conductivity of slurries: (f)–(h) mechanical mixing with carbon and (i) carbon coating. Adapted from ref. 82 with permission from The Royal Society of Chemistry, copyright 2010.

the slurry and the electrode. These features are conducive to the electrochemical reactions of the active materials in the slurry, thereby enhancing battery performance.

3.1.3. Li–O_2 HFBs. Li–O_2 batteries are widely regarded as one of the most promising energy storage systems, attributed to their exceptional energy density, which can reach up to 3500 Wh kg^{-1}, and the utilization of oxygen as a clean and plentiful energy source. The most significant distinction between Li–O_2 HFBs and Li–O_2 batteries lies in the decoupling of maximum energy storage from power capability. The energy density and power density of Li–O_2 HFBs are primarily governed by the volume of the electrolyte reservoir and the electrochemical reactor, respectively. In comparison to other Li-based HFBs, Li–O_2 HFBs incorporate an air inlet within their electrolyte reservoirs. This design ensures that an ample supply of oxygen can penetrate into the electrolyte, subsequently being circulated to the electrodes where it undergoes redox reaction. On the anodic side of Li–O_2 HFBs, which utilize a non-aqueous electrolyte, the processes of Li deposition and dissolution take place, primarily confronted with the issue of lithium dendrite formation. As a configuration of Li–O_2 HFBs, when the cathodic side employs a non-aqueous electrolyte, oxygen reacts with Li^+ ions in the electrolyte through a two-electron process to produce Li_2O_2, achieving a discharge voltage of approximately 2.7 V, as shown in eqn (1).[83] However, major challenges still remain (as depicted in Fig. 6a), including low oxygen solubility in non-aqueous electrolytes, slow diffusion rates of oxygen and Li^+ ions, and instability of non-aqueous electrolytes that are prone to decomposition, forming insulating byproducts (such as Li_2O_2, $LiCO_3$, LiOH, and some organic compounds) that coat the electrode surface and adversely affect the battery's energy conversion efficiency and lifespan. Besides, the cathode faces a significant challenge of requiring a membrane that can block CO_2 and H_2O while allowing O_2 to pass through. Another configuration of Li–O_2 HFBs involves the use of an aqueous electrolyte on the cathodic side, where oxygen undergoes a reversible four-electron redox reaction (as shown in eqn (2) and (3)), achieving voltages of 3.4 and 4.2 V in acidic and alkaline electrolytes, respectively.[84] Since the cathodic side itself employs an aqueous electrolyte, there is no longer a need to prevent atmospheric H_2O from entering the cathode, which represents one of the most critical factors in achieving stable cycling performance for Li–O_2 HFBs.

$$O_2(g) + 2Li^+ + 2e^- \rightarrow Li_2O_2 \quad \varphi \approx 2.7\ \text{V}\ vs.\ Li^+/Li \tag{1}$$

$$O_2(g) + 2H_2O + 4e^- \rightarrow 4OH^-(aq.) \quad \varphi^\circ \approx 3.4\ \text{V}\ vs.\ Li^+/Li \tag{2}$$

$$O_2(g) + 4H^+(aq.) + 4e^- \rightarrow 2H_2O \quad \varphi^\circ \approx 4.2\ \text{V}\ vs.\ Li^+/Li \tag{3}$$

Alkaline catholyte generally opt for LiOH as supporting salt, with the co-existence of $LiClO_4$, $LiNO_3$ or LiCl, which can

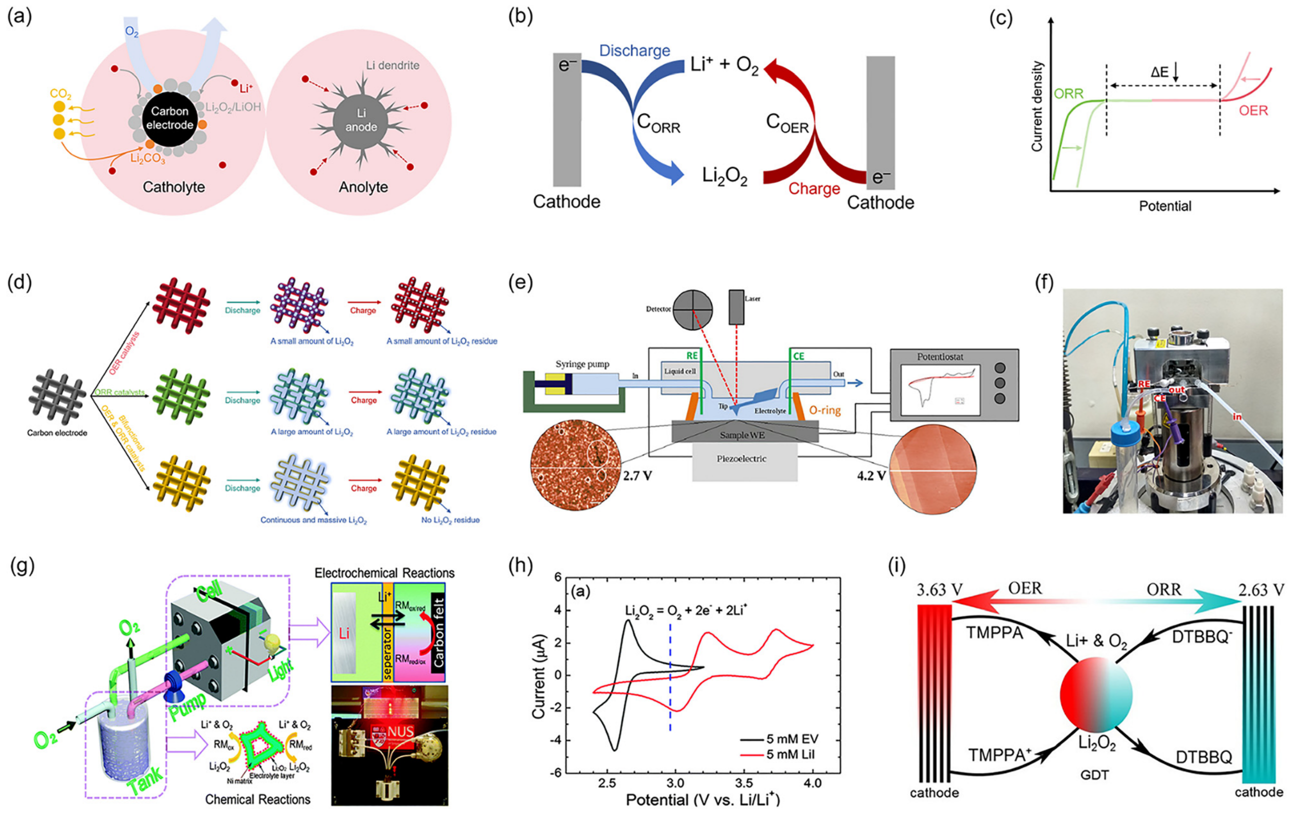

Fig. 6 (a) A schematic diagram illustrating the major challenges faced by the cathode and anode during the charging and discharging processes of non-aqueous Li–O_2 HFBs. (b) and (c) The working principles of oxygen reduction reaction (ORR) and oxygen evolution reaction (OER) catalysts in non-aqueous Li–O_2 HFBs. (d) The working principles of bifunctional OER/ORR catalysts in non-aqueous Li–O_2 HFBs. (e) and (f) Scheme and installation of the Flowing Electrochemical Atomic Force Microscopy (FE-AFM). Reproduced from ref. 85 with permission from Elsevier, copyright 2021. (g) Schematic illustration of the configuration and working process of Li–O_2 HFBs with redox mediators. Reproduced from ref. 86 with permission from The Royal Society of Chemistry, copyright 2015. (h) Cyclic voltammograms of redox mediators (ethyl viologen and LiI) in tetraethylene glycol dimethyl ether. Reproduced from ref. 86 with permission from The Royal Society of Chemistry, copyright 2015. (i) Diagram describing DTBBQ/TMPPA-catalyzed ORR and OER reactions during the charging and discharging processes of Li–O_2 HFBs. Reproduced from ref. 87 with permission from American Chemical Society, copyright 2016.

effectively furnish an alkaline environment, favorable for the oxygen reduction reaction (ORR), and exhibit adequate Li^+ ions conductivity. Furthermore, the discharge product primarily consists of LiOH, which is highly soluble in water. This solubility effectively mitigates issues of electrode passivation and blockage, thereby enhancing cyclic stability. However, for Li–O_2 HFBs with alkaline electrolyte, the intrusion of CO_2 may lead to the formation of Li_2CO_3, which is difficult to dissolve and decompose. Therefore, it is necessary to coat the outer surface of the cathode with a protective membrane to allow O_2 diffusion while blocking CO_2, or alternatively, to pre-remove CO_2 from the air. For acidic catholyte, weak acids with high dissociation constants are preferred as the active species, with CH_3COOH/CH_3COOLi and H_3PO_4/LiH_2PO_4 buffers serving as prime examples. Compared to alkaline catholyte, the adverse effects of CO_2 infiltration are less significant in acidic catholyte. However, both acidic and alkaline catholyte face nearly identical challenges in terms of separators, due to the use of aqueous and non-aqueous electrolytes on the cathodic and anodic sides respectively. The qualified separators must effectively isolate water and organic solvents, facilitate rapid Li^+ ions conduction, and exhibit tolerance to organic solvents, acidic and alkaline environments.

The pursuit of highly efficient, durable, and cost-effective oxygen evolution reaction (OER)/ORR catalysts is the other key to the advancement of Li–O_2 HFBs. As depicted in Fig. 6b and c, OER catalysts are capable of reducing the activation energy for the oxidation of discharge products, which leads to a decrease in OER voltage and facilitates the oxidation reaction, thereby enhancing the charging rate of batteries. Conversely, ORR catalysts decrease the activation energy for the oxygen reduction reaction, resulting in an increase in ORR voltage and enabling oxygen to more readily accept electrons and undergo reduction, ultimately improving the discharge rate of batteries. Initially, cathode materials with special structures coupled with high-performance heterogeneous catalyst were extensively investigated to enhance the kinetics of Li–O_2 HFBs. These materials encompassed carbonaceous materials, metal oxides (including perovskites and spinels), metal nitrides, noble metals, and others. Currently, the primary directions for catalyst development are focused on bifunctional OER/ORR catalysts, homogeneous catalysts, and single-atom catalysts. As depicted in Fig. 6d, when Li–O_2 HFBs employ only an OER catalysts, the discharge process remains unaffected. However, during charging, the electrochemical deposition of Li_2O_2 onto the cathode causes cathode passivation, which hinders the effectiveness of the OER catalysts and even results in incomplete decomposition of Li_2O_2. When only ORR catalysts are introduced into Li–O_2 HFBs, the discharge capacity is enhanced. However, this enhanced discharge process is detrimental to the decomposition of Li_2O_2 during charging, leading to poor rechargeability. Therefore, only by utilizing highly active and stable bifunctional OER/ORR catalysts can both the discharge capacity and rechargeability of Li–O_2 HFBs be simultaneously improved, enabling more stable battery operation. Corti and colleagues utilized an advanced Flowing Electrochemical Atomic Force Microscopy (FE-AFM) technology to enable *in situ* characterization of the morphology of Li_2O_2 during discharging and charging (Fig. 6e and f).[85] This technique offers a more intuitive view into the mechanisms underlying the formation and decomposition of Li_2O_2, thereby facilitating the screening of suitable catalysts and enabling *in situ* investigations into the mechanisms of ORR/OER. However, the majority of existing bifunctional OER/ORR catalysts belong to the category of heterogeneous catalysts, which still cannot avoid the issues of cathode passivation and clogging, ultimately leading to catalyst deactivation, especially under conditions of deep discharge. Consequently, employing redox mediators as soluble homogeneous catalysts not only fulfills the catalytic requirements for OER/ORR but also alleviates the problems of electrode passivation and clogging. Wang and his team, for the first time, simultaneously introduced two distinct redox mediators to separately catalyze the ORR and OER of O_2 during the discharge and charge processes, completely circumventing the need for traditional catalysts on the cathode.[86] The gas diffusion tank (GDT) is filled with a porous material, maintaining a constant O_2 pressure through gas inlet and outlet valves (Fig. 6g). Owing to the redox potentials of ethyl viologen (EV^+/EV^{2+}) and iodide ($I^-/I_3^-/I_2$) span precisely the redox potential of Li_2O_2 (Fig. 6h), EV^{2+} and I^- have been identified as the mediators for the ORR) and OER, respectively. Furthermore, Wang and his team employed a pair of soluble redox catalysts, namely 2,5-di-*tert*-butyl-*p*-benzoquinone (DTBBQ) and tris{4-[2-(2-methoxyethoxy)ethoxy]phenyl}amine (TMPPA), in Li–O_2 HFBs.[87] As shown in Fig. 6i, during discharge, oxygen is rapidly reduced by $DTBBQ^{\bullet -}$ to form Li_2O_2 in the presence of Li^+. Upon charging, Li_2O_2 is oxidized by $TMPPA^{\bullet +}$ to release oxygen. It is noteworthy that this redox-mediated ORR and OER process enables the formation and oxidation of Li_2O_2 to occur in a separate gas diffusion tray rather than directly on the cathode of the battery, thereby circumventing the issues of surface passivation and pore blockage of the electrode.

3.1.4. Li-soluble HFBs. The primary cathodic active materials commonly employed in Li-soluble HFBs include metal complexes, halogens, polysulfides, and organic substances. In 2011, Lu *et al.* pioneeringly reported the utilization of the $Fe(CN)_6^{3-}/Fe(CN)_6^{4-}$ redox couple in a neutral aqueous electrolyte as the cathode, coupled with a non-aqueous Li anode, to assemble Li-soluble HFBs.[88] The battery demonstrated a stable discharge platform of approximately 3.4 V and exhibited good coulombic efficiency (Fig. 7a). However, the limited solubility of $Fe(CN)_6^{3-}/Fe(CN)_6^{4-}$ resulted in an unsatisfactory energy density. Zhao *et al.* have formulated non-aqueous Li-soluble HFBs by dissolving ferrocene in an organic solvent to serve as the cathodic electrolyte. After enduring 250 full charge–discharge cycles, the battery demonstrated a coulombic efficiency of approximately 95% and a capacity retention rate of roughly 90%.[89] Building upon this foundation, Wang's team synthesized ferrocenylmethyl dimethyl ethyl ammonium bis(trifluoromethanesulfonyl)imide (Fc1N112-TFSI) with enhanced solubility and voltage to serve as the cathodic active material (as depicted in Fig. 7b). Additionally, they employed a Li–graphite composite anode and incorporated 2.0 wt% fluoroethylene carbonate (FEC) into the electrolyte to mitigate lithium anode dendrite growth and stabilize the solid electrolyte interphase (SEI). The battery exhibited a voltage of 3.5 V, an energy density of approximately 50 Wh L^{-1}, and an energy efficiency greater than 75%.[90] Li and colleagues have introduced alkyl pyridine derivatives into ferrocene, enabling multi-electron transfer with enhanced solubility and voltage.[91] Beyond molecular synthesis strategies, Yu and colleagues have leveraged strong molecular interactions to achieve high concentrations of redox-active materials by forming organic eutectic electrolytes without the need for auxiliary solvents.[92] More specifically, their experiments involved mixing methoxy-functionalized ferrocene derivatives with LiTFSI to form a high-concentration liquid electrolyte at room temperature (Fig. 7c). This electrolyte led to over a three-fold increase in solubility and achieved a high discharge energy density of 188 Wh kg^{-1}. In addition to ferrocene and its derivatives, cobaltocene has also been demonstrated to exhibit good applicability in Li-soluble HFBs.[93]

Halogen-based redox couples, such as Br_3^-/Br and I_3^-/I^-, exhibit significant potential in Li-soluble HFBs due to their low molecular weights, good conductivity, rapid redox reactions, and high redox reversibility. In addition, halogen-based cathodic electrolytes have high redox potential, multiple electron transfer, and high solubility, which can construct high energy density Li-soluble HFBs. Furthermore, the I_3^-/I^- redox reaction exhibits favorable redox rate kinetics of 10^{-2} cm s^{-1} in a neutral pH environment, a characteristic that is pivotal for preserving the structural stability of the majority of water-stable ceramic electrolytes. Byon and co-workers have successfully demonstrated the I_3^-/I^- redox couple as a cathode active material in lithium batteries and Li-soluble HFBs for the first time.[94,95] The battery exhibited a high energy density (280 Wh kg^{-1}), attributable to the substantial solubility of LiI in aqueous solution (8.2 M), coupled with a reasonably elevated power density (130 mW cm^{-2}). As shown in Fig. 7d, Wu *et al.* demonstrated the concept of an aqueous lithium–iodine solar flow battery by integrating a built-in dye-sensitized TiO_2 photoelectrode within a Li–I HFBs, which has a three-electrode configuration, including a Li anode, a Pt counter electrode and a dye-sensitized TiO_2 photoelectrode.[96] Both the counter electrode and the photoelectrode were in contact with the flowing I_3^-/I^- catholyte, which was stored in a reservoir connected to the catholyte chamber and pumped through the device using a peristaltic pump. The Li anode and the I_3^-/I^- catholyte were separated by a ceramic Li^+-ion

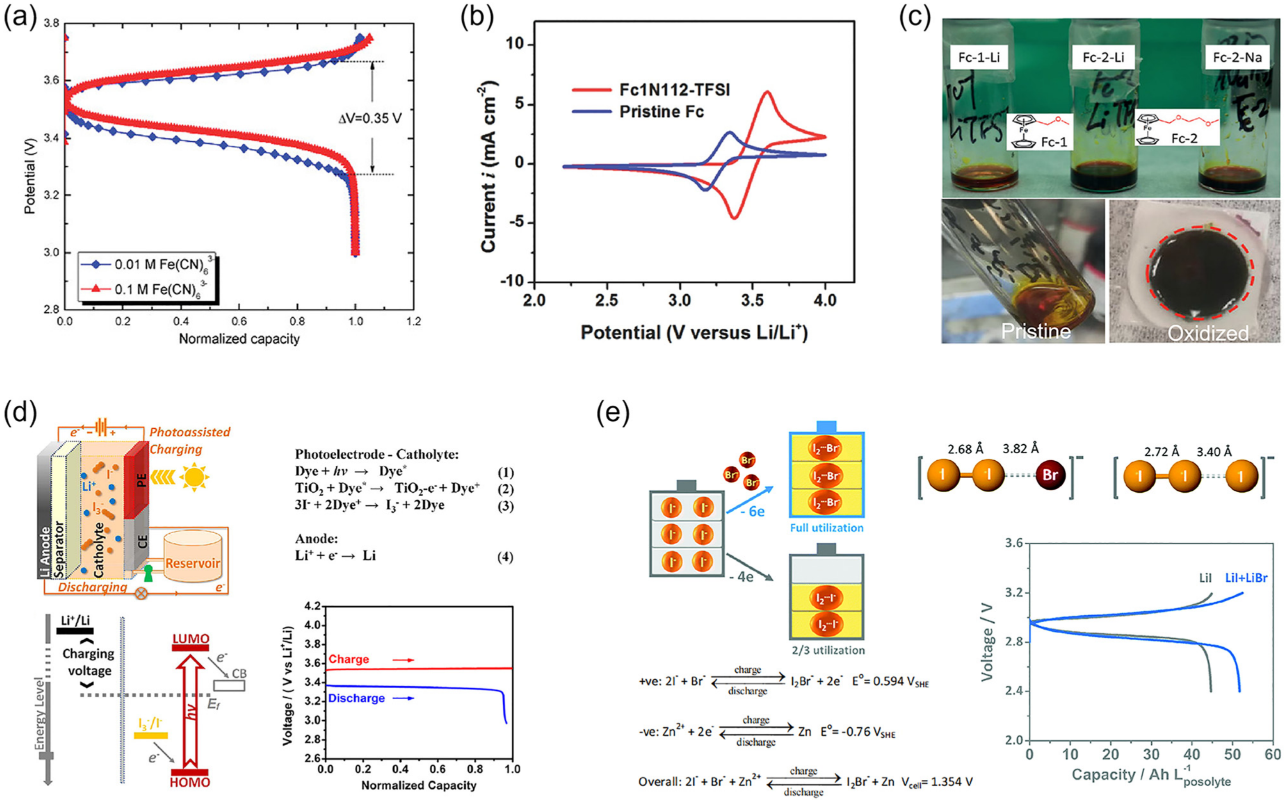

Fig. 7 (a) Charge/discharge curves of the Li||Fe(CN)$_6^{3-}$ battery with different concentrations of catholyte. Reproduced from ref. 88 with permission from American Chemical Society, copyright 2011. (b) Comparison of cyclic voltammetry curves between 0.04 M pristine ferrocene and 0.1 M Fc1N112-TFSI. Reproduced from ref. 90 with permission from Wiley-VCH, copyright 2015. (c) Photos of ferrocene-based organic eutectic electrolyte. Reproduced from ref. 92 with permission from Wiley-VCH, copyright 2021. (d) Schematic of a Li–I solar flow battery device and energy diagram for the photoassisted charging process. Reproduced from ref. 96 with permission from American Chemical Society, copyright 2015. (e) Concept illustration of bromide as the complexing agent to stabilize iodine and galvanostatic voltage profiles of the battery with 1.25 M I_2Br^- catholyte. Reproduced from ref. 97 with permission from The Royal Society of Chemistry, copyright 2017.

conductive membrane. Due to illumination, the dye molecules chemically adsorbed on the surface of the TiO_2 semiconductor were photoexcited and injected electrons into the conduction band of TiO_2. These electrons then oxidized I^- to I_3^- by regenerating the oxidized dye molecules. Simultaneously, Li^+ ions crossed the ceramic membrane and were reduced to Li on the anodic side, thus completing the charging process. During discharging, Li was electrochemically oxidized to Li^+ on the anodic side, while I_3^- was electrochemically reduced to I^- in the cathodic side. To further improve the stability of the iodine catholyte and the energy density of Li–iodine HFBs, Lu and colleagues demonstrated that bromide ions could serve both as complexing agents to stabilize free iodine, forming iodine–bromide ions (I_2Br^-), and increased the capacity of the iodide cathode without involving the Br^-/Br_3^- redox reaction (Fig. 7e).[97] Asymmetric I_2Br^- has linear (or nearly linear) trihalide structure and is thermodynamically stable. Compared to I_3^- catholyte, the batteries with I_2Br^- catholyte exhibited higher capacity (>50 Ah L^{-1}), excellent stability, and an energy efficiency of 88%. The elemental abundance of bromine is higher than that of iodine, and bromine readily coordinates with other halides in solution to form polybrominated compounds, thereby significantly enhancing its solubility. However, the direct use of Br^- as an active material leads to rapid capacity fade and a swift decline in discharge potential. This is attributed to the proximity of the standard electrode potentials between Br_2/Br^- and BrO^-/Br^-, coupled with the irreversible reaction of Br^-/BrO^-. Providing an acidic environment, combining suitable complexing agents, or utilizing specific ionic liquids have been proven to effectively inhibit the formation of BrO^- and stabilize the bromine cathode.[98]

Sulfur has emerged as a highly promising cathodic active material for advanced energy storage systems, owing to its exceptional combination of natural abundance, low cost, and remarkable theoretical capacity. However, conventional lithium–sulfur batteries face fundamental challenges arising from the intrinsic limitations of sulfur: low conductivity, sluggish redox kinetics, substantial volumetric expansion during cycling, and the detrimental shuttle effect caused by soluble lithium polysulfide migration. These interrelated issues collectively compromise the electrochemical reversibility and long-term cyclability of the system. The utilization of polysulfide catholytes as an alternative to conventional solid sulfur-based electrodes represents a promising strategy to fundamentally addresses these intrinsic limitations of solid sulfur. Li_2S_8 has been extensively utilized as the catholyte in lithium-polysulfide flow batteries. However, a critical challenge arises from the formation of insoluble and insulating

Li_2S_x ($x < 4$) during battery cycling. The Li_2S_x ($x < 4$) deposits on electrode surfaces, leading to continuous capacity degradation and battery failure, which represents a fundamental limitation in current lithium-polysulfide flow battery technology. From the point of view of electrolyte composition and solvent selection, Liu and colleagues conducted a comprehensive investigation into the solubility characteristics of Li_2S_x across three distinct non-aqueous electrolytes: dimethyl sulfoxide (DMSO), tetrahydrofuran (THF), and 1,3-dioxolane/1,2-dimethoxyethane (DOL/DME) mixture.[99] As shown in Fig. 8a, their findings revealed that in lithium-polysulfide flow batteries, prompting the selection of DMSO as the optimal solvent due to its superior solubility for Li_2S_x ($x < 4$). Furthermore, the researchers leveraged the strong ion association strength of $CF_3SO_3^-$(Tf^-) anions to enhance polysulfide solubility through the formation of ionic aggregates, effectively preventing the precipitation of insoluble short-chain lithium polysulfides during battery operation (Fig. 8b). Beyond enhancing the solubility of polysulfides in electrolyte, the development of effective catalyst is crucial for accelerating the redox kinetics between polysulfides (particularly in the critical Li_2S_2/Li_2S conversion process) in order to obtain higher capacity and rate performance.[100] Furthermore, Cui and colleagues pioneered an innovative "dead sulfur" regeneration strategy, wherein inactive Li_2S_x ($x < 4$) species were reactivated through a thermal-mechanical process involving stirring and heating with elemental sulfur powder (as depicted in Fig. 8c).[101] This strategy not only enabled capacity recovery but also demonstrated a lithium-polysulfide flow battery system, which achieved a high volumetric energy density of 135 Wh L^{-1}, extended cycle life, and superior single-cell capacity. Fu introduced two highly soluble organic small molecules, namely 2,2′-dipyridine disulfide (PySSPy) and diphenyldiene (PhSeSePh), also to obtain self-healing lithium-polysulfide flow batteries with selectable reaction pathways.[102] The development of sulfur-based cathodic suspensions emerges as another promising alternative to conventional solid sulfur electrodes. The sulfur-based suspensions synergistically combine the advantages of liquid-phase electrochemistry with particulate active materials, offering superior adaptability to volume changes during cycling

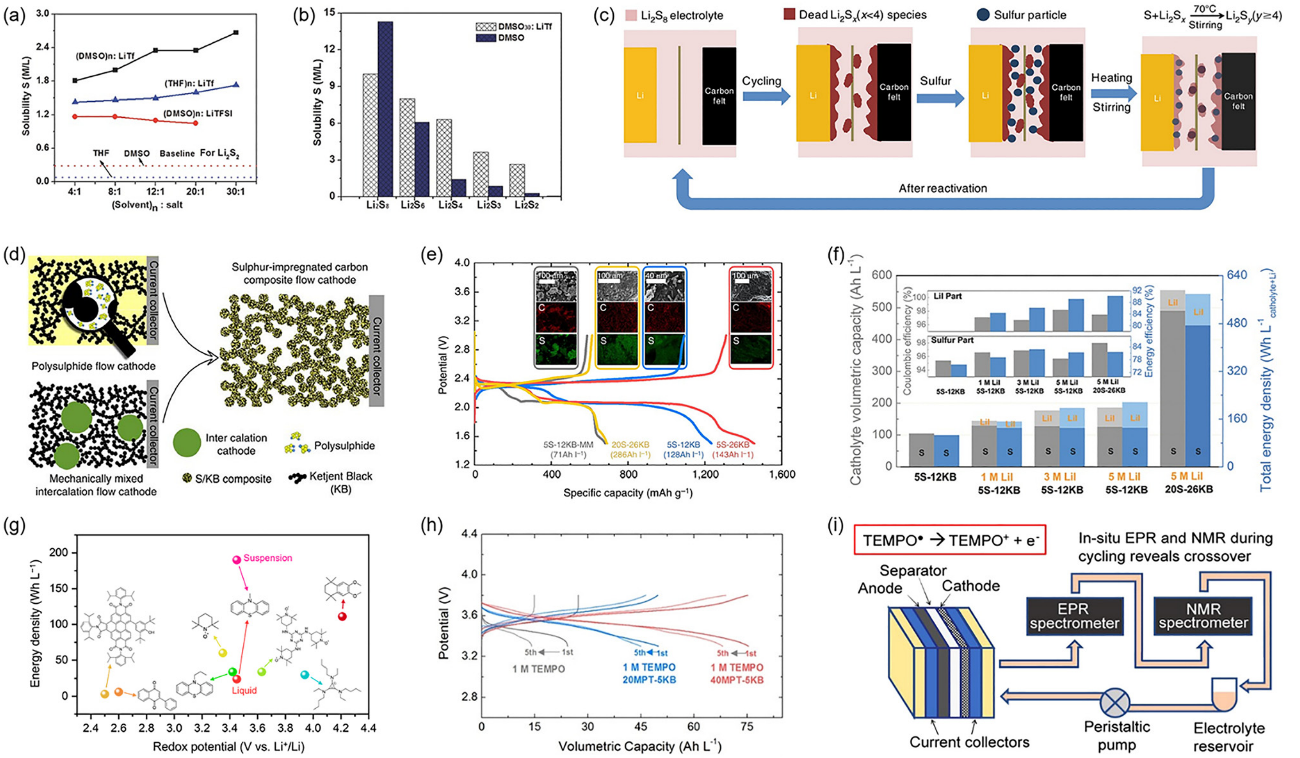

Fig. 8 (a) The solubility of Li_2S_2 in DMSO or THF solvents with the addition of LiTFSI or LiTf. Reproduced from ref. 99 with permission from Wiley-VCH, copyright 2015. (b) The solubility comparison of Li_2S_x in $DMSO_{30}$: LiTf and DMSO solvents. Reproduced from ref. 99 with permission from Wiley-VCH, copyright 2015. (c) Schematic of the reactivation process by reaction of sulfur particles with dead sulfide species, Li_2S_x ($x < 4$), under stirring and heating condition. Reproduced from ref. 101 with permission from Springer Nature, copyright 2017. (d) Concept of a sulfur-impregnated carbon composite flow cathodic suspension. Reproduced from ref. 103 with permission from Springer Nature, copyright 2015. (e) Galvanostatic voltage profiles and scanning electron microscopy/energy dispersive X-ray spectroscopy (SEM/EDX) images of lithium–sulfur flow batteries using sulfur-impregnated carbon composite flow cathodic suspensions. Reproduced from ref. 103 with permission from Springer Nature, copyright 2015. (f) Volumetric capacity and energy density (based on the volume of catholyte and lithium) for catholytes of sulfur-impregnated carbon composite suspensions with LiI electrolyte. The inset shows the corresponding coulombic efficiency and energy efficiency. Reproduced from ref. 104 with permission from Wiley-VCH, copyright 2016. (g) Comparison of redox potentials and energy densities across various organic compounds in lithium-based HFBs.[110–116] (h) The initial and fifth galvanostatic charge–discharge profiles of diverse catholytes comprising TEMPO-MPT-KB. Reproduced from ref. 112 with permission from Wiley-VCH, copyright 2021. (i) Schematic of *in situ* investigation of organic active materials for lithium flow batteries utilizing combined NMR and EPR techniques. Reproduced from ref. 113 with permission from American Chemical Society, copyright 2021.

while substantially enhancing both the capacity and energy density of flow battery systems. As depicted in Fig. 8d, Lu and colleagues developed a sulfur-impregnated carbon composite suspension, representing a significant departure from conventional mechanical mixing of solid sulfur powder with carbon conductive agents.[103] This sulfur-impregnated carbon composite suspension achieved more uniform integration of active material (solid sulfur) with a conductive carbon network (KB), significantly improving the utilization efficiency of insulating sulfur species. Furthermore, this sulfur-impregnated carbon composite suspension exhibited substantially reduced viscosity, enabling the utilization of solid sulfur powder instead of soluble polysulfides. Thus, this sulfur-impregnated carbon composite cathode facilitated maximization of solid sulfur active material concentration in the suspension, effectively surpassing the solubility limit of sulfur and thereby enhancing the theoretical volumetric capacity and energy density of the battery (as shown in Fig. 8e). Building upon the sulfur-impregnated carbon composite flow cathode architecture, Lu and collaborators introduced LiI electrolyte, which enhanced the redox reversibility and capacity of the cathodic suspension, improved the electrochemical utilization of solid sulfur, and reduced the viscosity of the cathodic suspension.[104] The result shown in Fig. 8f indicated that the high-concentration and synergistic combination of liquid LiI electrolyte and solid sulfur enabled multiple redox reactions, ultimately achieving a record-breaking capacity of 550 Ah L^{-1} (based on the catholyte). In addition to the traditional mechanical mixture and high temperature impregnation method, the sulfur and carbon-based materials can also be tightly bonded through physical adhesion, chemical reaction, and codeposition.[105,106] These methods enable more intimate contact between sulfur species and carbon matrices, thereby facilitating electron transfer, improving sulfur utilization and decreasing viscosity. Mitigation of the polysulfide shuttle effect requires a dual-pronged approach, encompassing not only electrolyte optimization but also the development of advanced functional separators (such doped/blended polymer membrane and solid electrolyte).[107,108] The design of high selectivity separators represents a critical component in suppressing polysulfide migration while maintaining efficient ion transport. In addition to sulfur/polysulfides, organic sulfur compounds and selenium/polyselenides share comparable operational mechanisms, applications, as well as face similar challenges.[109]

Organic compounds have gained widespread favor in Li-based HFBs due to their advantages of low cost, diverse structural designs, and tunable properties (Fig. 8g).[110–116] 1,2,3,4-tetrahydro-6,7-dimethoxy-1,1,4,4-tetramethylnaphthalene (TDT) demonstrated a high oxidation potential of 4.21 V (*vs.* Li^+/Li) and remarkable solubility of up to 1.0 M in DME solvent.[110] When paired with a hybrid lithium-graphite anode, the Li-TDT flow battery could achieve an impressive energy density of 111 Wh L^{-1}. Furthermore, the presence of Li^+ ions has been confirmed to significantly enhance the electrochemical reversibility and stability of TDT, as evidenced by subtractively normalized *in situ* Fourier transform infrared spectroscopy experiments and calculations from density functional theory. 2,2,6,6-Tetramethylpiperidine-1-oxyl (TEMPO) and its derivatives have emerged as prominent cathodic active materials in non-aqueous lithium-organic flow batteries, exhibiting high redox potential of 3.35 V (*vs.* Li^+/Li), high solubility, and excellent reversibility. In addition to highly soluble organic compounds, sparingly soluble or even insoluble organic materials have demonstrated significant potential in lithium-based HFB systems. Lu and colleagues melted solid organic 10-methylphenothiazine (MPT) into the interconnected pores of a conductive carbon network, creating an organic/KB composite suspension, which achieved a high voltage (3.45 V *vs.* Li^+/Li), a remarkable capacity of 55 Ah L^{-1} (8 fold that of the liquid-MPT flow battery), and an impressive energy density of 190 Wh L^{-1}.[111] Due to TEMPO or MPT exhibited nearly redox potentials and has been independently validated in a liquid-phase or semi-solid lithium-based HFB respectively, Chen combined the high solubility of liquid-phase TEMPO with the high concentration of solid-phase MPT, resulting in a multiple redox semi-solid–liquid suspension for lithium-organic flow batteries. The battery exhibited a stable operating voltage of 3.4 V (*vs.* Li^+/Li), enhanced capacity of 75 Ah L^{-1}, and superior energy density of 260 Wh L^{-1}.[112] It was ingenious that the synergistic interaction between liquid-phase TEMPO and solid-phase MPT not only improved the stability of high-concentration TEMPO but also significantly reduced the viscosity of the catholyte (Fig. 8h). The lifespan degradation of lithium-organic flow batteries is primarily attributed to the self-degradation phenomenon caused by transmembrane contamination of soluble organic species. An online combination of *in situ* electron paramagnetic resonance (EPR) and nuclear magnetic resonance (NMR) spectroscopy techniques enabled real-time monitoring of organic radical redox behavior and crossover phenomena, including the identification and quantification of intermediate species and side reaction products (Fig. 8i).[113] Furthermore, the structural evolution of organic compounds and dynamic changes in radical concentrations could be precisely quantified and compared throughout the charge–discharge cycle. On one hand, the development of high-performance separators contributes significantly to enhancing the lifespan of lithium-organic flow batteries. On the other hand, the utilization of molecular approaches to create intrinsically stable organic active materials also plays a pivotal role in improving the durability of these batteries. Jiang and colleagues reported membrane-free biphasic lithium-organic flow batteries, employing 2,4,6-tri-(1-cyclohexyloxy-4-imino-2,2,6,6-tetramethylpiperidine)-1,3,5-triazine (Tri-TEMPO), *N*-propyl phenothiazine(C3-PTZ), and tris(dialkylamino)cyclopropenium (CP) as catholytes.[114] Among them, the Li||Tri-TEMPO battery demonstrated good cycling stability, maintaining 98% and 85% capacity retention after 100 cycles (over 50 days) under static and flow conditions, respectively.

3.1.5. Li-targeting HFBs. The Li-slurry HFB, while benefiting from the high-capacity advantage of solid active materials, faces significant challenges due to the high viscosity of the slurry, which severely compromises electrolyte flow dynamics. Conversely, the Li-soluble HFB circumvents viscosity-related issues by avoiding the use of solid active materials, yet is constrained by limited solubility and insufficient stability of active species in non-aqueous electrolytes, resulting in compromised capacity and cycle life. Building upon these insights, Wang's research team has conducted extensive research focusing on harnessing the combined strengths of high energy density from solid materials and high fluidity from electrolytes, with Li-flow batteries serving as the primary application scenario. They ultimately proposed the concept of "redox targeting reactions", which involves the circulation of soluble active species between the reactor and storage tanks, while insoluble solid particles are stored in the tanks without participating in the cycle, thereby avoiding any impact on the viscosity of the electrolyte. The soluble active species undergo electrochemical redox reactions at the electrodes in the reactor and chemical redox reactions with the solid particles in the storage tanks. In other words, in lithium-targeting HFBs, the soluble active species flowing with the electrolyte act as a bridge facilitating reactions between the electrodes in the reactor and the solid particles in the storage tanks, hence referred to as "redox mediators". The operation of a Li-targeting HFB involves two critical steps: In the first step, chemical delithiation/lithiation takes place between the flow redox mediators and the active Li^+-storage materials; In the second step, the oxidized/reduced redox mediators are regenerated at the electrode, preparing them for subsequent delithiation/lithiation cycles.

$LiFePO_4$ is a commonly used cathodic solid active material with a redox potential of approximately 3.45 V (*vs.* Li^+/Li). Wang and colleagues firstly verified the concept by selecting ferrocene (Fc) and 1,10-dibromoferrocene ($FcBr_2$) as redox mediators to match with $LiFePO_4$.[117] Cyclic voltammetry (CV) curves serve as an effective tool for constructing redox targeting reactions. As illustrated in Fig. 9a, the redox potentials of $FcBr_2$ and Fc were 3.78 V and 3.40 V *vs.* Li^+/Li, respectively, which just straddled the potentials for Li-extraction and Li-insertion of $LiFePO_4$.[118] As descripted in Fig. 9b, during the charging process, Fc was firstly oxidized to Fc^+ at the electrode (correspond to lower charging platforms a) and $FcBr_2$ was then oxidized to $FcBr_2^+$ at the electrode (correspond to higher charging platforms b).[117]

Subsequently, the oxidized species $FcBr_2^+$ flowed into the storage tank, where it came into contact with $LiFePO_4$ powders and was reduced back to $FcBr_2$ (correspond to charging platforms b). Simultaneously, Li^+ ions were released from the $LiFePO_4$ lattice, resulting in the oxidation of $LiFePO_4$ to $FePO_4$ (correspond to charging platforms b). Ultimately, the reduced $FcBr_2$ was redirected back to the electrode where it undergoed reoxidation to $FcBr_2^+$ (correspond to charging platforms b), thereby fully completing the charging half-cycle. In the discharge half-cycle, $FcBr_2^+$ was firstly reduced to $FcBr_2$ at the electrode (correspond to higher discharging platforms c) and Fc^+ was then reduced to Fc at the electrode (correspond to lower discharging platforms d). Subsequently, the reduced species Fc flowed into the storage tank, where it came into contact with $FePO_4$ powders and was re-oxidized back to Fc^+ (correspond to discharging platforms d). Simultaneously, Li^+ ions entered the $FePO_4$ lattice to form $LiFePO_4$ (correspond to discharging platforms d). Ultimately, the oxidized Fc^+ was returned to the electrode, where it underwent reduction back to Fc (correspond to discharging platforms d). Similarly, Wang and colleagues later employed bis(pentamethylcyclopentadienyl)cobalt ($CoCp_2$*) and cobaltocene ($CoCp_2$) as redox mediators paired with TiO_2, achieving comparable results.[118,119] Furthermore, they employed bis-(pentamethyl-cyclopentadienyl) chromium ($CrCp_2$*), which has a potential closer to that of $CoCp_2$, to replace $CoCp_2$*, resulting in mitigated voltage hysteresis and minimized voltage loss.[120] Lee's team has also played a significant role in advancing and extending the application of redox targeting reactions to lithium–sulfur flow batteries. By utilizing two redox mediators, $CrCp_2$* and bis-(pentamethyl-cyclopentadienyl) nickel ($NiCp_2$*), they enabled sulfur, which inherently exhibited poor conductivity, to participate effectively in the battery's charging and discharging processes (Fig. 10a).[121]

Compared to the introduction of two redox mediators, employing a single redox mediator capable of simultaneously enabling redox targeting during both the charging and discharging

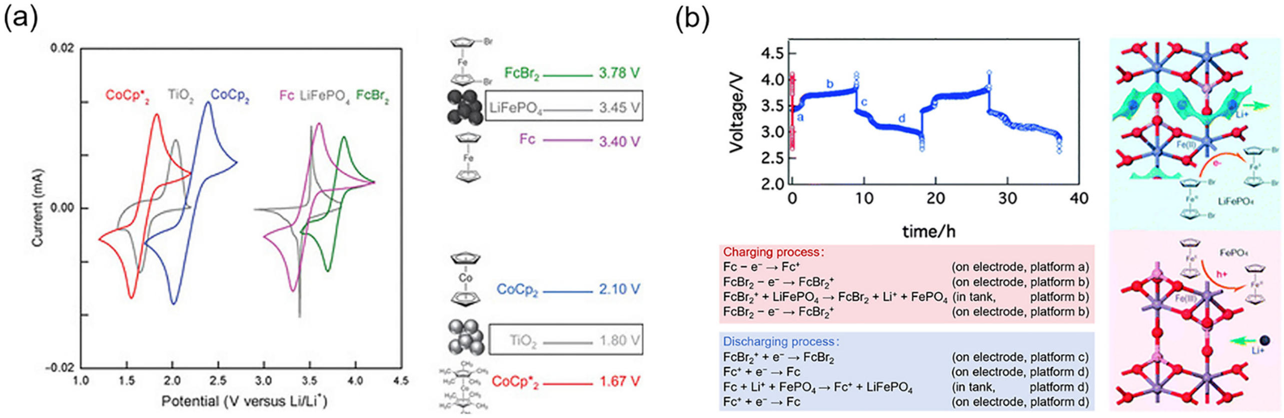

Charging process:
$Fc - e^- \rightarrow Fc^+$ (on electrode, platform a)
$FcBr_2 - e^- \rightarrow FcBr_2^+$ (on electrode, platform b)
$FcBr_2^+ + LiFePO_4 \rightarrow FcBr_2 + Li^+ + FePO_4$ (in tank, platform b)
$FcBr_2 - e^- \rightarrow FcBr_2^+$ (on electrode, platform b)

Discharging process:
$FcBr_2^+ + e^- \rightarrow FcBr_2$ (on electrode, platform c)
$Fc^+ + e^- \rightarrow Fc$ (on electrode, platform d)
$Fc + Li^+ + FePO_4 \rightarrow Fc^+ + LiFePO_4$ (in tank, platform d)
$Fc^+ + e^- \rightarrow Fc$ (on electrode, platform d)

Fig. 9 (a) Working principle of the redox targeting reactions, including cyclic voltammetry curves of the redox mediators and lithium storage materials. Reproduced from ref. 118 with permission from American Association for the Advancement of Science, copyright 2015. (b) The specific steps of the charge and discharge process of Li-targeting flow batteries, taking $FcBr_2$ and Fc as redox mediators and $LiFePO_4$ as lithium storage materials as an example. Reproduced from ref. 117 with permission from The Royal Society of Chemistry, copyright 2013.

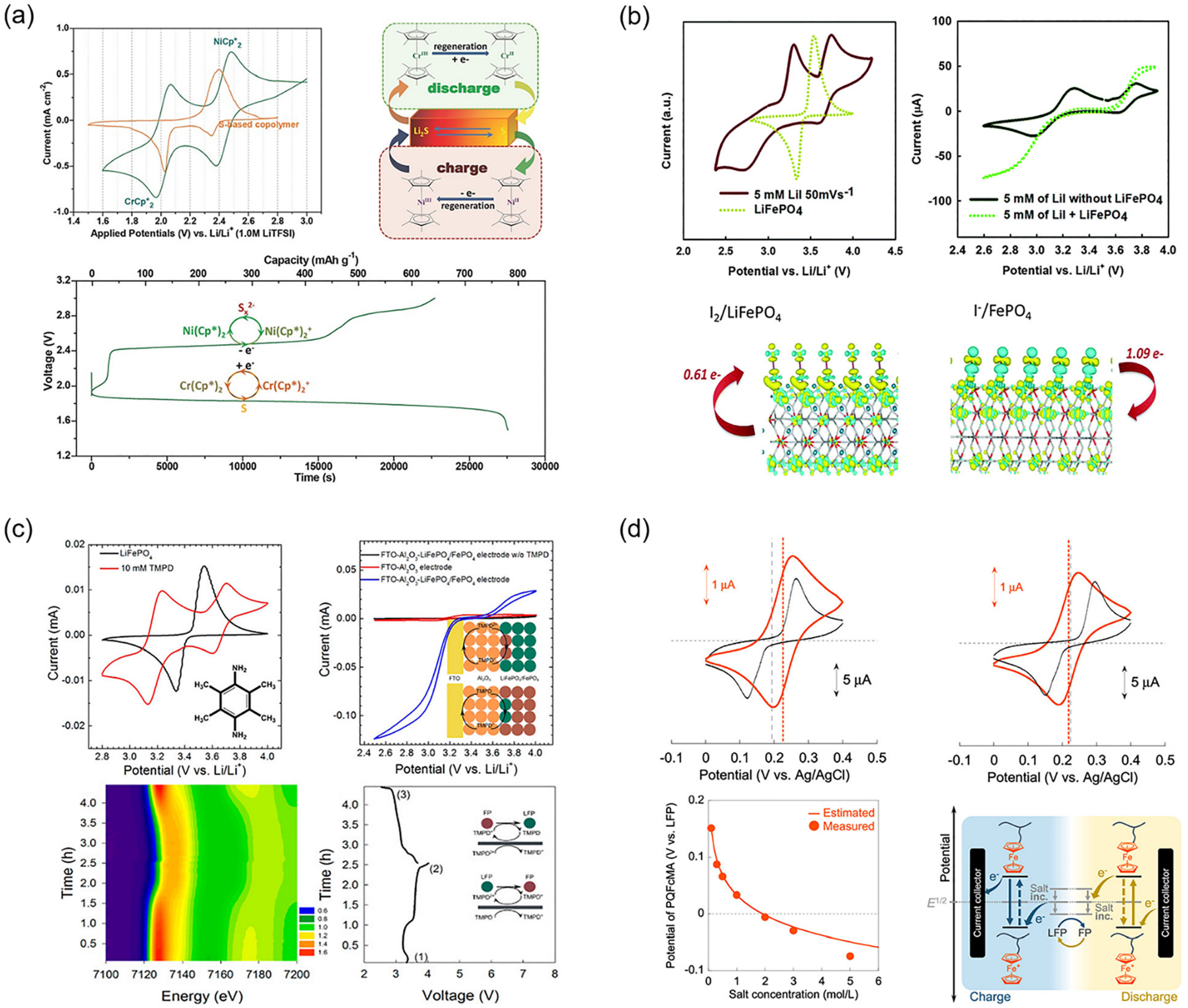

Fig. 10 (a) Application of redox-targeting reactions in lithium–sulfur flow batteries. Reproduced from ref. 121 with permission from Wiley-VCH, copyright 2015. (b) Demonstration of a Li-targeting flow battery utilizing a single inorganic redox mediator (LiI) and lithium storage material ($LiFePO_4$). Reproduced from ref. 122 with permission from The Royal Society of Chemistry, copyright 2016. (c) Demonstration of a Li-targeting flow battery utilizing a single organic redox mediator (TMPD) and lithium storage material ($LiFePO_4$). Reproduced from ref. 123 with permission from American Chemical Society, copyright 2017. (d) The strategy of regulating electrolyte salt concentration to align the redox potential of the redox mediator with that of the lithium storage material. Reproduced from ref. 124 with permission from American Chemical Society, copyright 2024.

processes significantly simplifies and stabilizes the electrolyte system. Based on this principle, Wang and colleagues investigated both inorganic and organic single redox mediators. As show in Fig. 10b, iodides exhibited two distinct redox reactions (I^-/I_3^- and I_3^-/I_2), and the potentials of these redox couples were precisely positioned around the delithiation/lithiation potential of $LiFePO_4$.[122] Consequently, a single redox species, I^-, was sufficient to facilitate both the charging and discharging processes of $LiFePO_4$. As show in Fig. 10c, the single-component 2,3,5,6-tetramethyl-*p*-phenylenediamine (TMPD) exhibited a two-step electron transfer process, as evidenced by the presence of two distinct redox peaks in its CV curve. These redox potentials spanned the delithiation/lithiation potential of $LiFePO_4$, fulfilling the fundamental requirements for constructing a redox-targeting flow battery.[123] And the evolution of $LiFePO_4$ was adeptly monitored through the utilization of the *operando* X-ray absorption near-edge structure (XANES) measurement, offering profound insights into the redox-targeting processes. Consequently, lithium-targeting redox flow batteries utilizing LiI and TMPD as redox mediators achieved remarkable energy densities of up to 670 Wh L^{-1} and 1023 Wh L^{-1}, respectively. In addition to the selection of multi-electron transfer redox mediators, the establishment of optimal conditions for a single redox mediator can be achieved by adjusting the electrolyte concentration to precisely tune the redox potentials. As shown in Fig. 10d, by increasing the concentration of LiCl in the electrolyte, the equilibrium potentials of the redox mediator (red line) and $LiFePO_4$ (black line) were aligned to be identical. When the redox potentials of the redox mediator and $LiFePO_4$ were nearly equivalent, the redox-targeting effect was distinctly observed for both charging and discharging processes.[124]

3.2. Sodium (Na)-based hybrid flow batteries

The development trajectory of sodium (Na)-based HFBs is broadly consistent with that of Li-based HFBs (Fig. 11a). Previously, Sprenkle and colleagues constructed a sodium-based HFB utilizing a room-temperature molten Na–Cs alloy as the flowing anode and an aqueous vanadium electrolyte as the flowing cathode.[20] This battery offered ultra-high volumetric and gravimetric energy densities, while also providing advantages in terms of power and energy decoupling design. To isolate the molten Na alloy anolyte from the aqueous catholyte, Na-β″-Al_2O_3 solid electrolyte was firstly employed as a separator in this system. However, the stability of the battery remained suboptimal with only 30 cycles. Na metal stands out as an optimal alternative to Na–Cs alloy for the anode in Na-based HFBs, owing to its cost-effectiveness and chemical stability. Similar to the Li–O_2 HFB, for the Na–O_2 HFB, the O_2 cathode can be configured with either an aqueous solvent or a non-aqueous solvent. The discharge products are NaOH and Na_2O_2, respectively. Although the reduction potential of Na (−2.71 V *vs.* SHE) is higher than that of Li (−3.04 V *vs.* SHE), replacing the Li-metal anode with a Na-metal anode offers significant economic advantages. Furthermore, the sodium superionic conductor (NASICON, $Na_3Zr_2Si_2PO_{12}$) solid electrolyte exhibits higher room-temperature ionic conductivity and stability than the lithium superionic conductor (LISICON) solid electrolyte. Compared with the Li–O_2 HFB, the Na–O_2 HFB can generate more soluble discharge products, NaOH and Na_2CO_3, through the chemical reaction of NaOH (aq.) with CO_2 in ambient air. Due to the high solubility of the discharge products, the Na–O_2 HFB can provide a theoretical energy density more than 2.5-fold higher than that of the Li–O_2 HFB, even though the voltage of the former is lower than that of the latter. Kim and colleagues fabricated a simply carbonized sponge featuring a highly interconnected microporous open three-dimensional scaffold structure, which demonstrated bifunctional electrocatalytic activity for both OER and ORR in seawater. Furthermore, the sodium-seawater HFB constructed using this carbon sponge exhibited improved voltage gap, voltage efficiency, power density, and cycling stability.[125] Bhattacharya and colleagues simulated the discharge process of a Na–O_2 flow battery and parametrically investigated various

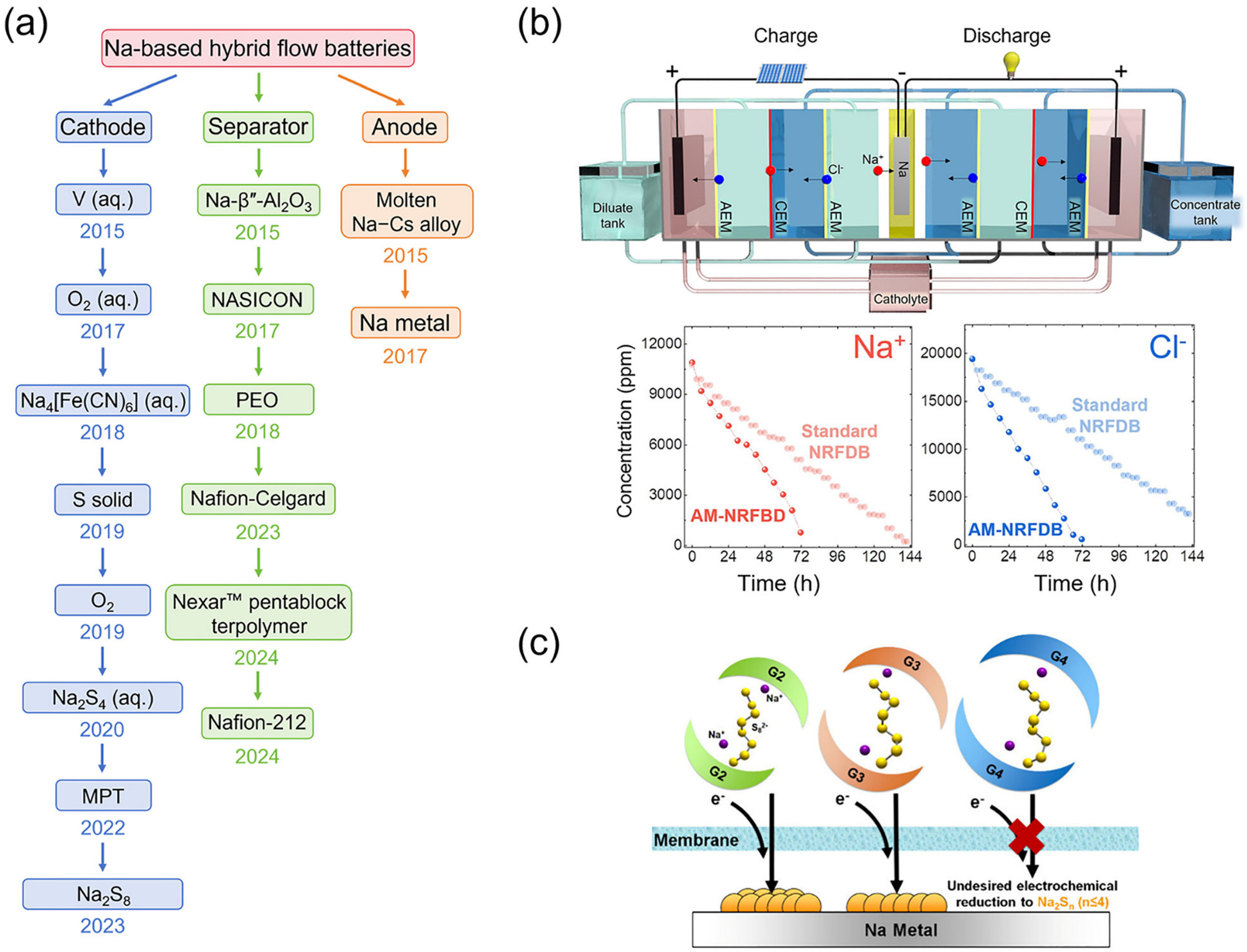

Fig. 11 (a) Notable breakthroughs in the evolution of Na-based HFBs over recent decades, in terms of cathode, separator, and anode. (b) Schematic and performance of Na-based hybrid redox flow desalination batteries with alternating ion exchange membrane. Reproduced from ref. 127 with permission from Elsevier, copyright 2024. (c) The role of glyme solvation effects in non-aqueous sodium-polysulfide flow batteries. Reproduced from ref. 22 with permission from American Chemical Society, copyright 2024.

factors influencing its discharge behavior. They discovered that applying pressure to the oxygen facilitated oxygen transport to the electrode, thereby enhancing the battery's discharge capacity. Specifically, at very low discharge current densities (<0.05 mA cm^{-2}), a small pressure gradient proved more effective, whereas at higher discharge current densities (>0.125 mA cm^{-2}), a larger pressure gradient yielded better performance.[126]

An aqueous solution of $Na_4[Fe(CN)_6]/Na_3[Fe(CN)_6]$ can also serve as the catholyte in high-energy-density Na-based HFBs, demonstrating a voltage exceeding 3 V (*vs.* Na^+/Na) and an energy density of 54.16 Wh L^{-1} (based on the volume of the catholyte).[21] Furthermore, Kim and colleagues integrated a $Na||Na_{3/4}[Fe(CN)_6]^{3-/4-}$ HFB with seawater desalination to construct a Na-based hybrid redox flow desalination battery (NRFDB), addressing the dual challenges of energy storage and desalination, as depicted in Fig. 11b.[127] On one hand, replacing liquid electrodes with sodium metal provided a significantly larger theoretical capacity (1128 Ah L^{-1}) and a Na^+ salt adsorption capacity (968 g_{Na^+} L^{-1}), exceeding that of traditional redox flow desalination batteries by more than threefold. On the other hand, continuous desalination during charge–discharge cycles was achieved by alternately placing cation- and anion-exchange membranes between the electrodes. By treating natural seawater, the system achieved a 95% ion removal rate, reduced energy consumption by over half (compared to the conventional seawater reverse osmosis technology), and increased the desalination flux by twofold (compared to standard NRFDBs). The similar design of NRFDBs gives new vitality to traditional Na-based HFBs. Owing to the high abundance and low cost of sulfur and sodium, as well as the multi-electron transfer process of polysulfides, Na-polysulfide flow batteries have garnered significant attention. However, although Na-polysulfide flow batteries are often considered analogous to Li-polysulfide flow batteries, the strategies employed for their development do not follow identical trends due to differences in electrochemical kinetics and physicochemical properties. To date, research on Na-polysulfide redox flow batteries remains in its early stages. As shown in Fig. 11c, Wu *et al.* have conducted research revealing a profound correlation between the chain length of glyme solvents and the coordination strength of Na^+ ions, as well as the reduction potentials of polysulfides.[22] Specifically, longer glyme chains exhibited a suppressive effect on the formation of short-chain polysulfides, subsequently mitigating capacity fade and enhancing battery longevity. Furthermore, their study elucidated the molecular interactions occurring among glyme solvents, Na^+ ions, and polysulfides, offering pivotal insights into the optimization of electrolyte design for Na-polysulfide flow batteries.

3.3. Potassium (K)-based hybrid flow batteries

Owing to the large ionic radius and high reactivity of potassium, its direct application in flow batteries entails significant technical difficulties and safety risks, resulting in relatively few reports on potassium (K)-based HFBs. In contrast to the high toxicity of Hg in Na–Hg alloys and the rarity of Cs in Na–Cs alloys, the Na–K alloy boasts constituents that are abundant on earth, inexpensive, and environmentally benign. It exhibits a relatively low eutectic temperature, enabling a broad liquid range at room temperature. Furthermore, its low viscosity facilitates pumping. With a theoretical capacity of 580 mAh g^{-1} (equivalent to 19 M K) at room temperature, the Na–K alloy is viable for use in K-ion batteries. Consequently, Na–K alloy is exceptionally suited for the fabrication of high-voltage, high-energy-density room-temperature K-based HFBs. As shown in Fig. 12a and b, Rugolo and colleagues have demonstrated that K-β″-alumina was a high-selective and robust K^+ ion conductor, which remained stable with minimal Na exchange when in contact with Na–K alloy.[23] A K-based HFB constructed using a Na–K alloy anolyte, K-β″-alumina solid electrolyte, and either aqueous or non-aqueous catholyte exhibited an open-circuit voltage ranging from 3.1 to 3.4 V. At temperatures of 22 and 57 °C, the maximum power densities were 65 and 100 mW cm^{-2}, respectively, with stable operation maintained for over 100 hours.

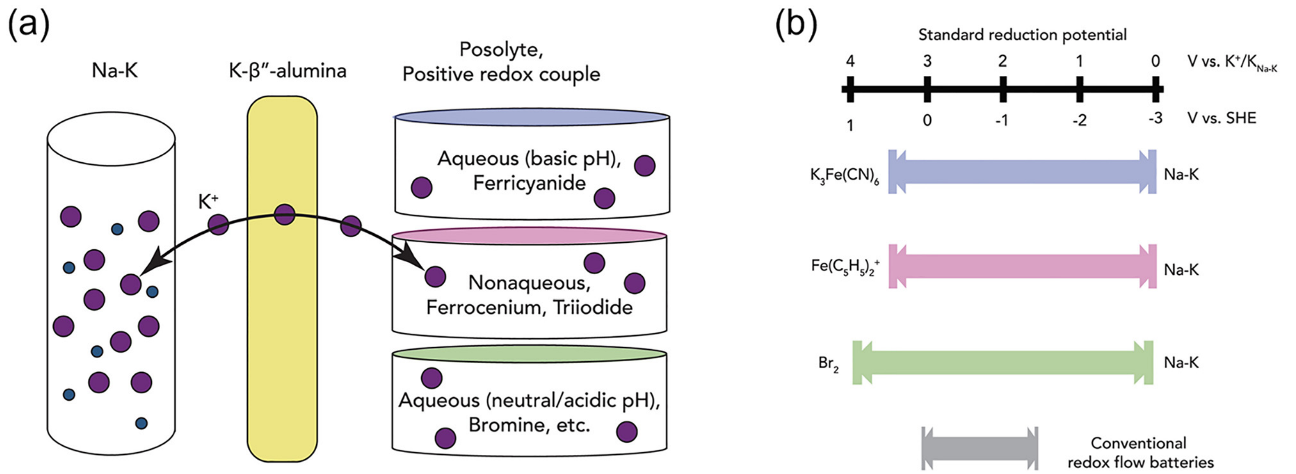

Fig. 12 (a) Schematic of the K-based HFBs, consisting of room-temperature Na–K liquid metal anolyte, K-β″-alumina separator, and multiple catholytes. Reproduced from ref. 23 with permission from Elsevier, copyright 2018. (b) Voltage comparison of K-based HFBs with different cathodes and conventional redox flow batteries. Reproduced from ref. 23 with permission from Elsevier, copyright 2018.

3.4. Magnesium (Mg)-based hybrid flow batteries

In contrast to the significant safety concerns associated with Li, Na, and K, magnesium (Mg) has garnered considerable attention in recent years due to its superior safety profile and higher theoretical volumetric capacity of 3833 mAh cm^{-3}.[24] Furthermore, Mg metal demonstrates a reduction in dendrite formation during battery cycling, compared with both Li and Zn, owing to its low diffusion barrier and unique planar hexagonal growth during electrochemical deposition. As a result, Mg-based HFBs hold promise as a viable and sustainable energy storage technology, although their development is still in the early stages (Fig. 13a). Schaefer and colleagues constructed a Mg-polysulfide flow battery utilizing MgS_x catholyte. Although the formation of solid discharge products was avoided by voltage cutoff, the formation of sulfur crystals could still be observed in the MgS_x catholyte over time, as the solvents and salts used in the electrolyte affected the morphology and stability of MgS_x. The study also pointed out that there is a dissolution competition between magnesium salts and MgS_x in the electrolyte, which may lead to serious problems such as poor reversibility and passivation of the Mg anode.[128] Through rational molecular engineering, Gao and colleagues successfully synthesized a polymer (PIPEG) by combining carbonyl groups with poly(ethylene glycol) segments, which exhibited both high voltage and high solubility in ether-based electrolytes (Fig. 13b). By integrating a Mg foil anode, a porous membrane, and this polymer catholyte, they reported the first non-aqueous Mg flow battery featuring a polymer catholyte, demonstrating a voltage of 1.74 V, a capacity of 250 mAh L^{-1}, and a cycle life of 50 cycles.[25] Hu and colleagues constructed a saltwater Mg–O_2 flow battery and for the first time attempted to utilize the airborne ultrasonic catalytic effect to enhance the ORR and discharge performance of the battery. Experimental results reveal that, when operated at an ultrasonic frequency of 608.4 kHz, the magnesium–air flow battery exhibited a 33.77% increase in peak power density compared to its untreated counterpart. Numerical simulations further elucidate that the acoustic pressure and acoustically induced streaming at the cathode surface facilitate enhanced oxygen diffusion.[129] Jiang's research team developed a membrane-free, biphasic Mg-organic HFB based on aqueous/non-aqueous electrolytes.[26] To enhance the compatibility between the anolyte and the Mg anode, two strategies were implemented. On one hand, ethylene glycol and ionic liquids were introduced as additives to the aqueous solution of $MgCl_2$ and magnesium bis-(trifluoromethanesulfonimide) ($Mg(TFSI)_2$), significantly expanding the stable electrochemical window of the aqueous electrolyte (Fig. 13c). On the other hand, a Mg^{2+}-conductive polymer coating was designed on the Mg anode to improve its reversibility in the aqueous

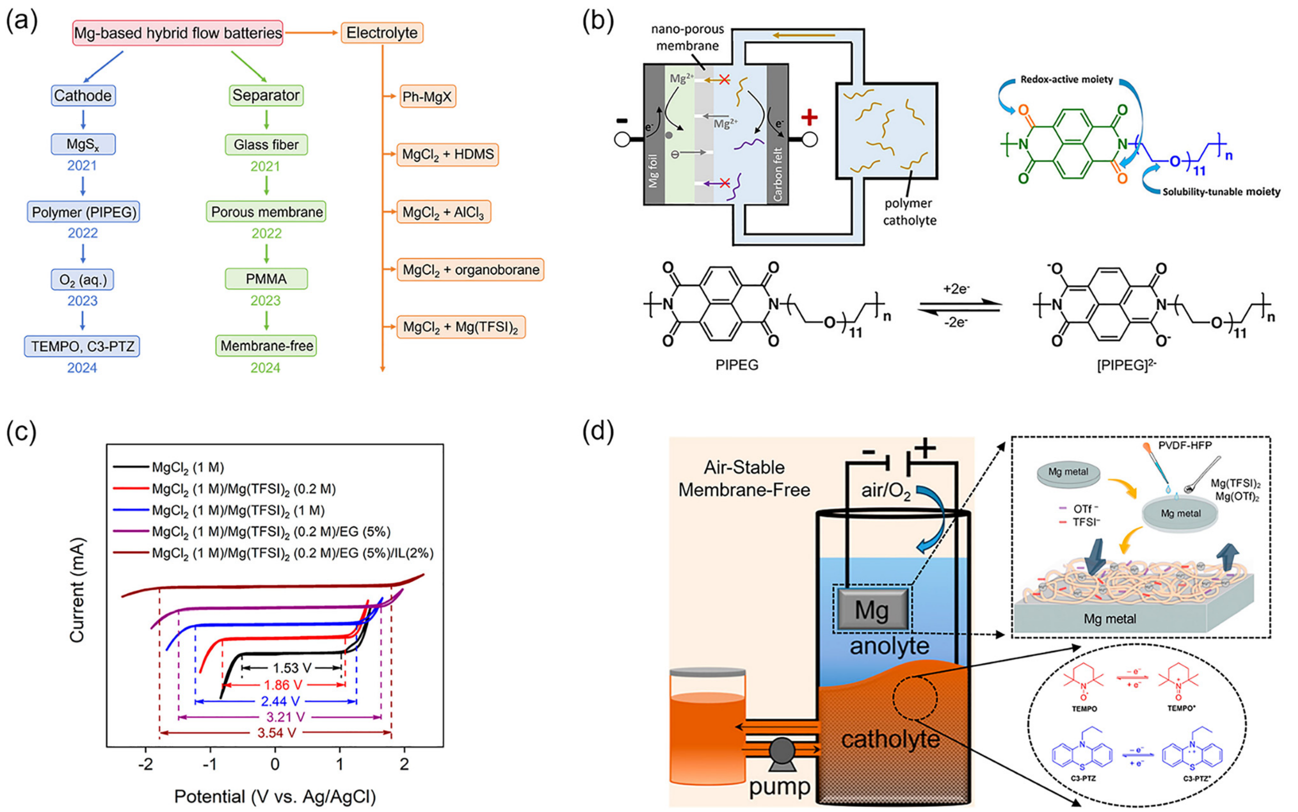

Fig. 13 (a) Notable breakthroughs in the evolution of Mg-based HFBs over recent decades, in terms of cathode, separator, and electrolyte. (b) Schematic of the Mg/polymer flow battery with the structure and reaction mechanism of the polymer. Reproduced from ref. 25 with permission from American Chemical Society, copyright 2022. (c) Electrochemical stability window of electrolytes with different concentrations of Mg salt and solvent additives. Reproduced from ref. 26 with permission from American Chemical Society, copyright 2024. (d) Schematic of the membrane-free, biphasic Mg-organic HFBs. Reproduced from ref. 26 with permission from American Chemical Society, copyright 2024.

electrolyte and prevent passivation. The catholyte consisted of dichloromethane as the solvent, with the soluble organic compounds TEMPO or C3-PTZ serving as the cathodic active materials. The anolyte was positioned above the catholyte. This design ensured the maintenance of a biphasic state under static, stirred, and flowing catholyte conditions (Fig. 13d). Both the Mg||TEMPO and Mg||C3-PTZ flow batteries demonstrated operating voltages of 2.07 V and 2.12 V, respectively, with coulombic efficiencies approaching 100% and energy efficiencies exceeding 90%. Furthermore, after 500 charge–discharge cycles, the capacity retention rates were 93.58% and 92.16%, respectively. Moreover, this membrane-free design enables the realization of low-cost Mg-based HFBs, as they are no longer constrained by the limited lifespan and high cost of ion-exchange membranes.

3.5. Aluminum (Al)-based hybrid flow batteries

In terms of resource abundance, aluminum (Al) ranks as the third most prevalent element in the Earth's crust and is notably the most abundant metallic element. Regarding cost, the mature production processes for Al result in a pricing level that is comparable to Na and Mg, rendering it a cost-effective option. From a safety perspective, Al exhibits superior chemical stability and a significantly lower risk of thermal runaway compared to lithium-ion batteries. In the realm of environmental sustainability, Al is non-toxic and benign, facilitating ease of recycling. When considering energy density, the stripping/deposition reactions of Al involve the transfer of three electrons, enabling a capacity of 3.0 Ah g^{-1} and 8 Ah cm^{-3}, along with a deposition potential of −1.66 V (*vs.* SHE).[130] Consequently, Al-based batteries emerge as a compelling candidate for efficient and low-cost energy storage systems. As shown in Fig. 14a, the initial development of aluminum batteries utilized room-temperature ionic liquids containing imidazolium salts and $AlCl_3$, which demonstrated excellent performance. However, the high cost and challenging synthesis of imidazolium salts limited their practical applicability. In 2017,

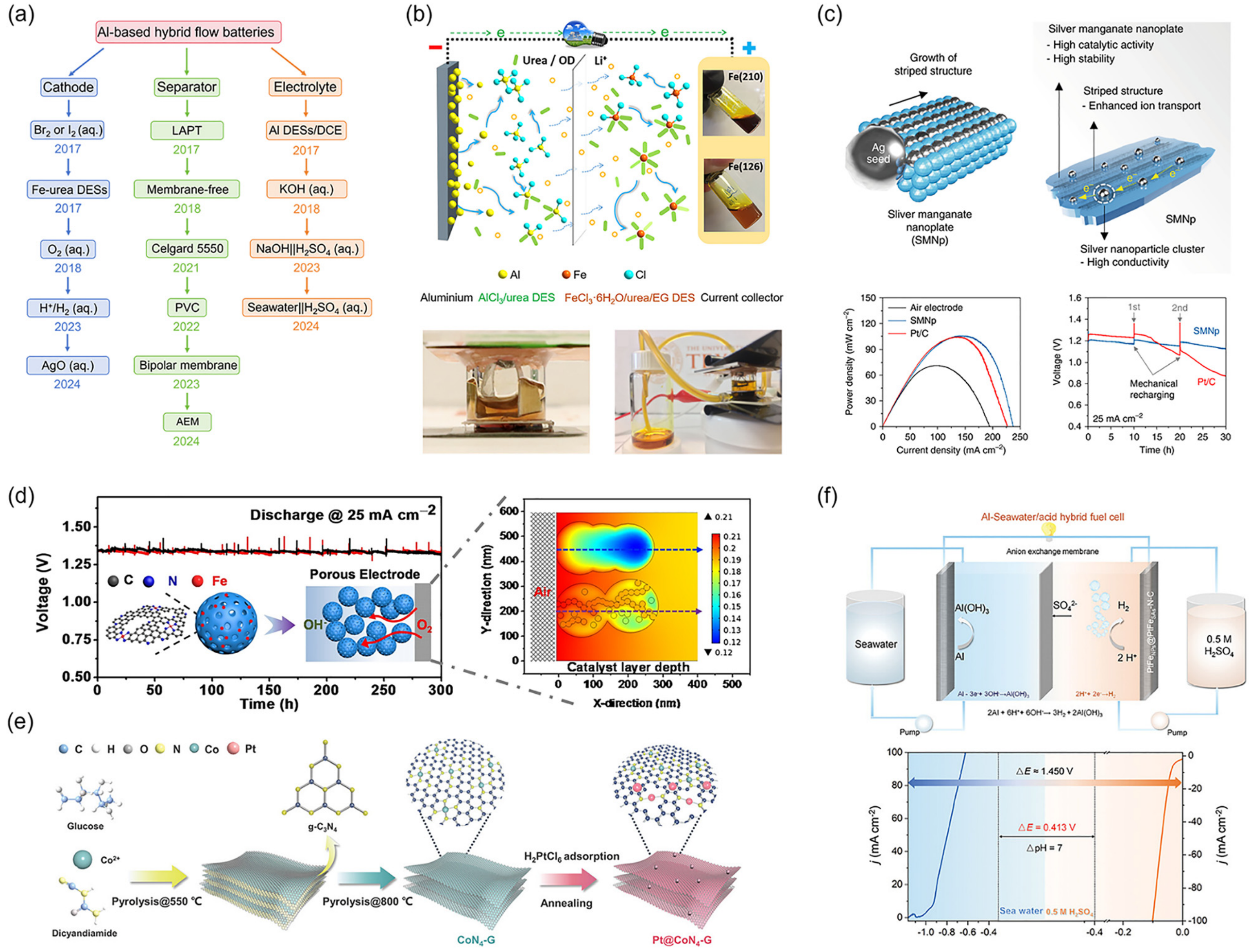

Fig. 14 (a) Notable breakthroughs in the evolution of Al-based HFBs over recent decades, in terms of cathode, separator, and electrolyte. (b) Schematic and photographs of an Al–Fe battery based on deep eutectic electrolytes. Reproduced from ref. 28 with permission from Elsevier, copyright 2017. (c) Structural schematic diagram and electrochemical performance of silver manganate nanoplates. Reproduced from ref. 131 with permission from Springer Nature, copyright 2018. (d) Structural schematic diagram and COMSOL multiphysics modeling of SA-Fe-N$_x$-MPCS catalyst. Reproduced from ref. 133 with permission from Elsevier, copyright 2021. (e) Synthetic illustration of the synthetic process for Pt@CoN4-G. Reproduced from ref. 134 with permission from Wiley-VCH, copyright 2023. (f) Schematic illustrations of a seawater-Al/acid HFB. Reproduced from ref. 135 with permission from Wiley-VCH, copyright 2024.

Yu and colleagues utilized inexpensive urea to form a deep eutectic electrolyte, Al-DES, in conjunction with $AlCl_3$. Subsequently, they employed 1,2-dichloroethane (DCE) to reduce the viscosity of the Al-DES. The resultant low-viscosity Al-DES/DCE enabled the reversible stripping and deposition of Al without serious dendrite formation, making it suitable for Al-based flow batteries.[27] Similarly, Fe-DES was formed by combining $FeCl_3\cdot6H_2O$, urea, and ethylene glycol, which was then diluted with ethylene carbonate (EC)/DMC to reduce viscosity and enhance ionic conductivity. As depicted in Fig. 14b, by pairing the Fe-DES catholyte (with an Fe concentration of 5.5 M) with the Al-DES/DCE anolyte, the battery achieved an average voltage of 1.41 V, delivering an energy density of 166.2 Wh L^{-1} and stable operation for over 50 cycles.[28]

Al–air flow batteries are among the most extensively studied Al-based HFBs, combining the dual advantages of cost-effectiveness and capacity provided by the Al anode and air cathode. The practical application of Al–air flow batteries is still confronted with several challenges, including the sluggish rate of ORR, the corrosion of Al anodes, rapid self-discharge, and the precipitation of solid discharged-products ($Al(OH)_3$ and Al_2O_3) on electrode surfaces, which contribute to a mismatch between the actual and theoretical capacities of the batteries. Cho's research team synthesized a striped silver manganate structure with abundant surface dislocations through a metal seed-mediated growth method (Fig. 14c). This structure demonstrated high catalytic activity for the ORR and enhanced electron transfer rates. Additionally, they successfully applied this catalyst to Al–air flow batteries, significantly alleviating side reactions and deposition issues within the batteries. This Al–air flow battery achieved an energy density of 2552 Wh kg_{Al}^{-1} at a high current density of 100 mA cm^{-2}.[131] Wang and colleagues employed a simple one-step solvothermal method to synthesize MnOOH nanorods decorated with CeO_2 nanoparticles (MnOOH@CeO_2). The incorporation of CeO_2 significantly enhanced the ORR activity of MnOOH, which was attributed to the synergistic effect between MnOOH and CeO_2. This synergy led to improved oxygen activation, enhanced oxygen enrichment, and effective inhibition of H_2O_2 formation. Consequently, the double-face Al–air flow battery demonstrated an energy density of 3595.4 Wh kg_{Al}^{-1} and a power density of 302.8 mW cm^{-2} at a current density of 400 mA cm^{-2}.[132] Chen and colleagues fabricated dense Fe–N_x single-atom sites on mesoporous carbon spheres, exhibiting superior ORR catalytic activity and stability compared to commercial Pt/C catalysts. Furthermore, the COMSOL multiphysics modeling demonstrated that the Fe–N_x single-atom mesoporous carbon catalyst formed a three-dimensional porous framework with abundant channels at the air cathode, facilitating mass transport and contact (Fig. 14d).[133] Zhang *et al.* encapsulated low-loading Pt and Co atoms within nitrogen-doped graphene (Pt@CoN_4-G) to serve as a cathode catalyst (Fig. 14e). When integrated with a bipolar membrane, this setup constructed an alkaline-Al/acid HFB that exhibited a remarkable power density of 222 mW cm^{-2} along with exceptional stability, enabling simultaneous hydrogen evolution and power generation.[134] The Earth is abundant with seawater resources, making it a more cost-effective, safe, and environmentally friendly alternative to alkaline anolyte. However, when using neutral seawater as an electrolyte, it exhibits lower conductivity, and the kinetics of OER and HER are sluggish. As depicted in Fig. 14f, Zhang's research team employed Al and seawater as the anode, utilizing $PtFe_{NPs}$@$PtFe_{SAs}$–N–C as the cathodic catalyst for the HER in an acidic electrolyte, with an anion exchange membrane separating the anode and cathode. The pH difference between seawater and the acidic electrolyte enhanced the voltage and output energy density of the seawater-Al/acid HFB.[135] In terms of modifying Al anodes, the utilization of femtosecond laser and friction-stir process to fabricate three-dimensional Al anodes led to enhanced corrosion resistance and an increased electrochemically active surface area when compared to commercial Al anodes.[136]

3.6. Challenges and prospectives of non-aqueous MBHFBs

3.6.1. Advantages and challenges. Non-aqueous MBHFBs represent a novel type of energy storage system that has garnered significant attention due to their integration of the advantages inherent in both metal batteries and flow batteries. The core mechanism of MBHFBs lies in the reversible deposition and dissolution of metals within electrolytes. The electrolytes can be categorized into aqueous electrolytes and non-aqueous electrolytes based on the solvent selected. The theoretical decomposition voltage of aqueous electrolytes is merely 1.23 V, whereas the stable electrochemical window of non-aqueous electrolytes (such as acetonitrile and carbonate esters) can exceed 4.5 V. Non-aqueous MBHFBs employ organic solvents as electrolytes, which enables the utilization of reactive metals, such as lithium, sodium, and potassium (which undergo vigorous reactions with water) or magnesium and aluminum (which suffer from severe hydrogen evolution in aqueous media), as viable anodes. These metals exhibit exceptionally low deposition/dissolution potentials and high specific capacities, collectively enabling non-aqueous MBHFBs to achieve both high operating voltages and remarkable energy densities.

Despite the promising prospects of this technology, attributed to its notable advantages in voltage and energy density, the current challenges and pain points remain highly conspicuous (as depicted in Fig. 15), thereby leaving significant potential for enhancing its actual performance. In preceding chapters, we have presented a thorough review of five representative non-aqueous MBHFBs (Li, Na, K, Mg, and Al). The development challenges they face not only share commonalities but also exhibit distinct individual characteristics stemming from the differences in their anode metals. Grasping the dialectical unity of this "commonality and individuality" is an essential path to advancing the further development of non-aqueous MBHFBs. In terms of commonalities, non-aqueous MBHFBs all face significant safety challenges. Both the non-aqueous electrolytes with organic solvents and the metals involved are flammable. The growth of anode metal dendrites can potentially puncture the separator, leading to battery short-circuits. This may ignite these non-aqueous and the metals themselves, resulting in substantial property losses and safety accidents. Moreover, given the volatility

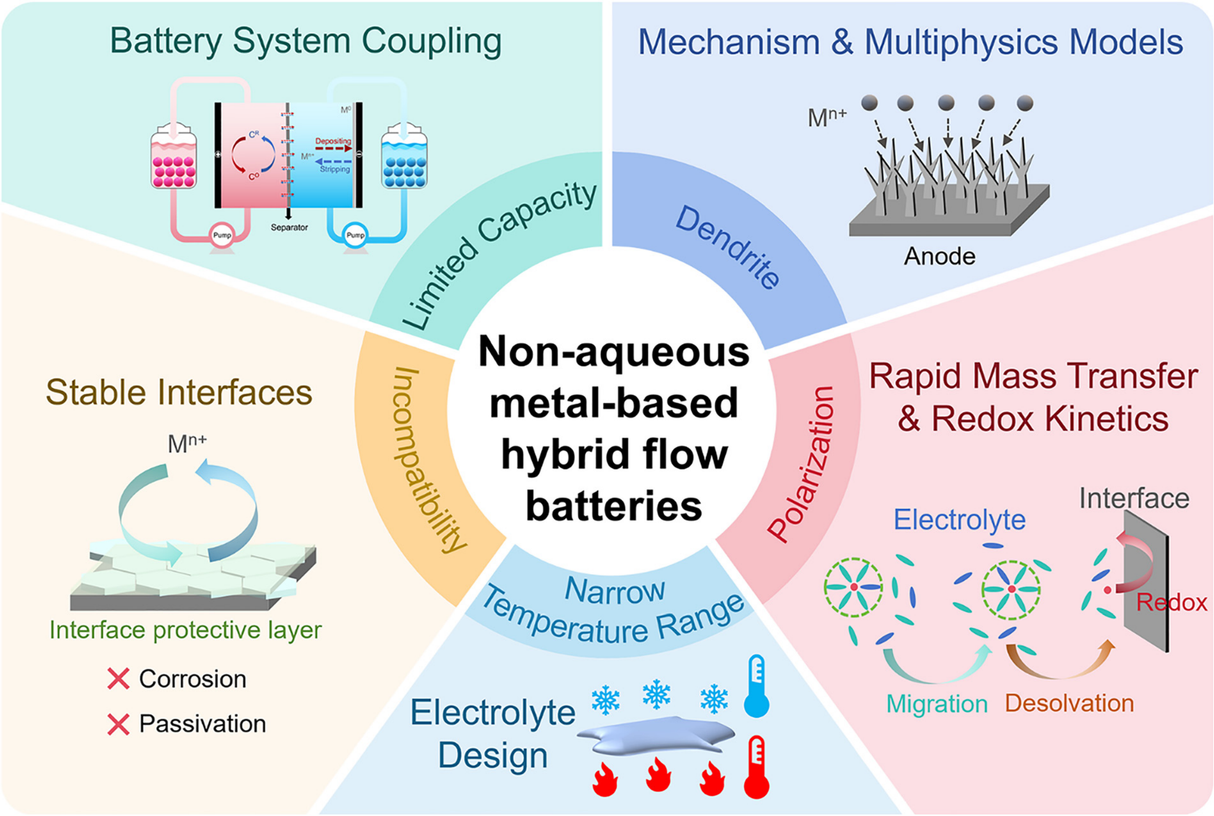

Fig. 15 Main challenges and corresponding strategies of non-aqueous MBHFBs.

and toxicity of organic solvents, the requirements for the sealing technology of the storage tanks are much more stringent. Beyond safety and environmental concerns, the intrinsic properties introduced by non-aqueous electrolytes (such as their relatively low ionic conductivity, high viscosity, sluggish mass transfer, and slow ion diffusion) result in battery performance that falls far short of application standards. Additionally, compatibility issues between the organic solvents and the metal anodes, as well as with the separators, can further shorten battery lifespan. Collectively, these factors constrain the commercialization of non-aqueous MBHFBs. In terms of individualities, Li-HFBs boast the greatest voltage advantage but suffer from limited lithium resources; Na-HFBs exhibit a significant cost advantage, but the practical energy density remains relatively low; K-HFBs offer a cost advantage, yet potassium's high reactivity and the lack of suitable electrolytes become obstacles; Mg-HFBs generate fewer magnesium dendrites, but Mg is prone to passivation and exhibits poor reversibility; lastly, Al-HFBs feature a high theoretical capacity due to three-electron transfer, but the ionic liquids they employ have high viscosity and cost. Furthermore, benefiting from the first-mover advantage of lithium metal batteries, research on non-aqueous MBHFBs has predominantly focused on Li-HFBs. In contrast, the later development of post-lithium batteries has resulted in relatively limited research on the other four types of non-aqueous MBHFBs, with many issues yet to be uncovered.

3.6.2. Strategies and prospectives. Tackling these challenges is essential for propelling the progress of non-aqueous MBHFBs. To effectively tackle these challenges and achieve promising advancements, future targeted research should prioritize the following critical dimensions:

(1) Investigating the formation mechanism and influencing factors of dendrites in non-aqueous electrolytes. The formation mechanism of anodic dendrites in nonaqueous systems involves complex interplay among electrochemical kinetics, crystallography, interfacial thermodynamics, and fluid dynamics. The dendrites arise from anisotropic interfacial energy during metal deposition on electrode surfaces, which drives nonuniform nucleation and subsequent anisotropic growth. Non-aqueous electrolytes typically exhibit low ionic conductivity and dielectric constants, resulting in sluggish ion migration within the electrolyte. When the local current density exceeds a critical threshold, concentration polarization intensifies, triggering a "tip effect" that accelerates nucleation at protrusions and induces dendritic branching *via* anisotropic growth. While electrolyte flow effectively mitigates concentration polarization, excessive flow velocities may dislodge nascent nuclei, resulting in loosely deposits. Conversely, insufficient flow rates promote dendritic growth longitudinally. Consequently, electrolyte composition, electrode interface, current density, and flow rate collectively govern dendritic nucleation and growth. To elucidate these dynamics, high spatiotemporal-resolution *in situ* characterization techniques should be deployed to monitor real-time dendritic evolution, complemented by density functional theory (DFT) calculations and multiphysics coupling simulations to establish unified thermodynamic-kinetic

models. These efforts will deepen mechanistic insights into the full sequence of crystal nucleation, dendritic growth, and separator puncture.

(2) Enhancing compatibility between non-aqueous electrolytes, metal anodes, and separators to construct highly stable interfaces for suppressing side reactions and promoting uniform metal deposition. The compatibility of non-aqueous electrolytes with different metal anodes (Li, Na, K, Mg, Al, *etc.*) varies, mainly depending on the chemical reactivity of the metal, the reduction stability of the electrolyte, and the interfacial reaction mechanism. Organic solvents (*e.g.*, carbonates, ethers) often undergo reduction by active metals at low potentials, forming a solid electrolyte interphase (SEI) composed of inorganic and organic components. However, this native SEI often exhibits insufficient mechanical robustness, leading to fracture under dendrite-induced stress and subsequent parasitic reactions. Na exhibits a slightly higher reduction potential than Li, resulting in comparatively weaker reductive reactivity toward electrolytes. The composition of the SEI formed on Na resembles that of Li; however, it tends to be more porous and exhibits lower ionic conductivity. K exhibits a reduction potential comparable to that of Li; however, the lower solvation energy of K^+ ions facilitates faster interfacial kinetics. The SEI formed on K anode is thicker and more porous, which predisposes it to sustained electrolyte decomposition. The stability of the electrolyte/electrode interface for Li, Na, and K-HFBs can be further enhanced by using high-concentration electrolytes, fluorine-containing additives, artificial SEI layers, three-dimensional porous electrode. The reversible deposition/dissolution of Mg^{2+} ions in conventional non-aqueous electrolytes with organic solvents is hindered by strong solvation interactions between Mg^{2+} ions and solvent molecules. The passive layer formed on Mg impedes Mg^{2+} ions transport. Specialized non-nucleophilic or Grignard reagent electrolytes must be developed to facilitate reversible plating/stripping for Mg. Al metal exhibits negligible deposition in conventional non-aqueous electrolytes with organic solvents. A dense Al_2O_3 passivation layer readily forms on the Al surface, completely obstructing ionic transport. Al deposition is exclusively achievable in ionic liquids or molten salt systems. Overall, the deposition interface can be effectively regulated through a three-pronged strategy encompassing electrolyte optimization (*e.g.*, localized high-concentration, weakly solvating solvents, and additives), electrode modification (*e.g.*, artificial interfacial protective layers, three-dimensional porous electrodes, and alloying), and separator engineering (*e.g.*, surface modification with electrostatic or metallophilic coatings, composite with high-strength or fast-ion conductor materials, and self-healing separator).

(3) Optimizing the composition of non-aqueous electrolytes to enhance their intrinsic properties, and refining battery architecture to improve non-aqueous electrolyte fluidity, thereby elevating overall battery. The performance of flow batteries is highly dependent on electrolyte mass transport and electrode–electrolyte interfacial contact. The core performance metrics of electrolytes include ionic conductivity, viscosity, and redox stability. Among these, the ionic conductivity serves as a critical parameter for evaluating ion migration capability in electrolytes, directly influencing key battery performance indicators such as polarization, efficiency, power density, rate capability, response speed, and temperature adaptability. Viscosity directly governs mass transport, ionic diffusion, and fluidity, particularly critical for flow batteries. Viscosity exhibits a strong inverse correlation with ionic conductivity. Typically, solvent sheath modulation can be employed to simultaneously reduce electrolyte viscosity and enhance ionic conductivity. Strategies include blending low-viscosity, high-dielectric-constant solvents, employing localized high-concentration electrolytes, and incorporating functional additives. Furthermore, integrating artificial intelligence and machine learning enables accelerated discovery of optimal electrolyte formulations through high-throughput computational screening. On the other hand, structural optimization of the battery architecture can mitigate polarization losses and enhance energy conversion efficiency. Three-dimensional cathodes with high specific surface areas can improve electrolyte permeability. The electrode architecture features a gradient porosity design, wherein macropores at the inlet facilitate fluid flow, while micropores at the outlet increase the reactive surface area. Rational optimization of flow channels is conducive to enhancing electrolyte mass transfer, thereby improving battery performance. Specifically, the serpentine flow channel facilitates the prolongation of electrolyte residence time, leading to an increase in reaction efficiency; while the interdigitated flow channel is advantageous for intensifying turbulence and mitigating concentration polarization. In addition, some specialized battery testing protocols can also be adopted. For instance, employing pulsed flow technology to intermittently scour the electrode surface can prevent the accumulation of lithium dendrites while avoiding continuous high-voltage losses.

(4) Striving toward aqueous or hybrid electrolyte systems to fundamentally enhance battery safety and improve intrinsic electrolyte properties while preserving a broad voltage window. Non-aqueous MBHFBs, including Li-, Na-, K-, Mg-, and Al-based systems, demonstrate considerable promise for long-duration energy storage applications due to their high theoretical energy density and broad electrochemical stability windows. Nevertheless, the inherent safety risks posed by flammable organic solvents remain a critical barrier to their commercial viability. Transitioning towards aqueous or hybrid electrolytes, integrated with high safety and wide voltage windows, constitutes a critical pathway for surmounting these technological barriers. While aqueous electrolytes provide inherent safety benefits, their narrow electrochemical stability windows significantly hinder reversible metal deposition/dissolution in systems employing low-redox-potential metals. Consequently, prioritizing the development of hybrid electrolytes that simultaneously offer nonflammability and broad voltage operation ranges is critical. This approach involves two complementary focuses: first, revolutionizing electrolyte design paradigms through solvation structure innovation to create hybrid electrolytes compatible with both cathodes and anodes; second, engineering novel separators featuring hydrophilic/hydrophobic heterostructures to enable localized phase separation between aqueous catholytes and non-aqueous anolytes. In terms of anode metal selection, Li,

Na, and K possess deposition potentials well below the water reduction potential, and react vigorously with water. Conversely, Mg and Al display deposition potentials closer to the water reduction potential and demonstrate comparatively mild reactivity with aqueous environments. Consequently, through strategic modulation of electrolyte solvation structures and electrolyte–anode interface engineering, reversible deposition/dissolution of Mg and Al in aqueous or hybrid electrolytes appears achievable. This approach thus achieves a synergistic integration of high safety and high energy density, aligning more closely with the future development goals of flow batteries.

(5) Integrating strategies such as slurry electrodes or redox-targeting reactions to increase the practical concentration of active materials, thereby unlocking the full high-energy-density potential of non-aqueous MBHFBs. Energy density can be calculated as the product of the average voltage and capacity. Non-aqueous MBHFBs inherently demonstrate high voltage advantages owing to the exceptionally low deposition/dissolution potentials of their anodic materials. However, the capacity of conventional non-aqueous MBHFBs remains fundamentally constrained by the solubility limits of active species in the electrolyte. It is noted that in legacy non-aqueous MBHFBs, high-energy-density metal foils are typically employed as anodes, while the volume and concentration of catholyte remain limited, resulting in a substantial capacity excess of anode relative to the cathode. Strategies employing slurry electrodes or redox-targeting reactions have been experimentally validated to circumvent the solubility-driven capacity ceiling of cathodic active materials, enabling multi-fold capacity enhancement of the cathode and thereby significantly improving both the overall battery capacity and energy density. However, these two strategies still harbor distinct and notable defects that necessitate further resolution. For instance, slurry electrodes compromise the homogeneity of the electrolyte and impede its fluidity; meanwhile, the selection criteria for redox-targeting reaction intermediates are stringent, and their stability remains inadequate. Nevertheless, the next-generation non-aqueous MBHFBs, which integrate high-voltage potential with high-capacity strategies, represent a promising and worthwhile avenue for further exploration and development.

4. Aqueous metal-based hybrid flow batteries

With the rapid expansion of the installed capacity of renewable energy, the scale of long-duration energy storage technologies has also experienced substantial growth. Aqueous MBHFBs have emerged as a research hotspot in the energy storage field in recent years, attributed to their high safety, low cost, and environmental benignity. By substituting conventional non-aqueous electrolytes with aqueous electrolytes, these MBHFBs significantly mitigate flammability risks and toxicity. Meanwhile, they capitalize on the high specific capacity characteristics of metals (*e.g.*, zinc, iron) and integrate soluble-type or deposition-type cathodes, thereby achieving the synergistic enhancement of energy density and power density. Nevertheless, their practical application progress is still hampered by intricate challenges, including uneven deposition and dendrite growth during metal deposition/dissolution processes, water decomposition (hydrogen evolution and oxygen evolution), interfacial side reactions, cross-contamination of active materials, and water migration. In recent years, six typical aqueous MBHFBs represented by zinc, iron, cadmium, tin, copper, and lead have achieved rapid development, and various strategies have been demonstrated to effectively alleviate these issues. Sustained tracking of their research progress is conducive to enabling researchers to better advance the development of next-generation aqueous MBHFBs technologies.

4.1. Zinc (Zn)-based hybrid flow batteries

Aqueous zinc-based HFBs have garnered significant attention in recent years as an emerging electrochemical energy storage technology, which demonstrates notable advantages in terms of safety, cost-effectiveness, and environmental compatibility. The utilization of aqueous electrolytes eliminates the flammability and explosion risks associated with non-aqueous electrolytes, thereby substantially enhancing the safety profile of the battery system. The adoption of water as the solvent precludes the use of toxic or hazardous solvents, aligning with the principles of green and sustainable development. Furthermore, zinc, ranking as one of the most abundant metallic elements in the Earth's crust, offers distinct advantages for large-scale energy storage applications due to its global abundance, mature extraction-refining technologies, and low cost. Zinc is also recognized as an environmentally benign metal, characterized by minimal environmental impact during both production and recycling processes. When compared to other metal- based HFBs (*e.g.*, lithium, lead), Zn-HFBs demonstrate superior alignment with the principles of green chemistry and sustainable development. Moreover, zinc, as the core redox-active material, exhibits a relatively low redox potential (−0.76 V *vs.* SHE), which enables Zn-HFBs to achieve a high operating voltage.[137] With a theoretical specific capacity of 820 mAh g^{-1}, zinc exhibits higher energy density than many other metallic anode materials (*e.g.*, lead, nickel). The rapid reaction kinetics of zinc dissolution and deposition in the electrolyte facilitates high power output capabilities. Therefore, Zn-HFBs emerge as a highly promising energy storage technology, combining compelling economic and environmental benefits with exceptional electrochemical performance characteristics, including high operating voltage, energy density, and power output capabilities.

Building upon these substantial advantages, Zn-HFBs technology has witnessed remarkable progress and rapid development, with particularly accelerated advancements since 2019, marking a significant milestone in the evolution of this energy storage technology (Fig. 16a). The family of Zn-HFBs encompasses a diverse range of configurations, which can be broadly categorized into zinc–bromine HFBs, zinc–iodine HFBs, zinc–cerium HFBs, zinc–nickel HFBs, zinc–manganese dioxide HFBs, zinc–iron HFBs, zinc–organic HFBs, and zinc–air HFBs. As shown in Fig. 16b, these Zn-HFBs exhibit distinct advantages and limitations in terms of economic viability, environmental safety,

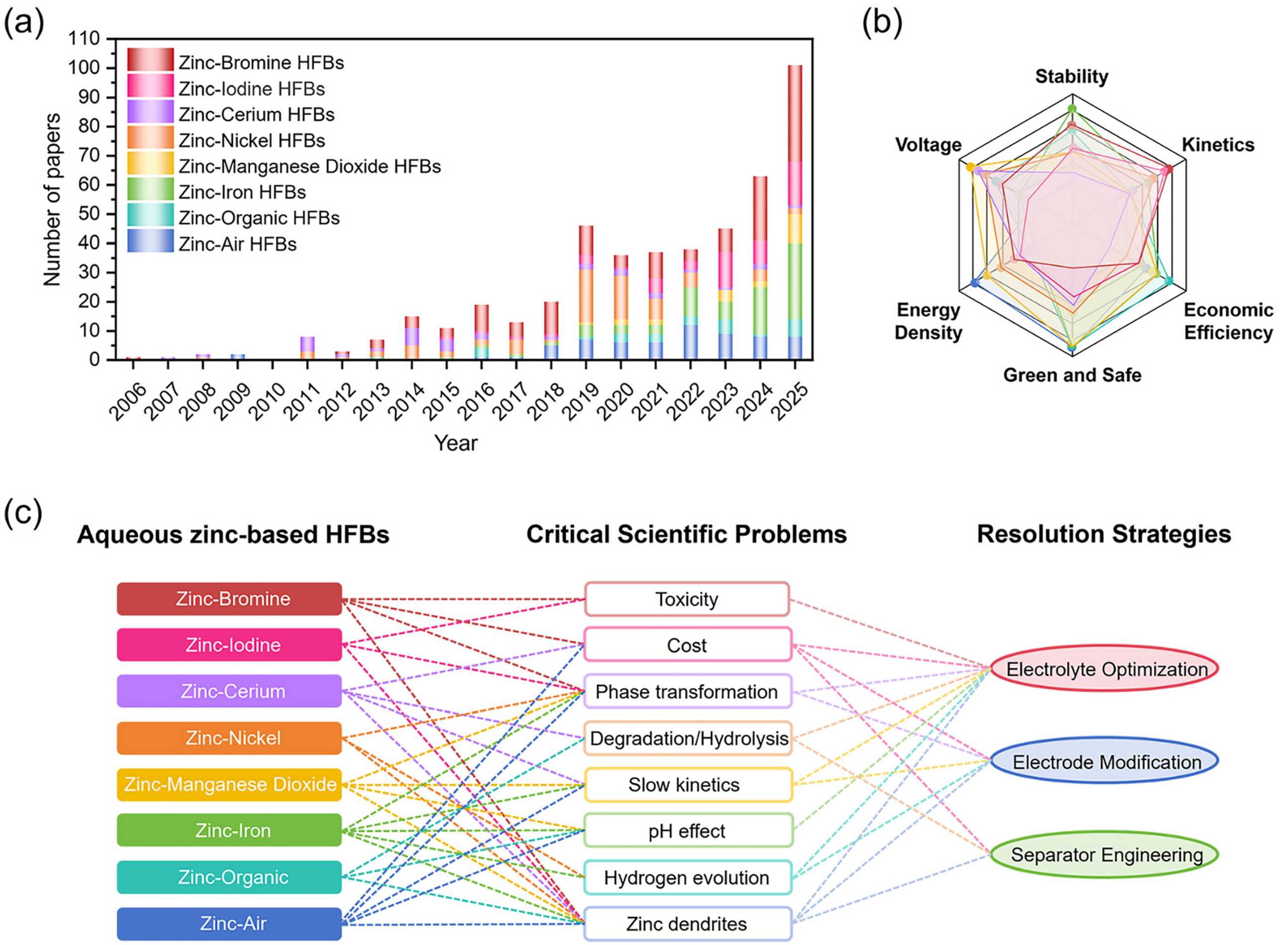

Fig. 16 (a) Number of publications devoted to different zinc-based HFBs. Data were collected from January 2006 to December 2025 on Web of Science. (b) Radar chart of performance for different zinc-based HFBs (the colors correspond to those in (a), in terms of voltage, stability, kinetics, economic efficiency, green and safety, and energy density. (c) Schematic diagram of key scientific issues and corresponding resolution strategies for different zinc-based HFBs.

energy density, operating voltage, cycling stability, and reaction kinetics, as will be comprehensively reviewed and analyzed in subsequent sections. As depicted in Fig. 16c, the primary challenges confronting Zn-HFBs predominantly stem from multiple intrinsic limitations, including toxicity concerns, cost constraints, phase transition issues, material degradation/hydrolysis, sluggish reaction kinetics, pH fluctuations, hydrogen evolution reactions, and zinc dendrite formation. To address these critical issues, three fundamental strategies have emerged as the most promising solutions: advanced electrolyte optimization, sophisticated electrode modification, and innovative membrane engineering approaches.

4.1.1. Zinc–bromine HFBs. The zinc–bromine HFBs operate through the reversible redox reactions of bromine ion in catholyte and zinc ion in anolyte (as depicted in Fig. 17a). The catholyte of zinc–bromine flow batteries typically consists of bromide salts and bromine complexing agents. During the charging process, bromide ions (Br^-) at the cathode are oxidized to elemental bromine (Br_2). The bromine complexing agents (BCAs) combine with Br_2 to form oily polybromide complexes (OPCs) to reduce the concentration of free bromine species, mitigating bromine diffusion to the anode and minimizing bromine volatility and its associated corrosion risks.[138,139] The zinc–bromine HFBs, currently in the commercialization demonstration phase (successfully for the kW to MW scale applications), have garnered increasing attention as a promising energy storage technology due to their compelling advantages, including abundant raw material availability, cost- effectiveness, and high energy density characteristics.

Nevertheless, both the cathode and anode in zinc–bromine HFBs face distinct technical challenges that require specific attention. (i) Although bromide ions themselves exhibit relatively low toxicity, the electrochemical processes during battery operation can lead to the formation of Br_2, thereby introducing potential toxicity concerns and safety risks.[140] (ii) The practical implementation of zinc–bromine HFBs is significantly hindered by the crossover of polybromide anions through the membrane, leading to substantial capacity fade and low coulombic efficiency.[141] (iii) Despite the inherently low cost of zinc and bromine elements, the overall system economics of zinc–bromine flow batteries remain constrained by the relatively high cost of bromine complexing agents. (iv) The highly corrosive

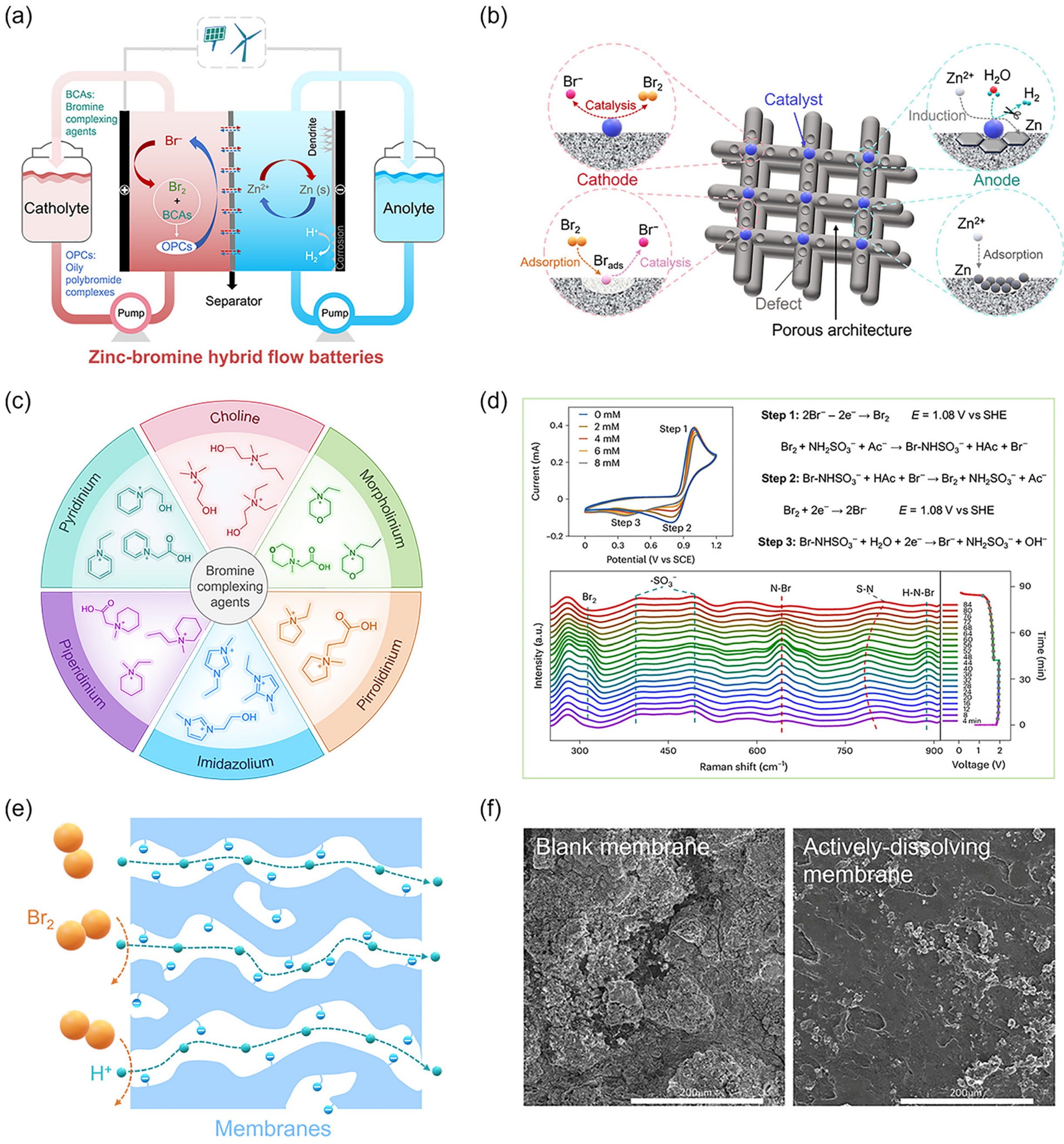

Fig. 17 (a) Schematic diagram of the typical structure of zinc–bromine HFBs and the major challenges. (b) The synergistic design strategy for Br_2/Br^- and Zn^{2+}/Zn electrodes. Adapted from ref. 144 with permission from Wiley-VCH, copyright 2021. (c) The types of bromine complexing agents. (d) Cyclic voltammetry curve, corresponding electrochemical reaction equations and *in situ* Raman spectroscopy of NaBr-SANa electrolyte. Reproduced from ref. 32 with permission from Springer Nature, copyright 2025. (e) Schematic diagram of the designed membranes for zinc–bromine HFBs with high ion selectivity. Adapted from ref. 151 with permission from Wiley-VCH, copyright 2024. (f) SEM images of blank membrane and actively-dissolving membrane after 100 cycles. Reproduced from ref. 153 with permission from Wiley-VCH, copyright 2025.

nature of bromine poses significant challenges to battery components, including pipelines, pumps, and sealing materials. This corrosion phenomenon not only increases maintenance complexity but also escalates operational costs, thereby presenting a substantial barrier to long-term system reliability and economic viability. (v) The standard rate constants for the Zn^{2+}/Zn and Br_2/Br^- redox couples are 7.5×10^{-5} and 4×10^{-7} m s^{-1}, respectively. This substantial difference in kinetic parameters, spanning two orders of magnitude, indicates significantly slower reaction kinetics for the Br_2/Br^- redox couple compared to Zn^{2+}/Zn, resulting in pronounced kinetic mismatch.[142] (vi) Zinc–bromine HFBs operate within a narrow pH window, making them particularly susceptible to hydrogen evolution reactions and zinc corrosion. (vii) Similar to other zinc-based HFBs, zinc–bromine HFBs are also confronted with the persistent challenge of zinc dendrite formation, which may penetrate the membrane and lead to internal short circuits, significantly compromising the cycle life performance. These critical limitations underscore the urgent need for developing effective bromine and zinc management strategies to enable stable and high-performance zinc–bromine HFBs.

Researchers have primarily focused on three strategic approaches to address these aforementioned challenges in zinc–bromine HFBs: electrode design, electrolyte optimization, and membrane engineering. (i) The design of Br_2/Br^- electrode includes catalyst integration, surface functionalization, and hierarchical porous architecture engineering (Fig. 17b). Liu and colleagues successfully synthesized a wo-dimensional conjugated nickel polyphthalocyanine (NiPPc) as an adsorption-catalytic host matrix. The atomically dispersed $Ni–N_4$ active sites within NiPPc not only provided highly efficient catalytic centers for bromine redox reactions but also demonstrated strong polar adsorption capabilities towards both elemental bromine and polybromide species.[143] Li and colleagues developed a nitrogen-rich defective carbon felt electrode with multifunctional characteristics, which demonstrate exceptional catalytic activity towards the Br_2/Br^- redox reactions owing to abundant nitrogen-functionalized defect sites.[144] Li's team also devised a type of carbon nanospheres with a unique hollow core–shell structure. This structure consisted of a carbon core and a hollow carbon shell, offering an abundant hierarchical pore structure, a high specific surface area, and exceptional bromine adsorption capacity. This structure not only enhanced the catalytic activity of the electrode, but also strengthened the bromine immobilization capability, effectively suppressing bromine diffusion and battery self-discharge.[145] (ii) The design of Zn^{2+}/Zn electrode primarily focuses on interfacial modification and structural optimization (Fig. 17b). Archer and colleagues employed a facile electrospray technique to create an artificial graphene interface on the anodic electrode. This approach not only enabled precise alignment of graphene sheets through electrostatic forces but also allowed for controlled regulation of graphene quantity and morphology, thereby effectively modulating zinc deposition patterns and suppressing undesirable side reactions.[146] Cheng *et al.* employed an *in situ* electrodeposition strategy to uniformly pre-deposit lead nanoparticles on carbon felt electrodes, serving as nucleation sites for zincophilic nucleation. This approach effectively induced uniform zinc deposition and suppressed the growth of zinc dendrites.[147] (iii) Electrolyte optimization strategies center on deploying cost-effective, low-toxicity, high-affinity bromine complexing agents in the catholyte (Fig. 17c), coupled with anolyte additives designed to mitigate zinc dendrite growth.[139,148,149] Liang's team developed a highly hydrophilic bromine-complexing agent, *N*-methyl-*N*,*N*-bis(2-hydroxyethyl)-1-propanaminium bromide (PMDA), which formed a larger-size $PMDABr_{2n+1}$ complex with polybromides (Br_{2n+1}^-), enabling stable high-concentration bromine operation with a low bromine crossover.[148] Li's team demonstrated that incorporating either *n*-propyl-(2-hydroxyethyl)-dimethylammonium ($N[1,1,3,2OH]^+$) or diethyl-(2-hydroxyethyl)-methylammonium ($N[1,2,2,2OH]^+$) as bromine-complexing agent cations in the electrolyte enabled precise modulation of polybromide polarity, thereby significantly enhancing bromine capture capacity and improving performance of zinc–bromine HFBs at low temperature.[149] Xu *et al.* employed sodium sulfamate (SANa) as a Br_2 scavenger, which reacts rapidly with Br_2 to form the mild product *N*-bromo sodium sulfamate (Br-SANa; Br^+), as shown in Fig. 17d. This reduced free Br_2 to 7 mM and eliminated corrosion, while enabling a two-electron transfer process in the Br-SANa/Br^- redox couple. The energy density was thus enhanced from 90 Wh L^{-1} in conventional zinc–bromine flow batteries to 152 Wh L^{-1}. A 5 kW system exhibited stable operation for 700 cycles (1400 hours).[32] For the anolyte, the solvation structure of Zn^{2+} ions within it can be precisely regulated by introducing dimethyl sulfoxide (DMSO) as a co-solvent additive. Acting as a strong hydrogen bond acceptor, DMSO selectively occupies the second solvation shell of Zn^{2+} ions, thereby stabilizing the coordination environment of Zn^{2+}. This process suppresses the HER and enhances the reversibility of zinc deposition/stripping.[150] (iv) Since both the cathodic and anodic active materials are $ZnBr_2$, the membrane does not need to function to prevent cross-contamination between the electrolytes. Its primary roles are to impede the diffusion of bromine from the cathodic electrolyte into the vicinity of the anode and to maintain ionic equilibrium between the cathodic and anodic electrolytes. The design of membranes for zinc–bromine HFBs necessitates a multi-objective optimization balancing ion selectivity, ionic conductivity, chemical stability, and economic viability (Fig. 17e).[151] These parameters exhibit inherent trade-offs: enhancing ionic selectivity against polybromide species often compromises proton conductivity, while materials resilient to bromine penetration may introduce cost barriers or mechanical fragility. Shanmugam's team prepared tungsten trioxide (WO_3) nanoparticle-decorated graphene oxide (WO_3@GO)-loaded sulfonated poly (ether ether ketone) (SPEEK) membranes. The WO_3-loaded GO nanosheets, featuring enhanced hydrophilic properties and uniform dispersion, established robust interactions with the sulfonic acid groups of the SPEEK matrix. Thus, the WO_3@GO/SPEEK membrane created a highly effective barrier against transmembrane bromine contamination.[152] Cheng *et al.* proposed a zinc dendrite dissolution membrane by coating a layer of tetrabutylammonium tribromide ($TBABr_3$) onto the surface of a polyolefin membrane. This membrane could spontaneously oxidize metallic zinc (Zn^0) to zinc ions (Zn^{2+}), thereby enabling the dissolution of zinc dendrites (as depicted in Fig. 17f). This approach effectively prevents the issue of battery internal short-circuits caused by zinc dendrites penetrating the membrane.[153]

4.1.2. Zinc–iodine HFBs.

Both zinc–iodine HFBs and zinc–bromine HFBs belong to the zinc–halogen HFBs family, sharing similar cell architectures and reaction mechanisms in their cathodic/anodic electrolytes (as depicted in Fig. 18a). However, iodine offers distinct advantages over bromine:[154] (i) the iodine-based electrolyte exhibits significantly lower toxicity and volatility, enhancing environmental compatibility and operational safety; (ii) iodine achieves natural dissolution as I_3^- without requiring complexing agents or strongly acidic conditions for stabilization; (iii) the iodine shuttle effect is less pronounced than that of bromine, reducing membrane requirements; (iv) faster redox kinetics eliminate the need for expensive catalysts; (v) the

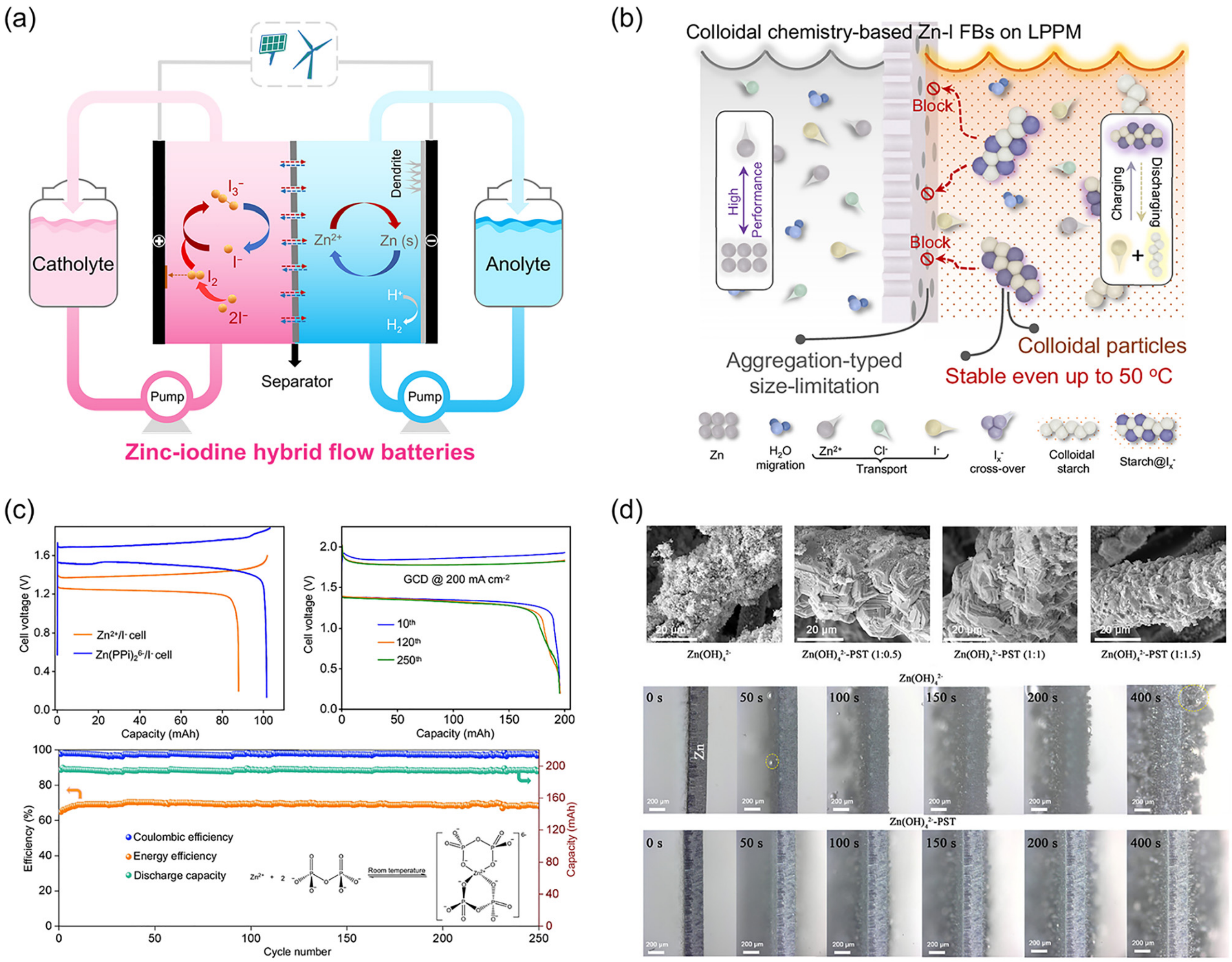

Fig. 18 (a) Schematic diagram of the typical structure and major challenges of zinc–iodine HFBs. (b) Working principle of colloidal chemistry-based electrolytes: restricting the cross-over of active materials (I_x^-) through the size limitation induced by the colloidal aggregation effect. Reproduced from ref. 159 with permission from Springer Nature, copyright 2024. (c) Electrochemical performance of $Zn(PPi)_2^{6-}$ based zinc–iodine HFBs. Reproduced from ref. 160 with permission from Springer Nature, copyright 2024. (d) The morphologies and *in situ* optical microscopic images of Zn anode in $Zn(OH)_4^{2-}$ electrolytes (without/with potassium sodium tartrate additive). Reproduced from ref. 162 with permission from Wiley-VCH, copyright 2025.

multi-electron transfer capability of iodine enables higher theoretical capacity. Thus, zinc–iodine HFBs are regarded as a promising candidate for next-generation large-scale energy storage, owing to their high theoretical energy density, low cost, inherent safety, and environmental benignity.[155,156] However, iodine shuttle effect and zinc dendrite growth lead to poor cycling stability and rapid capacity degradation. The practical energy and power densities are fundamentally limited by low iodide utilization efficiency, sluggish reaction kinetics of iodine species, asynchronous multi-step redox processes, and the formation of passivating iodine films.[157,158]

The development of high-performance zinc–iodine HFBs hinges on advanced material design and critical component optimization. (i) Electrolyte design: for cathodic electrolytes, Zhi and co-workers utilized starch–iodine colloidal complexes to control the size of active iodine species. This approach leveraged a chemisorption-induced colloidal aggregation mechanism, which substantially enlarged the iodine species' dimensions. The resulting macromolecular complexes could be effectively retained by low-cost porous membranes, thereby addressing the long-standing challenges of cross-contamination-induced capacity decay and coulombic efficiency loss in conventional zinc–iodine HFBs (Fig. 18b).[159] For the anodic electrolyte, Wang *et al.* proposed using the chelating electrolyte $Zn(P_2O_7)_2^{6-}$ for the anolyte in zinc–iodine HFBs, which effectively modulated zinc deposition behavior, suppressing dendrite formation and enhancing cycling stability (Fig. 18c). Remarkably, the $Zn(P_2O_7)_2^{6-}$ chelation complex elevated the voltage from 1.29 V (conventional system) to 1.61 V, substantially enhancing the energy density. The large molecular size and multi-negative charges of the $(P_2O_7)_2^{8-}$ chelating ions simultaneously improved Zn^{2+} selectivity while minimizing crossover effects.[160] Optimally, central to this electrolyte engineering approach is the design of bifunctional additives capable of simultaneously modulating the solvation structure of iodine species and the deposition behavior of zinc ions, thereby cooperatively enhancing both iodine redox utilization efficiency and zinc anode deposition homogeneity. For instance, a ternary hydrated eutectic electrolyte composed of zinc bromide and acetamide was designed to enable concurrent favorable interface engineering at both cathode and anode through solvation structure modulation. The incorporation of Br^- into the Zn^{2+} solvation sheath facilitated strong halogen-bond formation, which kinetically accelerates the reversible I^-/I_2Br^- conversion reaction. As a result, this electrolyte enabled almost 100% iodine utilization while concurrently suppressing zinc dendrite formation.[161] Tang *et al.* utilized potassium sodium tartrate as a bifunctional electrolyte additive. This additive not only effectively regulated the zinc deposition behavior, suppressing the formation of zinc dendrites (as shown in Fig. 18d), but also enhanced the open-circuit voltage and energy density of the battery.[162] (ii) Electrode design: the iodine redox reaction kinetics and uniformity of zinc deposition are enhanced by modifying electrode surfaces with catalysts or functional groups, thereby accelerating charge transfer and spatially regulating nucleation/growth processes. For instance, a bifunctional electrocatalytic graphite felt was fabricated by embedding FeP nanoclusters within an N- and P-codoped carbon layer. Through the synergistic effects of efficient iodine species adsorption and electrocatalytic conversion, the kinetics of the I^-/I_3^- redox reaction were accelerated, and the shuttle effect of polyiodides was suppressed.[163] Zhi and co-workers have pioneered the development of a carbon felt electrode modified with gradient-distributed copper nanoparticles (as shown in Fig. 19a). By strategically engineering spatial gradients in electrical conductivity and zincophilicity, the electrode induced a directional migration of zinc ions from the apical surface to the basal region, enabling a controlled bottom-up zinc deposition pathway that effectively suppresses dendritic zinc growth.[164] (iii) Membrane design: compared with single porous membranes, composite porous membranes are more conducive to suppressing the shuttle effect of polyiodides. For instance, by leveraging adduct chemistry and strong chemisorption between iodine species and a series of low-cost metal oxides (*e.g.*, MgO), a stable localized high-iodine-concentration layer could be formed on composite membranes (Fig. 19b).[165] (iv) Electrolyte flow structure design: the deliberate design of flow channel structures is aimed at enhancing electrolyte mass transfer processes, optimizing zinc deposition morphology, and ultimately improving battery performance. Roberts *et al.* have integrated the "Flow-By" and "Flow-Through" flow field modes, enabling the main electrolyte to traverse the gap between the electrode and the membrane, efficiently dissipating heat and removing reaction products from the electrode surface. Meanwhile, a fraction of the electrolyte directly permeated through the interior of the porous electrode, increasing the contact area between the electrolyte and the electrode interior, thereby enhancing mass transport efficiency.[166]

4.1.3. Zinc–cerium HFBs.

As an emerging hybrid redox flow battery, the zinc–cerium HFB has been extensively investigated at both laboratory and industrial pilot scales since the early 21st century.[167] The zinc–cerium HFBs employ zinc as the anode and cerium as the cathode, offering a high open-circuit voltage that can exceed 2.4 V when fully charged. Cerium species exhibit limited solubility in most supporting electrolytes, rendering them inadequate for practical flow battery operations. Methanesulfonic acid (MSA) has been predominantly employed as the supporting electrolyte in reported Zn–Ce HFBs due to its capacity to solubilize cerium ions at relatively high concentrations. Overall, the research landscape for zinc–cerium HFBs remains sparse, with limited progress reported in recent years. A discernible decline in research enthusiasm has been observed, primarily attributable to the irreconcilable incompatibility between the anolyte and catholyte systems, which remains unresolved despite extensive efforts.

For cathodic electrolytes, the Ce^{4+}/Ce^{3+} redox pair possesses a very high positive standard potential (+1.44 V *vs.* SHE), which is conducive to enhancing the energy density and output power

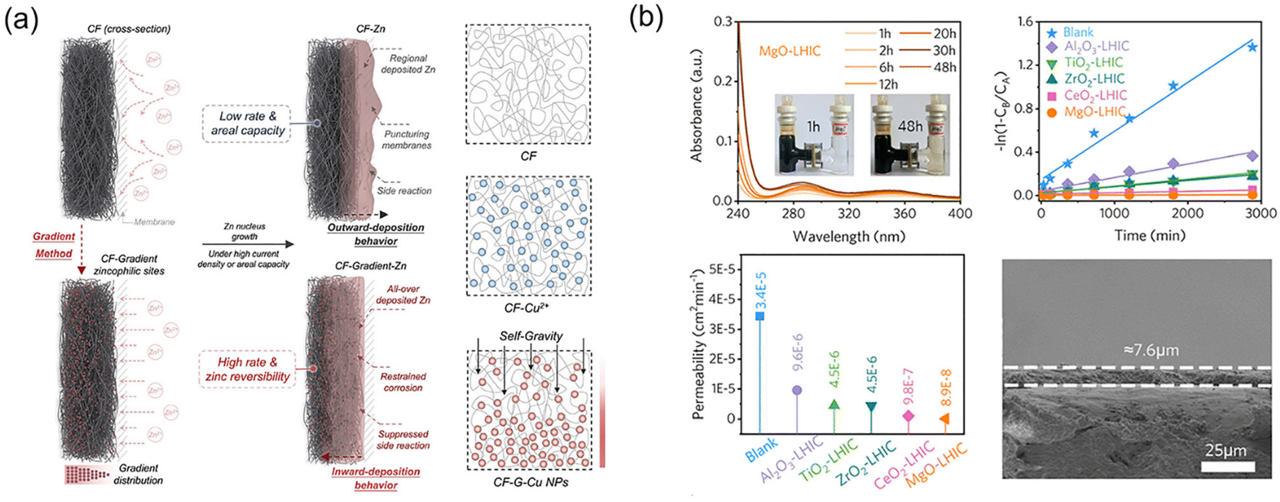

Fig. 19 (a) Working principle of uniform zinc deposition induced by carbon felt electrodes modified with gradient-distributed copper nanoparticles. Reproduced from ref. 164 with permission from Wiley-VCH, copyright 2024. (b) Permeability test of MgO-doped composite membranes for active materials (I_x^-). Reproduced from ref. 165 with permission from The Royal Society of Chemistry, copyright 2024.

of the zinc–cerium HFBs.[168–170] However, precisely due to the high redox potential of Ce^{4+}/Ce^{3+}, the oxygen evolution reaction (OER) becomes a significant competing and side reaction, leading to lower charge–discharge efficiency in zinc–cerium HFBs. The composition and concentration of the supporting electrolyte critically dictate the reaction kinetics and operational stability of the Ce^{4+}/Ce^{3+} redox couple, necessitating the incorporation of electrolyte additives or mixed-acids to enhance reaction kinetics and prolong the electrochemical durability.[171] For anodic electrolytes, the highly acidic electrolyte environment exacerbates hydrogen evolution reactions (HER) and zinc corrosion, which collectively degrade the coulombic efficiency of zinc-cerium HFBs. Pritzker's research found that adding Cl^- ions to the MSA electrolyte could significantly reduce the nucleation potential of zinc, improve the deposition behavior of zinc and increase the exchange current density of the redox reaction of zinc.[172] For electrodes, research efforts have primarily focused on surface modification of electrodes *via* electrocatalytic coatings (*e.g.*, Pt, reduced graphene oxide) to enhance the kinetics of the Ce^{4+}/Ce^{3+} redox reaction. However, the strongly oxidative environment (MSA electrolyte with high Ce^{4+} concentration) adversely affects the long-term stability of electrode materials, particularly the carbon-based electrodes, causing carbon oxidation, surface degradation, and catalyst deactivation. Regrettably, research addressing these issues remains remarkably scarce. For membranes, stringent requirements are imposed on membrane design due to the inherent incompatibility between the anolyte and catholyte in zinc–cerium HFBs. As previously reported, the Ce^{4+}/Ce^{3+} redox couple necessitates elevated proton concentrations to maintain sufficient solubility, whereas the zinc electroplating/stripping process exhibits extreme sensitivity to H^+ activity. Daoud proposed an innovative dual-membrane configuration comprising a cation exchange membrane (CEM) oriented toward the Zn electrode and an anion exchange membrane (AEM) adjacent to the Ce electrode, separated by an electrolyte-filled graphite felt (as depicted in Fig. 20a).[173] This dual-membrane configuration enabled physical segregation of the anolyte and catholyte, allowing selective utilization of electrolyte-compatible charge carriers (*e.g.*, $CH_3SO_3^-$ and K^+) to mitigate H^+-induced side reactions for Zn anode, thereby enhancing both cell efficiency and operational stability. The integration of a conductive graphite felt within the dual-membrane configuration further optimized local electric field distribution, minimizing polarization losses and facilitating ion transport kinetics (Fig. 20b).

4.1.4. Zinc–nickel HFBs. Since its emergence in 2007, the zinc–nickel HFB has become as one of the promising technologies in electrochemical energy storage, owing to its advantages of safety, stability, low cost, and high energy density.[174] During the charging process, $Zn(OH)_4{}^{2-}$ in the anolyte is reduced to elemental zinc, which precipitates onto the anodic materials. Concurrently, $Ni(OH)_2$ at the cathode is oxidized to NiOOH. During the discharging process, the zinc metal deposited on the anode is oxidized back to $Zn(OH)_4{}^{2-}$ and dissolves into the anolyte, while NiOOH at the cathode is reduced to $Ni(OH)_2$.[175] It is noteworthy that the zinc–nickel single-flow battery employs a unilateral electrolyte circulation configuration, which effectively eliminates the issue of cross-contamination between cathodic and anodic electrolytes.[176,177] Consequently, it enables a membrane-free design, streamlining the battery system architecture while simultaneously reducing manufacturing costs. However, as research progresses, it has become evident that the development of zinc–nickel HFBs is hindered by the issues, including zinc dendrite formation, zinc accumulation, polarization effects, and gaseous side reactions.[178,179]

Over the past two decades, researchers have made lots of efforts to address the aforementioned challenges through experimental investigations and computational modeling, holding significant implications for future research endeavors in this field. (i) Researches have demonstrated that factors such as electrolyte flow rate, current density, anode material selection, and electrolyte additives significantly influence the morphological evolution of zinc deposition during electrochemical processes. Battaglia *et al.* proposed a straightforward method for the effective removal of zinc dendrites grown on the anode surface by repeatedly raising and lowering the electrolyte level to expose the dendrites to atmospheric oxygen, thereby oxidizing the zinc dendrites into zinc oxide and subsequently dissolving the oxide into the electrolyte.[180] (ii) When the charge consumed by side reactions at the zinc anode (HER and zinc corrosion) and the nickel cathode (OER and nickel corrosion) in zinc–nickel HFBs is unequal, it results in one electrode being fully discharged while the other remains incompletely discharged. The inherently higher kinetic rate of the zinc deposition/dissolution process leads to lower charge consumption by side reactions at the anode compared to the cathode. Consequently, zinc metal gradually accumulates on the anode during repeated cycling, which can induce internal short-circuiting (as depicted in Fig. 20c).[181] Therefore, suppressing side reactions at the cathode while promoting side reactions at the anode provides a fundamental solution to the issue of zinc accumulation in zinc–nickel HFBs. However, in practical implementation, considering the detrimental impact of side reactions on coulombic efficiency, there is a stronger tendency to suppress side reactions at the cathode. For instance, a composite cathode can be constructed by *in situ* coupling an additional oxygen redox couple at the nickel cathode. In this composite structure, zinc ions that cannot be fully consumed by the nickel redox couple during discharge can be oxidized by the oxygen redox couple, thereby mitigating the problem of zinc accumulation. (iii) Concentration polarization significantly impacts the performance of zinc–nickel HFBs, and mitigating or even eliminating concentration polarization is crucial for enhancing the battery's rate performance. Experimental and computational studies have demonstrated that optimizing flow channel configurations and adopting porous electrode architectures can effectively mitigate polarization issues.[182,183]

4.1.5. Zinc–manganese dioxide HFBs. Aqueous zinc–manganese dioxide HFBs operate through deposition–dissolution phase transition reactions, involving zinc metal at the anode and manganese dioxide at the cathode (as depicted in Fig. 21a). Among various zinc-based HFBs, the aqueous zinc–manganese

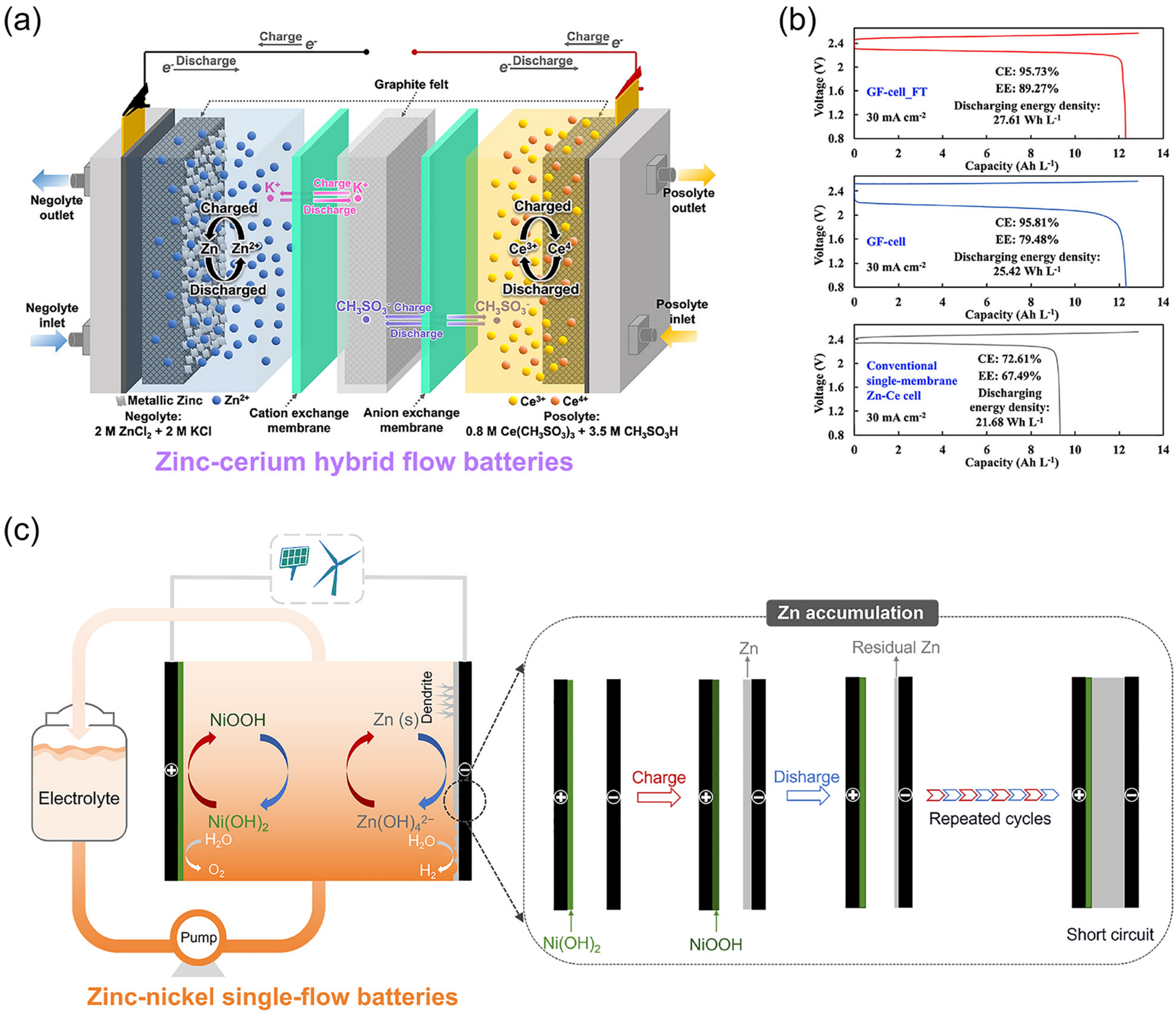

Fig. 20 (a) and (b) Working mechanism and electrochemical performance of the Zn–Ce RFB with a dual-membrane cell configuration. Reproduced from ref. 173 with permission from American Chemical Society, copyright 2022. (c) Schematic diagram of the typical structure of zinc–nickel HFBs and the issue of zinc accumulation. Adapted from ref. 181 with permission from Elsevier, copyright 2019.

dioxide flow battery has attracted significant attention due to its advantageous characteristics, including low cost, safety, environmental friendliness, high operating voltage, and superior energy density.[184] (i) Zinc and manganese offer significant economic advantages due to their abundant natural reserves and low costs, complemented by the use of aqueous electrolytes that are substantially more cost-effective compared to expensive organic solvents or ionic liquids. (ii) The inherent non-flammability of aqueous electrolytes, zinc and manganese dioxide, fundamentally eliminates safety hazards associated with thermal runaway, combustion, and explosive risks. (iii) The aqueous electrolyte, zinc, and manganese dioxide demonstrate exceptional environmental compatibility, being inherently non-toxic, ecologically benign, and readily recyclable, thereby offering a sustainable solution for large-scale energy storage applications.[185] (iv) The Zn^{2+}/Zn anode exhibits a low redox potential (−0.76 V *vs.* SHE) and a high theoretical specific capacity (820 mAh g^{-1}), while the MnO_2/Mn^{2+} cathode demonstrates a high redox potential (+1.22 V *vs.* SHE). This synergistic combination of electrode materials results in the aqueous zinc–manganese dioxide flow battery achieving significantly higher operating voltages and energy densities compared to conventional all-vanadium or other all-soluble flow batteries.[186–188]

However, the development of aqueous zinc–manganese dioxide flow batteries has been relatively recent with limited research quantity, which primarily stems from two fundamental challenges (as shown in Fig. 21b): (i) the electrochemical performance is significantly constrained by the poor reversibility, limited conductivity, and sluggish reaction kinetics of the manganese dioxide cathode, while the cycle life of the battery is predominantly compromised by inhomogeneous deposition on the cathode and zinc dendrite formation at the anode. (ii) The battery primarily relies on the reversible deposition–dissolution process onto the carbon felt electrodes to achieve the mutual conversion

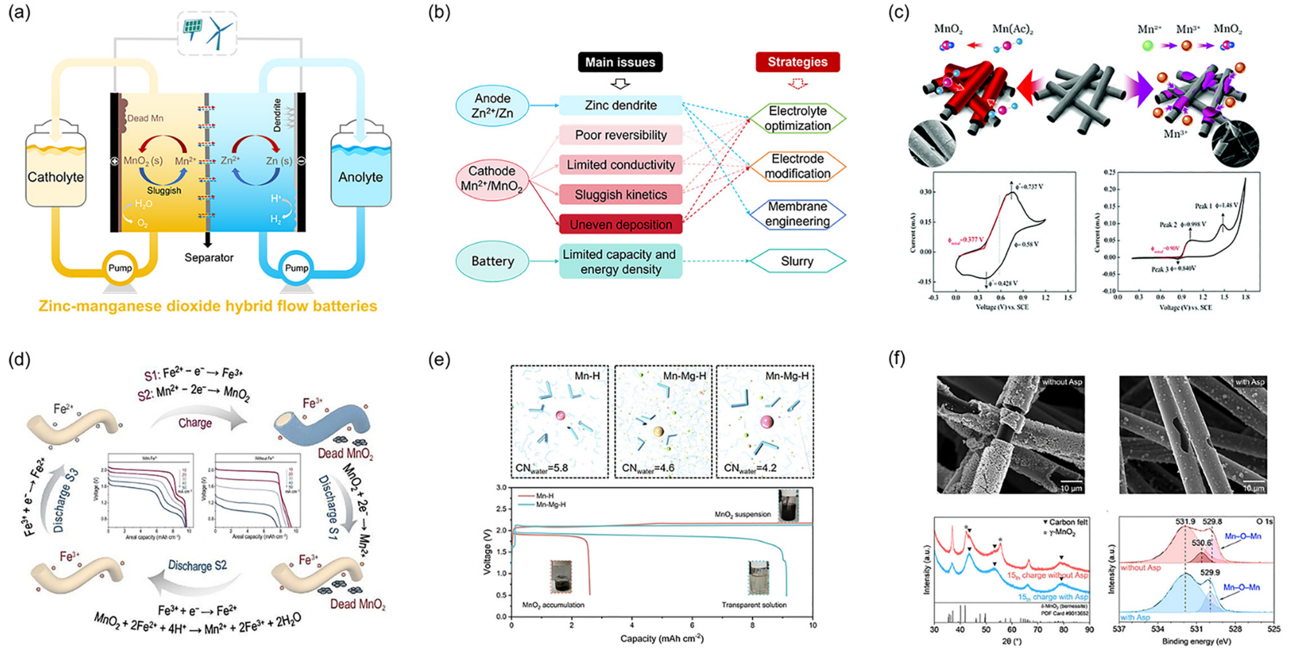

Fig. 21 (a) Structural schematic diagram of zinc–manganese dioxide HFBs. (b) Main issues and strategies of zinc–manganese dioxide HFBs. (c) The electrochemical mechanism and measurement of the $Mn(Ac)_2$ and $MnSO_4$ electrolyte. Reproduced from ref. 189 with permission from The Royal Society of Chemistry, copyright 2020. (d) Schematic illustration of redox targeted reaction and electrochemical performance of MnO_2 cathode with Fe^{2+} as redox intermediate. Reproduced from ref. 190 with permission from Oxford University Press, copyright 2024. (e) Top: The visualized solvation structures of Mn^{2+} and Mg^{2+} in Mn–H and Mn–Mg–H electrolytes. Bottom: Initial galvanostatic charge and discharge profiles of Zn–MnO_2 HFBs with different electrolytes. Reproduced from ref. 191 with permission from The Royal Society of Chemistry, copyright 2025. (f) SEM images, XRD patterns, and XPS spectra of the cathode charge products in the electrolyte without/with aspartic acid. Reproduced from ref. 192 with permission from Wiley-VCH, copyright 2025.

between chemical energy and electrical energy. This results in the deposition amount of active materials being constrained by the surface area of the carbon felt and the concentration of metal ions in the electrolyte. Increasing the volume of the electrolyte does not indefinitely enhance the battery capacity, meaning that battery capacity and power are not fully decoupled.

For the cathodic side, researchers have primarily developed two strategic approaches to address the critical challenges of poor reversibility, limited conductivity, sluggish reaction kinetics, and non-uniform deposition of manganese dioxide. (i) The first strategy focuses on systematic optimization of electrolyte composition. Li's research team utilized the coordination effect between CH_3COO^- and Mn^{2+} ions, enabling the direct and uniform deposition of MnO_2 on carbon felt electrodes (Fig. 21c).[189] Zhao and his collaborators introduced Fe^{2+} ions with fast redox kinetics as a redox mediator in the electrolyte, effectively enhancing the reaction kinetics of the Mn^{2+}/MnO_2 redox couple and improving electrochemical performance of the battery (Fig. 21d).[190] Zhi and colleagues introduced Mg^{2+} cations into the solvation sheath, which effectively immobilized free water molecules, facilitated the deposition of Mg-doped MnO_2 with expanded atomic spacing, and achieved highly reversible Mn^{2+}/MnO_2 redox reactions (Fig. 21e).[191] Aspartic acid effectively mitigated the formation of Mn^{3+} and the accumulation of inactive γ-MnO_2 through interactions between its carboxyl and amino groups with Cl^-, Mn^{2+}, and Zn^{2+} ions in the electrolyte, thereby significantly enhancing the battery's cycle life (Fig. 21f).[192] (ii) The second strategy involves surface modification and electrode engineering. Various modifications, including carbon coating, bismuth nanoparticle decoration, and silver-based metal–organic framework (MOF) functionalization of carbon felt electrodes, have demonstrated significant improvements in both reversibility and reaction kinetics of the Mn^{2+}/MnO_2 redox couple.[189,193,194] Shao-Horn's team pioneered an alternative approach to conventional electrode modification by developing a flowable slurry electrode system. This design involved the homogeneous dispersion of commercial electrolytic γ-MnO_2 powder blended with carbon black in a xanthan gum-modified electrolyte, significantly enhancing both the electrical conductivity and electrochemical reversibility of MnO_2 through improved particle connectivity and ionic transport.[195] For the anodic side, researchers have developed three primary approaches to mitigate zinc dendrite formation. (i) The first strategy focuses on electrolyte optimization through composition modification and additive engineering. (ii) The second strategy focuses on electrode modification *via* surface treatment and structural design. (iii) The third strategy focuses on advanced membrane engineering. He *et al.* developed a machine learning model using the gradient boosting decision tree algorithms to predict polymer functional group effects on ion conductivity. They synthesized sulfonated poly (terphenyl methyl-piperidone bromo-trifluoroacetophenone) membranes, enabling Zn–MnO_2 flow batteries to achieve peak power density of 150 mW cm^{-2} and maintain 71% capacity after 1000 cycles at 30 mA cm^{-2}.[196]

4.1.6. Zinc–iron HFBs. Zinc and iron are both abundant and inexpensive elements. The combination of zinc redox couples and iron redox couples enables a significantly low capital cost for energy storage systems. During charging, Zn^{2+} or $Zn(OH)_4{}^{2-}$ ions at the anode are reduced to metallic zinc, which deposits onto the anode surface, while Fe^{2+} ions at the cathode are oxidized to Fe^{3+} ions. During discharging, the deposited metallic zinc at the anode dissolves back into Zn^{2+} or $Zn(OH)_4{}^{2-}$ ions, and Fe^{3+} ions at the cathode are reduced to Fe^{2+} ions. Furthermore, the zinc–iron HFBs stand out as a formidable competitor for next-generation low-cost energy storage technologies due to its non-toxicity, environmental compatibility, and exceptional operational stability.[197–200] While zinc–iron HFBs represent a relatively nascent field in electrochemical energy storage, the past decade has witnessed a surge in interdisciplinary research efforts aimed at systematically addressing the distinct technical bottlenecks of their three dominant variants: alkaline, acidic, and neutral electrolyte systems. These endeavors have yielded transformative breakthroughs in electrolyte engineering, electrode microstructure optimization, and membrane-separator innovation, collectively shaping the technological trajectory of zinc–iron HFBs toward scalable commercial deployment.

Zinc–iron HFBs can operate across a broad pH range, enabling their classification into alkaline, neutral, and acidic zinc–iron HFBs based on electrolyte pH. In alkaline zinc–iron HFBs (Fig. 22a), the $Zn(OH)_4{}^{2-}/Zn$ and $Fe(CN)_6{}^{3-}/Fe(CN)_6{}^{4-}$ redox couples exhibit standard electrode potentials of −1.22 V and +0.53 V (*vs.* SHE), respectively, contributing to a high operating voltage. Furthermore, when paired with porous membranes and porous electrodes, alkaline zinc–iron HFBs achieve stable long-term cycling at high current densities.[201–203] However, alkaline zinc–iron HFBs also encounter challenges such as relatively low solubility of the catholyte, zinc dendrite formation and corrosion, as well as the non-negligible issue of water migration.[204,205] These problems hinder their application in long-duration, high-energy-density energy storage scenarios. Research on alkaline zinc–iron HFBs can be traced back to around 1980, with rapid advancements occurring after 2020. The rapid development of alkaline zinc–iron HFBs can be largely attributed to the designs of advanced membrane materials. The designed membrane should fulfill the requirement for high OH^- ion conductivity, thereby achieving high voltage efficiency. Simultaneously, it must have high selectivity towards $Fe(CN)_6{}^{3-/4-}$ to attain high coulombic efficiency and long lifespan. Additionally, the membrane also should effectively mitigate water migration and promote uniform zinc deposition. Li Xianfeng's team and Xu Zhi's team have made significant contributions to the evolution of membranes for alkaline zinc-iron HFBs. As shown in the left of Fig. 22b, Li's research group has pioneered the development of a novel polymer membrane

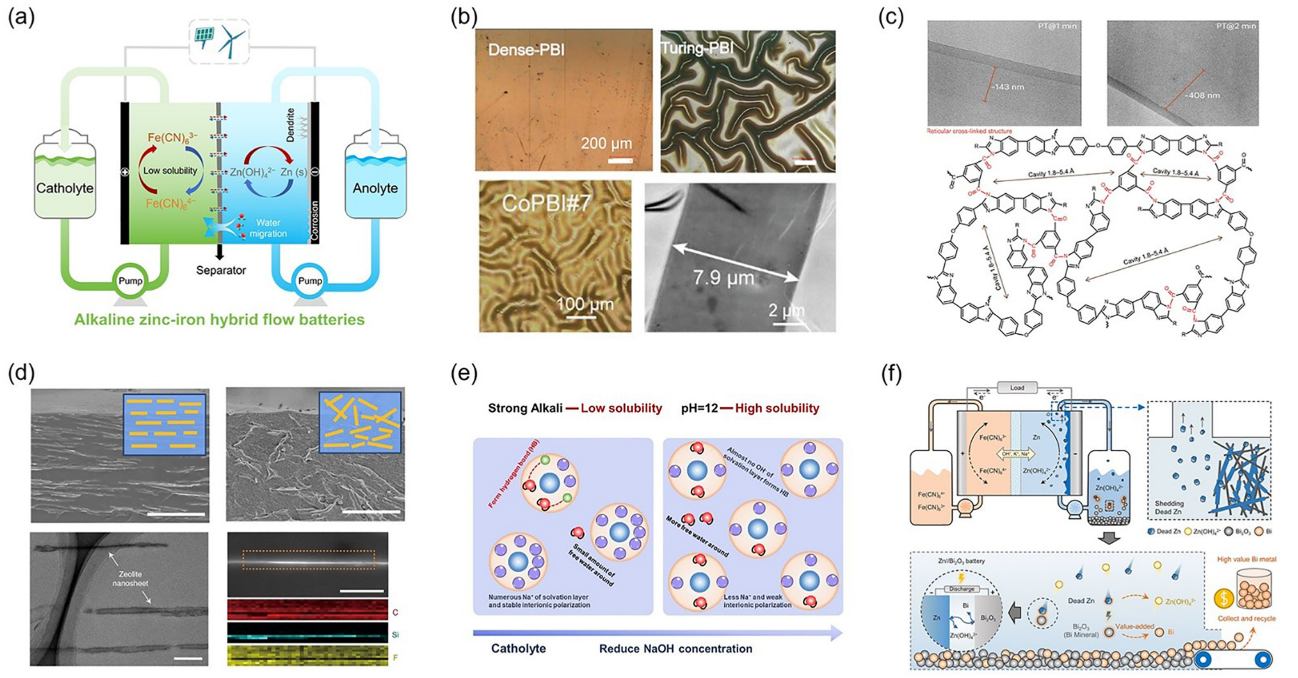

Fig. 22 (a) Schematic diagram of the typical structure configurations and major challenges of alkaline zinc–iron HFBs. (b) Surface morphology of dense/Turing/Co^{2+}-coordinated thin Turing-PBI membranes. Reproduced from ref. 206 with permission from American Chemical Society, copyright 2021. Reproduced from ref. 207 with permission from Wiley-VCH, copyright 2023. (c) Cross-sectional TEM images and polymer pore structure of the ultrathin membranes prepared through interfacial polymer cross-linking. Reproduced from ref. 208 with permission from Springer Nature, copyright 2025. (d) Morphology of aligned/misaligned composite membranes. Reproduced from ref. 209 with permission from Springer Nature, copyright 2022. (e) A schematic illustration of the enhancement of ferrocyanide ion solubility through the reduction of polarization between cations and anions, as well as the mitigation of hydrogen bonding interactions with water molecules. Reproduced from ref. 217 with permission from Wiley-VCH, copyright 2024. (f) A schematic diagram of "dead zinc" within zinc–iron flow batteries and strategies for its regeneration. Reproduced from ref. 219 with permission from The Royal Society of Chemistry, copyright 2024.

featuring ordered undulating stripes, designated as "Turing-PBI".[206] This membrane forms distinctive "Turing patterns" through the coordination interaction between copper ions (Cu^{2+}) and the pyridine nitrogen atoms within the polybenzimidazole (PBI) chains. This design has been demonstrated to facilitate uniform zinc deposition, thereby preventing dendrite formation and enhancing both battery capacity and stability. This strategy was later applied to an ultra-thin (7.9 μm) CoPBI membrane, featuring surface-periodic Turing structures *via* Co^{2+}-PBI coordination.[207] In 2025, Li's team fabricated ultra-thin yet robust polymer membranes *via* an interfacial polymer cross-linking strategy, which can be applied to various flow battery systems (Fig. 22c). These ultra-thin membranes have a thickness of only 3 μm and contain a nano-scale separation layer with a quasi-ordered network cross-linked structure, enabling high ion selectivity, ultra-low resistance, and rapid ion transport.[208] Xu's team exhibited a pronounced preference for *in situ* integrating rigid materials with well-defined pore channels (such as zeolite nanosheets and sulfonated hollow carbon spheres) into porous polymer membranes, thereby crafting composite membranes with superior performance characterized by a highly ordered pore structure (as displayed in Fig. 22d).[209–214] On one hand, the sub-nanometer-scale pores confer additional ion sieving capabilities to the membrane, significantly enhancing the efficiency of carrier ion transport. On the other hand, the formation of a sturdy array structure within the membrane offers multifaceted protection, effectively impeding the penetration of zinc dendrites. To address the challenges of low solubility and poor stability of the cathode $Fe(CN)_6^{3-/4-}$ couple in alkaline zinc–iron HFBs, several cathodic electrolyte modification strategies have been employed. For instance, immobilizing a $Ni(OH)_2$/NiOOH composite on the cathode or storing Prussian Blue in the cathodic reservoir could leverage redox-targeting reactions to indirectly elevate the concentration of the cathodic active species.[215,216] Furthermore, as depicted in Fig. 22e, reducing the alkali concentration and modulating the interaction between the $Fe(CN)_6^{3-/4-}$ ion and the solvent through chelating agents effectively enhanced salt dissociation, thereby increasing the solubility of $Fe(CN)_6^{3-/4-}$ to 1.7 mol L^{-1} (pH = 12). This approach not only suppressed zinc dendrite formation but also ensured stable operation across a broader temperature range (0–60 °C).[217] On the anodic side, the formation of "dead zinc" and dendrites (as depicted in Fig. 22f), particularly under conditions of high areal capacity and elevated current density, often compels alkaline zinc–iron HFBs to operate at a low anolyte utilization rate. The redox-targeting reaction strategy can also be extended to the anodic electrolyte, for instance, by introducing 7,8-dihydroxyphenazine-2-sulfonic acid (DHPS) or Bi_2O_3 as a redox mediator to mitigate the "dead zinc" issue.[218,219] This approach markedly enhanced the cyclic stability and capacity retention of alkaline zinc–iron HFBs under conditions of high zinc loading and deep cycling. Moreover, through comprehensive modulation of the anodic electrolyte solvation structure, the anode–electrolyte interface, and the anode architecture, it has been demonstrated that this approach facilitates the regulation of zinc nucleation behavior, enables rapid three-dimensional transport of zinc ions from the solution to the anode interface, and induces uniform, reversible zinc deposition on the anode.[220–222] Electrolyte concentration gradients, ionic strength disparities, and electric fields are key factors affecting water migration, and electrolyte additives can help mitigate this. Li's team found that inorganic additives like sodium sulfate (Na_2SO_4) do not significantly impair battery performance while suppressing water migration, whereas organic additives, though also effective in curbing water migration, increase electrode polarization and reduce battery performance.[223]

In acidic and neutral zinc–iron HFBs, the Zn^{2+}/Zn and Fe^{3+}/Fe^{2+} redox couples exhibit standard electrode potentials of −0.76 V and +0.77 V (*vs.* SHE), respectively. Therefore, compared to alkaline zinc–iron HFBs, both acidic and neutral zinc–iron HFBs exhibit lower cell voltages. In acidic zinc–iron HFBs (Fig. 23a), the higher solubility of Fe^{3+}/Fe^{2+} and enhanced

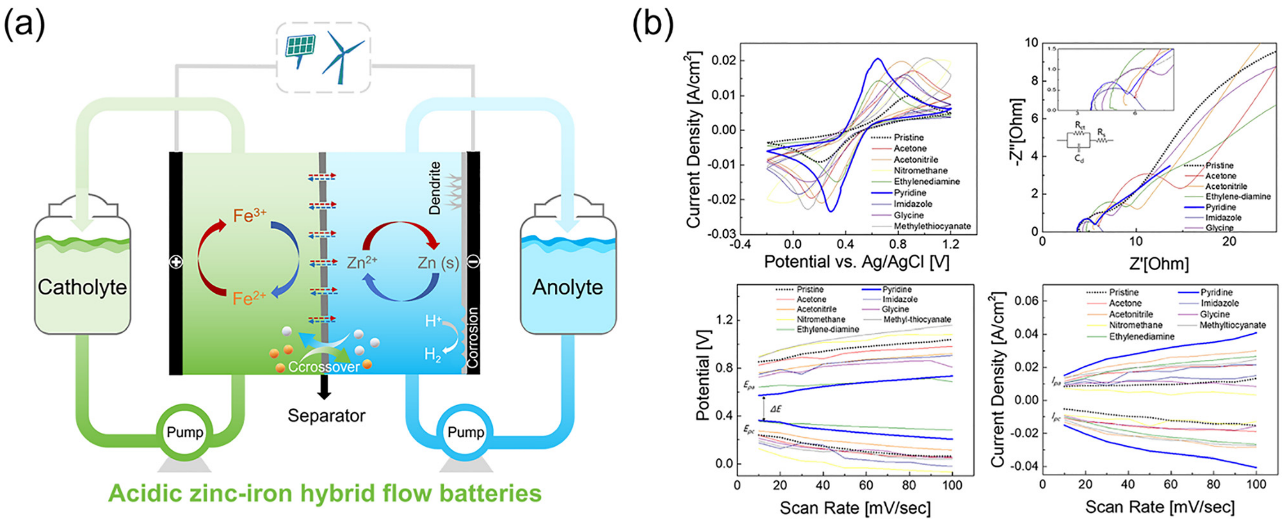

Fig. 23 (a) Schematic diagram of the typical structure configurations and major challenges of acidic zinc–iron HFBs. (b) Different electrochemical performance comparison of Fe^{3+}/Fe^{2+} complexing ligands. Reproduced from ref. 226 with permission from Elsevier, copyright 2020.

ionic conductivity contribute to improved energy density and efficiency. However, the acidic environment exacerbates HER and the formation of zinc dendrites, resulting in a relatively short battery life.[224] For acidic zinc–iron HFBs, different supporting electrolytes exert a profound influence on the reaction kinetics of the iron cathode and zinc anode. It has been found that a mixed solution of 1-butyl-3-methylimidazolium chloride (BMImCl) and NH_4Cl can effectively enhance the redox activity of the Fe^{3+}/Fe^{2+} couple, whereas a blended solution of $CaCl_2$ and NH_4Cl significantly promotes the zinc deposition/dissolution reaction.[225] The introduction of organic ligands (such as pyridine) to coordinate with Fe^{2+} ions can significantly enhance the stability and reversibility of the cathodic electrolyte (Fig. 23b). Through this coordination, the hydrolysis of Fe^{3+} ions was effectively suppressed, thereby reducing the formation of byproduct ferrihydrite precipitates.[226] In addition to the coordination strategy, another effective approach involves the utilization of buffer solutions (such as acetic acid/sodium acetate) to maintain the electrolyte pH within the range of 2.0–6.0, effectively suppressing the HER side reaction and enhancing the stability and coulombic efficiency of conventional acidic zinc–iron HFBs.[227]

Neutral zinc–iron HFBs (Fig. 24a) exhibit minimal corrosivity, high operational safety, and low maintenance costs. This inherent compatibility with cost-effective electrode and membrane materials reduces system expenses. However, in neutral zinc–iron HFBs, iron ions are prone to hydrolysis, which severely impacts the battery's operational lifespan.[228] Moreover, the inherently lower solubility and electrochemical activity of Fe^{3+}/Fe^{2+} in neutral electrolytes constrain both energy density and power density, limiting their suitability for high-performance applications. Neutral zinc–iron HFBs hold great promise for large-scale energy storage due to their mild operating conditions and low

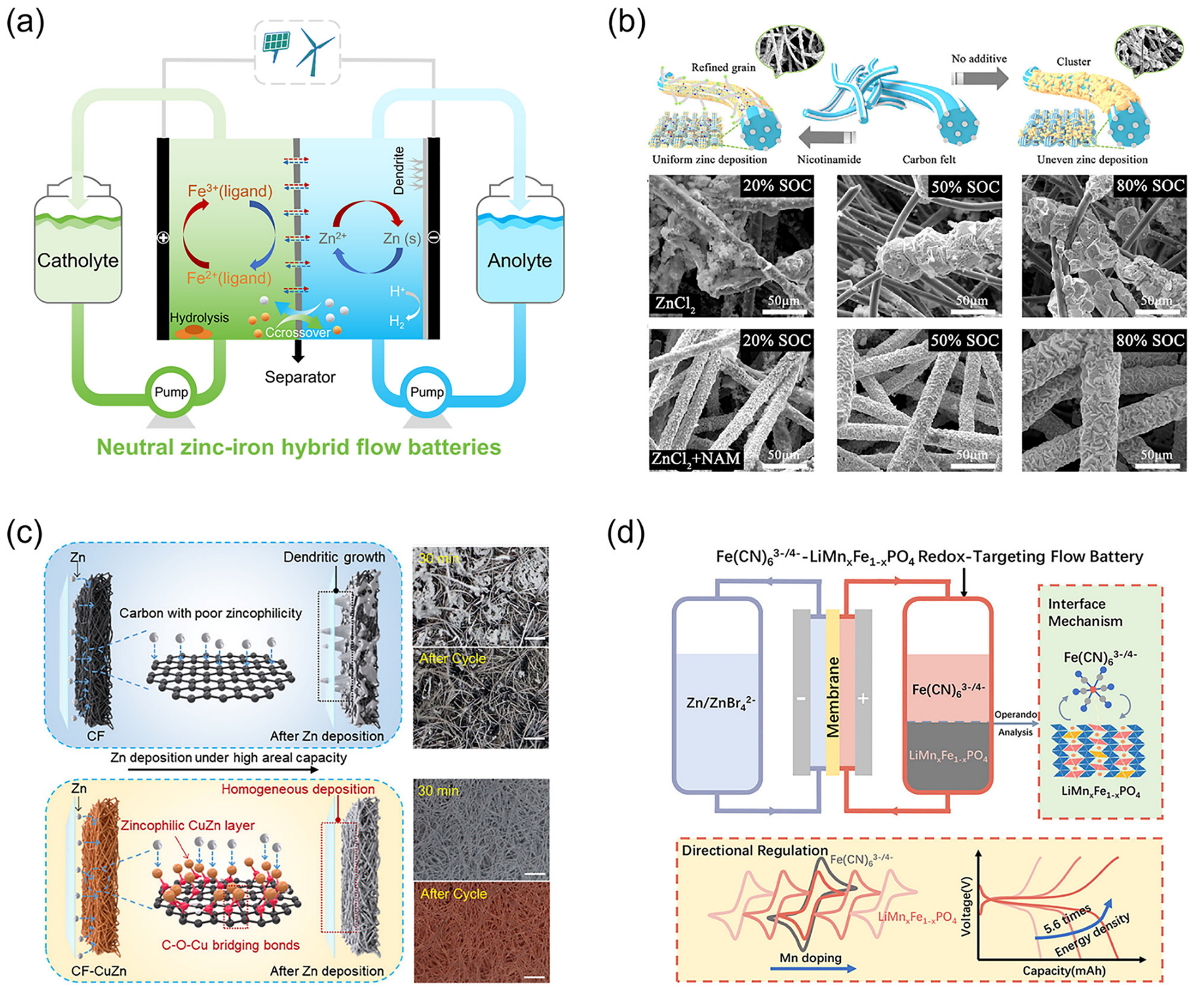

Fig. 24 (a) Schematic diagram of the typical structure configurations and major challenges of neutral zinc–iron HFBs. (b) Schematic diagram and morphologies of the Zn deposition in both $ZnCl_2$ and $ZnCl_2$-nicotinamide electrolytes in neutral zinc–iron HFBs. Reproduced from ref. 232 with permission from American Chemical Society, copyright 2022. (c) Zn deposition mechanism and morphologies of carbon felt electrode and carbon felt-CuZn electrode. Reproduced from ref. 234 with permission from Wiley-VCH, copyright 2025. (d) Schematic diagram of $Fe(CN)_6{}^{3-/4-}$-$LiMn_xFe_{1-x}PO_4$ redox-targeting zinc–iron flow batteries. Reproduced from ref. 235 with permission from Elsevier, copyright 2025.

cost. However, the issues of hydrolysis and shuttle effect of iron ions are more pronounced in these systems. Consequently, it is imperative to employ coordination chemistry strategies to optimize the cathodic electrolyte. Researchers have discovered that the introduction of either a single complexing agent (such as glycine) or a mixed-ligand complexing agent (for instance, multifunctional asymmetric bi-ligand iron chelating agents composed of pyridine and 4,5-dihydroxy-1,3-benzenedisulfonate) can effectively suppress the hydrolysis and shuttle phenomena of iron ions, thereby enhancing the cycle stability and efficiency of the battery.[229,230] For anodic side, through the interaction between coordinating ions (*e.g.*, Br^-) or molecules (*e.g.*, nicotinamide, glycine) and zinc ions, water molecules within the solvation shell of zinc ions are partially substituted. This process reconstitutes the solvation structure of zinc ions, thereby enhancing the kinetics of the zinc electroplating/stripping reaction (Fig. 24b). Concurrently, it suppresses the HER side reaction, mitigates the undesirable tip effect, and ultimately facilitates uniform, dendrite-free zinc deposition.[231–233] In addition to electrolyte additives, anode modification can also be used to enhance zinc adsorption, ensuring the uniformity of zinc deposition (Fig. 24c).[234] To address the issue of the relatively low solubility of $Fe(CN)_6^{3-/4-}$ in the catholyte, Ji *et al.* achieved directional regulation of the unimolecular redox-targeting reaction in neutral zinc–iron HFBs by precisely controlling the composition of the solid material ($LiMn_xFe_{1-x}PO_4$) and modulating its redox potential to match that of the redox mediator ($Fe(CN)_6^{3-/4-}$). This approach significantly enhanced the energy density of the battery (Fig. 24d).[235]

4.1.7. Zinc-organic HFBs. Zinc-organic HFBs represent a class of zinc-based HFBs that employ organic small molecules or polymers as the active materials for the catholyte (as depicted in Fig. 25a). Their core feature lies in the synergistic integration of the molecular designability of organic active materials with the high theoretical capacity, low cost, and environmental benignity of zinc anodes. This fusion endows them with three notable advantages: firstly, the redox potentials and solubilities of organic active materials can be precisely tuned through structural modifications, thereby transcending the resource dependency associated with traditional inorganic materials. Secondly, the abundance of both organic active materials and metallic zinc confers a distinct cost advantage. Thirdly, the non-toxicity and inherent safety of both organic active materials and metallic zinc align seamlessly with the principles of green and sustainable development.[236–239] However, this technology still grapples with critical challenges: organic active materials exhibit inadequate stability and are prone to decomposition or cross-contamination; issues such as dendrite growth, hydrogen evolution corrosion, and passivation at the zinc anode contribute to a decline in cycle life. Moreover, the relatively low solubility of organic active materials and the suboptimal ionic conductivity of the electrolyte constrain the energy density and power density. Currently, research efforts on zinc-organic HFBs are relatively limited, with a primary focus on the design of organic molecules. In the early stages of zinc-organic HFBs, the cathodic organic active materials predominantly comprised polymers existing in the form of slurries or micelles, such as polyaniline and poly(TEMPO).[240,241] Zinc-polymer HFBs can employ size-exclusion membranes fabricated from regenerated cellulose, which offer enhanced stability and reduced cost compared to the expensive Nafion membranes. However, the low solubility of these polymers, coupled with sluggish kinetics, results in batteries with notably low energy density, low current density, and energy efficiency. To improve these properties, the polymers were replaced by organic small molecules. Among them, TEMPO and its derivatives have garnered extensive research attention owing to their relatively high redox potentials, tunability, non-toxicity, and low cost. However, they still face serious side reactions involving ring-opening, particularly at high concentrations. The study reveals that by modulating the electronic and steric effects of the 4-position substituent, TEMPO derivatives with high redox potentials and prolonged cycle life can be designed (Fig. 25b).[242,243] For example, Song's team simultaneously introduced a "π–π"-conjugated imidazolium and a "p–π"-conjugated acetylamino at the 4-position of TEMPO, named MIAcNH-TEMPO. The presence of these dual-conjugated substituents significantly delocalized the electron density of the N–O head, thereby stabilizing both the radical and oxoammonium forms of TEMPO. As depicted in Fig. 25c, the larger molecular size and the strong electrostatic repulsion exerted by these dual-conjugated substituents effectively inhibited the cross-contamination of TEMPO derivatives through the membrane, leading to a further reduction in capacity loss.[244] In addition to TEMPO and its derivatives, a number of other promising organic small molecules have been developed. Liu and colleagues devised a bipolar zinc-ferrocene salt compound ($Zn[Fc(SPr)_2]$) that could be employed as both the cathodic and anodic active material. This ferrocene derivative exhibited a remarkably high solubility of 1.8 M and demonstrated excellent electrochemical performance.[245] Wang's team synthesized a phenazine radical cation, sodium 3,3′-(phenazine-5,10-diyl)bis-(propane-1-sulfonate) (PSPR), based on dihydrophenazine and employed it as the cathodic active material for neutral zinc-organic HFBs.[246] Within PSPR, the incorporation of two sulfonic acid groups as intramolecular counter ions not only boosted its water solubility but also effectively curbed radical dimerization through intramolecular coulombic repulsion and steric hindrance, thereby safeguarding its stability (as shown in Fig. 25d). Furthermore, by employing molecular engineering strategies, it is feasible to transform irreversible or unstable triphenylamine into a reversible two-electron transfer system (as shown in Fig. 25e), namely 4,4′,4″-trihydroxytriphenylamine.[247] 1,4-hydroquinone or 4,4′-biphenol functionalized with four (dimethylamino)methyl groups exhibited high redox potentials in acidic zinc-based HFBs.[248,249] However, to enable the coexistence of acidic and alkaline electrolytes and prevent cross-contamination of H^+ or OH^-, additional design of the battery system is required. In addition, due to the unique physical and chemical properties of the positive organic active materials and the negative inorganic (zinc) active materials, they are very suitable for the design of membrane-free flow batteries. Recently, Marcilla *et al.* used a "water-in-salt" electrolyte strategy, where two immiscible liquid

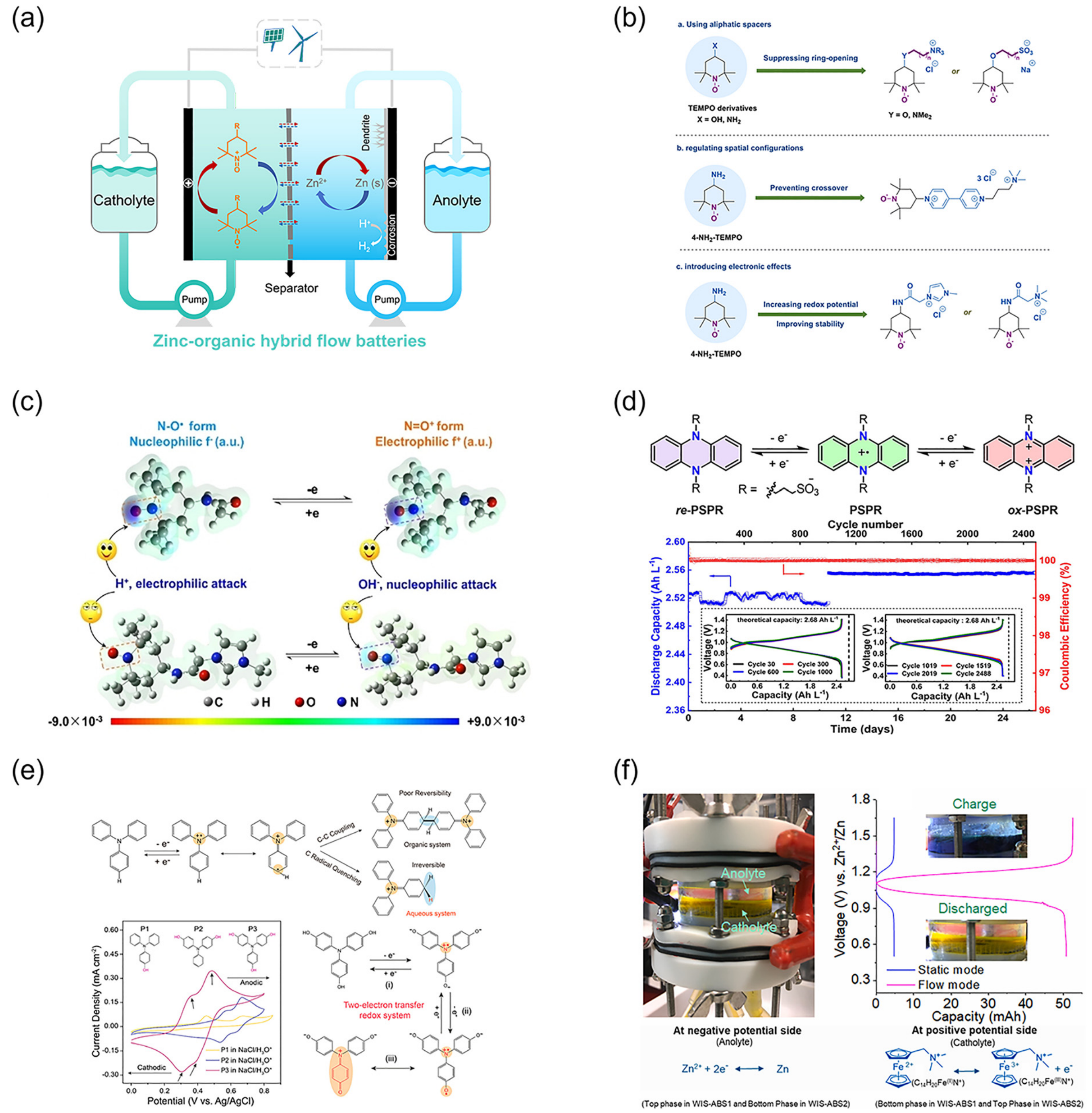

Fig. 25 (a) Schematic diagram of the typical structure configurations and major challenges of zinc-organic HFBs, taking the TEMPO cathode as an example. (b) Advanced strategies for modification of TEMPO. Reproduced from ref. 243 with permission from The Royal Society of Chemistry, copyright 2023. (c) The design strategy for more stable TEMPO derivatives, exemplified by the MIAcNH-TEMPO featuring dual conjugated substituents. Reproduced from ref. 244 with permission from Wiley-VCH, copyright 2022. (d) Redox reactions and cycling performance of PSPR. Reproduced from ref. 246 with permission from American Chemical Society, copyright 2023. (e) The redox instability mechanism for traditional triphenylamine (TPA) and the optimized redox pathways for P3 molecule. Reproduced from ref. 247 with permission from American Chemical Society, copyright 2021. (f) Digital pictures and charge–discharge curves of the static/flow membrane-free FcNCl-Zn HFBs with a "water-in-salt" electrolyte strategy. Reproduced from ref. 250 with permission from Elsevier, copyright 2024.

phases spontaneously form by mixing specific concentrations of $ZnCl_2$ and LiTFSI in aqueous solution. As depicted in Fig. 25f, one liquid phase served as the anodic electrolyte (enriched with Zn^{2+} ions), while the other acted as the cathodic electrolyte (dissolved with ferrocene derivatives, FcNCl, as the active material). This immiscible biphasic system obviated the need for ion-exchange membranes, thereby further reducing costs.[250]

4.1.8. Zinc–air HFBs. Zinc–air HFBs, as flow-type electrochemical reactors, combine the characteristics of inherent safety, high specific energy, environmental benignity and low cost. The non-flammable and environmentally benign aqueous electrolytes and electrodes endow zinc–air HFBs with inherent safety and environmental friendliness. The utilization of low-cost aqueous electrolytes, zinc anodes, and air as the core components of zinc–air HFBs confers a significant cost advantage.[251–253] Moreover, zinc–air HFBs exhibit a remarkable theoretical specific energy of up to 1086 Wh kg^{-1}, which surpasses that of most conventional flow batteries.[254] Although static zinc–air batteries also possess the aforementioned advantages, their performance is typically severely constrained by the sluggish kinetics and transport phenomena of gaseous reactants. In contrast, the adoption of a flowing electrolyte system in zinc–air HFBs effectively mitigates these adverse effects. As depicted in Fig. 26a, the battery structure of zinc–air HFBs comprises an air cathode, a membrane, and a zinc metal anode. The air cathode typically consists of a porous gas diffusion layer and supported electrocatalysts. The pores within the porous gas diffusion layer provide a continuous solid/liquid/gas three-phase interface, serving as the sites where the oxygen reduction reaction (ORR) and oxygen evolution reaction (OER) occur. The supported electrocatalysts

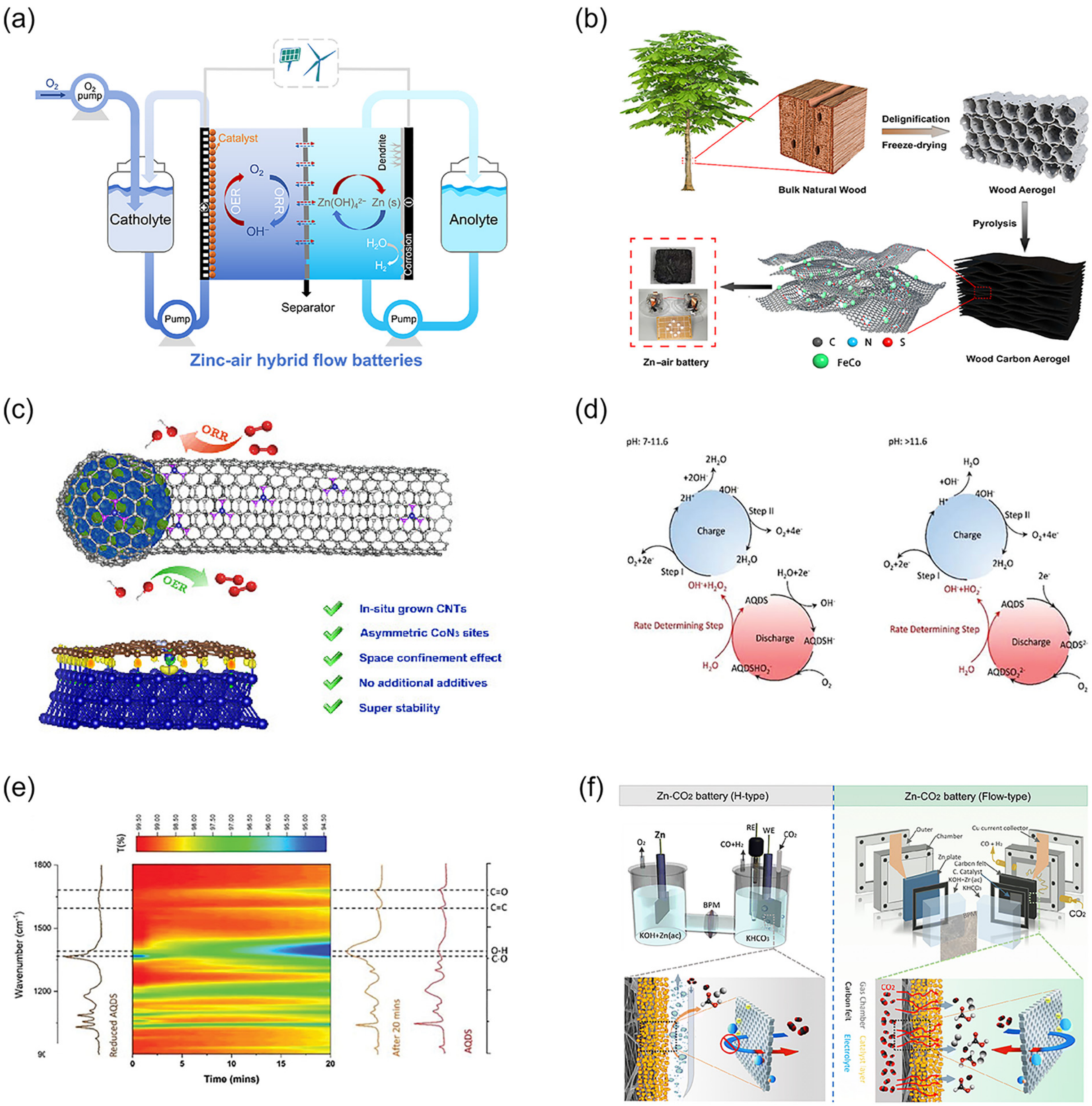

Fig. 26 (a) Schematic diagram of the typical structure configurations and major challenges of zinc–air HFBs. (b) Schematic illustration depicting the preparation of carbon aerogels with a hierarchical porous structure, co-doped with FeCo alloy and N, S heteroatoms, utilizing natural balsa wood as the precursor. Reproduced from ref. 255 with permission from American Chemical Society, copyright 2021. (c) Schematic representation of single-atom catalysts encapsulated within carbon nanotubes with spatial confinement effect. Reproduced from ref. 256 with permission from American Chemical Society, copyright 2024. (d) Mechanism of the AQDS-mediated Zn–air flow cells. Reproduced from ref. 260 with permission from Wiley-VCH, copyright 2022. (e) *In situ* FTIR spectroscopic study of the AQDS-mediated ORR. Reproduced from ref. 260 with permission from Wiley-VCH, copyright 2022. (f) Schematic illustration of the configurations and principles of H-type and flow-type zinc–CO_2 flow batteries, with the latter demonstrating enhanced CO_2 reduction reactions. Reproduced from ref. 273 with permission from The Royal Society of Chemistry, copyright 2024.

are employed to enhance the kinetics of both ORR and OER. The electrolyte is stored in an external tank and continuously circulated through a pump during operation to accelerate ion transport and mitigate concentration polarization. Moreover, the flow disturbance disrupts the formation of oxygen bubbles or carbonate precipitates (for alkaline system), thereby preventing electrode and pipeline blockages. The general operating principle and reaction mechanism of rechargeable zinc–air HFBs are highly dependent on the pH of the electrolyte. Taking the most common alkaline system as an example, during the discharge process, oxygen from the air diffuses through the gas diffusion layer and undergoes the ORR at the gas/liquid/solid three-phase boundary of the air cathode, generating OH^- ions in the solution. Simultaneously, on the anodic side, zinc metal is oxidized to Zn^{2+} ions, which further combine with OH^- ions to form $[Zn(OH)_4]^{2-}$ ions. During the charging process, the OER occurs at the cathode, while $[Zn(OH)_4]^{2-}$ ions are reduced to zinc metal and deposited at the anode. The primary challenges in zinc–air HFBs stem from the cathodic and anodic sides. At the cathode, the electrocatalysts must possess dual catalytic activities for both the ORR and OER, along with physical and chemical robustness to prevent detachment and deactivation during prolonged operation. Additionally, the formation of oxygen bubbles and carbonate by-products may block active sites and impede gas and liquid transport. On the anode, major side reactions such as hydrogen evolution, self-corrosion of the zinc metal, and the formation of a ZnO surface passivation layer significantly shorten the battery's lifespan. Addressing these issues necessitates both material innovation and system optimization. Material innovation encompasses the development of core components such as electrodes, electrocatalysts, electrolytes, and membranes, while system optimization involves fine-tuning critical parameters like battery architecture, electrolyte flow rate/velocity, and current density.

The air cathode of zinc–air HFBs features a bilayer structure, comprising a gas diffusion layer and a catalyst-loaded layer. Consequently, the two primary avenues for material innovation in air cathode design are as follows: (1) engineering air cathode architectures with sufficiently exposed active sites and tunable mass transport behaviors to fully harness the intrinsic activity of electrocatalysts; (2) developing bifunctional active sites with high intrinsic activity and robustness, enabling efficient catalytic performance for both the ORR and OER. As shown in Fig. 26b, Kong's team successfully fabricated carbon aerogels with a hierarchical porous structure using natural balsa wood through a facile process. This unique structure not only offered abundant active sites, enhancing the specific surface area and porosity of the material, but also facilitated the rapid transport of electrolyte ions and electrons. Furthermore, the simultaneous incorporation of FeCo alloy and N, S heteroatom doping into the carbon aerogels synergistically optimized the electronic structure and surface properties of the material, thereby improving the catalytic activity for both the ORR and OER.[255] Researchers also encapsulated single atoms or heterojunctions within carbon nanotubes (as shown in Fig. 26c), leveraging the spatial confinement effect to achieve more efficient catalysis. Meanwhile, enhancing the graphitization degree of the carbon nanotubes contributes to improving the overall stability and durability of the catalysts.[256,257] In addition, covalent organic polymers (COPs) and metal–organic frameworks (MOFs) can also offer porous scaffolds and abundant catalytic sites.[258,259] Furthermore, by optimizing the electrolyte pH and selecting appropriate redox mediators (such as anthraquinone-2,7-disulfonic acid disodium salt, AQDS), the ORR can be promoted through chemical redox reactions (Fig. 26d). This approach enables the achievement of ultrafast kinetics in the AQDS-mediated ORR process. Furthermore, they investigated the intrinsic mechanism of AQDS-mediated ORR in depth *via operando* UV-vis spectroscopy and *in situ* FTIR spectroscopy (as shown in Fig. 26e).[260]

In the realm of zinc anodes, the primary focus lies on electrode engineering and electrolyte optimization. The adoption of zinc anodes with a high specific surface area featuring a three-dimensional structure is advantageous in breaking the mass transport limitations, reducing the diffusion-limited current density, and facilitating uniform electrodeposition. Chen *et al.* introduced a bilayer porous zinc electrode architecture in zinc–air flow batteries. By comparing the impacts of different porosity distributions, namely step-increasing porosity, step-decreasing porosity, and constant porosity, on the discharge performance of the batteries, they unveiled the pivotal role of porosity distribution in determining battery performance. Among these, the zinc anode with a step-increasing porosity exhibited the most superior performance in terms of discharge duration and zinc utilization efficiency.[261] The electrolyte optimization strategies primarily involve introducing specific functional additives into the anolyte to mitigate the formation of zinc dendrites and surface passivation.[262–264] Some researchers have integrated the zinc anode with the anolyte to form a zinc slurry, aiming to enhance the utilization of zinc. By optimizing the formulation of zinc slurries, they aim to enhance the performance of zinc–air HFBs.[265,266] However, given the sensitivity of the air cathode to the electrolyte composition—for instance, electrolyte additives such as metal ions or organic molecules may adversely affect the activity and lifespan of the catalyst—employing membrane engineering to regulate the zinc anode might be a more preferable option.[267] On one hand, through innovative membrane design, it's possible to achieve excellent ion conductivity of OH^- ions while minimizing the permeability of $[Zn(OH)_4]^{2-}$ ions, preventing clogging of the air electrode. On the other hand, we can draw inspiration from the membrane preparation techniques used in alkaline zinc–iron HFBs to induce uniform deposition on the zinc anode. This membrane engineering approach not only elevates the overall performance and stability of zinc–air HFBs but also significantly prolongs their operational lifespan by effectively resolving critical challenges associated with ion transport dynamics and electrode deposition patterns.

The operational parameters (such as electrolyte flow, current density, *etc.*) significantly influence the performance of zinc–air HFBs.[268] Kheawhom *et al.* employed *in situ* synchrotron radiation X-ray tomography (SRXTM) technology to achieve high-resolution three-dimensional imaging of the zinc deposition process. This enabled them to systematically investigate the impact of the interaction between current density and electrolyte flow on the zinc deposition morphology and the cycling performance of zinc–air HFBs. Their research revealed that, under moderate current density (50 mA cm^{-2}) combined with a flowing electrolyte, the anode exhibited smoother dendrite tips, and thinner and more uniform deposition layers. Consequently, the battery demonstrated optimal cycling performance and stability.[269] Kheawhom *et al.* systematically studied the interaction between electrolyte flow rate and current density on zinc electrodeposition morphology and battery performance *via* real-time monitoring of surface evolution, bubble formation, and electrochemical properties. They found that increasing the flow rate improved zinc deposition uniformity and suppressed dendrite growth, especially at high current densities. Optimizing the current density-flow rate match could further regulate the thickness and compactness of the deposition layer, enhancing overall battery performance.[270]

Zinc–air flow batteries can be further extended to zinc–gas flow batteries. Among these, carbon dioxide (CO_2), as an important component of the air and a primary target for emission reduction under low-carbon policies, has garnered significant attention. Zinc–CO_2 batteries offer an economical and efficient approach for CO_2 utilization, integrating emission reduction with electricity generation.[271] Hu *et al.* developed a zinc–CO_2 flow battery using carbon nanotube hollow fibers (cathode), a zinc wire (anode), and 1-ethyl-3-methylimidazolium tetrafluoroborate (electrolyte). It continuously converted CO_2 to CH_4 under ambient conditions with a faradaic efficiency of 94%.[272] Furthermore, as shown in Fig. 26f, Duan *et al.* presented a zinc–carbon dioxide (Zn–CO_2) flow battery that addresses the issues of low CO_2 solubility and poor diffusion efficiency in conventional H-type batteries. Additionally, they developed a high-performance bifunctional electrocatalyst based on Pd/SnO_2@C. This catalyst exhibited remarkably high formate selectivity and faradaic efficiency (up to 95.86%) in the CO_2 reduction reaction. Moreover, it effectively oxidizes formate during the charging process, enhancing the battery's reversibility.[273]

4.2. Iron (Fe)-based hybrid flow batteries

Aqueous iron-based flow batteries have garnered extensive attention in the field of energy storage in recent years, owing to the natural abundance, high safety, environmental friendliness, and low redox potential of the iron anode.[274,275] All-iron flow batteries, which employ a flow battery system utilizing the same redox-active element in different valence states, can to some extent mitigate the capacity fading issue arising from electrolyte cross-contamination. Compared to all-vanadium flow batteries, all-iron flow batteries exhibit lower chemical toxicity and more affordable material costs, thus holding immense potential. Based on the presence or absence of iron deposition and dissolution at the anodic side, all-iron flow batteries can be categorized into two types: fully soluble flow batteries and HFBs.[35] All-iron fully soluble flow batteries still face the risk of electrolyte cross-contamination due to the use of distinct ligands in the cathodic and anodic electrolytes. Free ligands in the anolyte may permeate through the ion-exchange membrane, indirectly reducing the cathodic active species, leading to charge imbalance and subsequent capacity fading. As depicted in Fig. 27a, the all-iron HFBs utilize Fe^{3+}/Fe^{2+} and Fe^{2+}/Fe^0 as the redox couples at the cathode and anode, respectively. For instance, an all-iron HFB employing highly soluble $FeCl_2$ as the active material for both the cathode and anode not only circumvents cross-contamination issues but also boasts a high standard cell voltage of 1.2 V.[276] However, the long-term stability of this system remains constrained by the inherently poor anode reversibility associated with the metal iron deposition/dissolution process. Additionally, the reduction potential of the anode Fe^{2+}/Fe^0 couple is lower than the hydrogen evolution potential, which triggers the hydrogen evolution reaction and compromises the cycling stability, particularly under low pH conditions where this side reaction is thermodynamically more favorable. The primary focus of this section is to discuss several strategies for improving the deposition behavior of the iron anode and suppressing the hydrogen evolution side reaction in all-iron HFBs.

Modifying the electrode structure and surface/interface of iron anodes can effectively enhance the reversibility of iron deposition–dissolution, mitigate the formation of iron dendrites, and suppress hydrogen evolution on the surface of iron anodes.[277] By introducing nanoscale pores and abundant carbon defects onto the surface of carbon felt, the kinetics of iron deposition/dissolution can be effectively accelerated, and the nucleation and growth morphology of iron can be improved. This modification enables the iron anode to exhibit higher reversibility and stability during the charge–discharge processes.[278] In addition to modifying the carbon felt structure, catalysts (such as heteroatom-doped carbons, metal oxides, *etc.*) or conductive polymer coatings can be applied onto the carbon felt. As illustrated in Fig. 27b, by coating the carbon paper with poly(pyrrole)/poly(4-styrenesulfonate) (PPy/PSS) or poly(3,4-ethylenedioxythiophene)/poly(4-styrenesulfonate) (PEDOT/PSS), the reaction selectivity was controlled. The PPy/PSS coating layer significantly reduced the HER current and hydrogen quantity, thereby enhancing the coulombic efficiency and cyclic stability of the battery.[279] Compared to polymer coatings, ligand-functionalized layers (LFLs) feature a straightforward fabrication process and exhibit stable adhesion during electrodeposition/stripping procedures. For instance, when 3-mercaptopropionic acid (MPA) was employed as the molecular ligand, a stable and corrosion-resistant LFL (Fe-MPA) was constructed on the iron anode (as depicted in Fig. 27c). On one hand, owing to the strong affinity of thiol-based functional ligands for metals, they can spontaneously and uniformly modify the electrode surface. Even after forced dissociation, these ligands can readily re-anchor to the surface, thereby ensuring the stability and durability of the LFL. On the other hand, as shown in Fig. 27d, the carboxyl group ($-COO^-$) in MPA can capture Fe^{2+} ions, facilitating uniform Fe deposition and effectively suppressing the growth of iron dendrites. The MPA-LFL reduces concentration polarization, accelerates the electrode kinetics, and enhances the reversibility of the Fe deposition/stripping process.[36] Furthermore, an alternative approach can be pursued, such as employing

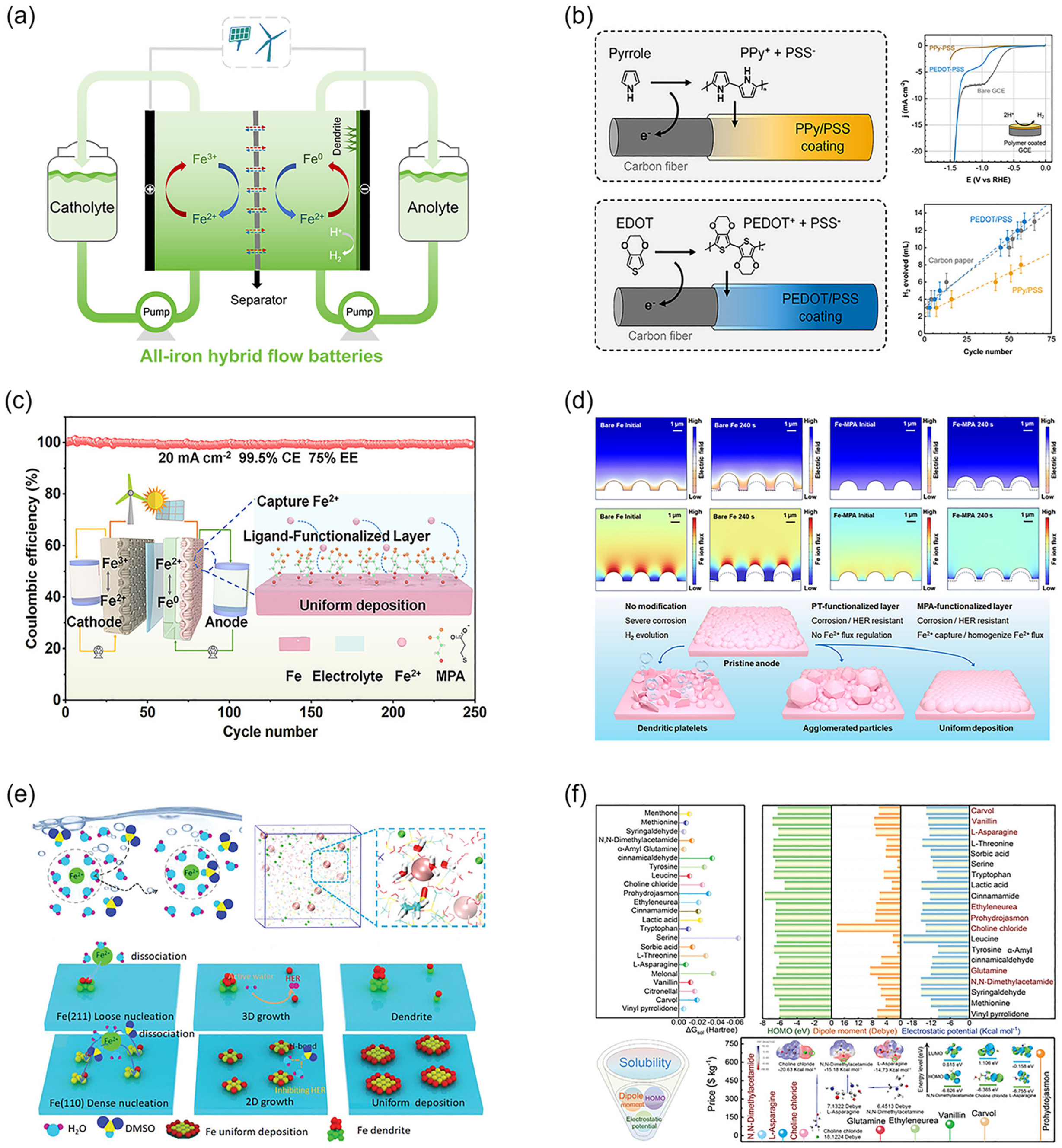

Fig. 27 (a) Schematic diagram of the typical structure configurations and major challenges of all-iron HFBs. (b) Schematic diagram of the conductive polymer-coated electrode for suppressing the hydrogen evolution reaction. Reproduced from ref. 279 with permission from Wiley-VCH, copyright 2025. (c) and (d) Schematic illustration and simulation results of 3-mercaptopropionic acid (MPA)-functionalized layer modulating Fe^{2+} deposition behavior. Reproduced from ref. 36 with permission from American Chemical Society, copyright 2025. (e) Schematic diagram of the regulation strategy for the solvation structure of Fe^{2+} ions, taking additive dimethyl sulfoxide (DMSO) as an example. Reproduced from ref. 287 with permission from Wiley-VCH, copyright 2022. (f) Calculated parameters of various electrolyte additives for low-temperature electrolyte. Reproduced from ref. 288 with permission from Wiley-VCH, copyright 2024.

high-loading solid conversion electrodes (*e.g.*, $Fe_3O_4/Fe(OH)_2$) to replace conventional metal deposition electrodes (*e.g.*, Fe^{2+}/Fe^0). This substitution helps circumvent the dendrite issues that often arise in metal deposition electrodes under high areal capacity and high current density conditions. Lu *et al.* demonstrated that an all-iron HFB based on the $Fe_3O_4/Fe(OH)_2$ conversion electrode could achieve a high areal capacity of 126.6 mAh cm^{-2} at a current density of 50 mA cm^{-2}, and exhibited no capacity fade over 200 cycles (1000 hours).[280] When iron slurries are employed as the anode in an all-iron flow battery, iron metals can be deposited on flowing particles rather than being fixed on the electrode surface. This enables the decoupling of energy storage capacity from power output capability, as well as their flexible regulation.[281] However, this approach also introduces new challenges. For instance, the intricate relationships between the composition of iron slurries and the physical properties (such as electrical conductivity, fluidity, *etc.*) remain to be thoroughly investigated.[282] The incorporation of conductive agents, such as multi-walled carbon nanotubes (MWCNTs) and Ketjen Black, can effectively enhance the electrochemical performance of iron slurries and the kinetics of iron deposition.[283] When combined with optimized operating parameters (*e.g.*, flow velocity and flow rate) and a well-designed battery mold (especially the flow channels), all-iron hybrid redox flow batteries based on iron slurries are expected to achieve superior performance.[284,285]

Early studies have revealed that the composition of the electrolyte (encompassing the types and concentrations of cations, anions, and ligands), as well as the pH value, significantly influence the iron deposition potential and coulombic efficiency. Hence, electrolyte engineering holds critical importance for the performance of all-iron HFBs, with the primary strategies being the additive approach, coordination approach, and the eutectic electrolyte approach. For instance, when $NaHSO_3$ was employed as an additive, it significantly enhanced the iron deposition/stripping reactions by forming the $FeHSO_3^+$ complex, while concurrently mitigating the competitive HER. As a reducing agent, $NaHSO_3$ also aided in maintaining the stability of Fe^{2+} ions within the electrolyte, thereby reducing the degradation of electrolyte performance caused by oxidation.[286] As shown in Fig. 27e, dimethyl sulfoxide (DMSO), owing to its high Gutmann donor number, is capable of effectively displacing water molecules surrounding Fe^{2+} ions, resulting in the formation of a Fe^{2+}-DMSO-H_2O solvation structure. By reducing the direct interaction between Fe^{2+} ions and water molecules, this new structure inhibited the hydrolysis of Fe^{2+} and the HER. The addition of DMSO not only altered the solvation shell of Fe^{2+} ions but also induced preferential deposition of Fe on the (110) crystal plane. The Fe deposit layer featured a fine-grained and dense microstructure, which was conducive to suppressing the growth of iron dendrites and enhancing the reversibility and cyclic stability of the anode.[287] As illustrated in Fig. 27f, *N,N*-dimethylacetamide (DMAc) was screened out as an additive for low-temperature electrolytes through quantum chemical calculations. DMAc has high solubility, strong polarity, and good electron-donating capacity. It can effectively modulate Fe^{2+} solvation structure and hydrogen-bonding networks at low temperatures, acting as a multifunctional additive. Remodeling the solvation structure inhibited HER, enabled uniform Fe deposition/dissolution on electrodes, and boosted Fe^{2+}/Fe^0 redox reversibility. Regulating hydrogen-bonding networks lowered the electrolyte's freezing point and enhanced its low-temperature stability.[288] This computational-screening combined with experimental-validation method offers a general strategy for developing new electrolyte additives. In addition, regulating the coordination structure of Fe^{2+} ions through ligand strategies can also contribute to enhancing the reversibility and lifespan of the iron anode. Citrate ions, as strong ligands, form a highly stable coordination structure (Fe^{2+}-cit) with Fe^{2+} ions *via* their carboxyl groups. This effectively stabilized Fe^{2+} ions, suppressed the HER, and promoted uniform iron deposition.[289] The deep eutectic solvent strategy not only effectively addresses the shortcomings of traditional electrolytes in terms of mass-transport performance and conductivity, but also suppresses the hydrolysis reaction of Fe^{2+} ions by restructuring its solvation shell in the anolyte.[290] In addition to electrode and electrolyte, membrane materials are also particularly important for the performance of iron-based HFBs. The membrane must meet strict requirements for ionic conductivity while restricting the crossover of unwanted reactants (Fe^{3+}).[291] However, research in this area is still relatively limited.

4.3. Cadmium (Cd)-based hybrid flow batteries

Cadmium (Cd) metal is inexpensive and exhibits a significantly negative potential (−0.4 V *vs.* SHE) in sulfuric acid media. Furthermore, cadmium possesses a relatively high hydrogen evolution overpotential. Unlike other soluble metal ions, cadmium ions can undergo efficient electrodeposition and dissolution in acidic media such as sulfuric acid with minimal interference from the hydrogen evolution reaction. During the charging process of the battery, Cd^{2+} ions in the anolyte are deposited onto the anode as Cd metal. Conversely, during the discharging process, the deposited Cd metal redissolves into Cd^{2+} ions.

As early as 2009, a single-flow acid Cd-chloranil battery was proposed. This system integrated the deposition/dissolution reaction of cadmium with the reversible redox reaction of the organic compound chloranil (QCl_4), thereby forming a single-flow battery that did not require an ion-exchange membrane. The battery demonstrated a discharge plateau of 1.1 V. At a current density of 10 mA cm^{-2}, the battery was able to maintain an average coulombic efficiency of 99% and an energy efficiency of 82% after 100 charge–discharge cycles.[292] Namazian *et al.* employed two fluorinated organic compounds, tetrafluoro-*p*-hydroquinone ($TFQH_2$) and 3-fluorocatechol ($3FQH_2$), as cathodic electroactive materials for Cd-based HFBs. It was found that fluorination could elevate the redox potential of the organic compounds, increase the open-circuit voltage of the battery, and thereby enhance the energy efficiency of the battery. Moreover, cadmium nanoparticles were utilized as anodic electroactive materials, which not only improved the electrochemical activity of the anode but also contributed to the overall performance enhancement of the battery. Additionally, a membrane-free battery structure was adopted, which reduced costs and improved the reliability and durability of the battery.[293] In addition to organic cathodes, inorganic substances can also be selected as cathodic active materials for Cd-based HFBs. In 2013, a single-flow acidic Cd–PbO_2 battery was proposed, which was based on the deposition/dissolution reaction of Cd and the redox reaction of lead dioxide (PbO_2). Moreover, the addition of the DPE-3 additive significantly improved the deposition morphology of the Cd anode, suppressed dendrite formation, and reduced the self-discharge phenomenon, thereby enhancing the coulombic efficiency and cycle stability of the battery. Finally, by optimizing the electrolyte composition and battery structure, the authors achieved a high discharge voltage (2.06 V) and energy efficiency

(90.3%) for the Cd–PbO_2 HFBs.[37] Leveraging the reversible redox reactions of Fe^{3+}/Fe^{2+} and Cd^{2+}/Cd^0 in a sulfuric acid electrolyte, the designed Fe–Cd HFB exhibited relatively low material costs. This cost-effective design endows the battery with significant economic potential in the energy storage field, facilitating the commercialization of flow battery technology. Conventional Fe–Cd HFBs suffer from the issue of cross-contamination between the catholyte and anolyte due to ion permeation. Jiang *et al.* adopted a strategy of using a pre-mixed electrolyte to address this problem, thereby reducing the need for electrolyte management and subsequent separation. This approach not only decreased the system's complexity and maintenance costs but also enhanced the overall reliability and lifespan of the battery.[38]

Indeed, the inherent advantages of cadmium once attracted some research attention in the early stage. Cd was selected as the anode primarily for the favorable redox potential matching, the excellent compatibility with the acidic system and the absence of side reactions, which allowed the cathodic performance to be maximized and thus realized the breakthrough of ultrahigh energy density for aqueous batteries. However, its high toxicity and severe environmental pollution risks have greatly hindered the prospect of large-scale applications, leading researchers to gradually abandon this system. Consequently, research on Cd-based HFBs has declined progressively. To date, cadmium is still employed in some small-scale laboratory tests to match certain specialized cathode materials. Recently, Xie *et al.* reported an I^-/Br^- hetero-halogen catholyte enabling reversible six-electron transfer, which was coupled with a Cd^{2+}/Cd^0 anode to construct Cd-based HFBs (as illustrated in Fig. 28a).[39] This battery achieved an ultrahigh energy density of over 1200 Wh L^{-1} (calculated on the basis of catholyte volume). To reduce possible cadmium pollution, reference can be made to green recovery processes for cadmium recovery in spent nickel–cadmium batteries, including pyrometallurgy, hydrometallurgy and hybrid processes: pyrometallurgy separates cadmium at high temperatures, hydrometallurgy leaches and then purifies cadmium, and hybrid processes combine the advantages of both.[294,295]

4.4. Tin (Sn)-based hybrid flow batteries

Metallic tin (Sn) has garnered extensive applications across diverse fields, including construction materials, medical devices, food packaging, and aerospace engineering, owing to its low cost, non-toxicity, and exceptional corrosion resistance. Furthermore, Sn exhibits rapid electrochemical kinetics and a high hydrogen evolution overpotential, which effectively suppresses the hydrogen evolution reaction (HER), rendering it a promising candidate for anode materials. Notably, Sn adopts a body-centered tetragonal crystal structure with relatively small surface energy disparities among its various lattice planes. This characteristic enables the formation of layered tetragonal metallic microcrystals *via* electrodeposition, yielding a uniform and isotropic

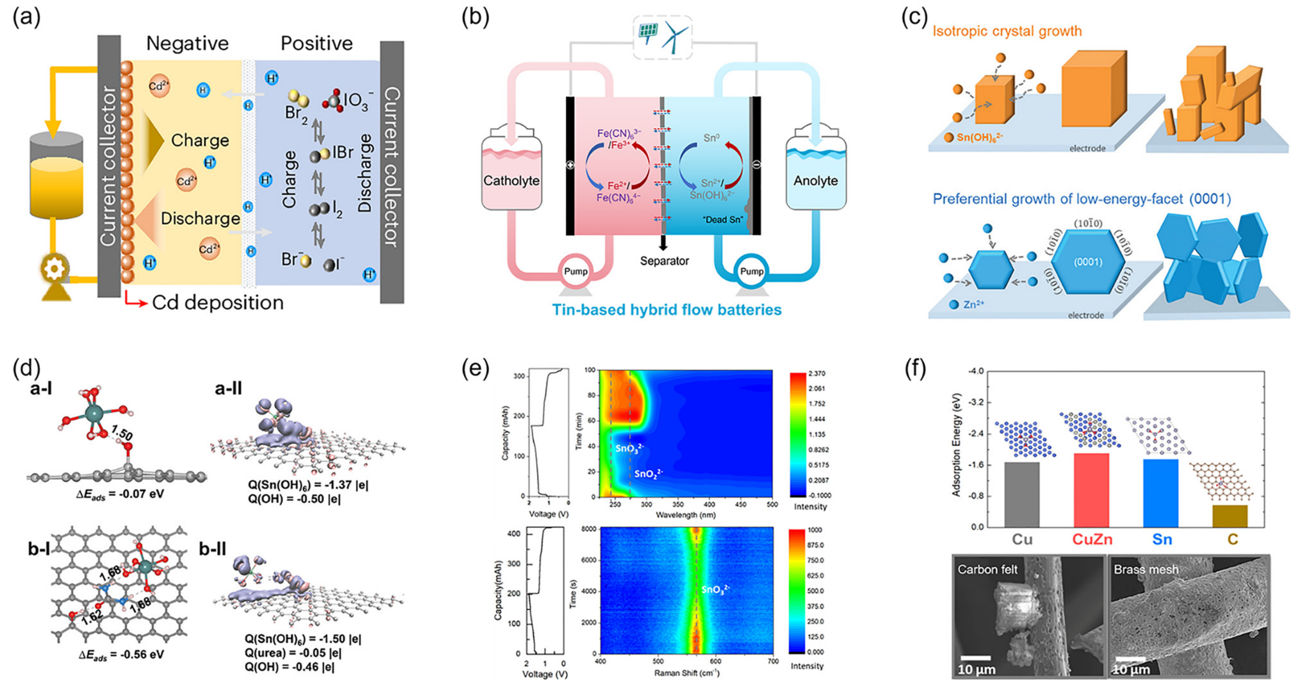

Fig. 28 (a) Schematic of a cadmium-based HFBs with a multielectron transfer cathode. Reproduced from ref. 39 with permission from Springer Nature, copyright 2024. (b) Schematic diagrams of the typical structure configurations and major challenges of tin-based HFBs. (c) Schematic representation of the growth mechanism of Sn cubes and Zn dendrites. Reproduced from ref. 42 with permission from Wiley-VCH, copyright 2021. (d) Adsorption configurations of isolated $Sn(OH)_6{}^{2-}$ and urea-mediated $Sn(OH)_6{}^{2-}$ on current collector surfaces. Reproduced from ref. 302 with permission from Wiley-VCH, copyright 2024. (e) *Operando* UV–vis spectra and Raman spectra of $K_2Sn(OH)_6$ in a Sn–Fe HFB. Reproduced from ref. 43 with permission from American Chemical Society, copyright 2025. (f) Top: Binding energies of $SnO_3{}^{2-}$ on different atom matrixes. Bottom: SEM images of carbon felt and brass mesh after depositing Sn. Reproduced from ref. 43 with permission from American Chemical Society, copyright 2025.

morphology. In MBHFBs, this advantageous growth mechanism of Sn effectively inhibits dendrite formation, thereby enhancing electrochemical performance and ensuring battery safety. Moreover, the relatively low Young's modulus of Sn mitigates the risk of membrane puncture, thereby further extending the cyclic lifespan of the battery. Consequently, Sn-based HFBs are regarded as one of the most promising options due to their dendrite-free operation, low cost, and extended lifespan.

As depicted in Fig. 28b, the Sn anode exhibits distinct redox couple forms under varying pH conditions. Specifically, in acidic and neutral environments, the Sn^{2+}/Sn^0 redox couple demonstrates a relatively high plating/stripping potential of −0.138 V (*vs.* SHE) and involves a two-electron transfer process. In contrast, under alkaline conditions, the $Sn(OH)_6{}^{2-}/Sn^0$ redox couple displays a more negative redox potential (−0.921 V *vs.* SHE) and undergoes a four-electron transfer, thereby enabling higher battery voltage and theoretical energy density. While neutral environments are the most benign, Sn^{2+} ions in neutral media are prone to oxidation and hydrolysis, severely compromising battery operation. Although high-concentration acidic electrolytes can stabilize Sn^{2+} ions chemically, this approach limits the cell voltage and energy density of acidic Sn-based HFBs. Moreover, under acidic conditions, the active species in electrolytes exist as simple cations, whose small ionic sizes exacerbate crossover contamination between anolyte and catholyte, leading to degraded battery performance. In contrast, $Sn(OH)_6{}^{2-}$ ions remain stable under alkaline environments, and their larger ionic size mitigates transmembrane contamination issues. Furthermore, the $Sn(OH)_6{}^{2-}/Sn$ redox couple exhibits a lower redox potential and higher electron transfer count, offering attractive prospects for enhanced cell voltage and energy density. However, alkaline Sn-based HFBs may still encounter challenges associated with "dead Sn" during prolonged cycling. This arises because the binding energy between Sn atoms is higher than that with carbon-based substrates, favoring Sn deposition on existing Sn surfaces rather than uniform distribution across carbon felt electrodes. Consequently, rock-like Sn particles form and grow continuously; once their size exceeds a critical threshold, they detach from the carbon felt surface, obstructing electrolyte flow and causing capacity fade and significant fluctuations in coulombic efficiency. Thus, while Sn-based HFBs are largely free from Sn dendrite issues, the continuous growth and non-uniform deposition of Sn particles still elevate the risk of "dead Sn" formation. Therefore, regulating the homogeneous deposition of Sn at the anode remains imperative to optimize battery performance.

4.4.1. Acidic Sn-based HFBs. In 2015, Liu *et al.* confirmed Sn^{2+}/Sn as a viable anode pair for flow batteries in acidic conditions. The constructed tin-vanadium HFB achieved average coulombic, energy, and voltage efficiencies of 96%, 70%, and 72%, respectively, even under a high current density of 180 mA cm^{-2}.[296] Xie's team constructed a tin-bromine HFB by employing Br^-/Br_2 and Sn^{2+}/Sn^0 as the redox couples for the cathode and anode, respectively. Under a high current density of up to 200 mA cm^{-2}, the battery achieved an energy efficiency of 82.6%. Moreover, to address the potential cross-contamination issue of Sn^{2+} ions during battery operation, they proposed a tin reverse electrodeposition method, enabling *in situ* recovery of the battery's capacity.[297] Wang *et al.* drew inspiration from electrolyte optimization strategies in zinc-based HFBs and leveraged the coordination effect between $K_4P_2O_7$ and Sn^{2+} ions, which not only reduced the stripping potential of the Sn anode but also enhanced the stability of the anolyte. The constructed tin-iodine HFB demonstrated stable operation for over 250 cycles, as the coordination strategy effectively facilitated uniform deposition of Sn metal on the carbon felt, thereby preventing the formation of "dead Sn". However, it cannot be denied that after the formation of complexes with Sn^{2+} ions, the current density significantly decreased (80 mA cm^{-2}) at the same energy efficiency.[298] Wu *et al.* developed a cost-effective acidic Sn–Fe HFB by utilizing iron ions (Fe^{3+}/Fe^{2+}) at the cathode and tin metal deposition/stripping reactions at the anode. This battery maintained an impressive energy efficiency of up to 78.5% even under a high current density of 200 mA cm^{-2}. Although the battery efficiency exhibited minimal degradation after 700 cycles of operation, the capacity experienced a rapid decline.[299] Subsequently, they conducted a systematic investigation into the impacts of various electrode configurations (cavity, carbon paper, carbon cloth, and graphite felt), membrane types (cation and anion exchange membranes), and flow field designs (serpentine and interdigitated flow fields) on the performance of Sn–Fe HFBs. Although optimizing these parameters and employing a hybrid electrolyte approach exerted a certain positive effect on stabilizing the battery capacity, unfortunately, a satisfactory capacity retention rate was still not achieved.[300] Zhou *et al.* employed a conductivity-activity dual-gradient design strategy, whereby the carbon felt was electro-passivated at the electrode/membrane interface while chemically activated at the electrode/current collector interface. This design significantly improved the uniformity of current density distribution and electrodeposition within the electrode, enabling preferential and homogeneous tin deposition near the electrode/current collector region. Furthermore, the battery demonstrated improved areal capacity (268 mAh cm^{-2} at 80 mA cm^{-2}), energy efficiency, and capacity retention due to substantially enhanced electrode space utilization and unobstructed ion transport pathways.[301]

4.4.2. Alkaline Sn-based HFBs. In contrast to the aforementioned acidic tin-based HFBs, Lu *et al.* validated an alkaline tin-based HFB featuring a dendrite-free tin anode based on the $Sn(OH)_6{}^{2-}/Sn^0$ redox couple. By coupling with the iodide/triiodide ($I^-/I_3{}^-$) redox couple, the continuously flowing Sn–I battery achieved an average discharge voltage of 1.3 V, an aerial capacity of 73.07 mAh cm^{-2}, and a discharge duration of 350 hours. This is primarily attributed to the isotropic crystal growth mechanism of tin metal during deposition, which results in a smooth and dendrite-free surface morphology. This advantage stems from tin's body-centered tetragonal crystal structure, where the surface energy differences between its various crystal planes are significantly smaller than those in zinc (as depicted in Fig. 28c). Consequently, this minimizes the anisotropic surface energy-driven dendrite formation commonly observed in zinc-based redox couples.[42] By introducing electrolyte additives or employing electrode modification techniques, the deposition behavior of Sn can be further refined, thereby effectively minimizing the formation of "dead Sn". As illustrated in Fig. 28d, the incorporation of urea additive can enhance the adsorption and reaction between $Sn(OH)_6^{2-}$ and graphite felt. This, in turn, facilitates the uniform deposition of Sn, preventing the aggregation of Sn particles and the formation of "dead Sn" that typically occurs in conventional electrolytes.[302] As shown in Fig. 28e, Chen *et al.* conducted an in-depth investigation into the deposition/dissolution reaction mechanism of Sn in an alkaline Sn–Fe hybrid redox flow battery using *operando* ultraviolet-visible (UV-Vis) and Raman spectroscopic techniques. The results revealed that the conversion process of tin to SnO_3^{2-} must proceed through a stable SnO_2^{2-} intermediate state. Moreover, when brass mesh is employed as the anode current collector instead of carbon felt, a marked improvement in the deposition morphology of tin is achieved. This phenomenon is primarily attributable to the fact that the binding energy between the copper-based material surface and SnO_3^{2-} is higher than that between the carbon-based material and SnO_3^{2-} (as shown in Fig. 28f), which facilitates the formation of uniformly sized small-particle nuclei.[43]

4.5. Copper (Cu)-based hybrid flow batteries

4.5.1. All-copper HFBs. Copper is a low-cost and abundant element, with well-established technologies and a comprehensive value chain spanning from mining to recycling and re-application. Copper exists in three stable oxidation states: Cu(0), Cu(I), and Cu(II). During the charging process, Cu^+ ions are oxidized to Cu^{2+} ions at the cathode and are electrochemically deposited as Cu^0 metal at the anode.[303] Consequently, similar to the all-vanadium redox flow batteries (VRFBs), all-copper HFBs can be constructed based on the Cu^{2+}/Cu^+ and Cu^+/Cu^0 redox couples, as depicted in Fig. 29a. In recent years, the all-copper HFBs have attracted considerable attention due to their self-balancing characteristics. Although their cell voltage is lower than that of VRFBs, the all-copper HFBs can deliver comparable energy at a lower cost. The concentration of copper in the electrolyte can reach 2.5–3.0 M, which is significantly higher than that of vanadium (1.0–1.6 M). This substantial increase in electrolyte concentration greatly enhances the energy density of the electrolyte, thereby reducing both the cost and the footprint of the battery system. Moreover, all-copper HFBs exhibit superior stability at high temperatures compared to VRFBs. All-copper HFBs do not form precipitates similar to V^{5+} when the temperature exceeds 50 °C, enabling normal operation without the need for an auxiliary cooling system. Additionally, the pH of the all-copper HFBs electrolyte is typically below 1. This highly acidic electrolyte offers high electrical conductivity, effectively reducing the ohmic resistance of the system and thus minimizing energy losses. These advantages render the all-copper HFBs a highly promising candidate for next-generation flow batteries. However, at present, the full advantages of all-copper HFBs have not been fully realized, primarily due to the insufficient research on their core components. Key issues such as the selection and optimization of electrode materials, the stability and lifespan of electrolytes, the selection and performance of membranes, as well as battery efficiency and energy density remain unresolved, necessitating the investment of more efforts.

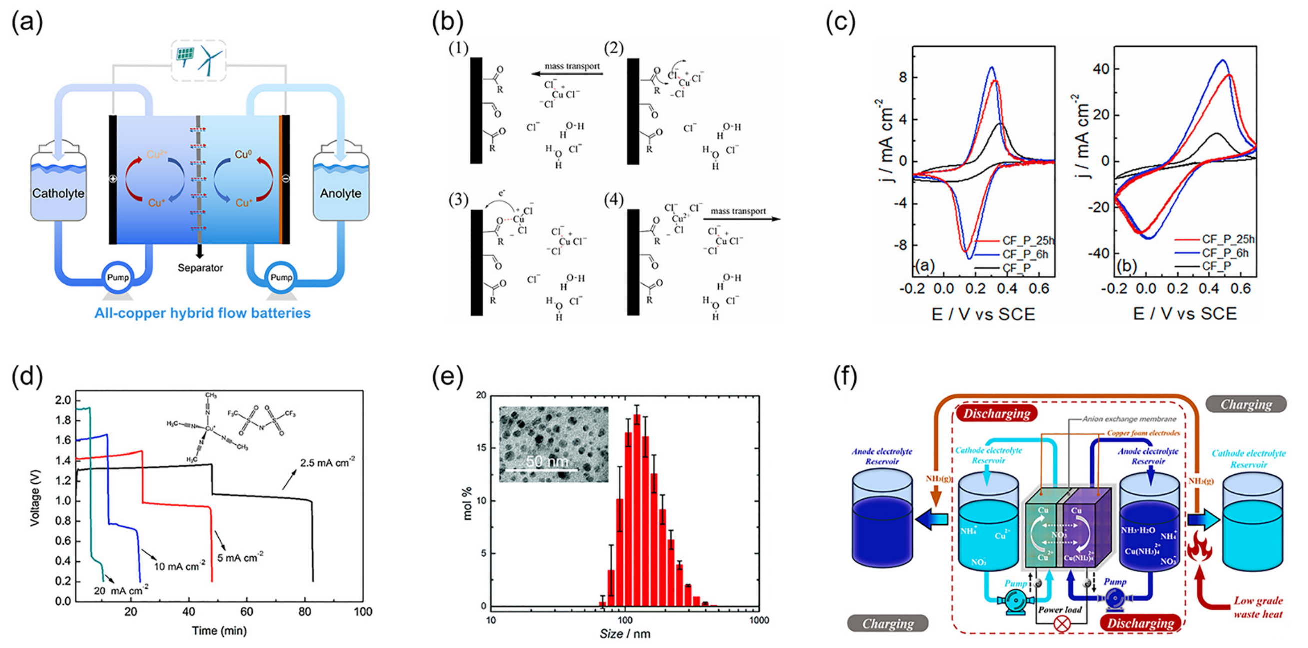

Fig. 29 (a) Schematic diagram of the typical structure configuration of all-copper HFBs. (b) Mechanism for Cu^{2+}/Cu^+ redox reaction with C=O functional groups on the electrode surface as high affinity coordinating site. Reproduced from ref. 305 with permission from Elsevier, copyright 2022. (c) Cyclic voltammetry curves of pristine, and treated polyacrylonitrile-based carbon felts in 5 mM $CuCl_2$-1 M HCl solution. Reproduced from ref. 305 with permission from Elsevier, copyright 2022. (d) Discharge curves of single cell with 0.3 M $[Cu(MeCN)_4][Tf_2N]$ at various current densities. Reproduced from ref. 308 with permission from Elsevier, copyright 2017. (e) The size distribution and TEM image of Cu nanoparticles after thermal regeneration. Reproduced from ref. 309 with permission from The Royal Society of Chemistry, copyright 2020. (f) Schematic representation of the copper–ammonia flow batteries to convert low-grade waste heat into electricity. Reproduced from ref. 312 with permission from Elsevier, copyright 2024.

To address the issue of excessive electrode polarization caused by two-dimensional electrodes, Anderson *et al.* employed copper fibers and carbon felt as the anode and cathode electrode materials, respectively. The three-dimensional electrode materials with lower overpotential enabled highly reversible electrochemical reactions, and the all-copper HFBs achieved a high coulombic efficiency of 99%.[304] Compared to untreated carbon felt, thermal treatment of carbon felt can markedly enhance the active surface area and reaction reversibility of the electrode. This is attributed to the fact that thermal treatment effectively increases the oxygen-containing functional groups (C═O) on the carbon felt surface, thereby promoting the reversibility of the Cu^{2+}/Cu^{+} redox reaction (as depicted in Fig. 29b).[305] However, traditional thermal treatment methods require a relatively long time (25–30 hours). Arbizzani *et al.* achieved comparable results through a short-time (6 hour) thermal treatment (as shown in Fig. 29c), significantly reducing both the processing time and energy consumption.[305] Electrolytes for all-copper HFBs can be classified into three categories: aqueous solutions, organic solvents, and ionic liquids. Researchers have demonstrated that the complexation of halide ions (Cl^{-} and Br^{-}) in aqueous electrolytes can enhance the redox potential and reversibility of Cu^{2+}/Cu^{+}, address precipitation issues in high-concentration copper electrolytes, and maintain stability at high temperatures (50–70 °C). Additionally, halide ions can effectively suppress HER at the anode as well.[306,307] $[Cu(MeCN)_4][Tf_2N]$, a copper-containing ionic liquid, exhibits both solvent and electrolyte functionalities, characterized by a high copper ion concentration and remarkable energy density (75 Wh L^{-1}).[45] However, the diffusion coefficient of Cu^{+} in the ionic liquid is inherently low (10^{-11} m^2 s^{-1}). Replacing the ionic liquids with eutectic electrolytes or organic solvents offers an effective strategy to enhance Cu^{+} mobility. Vankelecom *et al.* reported a non-aqueous Cu-HFB based on $[Cu(MeCN)_4][Tf_2N]$, exhibiting a remarkably high voltage of 1.24 V in acetonitrile (MeCN) with a solubility of up to 1.68 M, theoretically allowing for an energy density of 28 Wh L^{-1} (Fig. 29d).[308] Copper nanoslurry has significant potential as a substitute for conventional liquid electrolytes in all-copper HFBs. Peljo *et al.* introduced a copper nanoslurry-based thermally regenerative flow battery system capable of converting low-grade thermal energy (<200 °C) from industrial waste heat or solar thermal collectors into electricity. The system leveraged MeCN coordination to stabilize Cu(I), while thermal treatment induced MeCN removal, triggering Cu^{+} disproportionation into copper nanoparticles (Cu^{0}, as shown in Fig. 29e) and a Cu^{2+}-containing solution for battery charging.[309] The adoption of non-aqueous solvents overcomes the limited voltage window of conventional aqueous electrolytes, making higher operating voltages and energy densities possible. However, the nonaqueous all-copper HFBs demonstrated lower current density, coulombic efficiency, and energy efficiency compared to aqueous all-copper HFBs.

4.5.2. Copper-ammonia flow batteries. In addition to all-copper flow batteries, a thermally regenerative copper–ammonia flow battery (TRCAB) has been proposed, comprising electrochemical and thermal regeneration units.[310–312] As shown in Fig. 29f, the cathode features Cu^{2+} dissolved in ammonium sulfate electrolyte, while the anode utilizes $Cu(NH_3)_4^{2+}$ (a copper–ammonia complex) generated *via* reaction of metallic copper with aqueous ammonia. Energy storage and release are achieved through reversible redox reactions of copper (Cu^{2+}/Cu^{0}) and ammonia complexation/decomplexation with copper ions, with low-grade thermal energy (*e.g.*, industrial waste heat, solar thermal) driving electrolyte regeneration for thermoelectric conversion. For the cathode, Cu^{2+} is reduced to metallic copper (Cu^{0}) to complete the discharge process, and then the Cu^{2+} generated by the thermal regeneration of $Cu(NH_3)_4^{2+}$ re-enters the catholyte. Concurrently, at the anode, metallic copper dissolves to form $Cu(NH_3)_4^{2+}$ during discharge, releasing electrons; thermal treatment then decomposes $Cu(NH_3)_4^{2+}$ into Cu^{2+} and NH_3, with the ammonia recovered *via* distillation and reintroduced into the anolyte. Thus, the electrolytes can be recycled through the thermal regeneration process without the need for external charging. An anion exchange membrane is typically employed as the membrane, permitting selective passage of SO_4^{2-} and other anions while preventing the crossover of Cu^{2+} and $Cu(NH_3)_4^{2+}$, thereby minimizing self-discharge. For electrodes, foam copper, copper rod arrays, or copper meshes are utilized, with structural optimizations (*e.g.*, three-dimensional porous architectures, interdigitated arrangements) implemented to enhance reactive surface area and improve mass transport efficiency.

4.6. Lead (Pb)-based hybrid flow batteries

Traditional redox flow batteries generally require expensive membranes to separate the catholyte and anolyte, thereby increasing system costs. The all-lead HFB is regarded as a cost-effective system because it uses a single electrolyte and does not require any membranes.[313] As shown in Fig. 30a, the all-lead HFB has a single electrolyte storage tank. Typically, Pb^{2+} ions are dissolved in methanesulfonic acid (MSA) to serve as the electrolyte. During charging, on the cathodic side, Pb^{2+} ions deposit as PbO_2, and on the anodic side, Pb^{2+} ions deposit as metallic Pb. During discharging, PbO_2 and metallic Pb are redissolved into Pb^{2+} ions and then circulate between the battery and the storage tank along with the electrolyte.

Nevertheless, all-lead HFBs are confronted with a series of formidable challenges. These encompass the growth of lead dendrites at the anode, the evolution of oxygen at the cathode, and the suboptimal reversibility associated with PbO_2 deposition.[314] During the charging process, significant differences emerge in the concentration changes of various components in the electrolyte. Specifically, the concentration of H^{+} ions experiences an increment at a rate that is precisely twice that of the decline in the concentration of Pb^{2+} ions. This imbalance in ion concentrations subsequently leads to an asymmetry in the capacities of the anode and cathode. The growth of lead dendrites poses a significant threat to the battery's operational lifespan, as it can induce internal short-circuits within the battery. The evolution of oxygen at the cathode represents another detrimental factor, as it directly contributes to a reduction in the overall energy conversion efficiency of the battery.[315] Moreover, the sluggish reaction kinetics and limited reversibility of the PbO_2/Pb^{2+} redox couple are critical issues. These

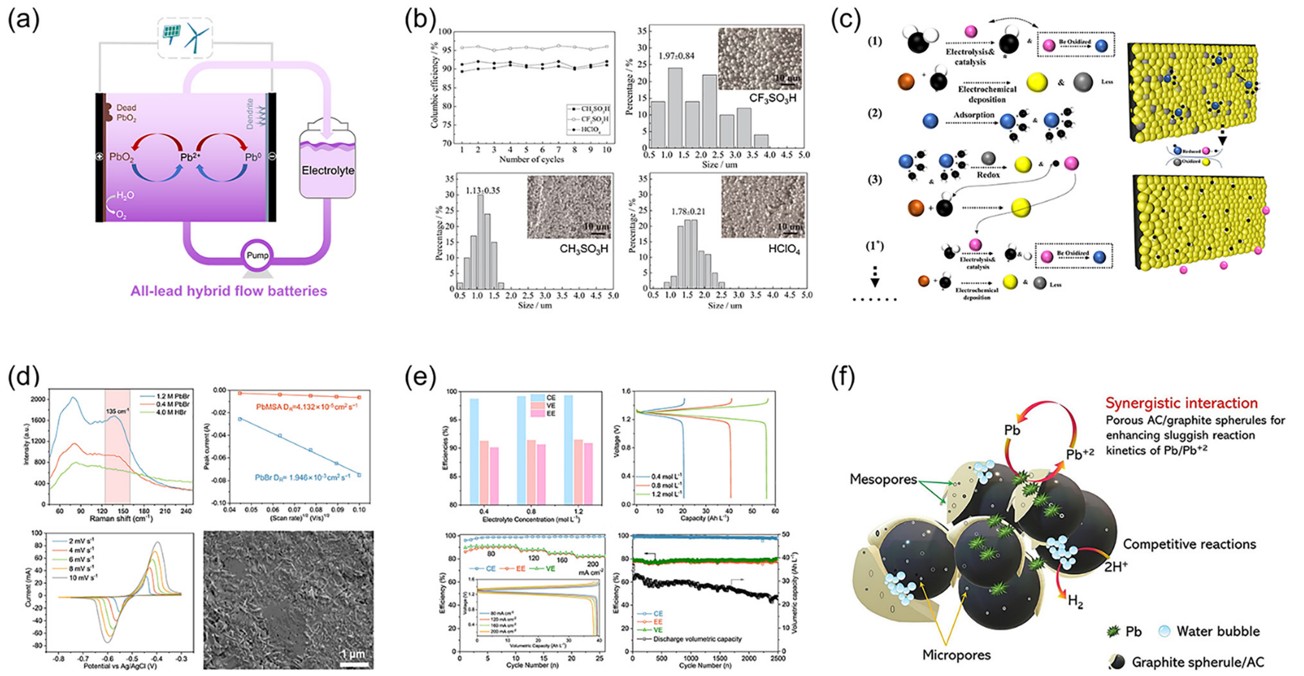

Fig. 30 (a) Schematic diagram of the typical structure configuration and major challenges of all-lead HFBs. (b) The coulombic efficiency and PbO_2 particle size distribution in different electrolytes. Reproduced from ref. 316 with permission from Elsevier, copyright 2020. (c) Mechanism of synergistic effects between Co^{2+} and tartaric acid for PbO_2 deposition in all-lead HFBs. Reproduced from ref. 320 with permission from Elsevier, copyright 2024. (d) Raman spectrum, diffusion coefficient, cyclic voltammetry curve, and deposition morphology of $PbBr(H_2O)_n^+$ anolyte. Reproduced from ref. 47 with permission from American Chemical Society, copyright 2024. (e) Battery performance of lead–bromine flow battery using $PbBr(H_2O)_n^+$ anolyte. Reproduced from ref. 47 with permission from American Chemical Society, copyright 2024. (f) Schematic illustration of the electrochemical reactions on composite anode (*e.g.* graphite spherule/activated carbon). Reproduced from ref. 328 with permission from Elsevier, copyright 2023.

factors result in polarization and the continuous build-up of PbO_2 at the cathode. Over time, this accumulation leads to the exhaustion of Pb^{2+} ions in the electrolyte, ultimately culminating in the failure of the battery system. Furthermore, the flow cell of all-lead HFBs demands supplementary design to ensure a range of optimal characteristics. These encompass the attainment of homogeneous current and potential distributions, fast mass-transport, minimized current dissipation, and reduced internal resistance. In an effort to mitigate these challenges, researchers in recent years have embarked on an in-depth exploration of a diverse array of strategies, such as adding electrolyte additives to improve electrode deposition behavior, optimizing electrolyte concentration and flow conditions to reduce dendrite growth, as well as optimizing battery components (electrodes, membranes, and bipolar plates) and designing novel battery structures to enhance overall performance.

For all-lead HFBs, the optimization strategies targeting the cathode material PbO_2 are of paramount importance. The composition of the electrolyte significantly influences the deposition morphology of PbO_2. Huang *et al.* conducted a comparative study on the impact of three electrolytes [$Pb(CF_3SO_3)_2/CF_3SO_3H$, $Pb(CH_3SO_3)_2/CH_3SO_3H$, and $Pb(ClO_4)_2/HClO_4$] on the reversibility of the PbO_2/Pb^{2+} cathode. The research revealed that the PbO_2/Pb^{2+} cathode exhibited the highest reversibility in the $Pb(CF_3SO_3)_2/CF_3SO_3H$ electrolyte, where the PbO_2 particles were of the smallest size, possessed the highest oxygen content, and achieved a coulombic efficiency of 96% (as depicted in Fig. 30b).[316] Furthermore, optimizing the concentrations of acid and Pb^{2+} ions in the electrolyte can also contribute to reducing the OER rate, thereby enhancing battery efficiency. Additives in the electrolyte exert a pronounced influence on the PbO_2/Pb^{2+} reaction kinetics, the mechanical properties and deposition morphology of PbO_2, and the OER. For instance, sodium acetate (NaOAc) as an electrolyte additive significantly enhanced the mechanical strength of PbO_2 electrodeposits by achieving anisotropic grain orientation, thereby reducing crack formation and spallation of PbO_2. Furthermore, through the adsorption of acetate ions (CH_3COO^-) onto the PbO_2 surface, NaOAc altered the reaction pathway, leading to a marked reduction in the OER rate.[317,318] Leveraging the synergistic effects of multiple additives represents a promising strategy for improving PbO_2 electrodeposit quality.[319] For instance, Co^{2+} and tartaric acid exhibited synergistic effects in promoting uniform PbO_2 deposition and extending the operational lifespan of all-lead HFBs. The low concentration of hydroxyl radicals ($^{\bullet}OH$) is identified as the primary reason for forming cathodic passivation layers composed of PbO. As depicted in Fig. 30c, Co^{2+} addressed this by catalyzing the OER to enhance $^{\bullet}OH$ generation, thereby favoring the oxidation of Pb^{2+} to PbO_2 over the formation of PbO. Meanwhile, tartaric acid—owing to its delocalized π-electron structure—simultaneously improves the electrical conductivity and reduces the impedance of PbO_2 electrodeposits.[320] Electrode modification strategies, such as metal impregnation, polymer film coating, and carbon felt doping, have proven effective in enhancing the quality of PbO_2 electrodeposits.[321] Altering testing conditions, such as deposition potential, current density, electrolyte flow speed, and temperature, exerts a significant influence on the oxygen content, crystal structure, and physical properties of PbO_2.[322–324] A high deposition potential promotes the formation of mixed α-PbO_2/β-PbO_2 phases, which exhibit superior cyclic stability and electrochemical activity. PbO_2 formed at a low temperature demonstrates increased oxygen content, a higher proportion of the α-phase, enhanced electrochemical activity, improved mechanical strength, and reduced particle size with more uniform distribution.

In addition to the challenges of poor reversibility of PbO_2/Pb^{2+} and oxygen evolution at cathode, the formation of Pb dendrites at anode poses a critical threat to the operational lifespan of all-lead HFBs. Electrolyte additive strategies have been demonstrated to be beneficial for improving the deposition behavior of Pb anodes. The catalytic action of non-precious metal ions (*e.g.*, Bi^{3+}) contributes to enhancing the reaction kinetics of Pb anodes.[325] The metal ion co-deposition (*e.g.*, Sn^{2+} and Pb^{2+}) strategy can improve the deposition morphology and crystal structure of Pb anodes.[326] The synergistic effect among additives can suppress the dendrite growth and HER on Pb anodes. For instance, cationic surfactants form a protective film on the electrode surface through electrostatic adsorption, guiding the uniform lateral deposition of Pb^{2+} ions. Meanwhile, the addition of NaF further promotes this process, effectively preventing dendrite growth.[327] In addition, as depicted in Fig. 30d, the anolyte of $PbBr(H_2O)_n{}^+$, designed by leveraging the weak coordination interaction between Pb^{2+} and Br^-, exhibits a high solubility and diffusion coefficient, enabling the realization of a highly reversible and stable Pb anode. Meanwhile, the specific adsorption of Br^- on the anode surface weakens the concentration gradient at the electrode interface, leading to unique under-potential deposition, enhancing the kinetic performance of the electrode reaction and the overall efficiency of the battery (Fig. 30e).[47] As the site where the Pb^{2+}/Pb^0 reaction occurs, the surface and internal structure of the electrode play a pivotal role in the deposition process. Modification of graphite felt electrodes through different methods, such as sulfuric acid treatment, heat treatment, and electrochemical oxidation, can significantly enhance electrochemical performance and catalytic activity. The composite anode strategy can achieve multiple effects. Typically, as depicted in Fig. 30f, high-specific-surface-area materials (such as activated carbon and carbon foam) are employed as the substrate, while high- conductivity materials (such as graphite spherule and metallic copper) are used as the composite coating. This design not only significantly enhances the charge-transfer rate and reaction reversibility of the anode, facilitating uniform Pb deposition, but also increases the contact area between the electrode and the electrolyte through the rich pore structure, promoting electrolyte permeation and rapid ion diffusion.[328–330]

4.7. Challenges and prospectives of aqueous MBHFBs

4.7.1. Advantages and challenges. Aqueous MBHFBs represent a novel electrochemical energy storage technology that integrates the design philosophy of aqueous flow batteries with the reversible deposition–dissolution reactions of metal electrodes. The typical structural configuration of these batteries involves utilizing metal ions dissolved in water (such as zinc, iron, cadmium, tin, copper, lead, *etc.*) as the active material for the anode, paired with an aqueous catholyte (*e.g.*, halogens, organic compounds, *etc.*). Owing to the high safety profile of aqueous electrolytes and the high theoretical capacities of metal materials, aqueous MBHFBs have attracted extensive attention in the field. Among them, aqueous MBHFBs employing zinc and iron as anodes also feature abundant reserves (low cost) and environmental friendliness, making them highly suitable for large-scale energy storage. Furthermore, through continuous iterative advancements in aqueous MBHFBs technology, combined with highly reversible deposition–dissolution reactions and a stable aqueous electrolyte environment, certain technical routes have demonstrated the capability to achieve over 10 000 cycles.

Although aqueous MBHFBs hold great promise, several outstanding issues remain to be urgently addressed, as depicted in Fig. 31. In terms of electrochemical performance and energy characteristic indicators, due to the relatively narrow voltage window of aqueous electrolytes, even with the presence of high overpotentials for some metals, the operating voltages of the aqueous MBHFBs are still restricted (typically less than 2.0 V). Furthermore, the deposition/dissolution reactions at the metal anode are not only governed by diffusion control but also exhibit sluggish kinetics, leading to a low utilization rate of active materials. Consequently, this necessitates the use of larger-volume electrolyte storage tanks and greater electrode areas. These are detrimental to achieving higher energy density and power. In terms of service lifespan and stability, metal anodes are prone to dendrite formation (*e.g.*, for zinc and iron) during the charge–discharge cycles. These dendrites can puncture the membrane, resulting in short circuits. Additionally, aqueous electrolytes are susceptible to side reactions (such as hydrogen evolution, oxygen evolution, and corrosion), which cause changes in electrolyte composition and degrade battery performance (*e.g.*, coulombic efficiency and energy efficiency). These issues significantly reduce the operational lifespan of aqueous MBHFBs far below its theoretical value, thereby increasing the long-term usage costs. In addition to the aforementioned common issues for aqueous MBHFBs, the selection of different metal anodes also introduces unique and distinct challenges that warrant individual attention and require a case-by-case analysis. For aqueous zinc-based and iron-based HFBs, the issues of dendrite growth and hydrogen evolution are particularly prominent, severely compromising battery lifespan. In the case of aqueous tin-based and copper-based HFBs, the relatively high deposition/dissolution potential of the anode results in a low overall voltage, significantly undermining energy density. As for aqueous cadmium-based and lead-based HFBs, the toxicity problem cannot be overlooked, necessitating well-developed sealing and recycling technologies.

4.7.2. Strategies and prospectives. Tackling these challenges is essential for propelling the progress of aqueous MBHFBs. To effectively tackle these challenges and achieve promising advancements, future targeted research should prioritize the following critical dimensions:

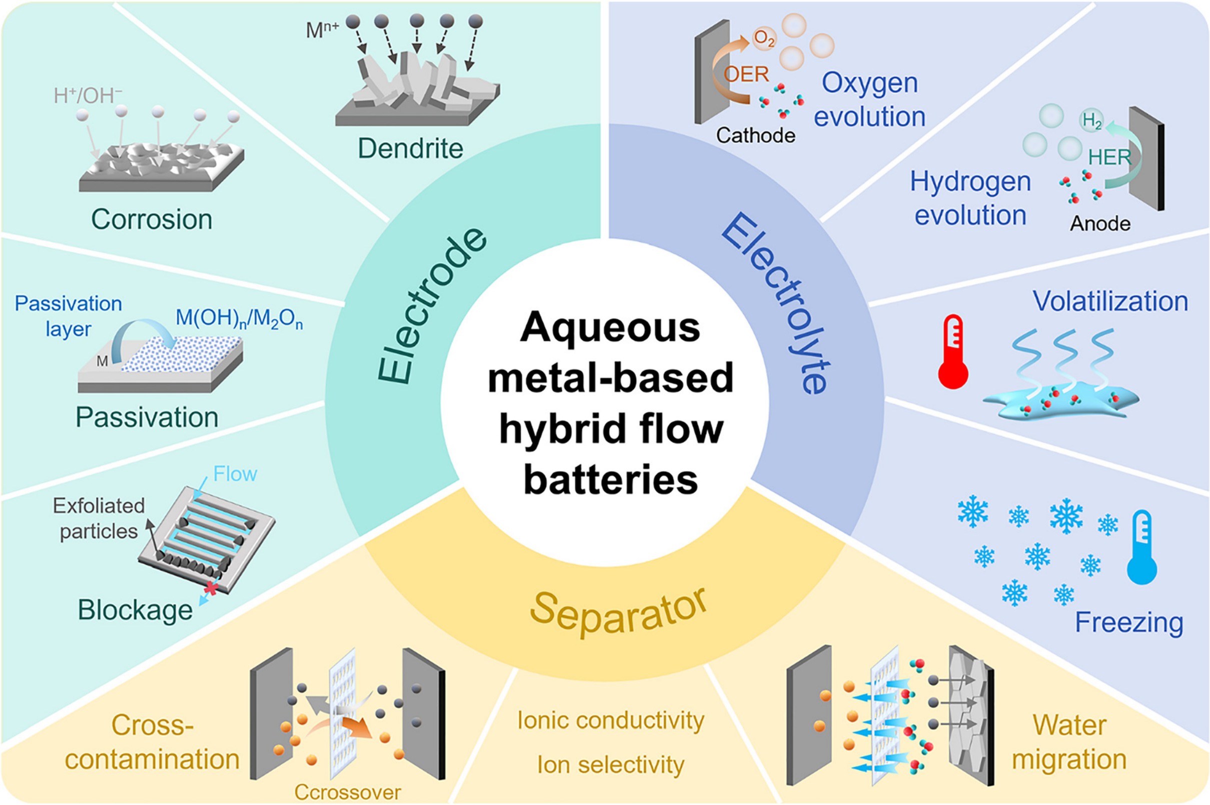

Fig. 31 Challenges of aqueous MBHFBs.

(1) A profound understanding of the dendrite formation mechanisms and growth patterns of different metal anodes in aqueous electrolytes is essential. By employing a combination of strategies to regulate the uniform deposition of metal ions, the practical lifespan of aqueous MBHFBs can be significantly enhanced. The intrinsic interface anisotropy of metals and the uneven distribution of local electric fields on electrode surfaces constitute the internal and external causes of dendrite growth, respectively. Regarding the internal cause, interface energy anisotropy drives the dendrite trunk to elongate along specific directions, forming the initial dendritic backbones. The varying atomic attachment rates on different crystal planes further amplify the growth rate disparities, resulting in the formation of more intricate side branches. Externally, the uneven distribution of local electric fields or differences in ion flux on the electrode surface prompt metal nucleation and growth preferentially at active sites, such as lattice distortion regions, leading to dendrite formation. The "tip discharge" effect of dendrites, coupled with ion concentration polarization and hydrogen evolution corrosion, further fuels dendrite growth.[331] Ultimately, uncontrolled dendrite growth can either puncture the membrane, causing short circuits, or lead to dendrite detachment, forming "dead metal" that blocks the electrodes and pipelines. To suppress dendrite growth, it is essential to focus on the three key materials—electrolyte, electrode, and membrane—and implement precise interfacial engineering at both the electrolyte/electrode and electrolyte/membrane interfaces. Drawing inspiration from advanced electrolyte strategies can effectively optimize the solvation structure of metal ions, thereby finely regulating their transport and deposition behaviors.[332] Meanwhile, designing high-conductivity electrodes with hierarchical pore architectures can induce uniform deposition by providing controlled nucleation sites.[333] Additionally, customizing porous conductive ion-selective membranes with high selectivity, conductivity, stability, and mechanical strength can enhance battery performance while preventing dendrite penetration, ensuring long-term operational safety and reliability.[334] These integrated approaches collectively address the critical challenges of dendrite growth in aqueous MBHFBs, paving the way for high-performance, durable energy storage systems.

(2) A thorough comprehension of the underlying principles governing the generation of side reactions within aqueous electrolytes, along with effective approaches to curb these detrimental reactions, is critically essential for prolonging the service life of aqueous MBHFBs. In addition to dendrite growth, the primary side reactions induced by aqueous electrolytes encompass hydrogen evolution reaction (HER), oxygen evolution reaction (OER), and electrode corrosion. The solvation structure of metal ions weakens the O–H bonds in water molecules, rendering them more susceptible to reduction into H_2. Moreover, given the close proximity between the hydrogen evolution potential of water and the deposition potential of metal ions, a competitive relationship emerges during battery charging: while metal deposition occurs on the anode surface, solvated water molecules are concurrently/preferentially reduced to generate H_2.

On the one hand, the HER results in a reduction of the battery's coulombic efficiency, and the evolved gas hinders the uniform deposition of metal ions. On the other hand, the HER triggers a localized increase in the electrolyte's pH, expediting the corrosion of the metal anode and thereby further degrading the battery's performance. Given the limited electrochemical stability window of water, when the redox potential at the cathode exceeds a critical threshold, it readily triggers the OER. This reaction not only induces electrolyte depletion and a decline in coulombic efficiency but also leads to the dissolution of evolved oxygen into the electrolyte, which subsequently promotes electrode corrosion. Furthermore, given that flow battery systems are typically enclosed, the continuous accumulation of gases resulting from persistent water decomposition poses potential safety hazards due to pressure buildup and the risk of gas leakage or explosion. In addition to HER and OER, factors such as strongly acidic or alkaline electrolytes, specific anions, and loose deposition layers can also significantly accelerate electrode corrosion. To suppress these side reactions, the core strategy lies in minimizing or restricting the availability of free water molecules within the bulk electrolyte or at the electrode–electrolyte interface. Key approaches include introducing additives to reconstruct the solvation sheath structure, incorporating hydrogen-bond acceptors to optimize the electrolyte's hydrogen-bonding network, and pre-forming or *in situ* constructing artificial protective layers on electrodes.

(3) Apart from dendrite growth and water decomposition, the detachment of metal particles at anode leading to bipolar plate channel blockage constitutes another primary cause of limited cycle life in aqueous MBHFBs. The primary causes of flow channel blockage in aqueous MBHFBs include metallic particle detachment, migration, and deposition. Particle detachment is directly correlated with non-uniform deposition, dendrite fracture, anode volume expansion/pulverization, and corrosion product shedding. Additionally, structural defects in channel design, such as unreasonable shape and size (*e.g.*, excessively small turning radius and width-to-depth ratio), no gradient design, and excessive surface roughness, can all lead to localized particle deposition and blockage. Electrochemical factors (*e.g.*, current density distribution) and fluid dynamics parameters (*e.g.*, flow velocity, turbulence intensity, electrolyte viscosity) further exacerbate particle detachment and deposition behaviors. Therefore, a multi-pronged approach integrating material design, operational control, and flow channel modification is required to prevent particle detachment and blockage. Optimizing electrolyte composition and electrode architecture promotes uniform metal deposition, refines grain structure, suppresses dendrite growth, and enhances metal adhesion, thereby fundamentally preventing metal particle detachment. Furthermore, optimizing flow channel geometry to reduce adhesion and integrating active cleaning mechanisms can serve as secondary safeguards against particle clogging.

(4) The membrane, functioning as a pivotal component that not only prevents direct contact between the catholyte and anolyte but also facilitates rapid and selective ion conduction, is of paramount importance to the stability of the battery. However, the membrane may suffer from manufacturing defects or undergo aging during operation, leading to a deterioration in its barrier performance. When the membrane's performance is compromised, cross-contamination between the catholyte and anolyte becomes more prone to occur, ultimately resulting in a decline in battery capacity. In addition to the cross-contamination of electrolytes, the issue of water migration within the electrolyte cannot be overlooked. Water migration is predominantly propelled by factors including concentration gradient, difference in ionic strength, and electric field. Differences in pH values, ion concentrations, or additives between the catholyte and anolyte can trigger osmotic pressure imbalances, prompting water molecules to migrate through the membrane in an effort to equalize concentration disparities. Particularly, when a substantial amount of metal ions deposit into a solid phase at the anode, the ion concentration in the anolyte drops significantly, prompting rapid water migration toward the cathode to balance the concentration disparity between the catholyte and anolyte. Furthermore, during the battery's charge–discharge cycles, electric field forces drive ion migration, concurrently pulling water molecules along. This effect is exacerbated under high current densities, accelerating the migration rate of water molecules. Moreover, defects or aging of the membrane may compromise its barrier properties, allowing water molecules to permeate through. To tackle this issue, we can suppress cross-contamination and water migration by designing high-performance membrane materials and optimizing electrolyte formulations. Firstly, developing novel porous membranes or ion-conductive membranes can enhance the ion selectivity, barrier performance, and chemical stability of the membrane. Secondly, introducing additives (such as Na_2SO_4 and hydroxyl-containing organic compounds) that can narrow the osmotic pressure and ionic strength disparities between the catholyte and anolyte can effectively mitigate the issue of water migration.

(5) Enhancing the energy density of aqueous MBHFBs is nearly as critical as improving their stability, as both parameters fundamentally govern the practical viability of these systems. While aqueous electrolytes enhance battery safety, their limited electrochemical stability window inherently restricts energy density—a fundamental trade-off faced by nearly all aqueous battery systems. Enhancing the energy density of batteries fundamentally relies on increasing both their operating voltage and capacity. Achieving higher voltage necessitates the development of electrolytes with an expanded stable electrochemical window, as well as the design of cathode and anode materials exhibiting a larger redox potential gap. Recent advancements demonstrate that substituting conventional aqueous electrolytes with "weakly solvating" electrolytes, organic-aqueous hybrid electrolytes, or additive-modified electrolytes can effectively broaden the stable voltage window to >2.0 V. This electrolyte engineering enables the utilization of anodes (*e.g.*, Mn, Al) with lower deposition–dissolution potential by mitigating HER through reduced water reduction potentials. The synergistic integration of low-potential anodes, high-potential cathodes, and wide-voltage-window electrolytes represents a promising strategy for elevating the overall operating

voltage of aqueous MBHFBs. On the other hand, developing multi-electron-transfer cathodic active materials and enhancing their solubility in catholytes represent primary strategies for increasing cathodic capacity. For instance, Li *et al.* demonstrated that utilizing a 6 M I^- electrolyte enables over 30 M electron transfer, resulting in an exceptional specific capacity exceeding 840 Ah $L_{catholyte}^{-1}$ for the I^-/IO_3^- redox couple.[39] Furthermore, the simultaneous enhancement of anode deposition/dissolution kinetics and deposition uniformity through electrolyte–electrode interface engineering, coupled with the design of three-dimensional porous anode architectures, represents a primary strategy for achieving high areal capacity in anodes.

(6) The low-temperature resilience of aqueous MBHFBs has emerged as a critical research focus in recent years, driven by the demand for high-performance energy storage under sub-zero conditions. The electrolyte represents the core limiting factor for temperature adaptability, necessitating compositional modulation to suppress low-temperature solidification and high-temperature decomposition. Compared to high-temperature (>50 °C), low-temperature (<0 °C) poses significantly greater challenges for aqueous MBHFBs due to exacerbated electrolyte freezing and sluggish ion transport kinetics. The incorporation of antifreeze additives (*e.g.*, ethylene glycol) into aqueous electrolytes effectively depresses the freezing point, thereby maintaining ionic conductivity and fluidity. Concurrently, elevating salt concentration reduces free water molecules, which not only suppresses ice nucleation but also enhances stability at high temperatures. Apart from the electrolyte, sluggish reaction kinetics of active materials under low temperatures constitute critical bottlenecks. Potential solutions include developing novel low-temperature active materials, selecting electrodes with catalytic activity and high electrical conductivity, enhancing electrolyte ionic conductivity, and implementing thermal management systems.

5. Optimization strategies and development directions for metal-based hybrid flow batteries

Over the past decade, research on the chemistry and materials in MBHFBs has grown significantly, with a gradual deepening of understanding particularly regarding the deposition–dissolution chemistry of metal anodes. However, breakthroughs in MBHFBs technology still face multiple bottlenecks, and the path to industrialization remains fraught with challenges. These bottlenecks and obstacles include, but are not limited to: (i) the electrodeposition behavior of metal ions at the interface is difficult to precisely control, and the intrinsic thermodynamics and kinetics of metals directly affect the reversibility of their deposition and dissolution; (2) although key materials have developed rapidly, the synergy between different materials is poor, and the contradiction between performance and cost remains prominent; (3) the integration with multi-dimensional characterization technologies and artificial intelligence technologies is still in its infancy and insufficiently mature; (4) the investment environment is initially in place, yet the manufacturing of battery materials and stacks as well as system integration have not yet achieved a sufficiently economical scale, and relevant industry standards are in urgent need of establishment. Therefore, systematically sorting out the core optimization paths of MBHFBs and clarifying the future direction of technological development are of great significance for breaking through existing technical bottlenecks and promoting their transition from laboratory research to practical application. Potential optimization strategies and development directions are proposed (as depicted in Fig. 32).

5.1. Electrolyte optimization strategy

The electrolyte is a critical component of MBHFBs, whose solubility, conductivity, stability, and other characteristics significantly influence the battery's performance and cycle stability. The ionic conductivity and ion transference number determine the upper limit of device power, while its solvation characteristics critically influence the pathways and kinetics of electrochemical conversion reactions.[335] Macroscopic adjustment of specific components in the electrolyte enables the optimization of electrolyte formulations, which essentially achieves precise regulation of its microscopic solvation structure. In addition, since the electrolyte is in contact with both electrodes and the membrane, it must also exhibit high electrochemical stability toward the electrode/membrane materials and operating voltages to prevent degradation reactions. Special attention should also be paid to the electrolyte–electrode and electrolyte–membrane interfaces. Several effective strategies have been proposed to optimize the solvation structure of electrolyte, electrolyte–electrode interface, and electrolyte–membrane interface, aiming to enhance the overall battery performance:

5.1.1. Electrolyte additive. As the critical component in the electrolyte beyond active materials and supporting solvents, additives often yield significant benefits even when used in trace amounts.[336] Electrolyte additives exhibit a diverse range of types, with each additive possessing distinct properties that enable unique functionalities. For instance, certain macromolecular additives can suppress electrolyte decomposition and broaden the stable electrochemical window, thereby enabling batteries to operate at higher voltages.[337] Certain low molecular polarity index anion additives can disrupt the binding between metal cations and water molecules, thereby mitigating water migration caused by the electro-migration of hydrated metal cations.[338] Certain cationic surfactant additives have been shown to induce uniform metal deposition and suppress dendrite growth.[339] Macrocyclic anion binding receptors, when used as additives, alter intermolecular interactions to enhance the dissociation of metal salts. This process increases the concentration of free cations while forming complexes with anions and impeding anion migration. Consequently, both ionic conductivity and ion transference number are improved.[340] Additionally, certain additives can reduce the electrolyte's freezing point, enabling batteries to operate at low temperatures.[341] Although the electrolyte additive strategy is simple and effective, the vast diversity of substances in the world means that identifying suitable electrolyte additives still requires extensive experimentation. Two notable shortcuts can be pursued: first, referencing additives already

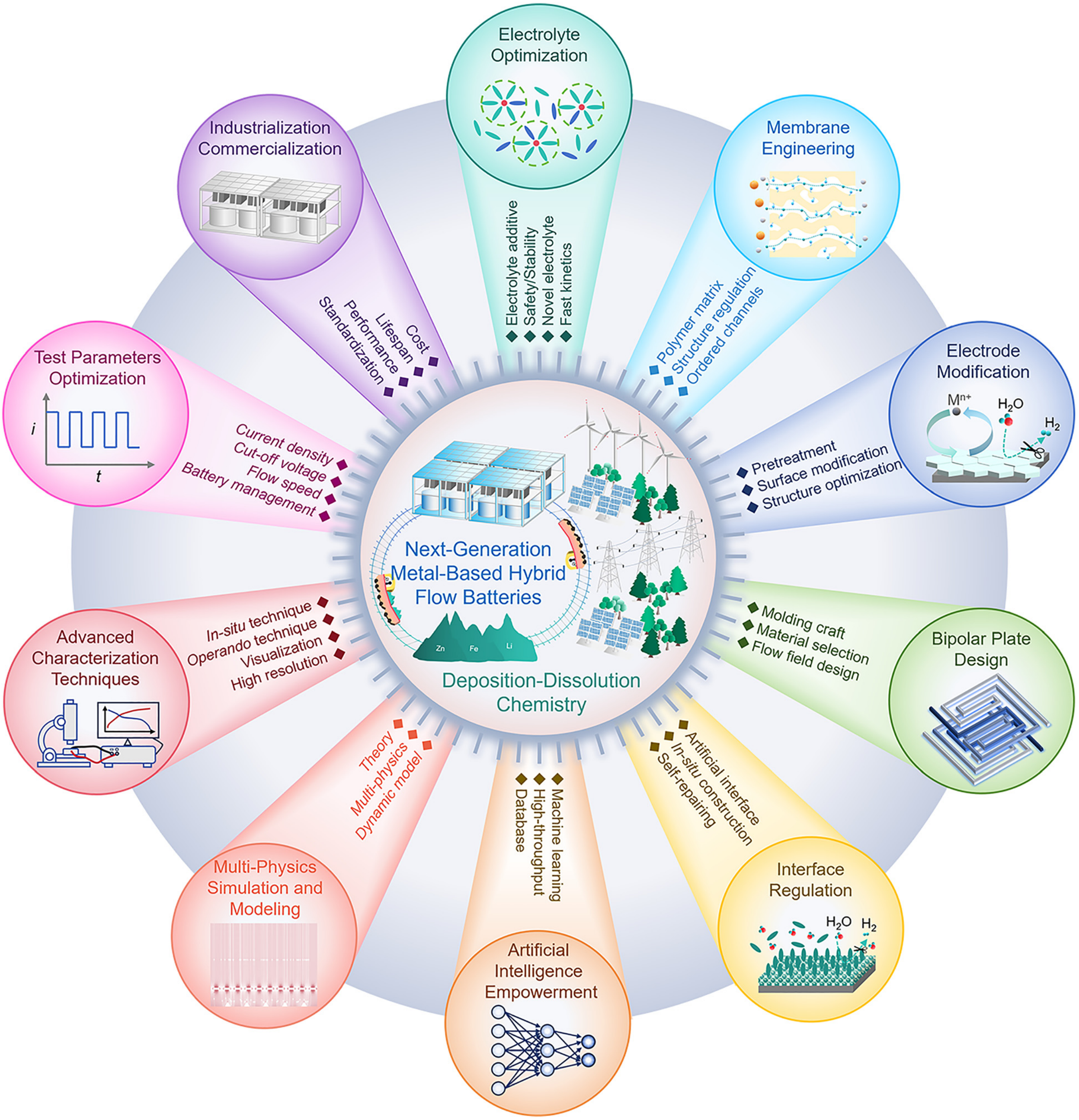

Fig. 32 Optimization strategies and development directions for the next-generation MBHFBs.

used in existing metal batteries, given the similarities between MBHFBs and metal batteries; second, leveraging artificial intelligence for pre-screening to reduce human effort and time while enhancing efficiency.

5.1.2. **Hybrid electrolyte exploration.** Existing single-solvent electrolyte systems face inherent bottlenecks that are difficult to overcome. The flammability and relatively low ionic conductivity of non-aqueous electrolytes hinder their large-scale application, while the narrow stable electrochemical window of aqueous electrolytes limits energy density and leads to some side-reactions. Therefore, developing new electrolyte systems based on these considerations is highly necessary.[342] Hybrid electrolytes, which inherit the advantages of organic and aqueous electrolytes, are emerging as a promising new alternative. Hybrid electrolytes can be obtained by mixing water with suitable organic solvents in specific ratios, exhibiting a simple and safe preparation method. Beyond their non-flammable nature, these hybrid systems inherit high electrochemical stability and a wide operating temperature range. They can demonstrate a potential window exceeding 2.5 V while maintaining high ionic conductivity at low temperatures.[343] Eutectic electrolytes, an emerging electrolyte system, are currently enjoying considerable prominence in the field of metal batteries.[344,345] Eutectic electrolytes offer significant advantages in stable voltage windows and low-temperature performance, but existing eutectic electrolytes exhibit high viscosity and low ionic conductivity, rendering them unsuitable for flow battery systems. However, if we consider introducing solvents with high fluidity and high ionic conductivity, such as water, into eutectic electrolytes, it may yield unexpected synergistic effects. Water-diluted eutectic electrolytes, as another hybrid electrolytes, can strike a balance between ionic conductivity and fluidity, thereby opening new possibilities for high-performance electrolytes in MBHFBs.

5.2. Membrane engineering strategy

The membrane isolates the catholyte and anolyte while conducting charges and balancing ions. The membrane should possess: high ionic conductivity to reduce battery resistance; high ionic selectivity to prevent self-discharge; excellent chemical stability to resist electrolyte corrosion; high mechanical strength to minimize the risk of dendrite penetration.[346] The aforementioned four key indicators of the membrane directly impact the performance and cycle life of MBHFBs. Rational design of the membrane's chemical structure and topological structure is required. Therefore, advancing membrane engineering is crucial for promoting practical application for MBHFBs. Several effective strategies for membrane engineering have been proposed:

5.2.1. Polymer matrix innovation. Currently, the available membrane materials in flow batteries include: Nafion membranes, sulfonated poly(ether ether ketone) (sPEEK) membranes, polyvinylidene fluoride (PVDF), and polypropylene (PP). The Nafion membranes, as typical ion-exchange membranes, stand out in the electrochemical field due to their high ionic conductivity, chemical stability, and selective ion transport capabilities.[347] However, their high costs, environmental and swelling risks are also significant disadvantages, particularly for large-scale production and applications. The sPEEK membranes, as non-fluoride ion-exchange membranes, are cost-effective, environmentally friendly, and exhibit strong ion selectivity. However, their ion conductivity is slightly inferior, and their long-term stability still requires further verification.[348] Porous membranes such as PVDF and PP are cost-effective but their pore size distribution is uneven. Polybenzimidazole (PBI) membranes, also known as "ion solvation membranes", have recently gained prominence in the flow battery field. Unlike ion-exchange membranes and porous membranes, the extremely low phase separation structure in PBI membranes enables ion conduction through the absorption of electrolyte into the polymer matrix. The adsorbed alkaline/acidic solutions provide the membrane with high ionic conductivity.[349,350] The development of advanced polymer materials for flow battery membranes has been a slow and incremental process. While groundbreaking materials have been rare over the past few decades, they remain worth anticipating.

5.2.2. Membrane structure regulation. In practice, synthesizing new materials or employing membranes from other technologies is highly challenging due to the unique operating environment of MBHFBs, characterized by high voltage, strong oxidizing conditions, and dendrite formation risks. A common and effective strategy is to optimize the structure of existing membrane systems. The simplest approach is to modify various preparation parameters during the membrane fabrication process to influence its morphology and structure. A more effective strategy would involve improving existing polymer monomers and polymerization processes to achieve precise control over the pore structure of membranes. Recently reported novel ion exchange membranes based on covalent triazine frameworks (CTFs) have constructed fully rigid confined micropores within the membrane and regulated ion-channel interactions, enabling nearly frictionless ion conduction.[351] Polymers of intrinsic microporosity (PIMs) possess a rigid and contorted polymer backbone structure that forms precisely controlled sub-nanometer pore structures within the material, endowing them with "intrinsic microporosity" and making them highly promising membrane materials. The introduction of hydrophilic functional groups onto PIMs allows precise modulation of pore size and pore size distribution by adjusting the local hydrophilic/hydrophobic balance around the pores, thereby achieving precise ion selectivity. Meanwhile, the synergistic effect between polymer chains and hydrophilic groups enables rapid ion conduction.[352,353] These methods, which achieve precise control of pore structure and rapid ion transport through polymer redesign, represent a promising direction for future membrane structure optimization. In addition to regulating the overall structure of membranes, local or hierarchical regulation of membrane architecture is also feasible. Mixed-matrix membranes (which lack distinct layered structures) are composed of a mixture containing multiple materials that each exert specific effects on performance. They can suppress swelling and enhance selectivity by incorporating nanoparticles.[354] However, mixed matrix membranes often face challenges in maintaining consistency during large-scale production due to filler agglomeration. Controlling the uniform and ordered dispersion of fillers and reducing interfacial defects may be key directions for future research on mixed matrix membranes.[355] For MBHFBs systems, beyond focusing on ion selectivity and ionic conductivity of the membrane, special considerations must also be given to the membrane's inductive effect on metal deposition for anode and its mechanical strength to address challenges posed by dendrite formation. Composite membranes consist of two distinct layers: a well-defined selective top layer and a high mechanical strength support layer.[356] The selection of top layer and support layer should be made with full consideration of their interfacial compatibility in order to enhance interfacial adhesion and reduce interfacial resistance. In addition to *in situ* growth, spin-coating sPEEK casting solution on a ceramic support layer has been proven to produce rigid hierarchical porous ceramic composite membranes with ultrathin (10 nm-scale) selective top layer, demonstrating excellent comprehensive performance in metal-based flow batteries.[357] Developing new composite membrane materials and advanced fabrication techniques constitute critical research priorities that merit intensive exploration in the field of composite membranes.

5.2.3. Ordered porous membrane. Ordered porous membranes with uniform pore size can theoretically achieve complete sieving of balanced ions and active species by selecting appropriate pore structures, thereby obtaining superior ion selectivity and conductivity, and enabling new breakthroughs in flow battery performance.[358] Zeolites, metal–organic frameworks (MOFs), covalent organic frameworks (COFs), covalent organic polymers (COPs) and other nanoporous materials with uniform pore sizes are commonly used materials for constructing regular channel membranes. At present, the fabrication of ordered porous membranes can be achieved through three primary approaches: (i) incorporating nanomaterials with ordered pore channels (such as zeolite nanosheets) into polymer matrices through uniform and oriented suspension, utilizing ordered arrays of pore channel materials to maximize ion recognition capability and proton transport efficiency of the membrane; (ii) forming membranes on porous support layers using ordered porous materials (such as 2D MFI-type zeolites) while maintaining directional alignment, leveraging channel dimensions and the consistency between the channel orientation and ion transport direction to achieve rapid ion sieving and conduction;[359] (iii) fabricating self-supporting membranes with high crystallinity and mechanical strength using ordered porous materials (such as COFs), leveraging ordered crystalline channels to achieve efficient ion conduction.[360] By utilizing inherent channels of ordered porous materials, channels formed through regular arrangement of these materials, and channels within the polymer matrix, it may be possible to construct hierarchical channels both on the surface and in the membrane, achieving enhanced ion sieving and transport. For MBHFBs systems, designing an ordered porous membrane with robust mechanical strength, hierarchical porosity, and well-defined pore structures represents a promising direction that also helps mitigate the trade-off effect in membranes.

5.3. Electrode modification strategy

Electrodes are a crucial component of MBHFBs, providing active sites for metal deposition and dissolution. Electrodes do not participate in the chemical reactions themselves and should be chemically and electrochemically inert. The electrocatalytic activity and reversibility of electrodes toward deposition–dissolution reactions determine the electrochemical polarization of batteries; the electronic conductivity and thickness of electrodes determine the ohmic polarization, while the pore structure and wettability determine the concentration polarization. Therefore, optimizing the physicochemical properties of electrodes is particularly crucial for enhancing the performance of MBHFBs. To meet the requirements of high electrocatalytic activity, high reversibility, high electrical conductivity, excellent mechanical strength and stability, as well as appropriate wettability and pore structure for electrode materials in MBHFBs, several strategies have been proposed:

5.3.1. Electrode pretreatment. Electrodes can be broadly classified into porous electrodes and plate electrodes based on their structural differences. The former has limited metal deposition capacity due to finite porosity, while the latter also suffers from limited deposition capacity due to spatial constraints. However, the areal capacity of MBHFBs can still be improved by enhancing the porosity of porous electrodes. Additionally, plate electrodes exhibit relatively low catalytic activity for redox reactions and significant concentration polarization, making them unsuitable for high-current-density applications. Therefore, carbon-based porous electrodes remain the mainstream choice in MBHFBs due to their high electrocatalytic activity and excellent electrochemical/chemical stability. The key challenge thus lies in further improving the catalytic activity and areal capacity of carbon-based porous electrodes, for which certain electrode pretreatment processes are worth adopting. Pretreatment *via* chemical or physical methods, such as acid activation, high-temperature calcination, and plasma treatment, can effectively increase the number of oxygen-containing functional groups on the surface of carbon felts, enhancing wettability and electrochemical activity.[361,362]

5.3.2. Electrode surface modification. Surface modification of electrodes can effectively improve the electrochemical reaction activity, corrosion resistance, and wettability of the electrode, enhancing the areal capacity and deposition reversibility of metals on the electrode and thereby further optimizing the energy density and cycle life of MBHFBs.[363] Materials suitable for electrode surface modification should possess properties such as high conductivity, chemical stability, high specific surface area and porosity, wettability, and catalytic activity. Metal nanoparticles, metal oxides, and nitrogen/sulfur-containing functional group materials exhibit excellent catalytic activity; functionalized carbon-based materials (such as carbon nanotubes) have good electrical conductivity and abundant catalytic functional groups; conductive polymers (such as polypyrrole) have good electrical conductivity and corrosion resistance; metal–organic frameworks (MOFs) have adjustable pore sizes and high specific surface areas, which can promote electrolyte penetration and ion adsorption; the ultrathin structure of two-dimensional materials (such as MXene, graphene) is conducive to shortening ion diffusion paths and reducing ohmic losses. In addition to single-material coatings, composite coatings composed of materials with different advantages will also be more widely used in the future. Meanwhile, simplifying the electrode surface modification process is also crucial, especially for large-scale production. The balance between performance and cost should be fully considered.

5.3.3. Electrode structure optimization. In addition to considering the modification of the electrode surface, optimizing the structure of the electrode itself to enhance mass transport and deposition uniformity is another widely recognized strategy. Areal capacity is one of the important indicators for evaluating the performance of MBHFBs. To deposit more metal within the limited volume and space of the anode, besides enhancing the compactness of the deposition layer, it is also necessary to increase the effective deposition area of the three-dimensional porous electrode. Combining three-dimensional skeleton design with porous structure construction provides lots of electron and ion transport channels with sufficient mechanical strength, thereby enhancing mass transport efficiency and increasing metal ion deposition sites, thus achieving faster reversible reactions and higher areal capacity. Additionally, to better balance the ion and electron transport, a hierarchical porous electrode with porosity and conductivity gradient can be ingeniously designed.[364] The macropores accelerate ion diffusion within the electrode, shortening the ion diffusion path, which can alleviate concentration polarization, reduce dendrite growth, and enhance deposition uniformity; whereas the mesopores facilitate increasing the electrode's surface area, thereby improving reaction kinetics and areal capacity. The electrode structure optimization achieves a balance between high energy density and high power density, representing a promising direction for future electrode design.

5.4. Bipolar plate design

The structural design of flow batteries revolves around core objectives such as decoupling power and capacity, ensuring high safety, and achieving long lifespan. The stack constitutes the core power module of flow batteries, comprising electrodes, membranes, and bipolar plates. The electrode and membrane will not be elaborated further here; this section primarily emphasizes the critical importance of bipolar plate and flow field design for stack performance. The bipolar plate functions as a current collector to gather and conduct electrons, while also serving as a support structure for the electrodes. Additionally, the bipolar plate serves as an electrolyte flow distributor, utilizing surface-engraved flow channels to enhance uniform electrolyte distribution.[365] Therefore, improving bipolar plate performance is crucial for the commercialization of MBHFBs. The development of bipolar plate materials and the design of bipolar plate surface structures (flow fields) constitute the two most prominent research directions. The bipolar plate should possess characteristics such as high electrical conductivity, high mechanical strength, high chemical/electrochemical stability, and low liquid permeability. The current mainstream bipolar plate materials primarily fall into three categories: graphite, metallic, and carbon-polymer composite bipolar plates.[366] Graphite bipolar plates are commonly used in low-power stacks due to their inferior mechanical strength and susceptibility to brittle fracture. Carbon–polymer composite bipolar plates are predominantly employed in high-power stacks due to suitable corrosion resistance, excellent mechanical properties, easy formability, low cost, and facile one-step flow channel fabrication. Subsequently, the material selection (polymers and fillers) and molding processes for carbon–polymer bipolar plates will become a key research focus. On the other hand, mass transfer dead zones inevitably exist during the operation of flow batteries, where impeded mass transport easily triggers side reactions such as hydrogen evolution and carbon corrosion. Bubble accumulation from these side reactions further obstructs active species transport, creating a vicious cycle.[367] Therefore, for MBHFBs, optimizing flow field to improve mass transfer in dead zones and promote uniform distribution of active species is particularly crucial for facilitating uniform metal deposition and stripping. The flow field patterns commonly used include the parallel flow field, the interdigitated flow field, and the serpentine flow field.[368] Some novel flow field designs include nonuniform flow channel design, topology optimization of flow field, and porous flow field. Unfortunately, currently available flow fields specifically tailored for MBHFBs remain scarce. Variations in geometric configurations of flow fields lead to different operating mechanisms, ultimately resulting in inconsistent impacts on battery performance. Additionally, the influence of flow fields on battery performance is further complicated by multiple parameters including electrode porosity, electrode thickness, magnetic permeability, applied current, and electrolyte flow rate, with these variables exhibiting interdependent interactions. To advance flow field design, future efforts will increasingly leverage multi-physics coupled simulations, visualization technology, and artificial intelligence-driven fast data analytics.[369]

5.5. Interface regulation strategy

In the research of MBHFBs, two critically important interfaces are involved: the electrolyte–electrode interface and the electrolyte–membrane interface. Among them, solid electrolyte interphase (SEI) is the well-known electrolyte–electrode interface layer in lithium batteries. These two interfaces can directly affect the battery's performance and operational lifespan. Rational design of the electrolyte–electrode and electrolyte–membrane interfaces can regulate mass transfer and reaction processes at the interfaces. The design of the interfaces is inseparable from the optimization and modification of the electrolyte, electrode, and membrane, that have been discussed in detail above. However, during the repeated cycling processes of MBHFBs, uneven deposition and side reactions can lead to the generation of local defects and interface layers aging. This vicious cycle exacerbates battery performance degradation and even failure. Therefore, the construction of self-healing interfaces with self-repairing capability appears to be a promising strategy for addressing severe side reactions and dendrite growth due to defects. Based on formation processes, self-healing interfaces can be classified into *in situ* and artificially constructed self-healing interfaces. Based on self-healing mechanism, self-healing interfaces can be classified into extrinsic and intrinsic self-healing interfaces. The extrinsic self-healing interfaces require the introduction of additional healing agents to facilitate repair. While intrinsic self-healing interfaces achieve repair through the migration of molecules or atoms within the interface layer and reconstruction *via* dynamic reversible interactions, without requiring additional healing agents.[370] Overall, self-healing interfaces can isolate harmful media, accelerate ion transport, induce preferential orientation deposition of metals, hinder dendrite growth, enable self-repair, and suppress defects. In the future, dedicated efforts to directly monitor interfacial self-healing processes will deepen the understanding of interface working mechanisms in MBHFBs, thereby enabling the design of more advanced self-healing interfaces.

5.6. Artificial intelligence (AI) empowerment

With the advancement of modern computational power, rapid development of mathematical algorithms, and continuous establishment of material databases, artificial intelligence (AI) represented by high-throughput computational screening and machine learning has demonstrated immense potential in fields such as chemistry and materials science.[371,372] In the future, AI is expected to guide the development of next-generation MBHFBs technology. The iteration of MBHFBs technology heavily relies on the refinement of related theories and breakthroughs in key materials. Compared to traditional trial-and-error experimentation, high-throughput screening and machine learning significantly reduce material development cycles, enabling researchers to predict material structures and properties, thereby guiding material design and optimizing battery performance.[373] In addition, the integration of quantum machine learning with reinforcement learning, transfer learning, time-series analysis, Bayesian optimization, active learning, and various generative models enables collaborative exploration spanning macroscopic to microscopic scales. This approach enhances efficiency in processing and analyzing vast experimental datasets and simulation results, holding promise to deepen understanding of the complex physical and (electro)-chemical processes involved in MBHFBs at atomic and ionic levels. It can be said that AI technologies have now comprehensively influenced the development of flow batteries. Machine learning, particularly deep learning, not only enables the design and optimization of key materials and systems but also facilitates the optimization of energy storage costs and efficiency. Despite this, the application of AI in flow batteries, particularly MBHFBs, remains in its infancy. For MBHFBs, there is currently a lack of comprehensive and standardized databases, as well as a shortage of precise descriptors for machine learning models. Researchers are called upon to collaboratively establish standardized methodologies and a centralized repository encompassing material development, performance evaluation, and data sharing, thereby fostering extensive global collaboration. Concurrently, efforts should be directed toward establishing precise descriptors to enhance the accuracy and efficiency of machine learning applications.

5.7. Multi-physics simulation and modeling

The uniform, dense, and controllable electrodeposition of metal ions is one of the most critical factors affecting the long-term operation of MBHFBs. However, current theories on metal electrodeposition lack consensus, and the influencing factors of different metal deposition morphologies are also complex and intricate, posing risks of confusion in establishing dynamic models for electrodeposition. Developing an electrodeposition theory tailored to MBHFBs by building upon existing theoretical frameworks represents both a critical necessity and a promising avenue for advancing uniform electrodeposition in next-generation energy storage systems. Moreover, due to thermodynamic and kinetic differences among various metal electro-deposition, and the influence of applied current density, temperature, electrolyte flow rate, and anode surface roughness—factors that induce variations in concentration, electric field, and flow field across the anode surface—their nuclei grow with distinct deposition patterns.[374] Common irregular deposition morphologies include whisker-like dendrites, tree-like dendrites, moss-like dendrites, interconnected platelets, and random spheres. In contrast, regular deposition morphologies are formed by the reversible epitaxial electrodeposition of metals along the most densely packed crystal planes, that is, the [110] crystal plane for body-centered cubic metals (Li, Na, K, and Fe), the [002] crystal plane for hexagonal close-packed metals (Zn and Mg), the [111] crystal plane for face-centered cubic metals (Cu and Al), and the [211] crystal plane for Sn.[375–383] To explore the origins of different deposition behaviors and predict anode deposition morphologies under various operating conditions, various models have been developed. Although these models have made some progress, there is still a gap before practical application, as they often insufficiently account for the complexity of electrodeposition under practical operating conditions of batteries. The coupling of key parameters, as well as their integration with phase-field methods, has also not been adequately explored. Since the integration between dendrites and crystallization theory remains insufficient, and the branching growth of dendrites is even more complex, the branching patterns of dendrites are still not well understood. Furthermore, previous studies have focused more on the metal deposition process rather than the stripping process. However, for MBHFBs, the inactive metal ("dead metal") formed during the stripping process severely impacts the reversibility of deposition, leading to performance degradation or even battery failure. Therefore, simultaneously modeling both metal deposition and stripping processes is crucial for achieving high-performance MBHFBs. The presence of fluid field in MBHFBs renders multiphysics coupling more complex compared to static metal batteries, and their dynamic nature makes accurate prediction and control of electro-deposition processes more challenging. To this end, in order to better conduct multi-physics simulations and establish a more accurate dynamic model, it is essential to incorporate critical parameters including but not limited to: concentration gradient, local electric field distribution, local temperature variations, localized stress fields, electrolyte flow velocity, anode surface roughness, charge–discharge cycle intervals, and flow channel geometry (width/depth). This integration aims to bridge the gap between theoretical models and the actual behavior of batteries in real-world applications.

5.8. Advanced characterization techniques

Historically, in the field of battery research, the development of characterization techniques has followed the overall trend of transitioning from *ex situ* to *in situ*/*in operando*, from low precision to high spatiotemporal resolution, and from single-technique approaches to multi-technique coupling. (i) Herein, *in situ* technology emphasizes conducting measurements at the original location of the sample or in a simulated natural environment, minimizing interference with the sample's state. The core of *in situ* technology lies in non-destructive observation, but it does not require strict matching of the dynamic conditions of real-world operating conditions. *In operando* technology (dynamic *in situ* during actual operation) places greater emphasis on conducting measurements during actual operations and aims to narrow the gap between experimental conditions and real-world applications, thereby more accurately revealing the working mechanisms.[384] The *in situ* and *in operando* techniques have their respective advantages in non-destructive monitoring and dynamic tracking. The combination of *in situ* and *in operando* techniques enables real-time monitoring of structural, compositional, and electrochemical performance changes under actual battery operating conditions. The experimental design of *in situ* characterization is relatively flexible, allowing intermittent data collection under simplified conditions. In contrast, *in operando* characterization requires a high degree of integration of experimental setups to support continuous dynamic monitoring. It should be noted that some "*in situ*" characterization techniques described in the literature are conducted outside the actual working environment of batteries, and therefore cannot be considered as *in operando* characterization techniques. Researchers have begun employing various *in situ* and *in operando* characterization techniques to investigate electrolytes circulating between the cell and the tanks during battery operation, such as nuclear magnetic resonance (NMR), electron paramagnetic resonance (EPR), Fourier transform infrared spectroscopy (FTIR) and ultraviolet-visible (UV-Vis) spectroscopy.[385–388] However, research on the electrode and membrane interfaces inside batteries still largely relies on *ex-situ* or *in situ* characterization techniques, and it is difficult to achieve *in operando* monitoring. Although researchers have simulated the operating conditions of MBHFBs as closely as possible and conducted *in operando* optical observations of dendrite growth, the electrolyte remains static in these experiments.[389] Consequently, such *in operando* characterization techniques remain deficient because dendrite growth is also influenced by electrolyte flow rate. For MBHFBs, how to utilize *in situ* and *in operando* techniques (such as lenses or electron microscopy) to directly observe the deposition/stripping behaviors of metals at the interfaces of electrode and membrane is particularly critical for subsequently targeted suppression of dendrite growth. *In situ* and *in operando* characterization techniques enable real-time observation and revelation of the dynamic growth processes of dendrites at interfaces. Based on this dynamic information, precise guidance can be provided for optimizing electrolyte composition, modifying electrode surfaces, and designing membrane structures, thereby achieving precise regulation of interfacial reactions. (ii) Furthermore, to better investigate plating/stripping behaviors of various metals at electrode and membrane surfaces in MBHFBs, as well as electrolyte concentration distributions within bipolar plates, it is essential to develop characterization and visualization techniques with higher spatiotemporal resolution. Examples include the high spatiotemporal resolution infrared microscopy and mapping imaging technologies developed at the Shanghai Synchrotron Radiation Facility.[390] High spatiotemporal resolution infrared microscopy technique above also exemplifies the integration of multiple characterization techniques. (iii) The coupling of electrochemical analysis, spectroscopy, microscopy, and structural characterization enables multiscale and multi-dimensional analytical results, providing comprehensive material insights. These advanced characterization techniques are critical for advancing theoretical understanding and performance optimization of MBHFBs.

5.9. Test parameters optimization

Besides optimizing the key materials of MBHFBs (electrode, electrolyte, membrane, and bipolar plate) to suppress dendrites, the battery's test methods and operating parameters can also be adjusted to alleviate severe dendrite problems. For test methods in MBHFBs, single cells typically adopt constant capacity charging and constant current discharging; while stacks generally use constant power charging and discharging. These key operating parameters include voltage, current, electrolyte temperature, flow rate, pressure, *etc.*, which often interact with each other. These key parameters can be measured and monitored in real time through a battery management system (BMS) to ensure they remain within safe limits, prevent hazardous situations, and guarantee the safe operation of the battery.[391] Additionally, leveraging the BMS can in turn optimize these key testing and operational parameters, enabling an optimal balance among various battery performance aspects. Typically, a BMS consists of sensors, controllers, actuators, signal processors, and intelligent algorithm models.[392] Currently, BMS is limited to measuring basic battery parameters above and cannot measure complex yet critical parameters such as state of charge (SOC) and state of health (SOH) during operation. However, for flow batteries, especially MBHFBs, SOC and SOH are extremely critical parameters that directly impact battery performance and lifespan.[393] Therefore, subsequent BMS development must establish appropriate battery models to indirectly estimate important parameters like SOC and SOH, in order to meet the core requirements of MBHFBs. Developing battery management systems equipped with advanced battery models, along with advanced thermal and flow management technologies, represents a critical step for MBHFBs to move beyond laboratory settings.

5.10. Exploration of industrialization and commercialization

Aqueous MBHFBs are regarded as a crucial enabling technology for new-generation power systems due to their advantages of high safety, low cost, and long-duration energy storage, holding great commercialization potential. Currently, the mainstream promoted MBHFBs technologies are zinc–bromine flow batteries and zinc-iron flow batteries. However, their commercial exploration still faces multiple challenges. At the technical level, dendrite growth and areal capacity limitations are the primary issues, directly impacting the service life and energy density of MBHFBs. On the economic front, material/production costs and system construction/maintenance costs cannot be overlooked. While anode electrolytes are inexpensive, the additives introduced to enhance electrolyte performance tend to incur extra costs. High-performance membrane materials contribute significantly to costs, accounting for approximately 40% of stack expenses. System maintenance costs are also elevated due to "dead metal" accumulation and metal shedding during battery operation. The cost of storage tanks is also frequently overlooked.[394] This is primarily because specialized battery materials (such as high-performance/low-cost membranes and modified electrodes), stack manufacturing, and system integration have not yet formed a scaled and standardized supply chain, resulting in high initial investment costs. Additionally, the industry lacks unified standards in areas such as stack design, system integration, and operational control, which hampers product interchangeability and large-scale adoption. To better promote the development of MBHFBs, efforts should be made in the following aspects: (i) the development of MBHFBs should focus on differentiated markets, accurately target specific customer segments, and become a key pillar in building the next-generation power system. It is essential to concentrate on the long-duration energy storage market exceeding 4 hours, particularly the 8–10 hours segment, where lithium-ion batteries face high costs and pumped hydro storage is constrained by geographical limitations. Key application scenarios include energy storage paired with large-scale wind and solar power bases, grid-side peak shaving, as well as energy smoothing and backup power for zero-carbon parks and microgrids. (ii) Drive key material innovation (*e.g.*, electrolyte, membrane, electrode, bipolar plate) through industry-university-research collaboration. Combine advanced AI and characterization technologies to address technical bottlenecks hindering industrialization. Integrate battery management systems (BMS) with energy management systems (EMS) to achieve more efficient energy management. (iii) Capitalize on policy advantages and market momentum to actively promote the layout of the key materials industry, further reducing costs by forming a complete industrial chain. Specifically, promote the construction of large-scale production lines for key materials (such as specialized electrolytes and membranes) to reduce costs through mass manufacturing. Advance the standardization and modular design of stacks and systems to simplify production, installation, and maintenance, thereby further reducing manufacturing and deployment costs.

6. Conclusions and outlooks

6.1. Conclusions

In summary, here we provide a comprehensive overview of MBHFBs, which exhibit significant potential across multiple dimensions due to the abundance of candidate metal materials and their unique deposition–dissolution chemistry. They demonstrate promising attributes in terms of cost-effectiveness, energy density, power density, safety, operational temperature range, and response rate, positioning them as versatile contenders for advanced energy storage applications. Early MBHFBs centered on lead electrochemistry and gained initial development by leveraging the research enthusiasm for lead–acid batteries. In recent years, batteries based on metal lithium and zinc anodes have developed rapidly, bringing new opportunities and injecting fresh impetus into the advancement of MBHFBs. Furthermore, this has sparked broader research interest in other metals (including but not limited to sodium, magnesium, aluminum, iron, copper, tin, *etc.*) and opened up more possibilities for the future development of MBHFBs. Nevertheless, MBHFBs remain confronted with persistent challenges, which inherently vary as a consequence of the distinct characteristics of electrolytes and electrodes utilized in diverse MBHFBs. Addressing these challenges is critical for enabling the large-scale deployment of MBHFBs. To systematically analyze and address these critical challenges and notable issues, this review endeavors to establish a comprehensive framework and conduct a structured discussion. Horizontally, MBHFBs have been categorized into two major classes based on electrolyte properties (i.e., non-aqueous and aqueous systems) and further divided into eleven subtypes according to anode categories (specifically, Li-, Na-, K-, Mg-, Al-, Zn-, Fe-, Cd-, Sn-, Cu-, and Pb-HFBs). A thorough exposition is provided on their respective operating principles, architectural configurations, advantages, and challenges, with a concern on common and unique issues to establish a unified overall perspective. Vertically, the review concentrates on the evolution and limitations of four core materials (electrolytes, electrodes, membranes, and bipolar plates) in MBHFBs, aiming to uncover the underlying interconnections and synergies among these components. By integrating the analyses from these two dimensions, optimization strategies and development directions for the next-generation MBHFBs have been proposed to overcome existing barriers. This review aims to improve the understanding of design principles and optimization strategies for MBHFBs, support the establishment of a unified theoretical framework for deposition–dissolution chemistry, and offer relevant insights for developing next-generation low-cost and high-energy-density energy storage technologies.

6.2. Outlooks

Looking ahead, with the vigorous development and continuous functional refinement of energy storage technologies, different types of MBHFBs may find their own targeted application scenarios. In the field of large-scale and long-duration energy storage, safety has become the primary consideration for the industry, followed by high durability, low cost, large power density, and fast response time. Therefore, the transformation from non-aqueous systems to aqueous systems represents the mainstream choice and dominant trend for large-scale energy storage applications. Non-aqueous MBHFBs are expected to develop toward application scenarios with relatively small energy storage scales but special demands for high voltage and high energy density. For aqueous MBHFBs, considering the core requirement of energy storage cost control, zinc-based and iron-based HFBs are expected to receive more research attention and industrial investment in the future, due to their advantages of lower cost and higher maturity, and thus may serve as feasible technical routes for large-scale commercialization. Tin-based HFBs have a low risk of dendrite formation and show considerable potential despite the relatively late start of related research. In contrast, cadmium-based and lead-based HFBs are limited by their inherent toxicity and environmental pollution risks, while copper-based HFBs suffer from poor cycling stability; thus, these systems have a low possibility of large-scale commercial application in the future.

Although zinc-based and iron-based HFBs possess inherent advantages for large-scale energy storage, they still face numerous urgent scientific challenges and technical bottlenecks, which directly restrict the cycling lifespan, efficiency, and industrialization process of the batteries, representing the key directions that must be broken through in this field. Notably, metal batteries have a long research history and well-established research systems. They share high intrinsic similarities with MBHFBs in terms of electrochemical reaction mechanisms and metal anode interface behaviors, and the core scientific challenges confronting the two types of batteries are highly consistent. Both face common scientific challenges, including poor interfacial stability, serious dendrite growth, and uncontrollable side reactions.[395–397] Consequently, the well-established research methods, efficient interface regulation strategies, and in-depth mechanism analysis approaches that have already been validated in the field of traditional metal batteries can provide valuable references and technical insights for the interface engineering optimization, working mechanism research, and comprehensive performance improvement of MBHFBs.

To effectively overcome the existing technical bottlenecks, solve core scientific problems, and promote the leap of MBHFBs from laboratory basic research to large-scale industrial application, coordinated efforts are required in four key dimensions in the future: theory, materials, technology, and industry. Gradually, a complete development chain covering basic mechanism research, core technology breakthroughs, and industrial implementation will be established, ultimately enabling MBHFBs to become one of the core energy storage technologies supporting global energy transition and ensuring the accommodation of renewable energy.

(1) Theory integration. Electrodeposition theory is instructive for electrodeposition behavior. However, traditional electrodeposition theory is already struggling to cope with static metal batteries, and it is obviously even more inadequate when facing MBHFBs, which incorporate more complex fluid mechanics. Establishing an atomic-scale understanding of the electrodeposition process and its dynamic evolution is crucial for enabling the controlled deposition of metal nanoparticles.[398] Therefore, there is an urgent need to establish a theory that can directly or even precisely guide the anodic metal electrodeposition behavior in MBHFBs. Conducting dialectical analysis and integration of classical theories with the latest perspectives is a feasible strategy. In addition, it is also necessary to promote the in-depth integration of multi-disciplinary theories such as electrochemistry, materials science, fluid mechanics, and thermodynamics in the future, clarify the thermodynamic causes and kinetic laws of electrodeposition morphologies, and provide a theoretical basis for the precise regulation of electrodeposition behavior.

(2) Material innovation. Materials are the core elements determining the performance and economics of MBHFBs. Future material innovation needs to break the limitation of ‘‘single material upgrading’’ and shift towards a new path of ‘‘synergistic optimization of the entire material system’’. The synergistic innovation of the material system focuses on four core components and two key interfaces. The core of electrode material innovation lies in improving the reaction activity, loading capacity, and stability of the anode while maintaining low costs; the core of electrolyte innovation is to improve ionic conductivity and stability on the one hand, and reduce costs as well as safety and environmental risks on the other; the core of membrane material innovation is to break through the trade-off between high ion selectivity and high electrical conductivity, and promote the development of low-cost, non-fluorinated, and high-stability membranes; the core of bipolar plate innovation lies in developing low-cost, short-process technologies and targeted flow channel designs. In addition, attention should also be paid to interface issues, focusing on the development of ‘‘induced deposition interfaces’’ to induce uniform metal deposition by regulating surface energy and crystal growth direction. Ultimately, through the overall upgrading of the material system, the comprehensive goal of ‘‘high energy density, long cycle life, low cost, and low pollution’’ will be achieved.

(3) Technology empowerment. Technology empowerment mainly includes the iteration of stack system integration technology and the construction of auxiliary technology platforms. The stack system integration technology will move away from single-index optimization and towards multi-dimensional collaborative iteration. Through the synergistic innovation of key materials, it will promote an order-of-magnitude leap in single-stack power and energy density, as well as a large-scale reduction in manufacturing costs. Reliable and simple sealing technologies will be developed to improve stack safety and simplify the stack assembly process. Furthermore, the construction of auxiliary technology platforms will completely transform the traditional research and development (R&D) model relying on the ‘‘trial-and-error method’’ and extensive operation management, significantly improving the capabilities of precise R&D and intelligent operation and maintenance for MBHFBs.[399,400] Meanwhile, the platform will break the limitation of ‘‘fragmented R&D’’ and build a full-chain supporting capability covering from material screening to system verification. On the R&D side, multi-physics coupled simulation and emulation platforms will be used to explore the conditions for uniform metal deposition and key control parameters; multi-dimensional *in situ*/*in operando* characterization technologies will be employed to real-time monitor metal deposition behavior during battery operation; artificial intelligence and machine learning technologies will be introduced to build an intelligent model of ‘‘material screening-parameter optimization-performance prediction’’, accelerating the development of new materials and the design of battery structures. On the application side, the integration of MBHFBs with intelligent control systems will be promoted. By real-time monitoring and timely feedback of battery parameters such as voltage, temperature, and electrolyte concentration, the operation strategy will be dynamically adjusted to avoid problems such as local overheating and uneven deposition, thereby improving the operational stability and lifespan of the system.

(4) Industrial layout. The industrialization of MBHFBs needs to break through the predicament of ‘‘technological isolation’’ and ‘‘lack of standards’’ and build a complete industrial ecosystem covering from upstream materials to downstream applications. Firstly, strengthen industrial chain collaboration, promote in-depth cooperation among upstream material suppliers (metal raw material, membrane, and electrolyte enterprises), midstream battery manufacturers (stack design and assembly), and downstream application terminals (power grids and users). Through large-scale production, reduce the manufacturing costs of materials and stacks, and solve the problem of ‘‘excellent laboratory performance but excessively high industrialization costs’’; secondly, accelerate the construction of industry standards, clarify the performance test indicators of MBHFBs, manufacturing process specifications, and safety

assessment methods to ensure product reliability and consistency, providing a basis for market access and large-scale application; thirdly, relying on policy guidance and capital support, build demonstration projects of MBHFBs (such as energy storage stations combined with photovoltaic and wind power), verify technical reliability and accumulate operational data, while attracting talents and resources to gather in this field, promoting the industry to move from the "conceptual stage" to the "growth stage". Based on these, MBHFBs are expected to become a key supporting technology for renewable energy conversion and smart grid construction, providing important impetus for the achievement of global "dual carbon" goals.

Author contributions

Jie Wei: resources, conceptualization, visualization, writing – original draft, writing – review and editing; Jingjie Sun: visualization, writing – review and editing; Sijia Bai: data curation, writing – review and editing; Liuxin Ding: data curation, writing – review and editing; Pengbo Zhang: visualisation, writing – review and editing; Yixing Wang: writing – review and editing; Yuzhu Liu: writing – review and editing; Kang Huang: funding acquisition, project administration, supervision, writing – review and editing; Zhong Jin: conceptualization, funding acquisition, project administration, supervision, writing – review and editing; Zhi Xu: conceptualization, funding acquisition, project administration, supervision, writing – review and editing.

Conflicts of interest

The authors declare no conflict of interest.

Data availability

No primary research results, software or code have been included and no new data were generated or analysed as part of this review.

Acknowledgements

The authors appreciate the National Natural Science Foundation of China (22278211, 22425802, 22479074, 22475096, 22561160129, U25A20628), the China Postdoctoral Science Foundation (2024M762325), the Equipment Pre-Research and Ministry of Education Joint Fund (8091B02052407), the Fundamental Research Program Key Project of Jiangsu Province (BK20253008), the Natural Science Foundation of Jiangsu Province (BK20240400, BK20241236), the Science and Technology Major Project of Jiangsu Province (BG2024013), the Scientific and Technological Achievements Transformation Special Fund of Jiangsu Province (BA2023037), the Academic Degree and Postgraduate Education Reforming Project of Jiangsu Province (JGKT24_C001), the Key Core Technology Open Competition Project of Suzhou City (SYG2024122), the Open Research Fund of Suzhou Laboratory (SZLAB-1308-2024-TS005), and the Chenzhou National Sustainable Development Agenda Innovation Demonstration Zone Provincial Special Project (2023sfq11).

Notes and references

1 M. Armand and J. M. Tarascon, *Nature*, 2008, **451**, 652–657, DOI: 10.1038/451652a.

2 B. Dunn, H. Kamath and J. M. Tarascon, *Science*, 2011, **334**, 928–935, DOI: 10.1126/science.1212741.

3 L. Y. Zhang, R. Z. Feng, W. Wang and G. H. Yu, *Nat. Rev. Chem.*, 2022, **6**, 524–543, DOI: 10.1038/s41570-022-00394-6.

4 F. L. Zhu, W. Guo and Y. Z. Fu, *Chem. Soc. Rev.*, 2023, **52**, 8410–8446, DOI: 10.1039/d3cs00703k.

5 Z. M. Zhao, X. H. Liu, M. Q. Zhang, L. Y. Zhang, C. K. Zhang, X. F. Li and G. H. Yu, *Chem. Soc. Rev.*, 2023, **52**, 6031–6074, DOI: 10.1039/d2cs00765g.

6 T. V. Sawant, C. S. Yim, T. J. Henry, D. M. Miller and J. R. McKone, *Joule*, 2021, **5**, 360–378, DOI: 10.1016/j.joule.2020.11.022.

7 P. Xiong, L. Y. Zhang, Y. Y. Chen, S. S. Peng and G. H. Yu, *Angew. Chem., Int. Ed.*, 2021, **60**, 24770–24798, DOI: 10.1002/anie.202105619.

8 Z. J. Li and Y. C. Lu, *Adv. Mater.*, 2020, **32**, 2002132, DOI: 10.1002/adma.202002132.

9 F. R. Brushett, M. J. Aziz and K. E. Rodby, *ACS Energy Lett*, 2020, **5**, 879–884, DOI: 10.1021/acsenergylett.0c00140.

10 C. K. Zhang, Z. Z. Yuan and X. F. Li, *ACS Energy Lett*, 2024, **9**, 3456–3473, DOI: 10.1021/acsenergylett.4c00773.

11 J. Y. Du, H. T. Lin, L. Y. Zhang and L. J. Wang, *Adv. Funct. Mater.*, 2025, **35**, 2501689, DOI: 10.1002/adfm.202501689.

12 J. Long, W. H. Huang, H. T. Li, X. Y. Liu, J. C. Li, L. Chen, Q. Chen, J. J. Chen, Z. J. Yang and Y. P. Zhang, *J. Membr. Sci.*, 2025, **717**, 123599, DOI: 10.1016/j.memsci.2024.123599.

13 H. R. Jiang, J. Sun, L. Wei, M. C. Wu, W. Shyy and T. S. Zhao, *Energy Storage Mater.*, 2020, **24**, 529–540, DOI: 10.1016/j.ensm.2019.07.005.

14 C. Y. Sun and H. Zhang, *ChemSusChem*, 2022, **15**, e202101798, DOI: 10.1002/cssc.202101798.

15 V. Muralidharan, R. A. Kim, J. E. Jang and H. W. Lee, *J. Mater. Chem. A*, 2026, **14**, 6403–6413, DOI: 10.1039/d5ta07955a.

16 M. He, X. L. Zhou and J. P. Liu, *Phys. Chem. Chem. Phys.*, 2024, **26**, 24735–24752, DOI: 10.1039/d4cp02483d.

17 S. Xu, Y. Y. Cheng, L. Zhang, K. H. Zhang, F. Huo, X. P. Zhang and S. J. Zhang, *Nano Energy*, 2018, **51**, 113–121, DOI: 10.1016/j.nanoen.2018.06.044.

18 S. S. Pan, W. H. Fang, J. Yan, S. J. Zhang and H. T. Zhang, *Energy Environ. Sci.*, 2025, **18**, 5868–5896, DOI: 10.1039/d5ee00569h.

19 F. C. Yang, S. M. A. Mousavie, T. K. Oh, T. R. Yang, Y. Q. Lu, C. Farley, R. J. Bodnar, L. Niu, R. Qiao and Z. Li, *Adv. Energy Mater.*, 2018, **8**, 1701991, DOI: 10.1002/aenm.201701991.

20 C. H. Liu, J. S. Shamie, L. L. Shaw and V. L. Sprenkle, *ACS Appl. Mater. Interfaces*, 2016, **8**, 1545–1552, DOI: 10.1021/acsami.5b11503.

21 S. T. Senthilkumar, J. Han, J. Park, S. M. Hwang, D. Jeon and Y. Kim, *Energy Storage Mater.*, 2018, **12**, 324–330, DOI: 10.1016/j.ensm.2017.10.006.

22 W. D. Wu, M. Lehmann, Y. S. Li, L. Cheng and G. Yang, *ACS Energy Lett.*, 2024, **9**, 5795–5800, DOI: 10.1021/acsenergylett.4c02113.

23 A. C. Baclig, G. McConohy, A. Poletayev, A. Michelson, N. Kong, J. H. Lee, W. C. Chueh and J. Rugolo, *Joule*, 2018, **2**, 1287–1296, DOI: 10.1016/j.joule.2018.04.008.

24 Y. N. Qin, V. Sethuraman, S. G. Choi, R. Gonzalez, C. X. Chen, L. Cheng, C. Luo and T. Gao, *Chem. Sci.*, 2025, **16**, 16205–16217, DOI: 10.1039/d5sc04532k.

25 Y. A. Qin, K. Holguin, D. Fehlau, C. Luo and T. Gao, *ACS Appl. Energy Mater.*, 2022, **5**, 2675–2678, DOI: 10.1021/acsaem.2c00363.

26 R. K. Gautam, J. J. McGrath, X. Wang and J. J. Jiang, *J. Am. Chem. Soc.*, 2024, **146**, 28414–28426, DOI: 10.1021/jacs.4c10106.

27 C. K. Zhang, Y. Ding, L. Y. Zhang, X. L. Wang, Y. Zhao, X. H. Zhang and G. H. Yu, *Angew. Chem., Int. Ed.*, 2017, **56**, 7454–7459, DOI: 10.1002/anie.201703399.

28 L. Y. Zhang, C. K. Zhang, Y. Ding, K. Ramirez-Meyers and G. H. Yu, *Joule*, 2017, **1**, 623–633, DOI: 10.1016/j.joule.2017.08.013.

29 Y. Q. Huang, L. P. Zhi, R. Bi, Z. Z. Yuan and X. F. Li, *Fundam. Res.*, 2026, **6**, 173–177, DOI: 10.1016/j.fmre.2024.06.002.

30 C. X. Xie, Y. Liu, W. J. Lu, H. M. Zhang and X. F. Li, *Energy Environ. Sci.*, 2019, **12**, 1834–1839, DOI: 10.1039/c8ee02825g.

31 Y. R. Bai, X. Y. Huo, X. Long, E. K. Fu, X. S. Gong, L. Wei and L. An, *Adv. Funct. Mater.*, 2026, e32116, DOI: 10.1002/adfm.202532116.

32 Y. Xu, T. Y. Li, Z. Q. Peng, C. X. Xie and X. F. Li, *Nat. Energy*, 2025, **10**, 1470–1481, DOI: 10.1038/s41560-025-01907-5.

33 S. C. Yu, X. J. Yue, J. Holoubek, X. Xing, E. Pan, T. Pascal and P. Liu, *J. Power Sources*, 2021, **513**, 230457, DOI: 10.1016/j.jpowsour.2021.230457.

34 C. L. He, Y. M. Zhang, S. B. Zhang, X. Y. Peng, J. Noack, M. Skyllas-Kazacos, L. Z. Wang and B. Luo, *Nat. Sci. Rev.*, 2025, **12**, nwaf218, DOI: 10.1093/nsr/nwaf218.

35 Z. Huan, C. Y. Sun and M. M. Ge, *Adv. Funct. Mater.*, 2024, **34**, 2302077, DOI: 10.1002/wene.541.

36 Z. K. Liu, H. Shi, C. Q. Song, J. Cui, J. Hou, Z. P. Hu and P. Kang, *ACS Energy Lett*, 2025, **10**, 3492–3499, DOI: 10.1021/acsenergylett.5c01049.

37 J. Q. Pan, M. Yang, X. Jia and Y. Z. Sun, *J. Electrochem. Soc.*, 2013, **160**, A1146–A1152, DOI: 10.1149/2.051308jes.

38 Y. K. Zeng, T. S. Zhao, X. L. Zhou, L. Wei and H. R. Jiang, *J. Power Sources*, 2016, **330**, 55–60, DOI: 10.1016/j.jpowsour.2016.08.107.

39 C. X. Xie, C. Wang, Y. Xu, T. Y. Li, Q. Fu and X. F. Li, *Nat. Energy*, 2024, **9**, 714–724, DOI: 10.1038/s41560-024-01515-9.

40 H. Chen, Z. J. Wang, S. R. Zhang, M. Cheng, F. Y. Chen, Y. Xu and J. H. Luo, *J. Electrochem. Soc.*, 2021, **168**, 110547, DOI: 10.1149/1945-7111/ac39db.

41 Y. F. Xue, X. L. Ye, Z. A. Yu, Z. H. Peng, S. Q. Xing, J. R. Chen, Q. X. Wu and X. L. Zhou, *J. Energy Storage*, 2025, **140**, 119018, DOI: 10.1016/j.est.2025.119018.

42 Y. X. Yao, Z. Y. Wang, Z. J. Li and Y. C. Lu, *Adv. Mater.*, 2021, **33**, 2008095, DOI: 10.1002/adma.202008095.

43 S. Y. Zhu, Y. Z. Liu and H. N. Chen, *ACS Appl. Energy Mater.*, 2025, **8**, 4176–4183, DOI: 10.1021/acsaem.4c02973.

44 D. M. Kabtamu, G. Y. Lin, Y. C. Chang, H. Y. Chen, N. Y. Hsu, Y. S. Chou, H. J. Wei and C. H. Wang, *RSC Adv*, 2018, **8**, 8537–8543, DOI: 10.1039/c7ra12926b.

45 S. Schaltin, Y. Li, N. R. Brooks, J. Sniekers, I. F. J. Vankelecom, K. Binnemans and J. Fransaer, *Chem. Commun.*, 2016, **52**, 414–417, DOI: 10.1039/c5cc06774j.

46 D. Roberts, E. J. Fraser, A. Cruden, R. G. Wills and S. Brown, *J. Power Sources*, 2023, **570**, 233058, DOI: 10.1016/j.jpowsour.2023.233058.

47 D. L. Yu, W. B. Xu, C. G. Yuan, Z. Z. Yuan and X. F. Li, *Ind. Eng. Chem. Res.*, 2024, **63**, 11485–11495, DOI: 10.1021/acs.iecr.4c01530.

48 X. B. Cheng, R. Zhang, C. Z. Zhao and Q. Zhang, *Chem. Rev.*, 2017, **117**, 10403–10473, DOI: 10.1021/acs.chemrev.7b00115.

49 R. K. Gautam, X. Wang and J. B. Jiang, *Nat. Commun.*, 2025, **16**, 8830, DOI: 10.1038/s41467-025-63878-1.

50 W. H. Fang, Y. X. Liu, Y. C. Zhao, J. Yan, S. J. Zhang and H. T. Zhang, *Nano Energy*, 2025, **137**, 110796, DOI: 10.1016/j.nanoen.2025.110796.

51 Y. J. Li, S. Kumar, G. L. Yang, J. Lu, Y. Yao, K. Kang and Z. W. Seh, *Sciecne*, 2025, **389**, 6766, DOI: 10.1126/science.adl5482.

52 X. R. Chen, B. C. Zhao, C. Yan and Q. Zhang, *Adv. Mater.*, 2021, **33**, 2004128, DOI: 10.1002/adma.202004128.

53 W. C. Shi, Z. J. Song, W. W. Zhang, S. T. Lian, F. Z. Huang, Q. Y. An and Q. Li, *Energy Environ. Sci.*, 2024, **17**, 7372–7381, DOI: 10.1039/d4ee02784a.

54 K. Xu, *Commun. Mater.*, 2022, **3**, 31, DOI: 10.1038/s43246-022-00251-5.

55 G. Gunawardena, G. Hills, I. Montenegro and B. Scharifker, *J. Electroanal. Chem.*, 1982, **138**, 255–271, DOI: 10.1016/0022-0728(82)85082-1.

56 Y. J. Li, G. L. Yang, S. N. Sun, C. Zhang, C. Y. J. Lim, A. J. Y. Wong, W. Y. Lieu, Z. Sofer, M. F. Ng, W. Liu and Z. W. Seh, *Nano Lett.*, 2022, **22**, 6808–6815, DOI: 10.1021/acs.nanolett.2c02829.

57 X. Liu, G. X. Wang, Z. L. Lv, A. B. Du, S. M. Dong and G. L. Cui, *Adv. Mater.*, 2024, **36**, 2306395, DOI: 10.1002/adma.202306395.

58 X. Y. Yu, Z. G. Li, X. H. Wu, H. T. Zhang, Q. G. Zhao, H. F. Liang, H. Wang, D. L. Chao, F. Wang, Y. Qiao, H. S. Zhou and S. G. Sun, *Joule*, 2023, **7**, 1145–1175, DOI: 10.1016/j.joule.2023.05.004.

59 X. Wang, W. Zeng, L. Hong, W. W. Xu, H. K. Yang, F. Wang, H. G. Duan, M. Tang and H. Q. Jiang, *Nat. Energy*, 2018, **3**, 227–235, DOI: 10.1038/s41560-018-0104-5.

60 X. Shen, R. Zhang, P. Shi, X. Chen and Q. Zhang, *Adv. Energy Mater.*, 2021, **11**, 2003416, DOI: 10.1002/aenm.202003416.

61 M. Duduta, B. Ho, V. C. Wood, P. Limthongkul, V. E. Brunini, W. C. Carter and Y. M. Chiang, *Adv. Energy Mater.*, 2011, **1**, 511–516, DOI: 10.1002/aenm.201100152.

62 Z. X. Qi, A. L. Liu and G. M. Koenig, *Electrochim. Acta*, 2017, **288**, 91–99, DOI: 10.1016/j.electacta.2017.01.061.

63 S. Hamelet, T. Tzedakis, J. B. Leriche, S. Sailler, D. Larcher, P. L. Taberna, P. Simon and J. M. Tarascona, *J. Electrochem. Soc.*, 2012, **159**, A1360–A1367, DOI: 10.1149/2.071208jes.

64 H. N. Chen, Y. Liu, X. F. Zhang, Q. Lan, Y. Chu, Y. L. Li and Q. X. Wu, *J. Power Sources*, 2021, **485**, 229319, DOI: 10.1016/j.jpowsour.2020.229319.

65 R. J. Wang, L. P. Yang, J. Li, S. S. Pan, F. J. Zhang, H. T. Zhang and S. J. Zhang, *Nano Energy*, 2023, **108**, 108174, DOI: 10.1016/j.nanoen.2023.108174.

66 W. H. Fang, S. S. Pan, F. J. Zhang, Y. C. Zhao, H. T. Zhang and S. J. Zhang, *Chem. Eng. J.*, 2024, **485**, 149572, DOI: 10.1016/j.cej.2024.149572.

67 J. J. Biendicho, C. Flox, L. Sanz and J. R. Morante, *ChemSusChem*, 2016, **9**, 1938–1944, DOI: 10.1002/cssc.201600285.

68 Y. H. Hu, S. Y. Cheng, P. J. Liu, J. Q. Zhang, Q. L. Duan, H. H. Xiao, J. H. Sun and Q. S. Wang, *Fire Technol*, 2023, **59**, 1199–1220, DOI: 10.1007/s10694-023-01384-w.

69 Z. Q. Yin, B. Xue, Y. F. Ren, L. S. Peng, W. J. Zuo, X. K. Wu and L. Zhang, *Energy Technol.*, 2023, **12**, 2300784, DOI: 10.1002/ente.202300784.

70 X. J. Bai, J. H. Wang, H. Y. Hao, J. Xing, J. J. Dong, H. Liu and L. B. Liao, *Small Methods*, 2023, **7**, 2300548, DOI: 10.1002/smtd.202300548.

71 P. P. Su, H. T. Zhang, L. P. Yang, C. X. Xing, S. S. Pan, W. Lu and S. J. Zhang, *Chem. Eng. J.*, 2022, **433**, 133203, DOI: 10.1016/j.cej.2021.133203.

72 M. Youssry, L. Madec, P. Soudan, M. Cerbelaud, D. Guyomard and B. Lestriez, *Phys.Chem. Chem. Phys.*, 2013, **15**, 14476–14486, DOI: 10.1039/c3cp51371h.

73 Z. X. Qi and G. M. Koenig, *J. Power Sources*, 2016, **323**, 97–106, DOI: 10.1016/j.jpowsour.2016.05.033.

74 S. Hamelet, D. Larcher and J. M. Tarascon, *J. Electrochem. Soc.*, 2013, **160**, A516–A520, DOI: 10.1149/2.002304jes.

75 H. N. Chen, N. C. Lai and Y. C. Lu, *Chem. Mater.*, 2017, **29**, 7533–7542, DOI: 10.1021/acs.chemmater.7b02561.

76 L. H. Liu, X. X. Zuo, Y. J. Cheng and Y. G. Xia, *ACS Appl. Mater. Interfaces*, 2022, **14**, 28748–28759, DOI: 10.1021/acsami.2c03145.

77 S. S. Pan, H. T. Zhang, C. X. Xing, L. P. Yang, P. P. Su, J. J. Bi and S. J. Zhang, *J. Power Sources*, 2021, **508**, 230341, DOI: 10.1016/j.jpowsour.2021.230341.

78 S. S. Pan, L. P. Yang, P. P. Su, H. T. Zhang and S. J. Zhang, *Small*, 2022, **18**, 2202139, DOI: 10.1002/smll.202202139.

79 Y. J. Tang, L. P. Yang, Y. M. Zhu, F. J. Zhang and H. T. Zhang, *J. Mater. Chem. A*, 2022, **10**, 5620–5630, DOI: 10.1039/d1ta10883b.

80 J. W. Long, T. L. Han, Y. Y. Ding, C. Q. Hu and J. Y. Liu, *Appl. Surf. Sci.*, 2022, **591**, 153220, DOI: 10.1016/j.apsusc.2022.153220.

81 B. J. Xin, R. Wang, L. L. Liu and Z. Q. Niu, *Chinese J. Struct. Chem.*, 2023, **42**, 100116, DOI: 10.1016/j.cjsc.2023.100116.

82 F. Y. Su, C. H. You, Y. B. He, W. Lv, W. Cui, F. M. Jin, B. H. Li, Q. H. Yang and F. Y. Kang, *J. Mater. Chem.*, 2010, **20**, 9644–9650, DOI: 10.1039/c0jm01633k.

83 Y. Zhao, Y. Ding, Y. T. Li, L. L. Peng, H. R. Byon, J. B. Goodenough and G. H. Yu, *Chem. Soc. Rev.*, 2015, **44**, 7968–7996, DOI: 10.1039/c5cs00289c.

84 Y. G. Zhu, F. W. Thomas Goh and Q. Wang, *Nano Mater. Sci.*, 2019, **1**, 173–183, DOI: 10.1016/j.nanoms.2019.02.008.

85 H. A. Cortes and H. R. Corti, *Ultramicroscopy*, 2021, **230**, 113369, DOI: 10.1016/j.ultramic.2021.113369.

86 Y. G. Zhu, C. K. Jia, J. Yang, F. Pan, Q. Z. Huang and Q. Wang, *Chem. Commun.*, 2015, **51**, 9451–9454, DOI: 10.1039/c5cc01616a.

87 Y. G. Zhu, X. Z. Wang, C. K. Jia, J. Yang and Q. Wang, *ACS Catal.*, 2016, **6**, 6191–6197, DOI: 10.1021/acscatal.6b01478.

88 Y. H. Lu, J. B. Goodenough and Y. Kim, *J. Am. Chem. Soc.*, 2011, **133**, 5756–5759, DOI: 10.1021/ja201118f.

89 Y. Zhao, Y. Ding, J. Song, G. Li, G. B. Dong, J. B. Goodenough and G. H. Yu, *Angew. Chem., Int. Ed.*, 2014, **53**, 11036–11040, DOI: 10.1002/anie.201406135.

90 X. L. Wei, L. Cosimbescu, W. Xu, J. Z. Hu, M. Vijayakumar, J. Feng, M. Y. Hu, X. C. Deng, J. Xiao, J. Liu, V. Sprenkle and W. Wang, *Adv. Energy Mater.*, 2015, **5**, 1400678, DOI: 10.1002/aenm.201400678.

91 C. X. Xie, W. B. Xu, H. M. Zhang, X. P. Hu and X. F. Li, *Chem. Commun.*, 2018, **54**, 8419–8422, DOI: 10.1039/c8cc04099k.

92 C. K. Zhang, H. Chen, Y. M. Qian, G. L. Dai, Y. Zhao and G. H. Yu, *Adv. Mater.*, 2021, **33**, 2008560, DOI: 10.1002/adma.202008560.

93 Y. Ding, Y. Zhao, Y. T. Li, J. B. Goodenough and G. H. Yu, *Energy Environ. Sci.*, 2017, **10**, 491–497, DOI: 10.1039/c6ee02057g.

94 Y. Zhao, L. N. Wang and H. R. Byon, *Nat. Commun.*, 2013, **4**, 1896, DOI: 10.1038/ncomms2907.

95 Y. Zhao and H. R. Byon, *Adv. Energy Mater.*, 2013, **3**, 1630–1635, DOI: 10.1002/aenm.201300627.

96 M. Z. Yu, W. D. McCulloch, D. R. Beauchamp, Z. J. Huang, X. D. Ren and Y. Y. Wu, *J. Am. Chem. Soc.*, 2015, **137**, 8332–8335, DOI: 10.1021/jacs.5b03626.

97 G. M. Weng, Z. J. Li, G. T. Cong, Y. C. Zhou and Y. C. Lu, *Energy Environ. Sci.*, 2017, **10**, 735–741, DOI: 10.1039/c6ee03554j.

98 S. Das, S. Voskian, K. P. Rajczykowski, T. A. Hatton and M. Z. Bazant, *J. Electrochem. Soc.*, 2021, **168**, 070542, DOI: 10.1149/1945-7111/ac1396.

99 H. L. Pan, X. L. Wei, W. A. Henderson, Y. Y. Shao, J. Z. Chen, P. Bhattacharya, J. Xiao and J. Liu, *Adv. Energy Mater.*, 2015, **5**, 1500113, DOI: 10.1002/aenm.201500113.

100 X. T. Ma, H. Z. Yang, Y. Li, X. X. Zhou, Z. L. Zhang, D. H. Duan, X. G. Hao and S. B. Liu, *Chem. Eng. J.*, 2022, **427**, 131586, DOI: 10.1016/j.cej.2021.131586.

101 Y. Jin, G. M. Zhou, F. F. Shi, D. Zhuo, J. Zhao, K. Liu, Y. Y. Liu, C. X. Zu, W. Chen, R. F. Zhang, X. Y. Huang and Y. Cui, *Nat. Commun.*, 2017, **8**, 462, DOI: 10.1038/s41467-017-00537-0.

102 Q. L. Chen, W. Guo, D. H. Wang and Y. Z. Fu, *J. Mater. Chem. A*, 2021, **9**, 12652–12658, DOI: 10.1039/d1ta01973b.

103 H. N. Chen, Q. L. Zou, Z. J. Liang, H. Liu, Q. Li and Y. C. Lu, *Nat. Commun.*, 2015, **6**, 5877, DOI: 10.1038/ncomms6877.

104 H. N. Chen and Y. C. Lu, *Adv. Energy Mater.*, 2016, **6**, 1502183, DOI: 10.1002/aenm.201502183.

105 S. Xu, L. Zhang, H. Zhang, M. Wei, X. Guo and S. Zhang, *Mater. Today Energy*, 2020, **18**, 100495, DOI: 10.1016/j.mtener.2020.100495.

106 S. Xu, Z. H. Sun, T. Zhang, G. H. Liu, M. Wei and J. H. Cui, *J. Power Sources*, 2024, **591**, 233813, DOI: 10.1016/j.jpowsour.2023.233813.

107 C. Y. Li, A. L. Ward, S. E. Doris, T. A. Pascal, D. Prendergast and B. A. Helms, *Nano Lett.*, 2015, **15**, 5724–5729, DOI: 10.1021/acs.nanolett.5b02078.

108 T. S. Wang, X. F. Wang, A. Pendse, Y. C. Gao, K. Wang, C. Bae and S. Kim, *J. Membr. Sci.*, 2021, **636**, 119539, DOI: 10.1016/j.memsci.2021.119539.

109 C. H. Wang, Q. Z. Lai, P. C. Xu, X. F. Li and H. M. Zhang, *Chin. Chem. Lett.*, 2018, **29**, 716–718, DOI: 10.1016/j.cclet.2017.12.025.

110 E. V. Carino, J. Staszak-Jirkovsky, R. S. Assary, L. A. Curtiss, N. M. Markovic and F. R. Brushett, *Chem. Mater.*, 2016, **28**, 2529–2539, DOI: 10.1021/acs.chemmater.5b04053.

111 H. N. Chen, Y. C. Zhou and Y. C. Lu, *ACS Energy Lett.*, 2018, **3**, 1991–1997, DOI: 10.1021/acsenergylett.8b01257.

112 X. F. Zhang, P. Y. Zhang and H. N. Chen, *ChemSusChem*, 2021, **14**, 1913–1920, DOI: 10.1002/cssc.202100094.

113 E. Wang, E. W. Zhao and C. P. Grey, *J. Phys. Chem. C*, 2021, **125**, 27520–27533, DOI: 10.1021/acs.jpcc.1c07886.

114 R. K. Gautam, X. Wang, A. Lashgari, S. Sinha, J. McGrath, R. Siwakoti and J. B. Jiang, *Nat. Commun.*, 2023, **14**, 4753, DOI: 10.1038/s41467-023-40374-y.

115 D. S. Shin, M. Park, J. Ryu, I. Hwang, J. K. Seo, K. Seo, J. Cho and S. Y. Hong, *J. Mater. Chem. A*, 2018, **6**, 14761–14768, DOI: 10.1039/c8ta04720k.

116 L. Li, H. X. Gong, D. Y. Chen and M. J. Lin, *Chem. Eur. J.*, 2018, **24**, 13188–13196, DOI: 10.1002/chem.201801443.

117 Q. Z. Huang, H. Li, M. Grätzel and Q. Wang, *Phys. Chem. Chem. Phys.*, 2013, **15**, 1793–1797, DOI: 10.1039/c2cp44466f.

118 C. K. Jia, F. Pan, Y. G. Zhu, Q. Z. Huang, L. Lu and Q. Wang, *Sci. Adv.*, 2015, **1**, e1500886, DOI: 10.1126/sciadv.1500886.

119 F. Pan, J. Yang, Q. Z. Huang, X. Z. Wang, H. Huang and Q. Wang, *Adv. Energy Mater.*, 2014, **4**, 1400567, DOI: 10.1002/aenm.201400567.

120 F. Pan, Q. Z. Huang, H. Huang and Q. Wang, *Chem. Mater.*, 2016, **28**, 2052–2057, DOI: 10.1021/acs.chemmater.5b04558.

121 J. F. Li, L. Q. Yang, S. L. Yang and J. Y. Lee, *Adv. Energy Mater.*, 2015, **5**, 1501808, DOI: 10.1002/aenm.201501808.

122 Q. Z. Huang, J. Yang, C. B. Ng, C. Jia and Q. Wang, *Energy Environ. Sci.*, 2016, **9**, 917–921, DOI: 10.1039/c5ee03764f.

123 Y. G. Zhu, Y. H. Du, C. K. Jia, M. Y. Zhou, L. Fan, X. Z. Wang and Q. Wang, *J. Am. Chem. Soc.*, 2017, **139**, 6286–6289, DOI: 10.1021/jacs.7b01146.

124 Y. Igarashi, K. Hatakeyama-Sato, K. Kitagawa, R. Shinozaki and K. Oyaizu, *ACS Appl. Polym. Mater.*, 2024, **6**, 10113–10120, DOI: 10.1021/acsapm.3c01723.

125 Y. Zhang, J. S. Park, S. T. Senthilkumar and Y. Kim, *J. Power Sources*, 2018, **400**, 478–484, DOI: 10.1016/j.jpowsour.2018.08.044.

126 V. Ranmode and J. Bhattacharya, *J. Energy Storage*, 2019, **25**, 100827, DOI: 10.1016/j.est.2019.100827.

127 N. Kim, C. M. Kim, S. Park, J. Park, K. H. Cho and Y. Kim, *Chem. Eng. J.*, 2024, **479**, 147628, DOI: 10.1016/j.cej.2023.147628.

128 P. He, H. O. Ford, S. Gonzalez, S. Rodriguez, A. G. Oliver and J. L. Schaefer, *J. Electrochem. Soc.*, 2021, **168**, 110516, DOI: 10.1149/1945-7111/ac33e2.

129 H. Y. Huang, P. Z. Liu, Q. X. Ma, Z. H. Tang, M. Wang and J. H. Hu, *Energy*, 2023, **270**, 126991, DOI: 10.1016/j.energy.2023.126991.

130 J. R. Li, Y. H. Xu, S. L. Wei, C. Tong, M. H. Shao, C. P. Li and Z. D. Wei, *Green Chem*, 2025, **27**, 5246–5256, DOI: 10.1039/d5gc00460h.

131 J. Ryu, H. Jang, J. Park, Y. Yoo, M. Park and J. Cho, *Nat. Commun.*, 2018, **9**, 3715, DOI: 10.1038/s41467-018-06211-3.

132 D. P. Liu, J. Tian, Y. G. Tang, J. S. Li, S. A. Wu, S. J. Yi, X. B. Huang, D. Sun and H. Y. Wang, *Chem. Eng. J.*, 2021, **406**, 126772, DOI: 10.1016/j.cej.2020.126772.

133 X. G. Fu, G. P. Jiang, G. B. Wen, R. Gao, S. Li, M. Li, J. B. Zhu, Y. Zheng, Z. Q. Li, Y. F. Hu, L. Yang, Z. Y. Bai, A. P. Yu and Z. W. Chen, *Appl. Catal., B*, 2021, **293**, 120176, DOI: 10.1016/j.apcatb.2021.120176.

134 M. T. Zhang, H. Li, J. X. Chen, F. X. Ma, L. Zhen, Z. H. Wen and C. Y. Xu, *Adv. Funct. Mater.*, 2023, **33**, 2303189, DOI: 10.1002/adfm.202303189.

135 H. Li, M. T. Zhang, M. Wang, M. H. Du, Z. J. Wang, Y. X. Zou, G. X. Pan and J. H. Zhang, *Adv. Sci.*, 2024, **11**, 2308923, DOI: 10.1002/advs.202308923.

136 L. Y. Zhang, D. Fieser, B. Bera, D. Aaron, M. M. Mench, A. M. Hu, Y. Li, J. Chen, Z. L. Feng, A. Gulino and G. Compagnini, *J. Power Sources*, 2024, **589**, 233752, DOI: 10.1016/j.jpowsour.2023.233752.

137 W. Li, S. G. Xu, Y. J. Chen, B. H. Wang and Q. W. Wang, *Energy*, 2025, **335**, 137896, DOI: 10.1016/j.energy.2025.137896.

138 M. Rana, N. Alghamdi, X. Peng, Y. Huang, B. Wang, L. Wang, I. R. Gentle, S. Hickey and B. Luo, *Exploration*, 2023, **3**, 20220073, DOI: 10.1002/EXP.20220073.

139 U. Jimenez-Blasco, J. C. Arrebola, A. Caballero and F. Bella, *Materials*, 2023, **16**, 7482, DOI: 10.3390/ma16237482.

140 M. Zhao, T. Cheng, T. Y. Li, C. X. Xie, Y. B. Yin and X. F. Li, *Small Methods*, 2025, **9**, 2401434, DOI: 10.1002/smtd.202401434.

141 H. Y. Zheng, J. W. Ding, J. Q. Huang, J. R. Wang, H. T. Zhang, C. W. Qin, J. P. Zhang, Y. J. Cai and X. Y. Ji, *Adv. Funct. Mater.*, 2025, e14730, DOI: 10.1002/adfm.202514730.

142 J. Y. Li, Z. Y. Xu and M. C. Wu, *ACS Appl. Mater. Interfaces*, 2025, **17**, 25206–25215, DOI: 10.1021/acsami.4c22329.

143 H. Wei, G. M. Qu, X. Y. Zhang, B. H. Ren, S. Z. Li, J. J. Jiang, Y. H. Yang, J. L. Yang, L. Z. Zhao, H. F. Li, C. Y. Zhi and Z. X. Liu, *Energy Environ. Sci.*, 2023, **16**, 4073–4083, DOI: 10.1039/d3ee01639k.

144 W. J. Lu, P. C. Xu, S. Y. Shao, T. Y. Li, H. M. Zhang and X. F. Li, *Adv. Funct. Mater.*, 2021, **31**, 2102913, DOI: 10.1002/adfm.202102913.

145 L. Y. Tang, C. G. Yuan, W. J. Lu and X. F. Li, *Adv. Funct. Mater.*, 2025, 2502455, DOI: 10.1002/adfm.202502455.

146 S. Jin, Y. Q. Shao, X. S. Gao, P. Y. Chen, J. X. Zheng, S. F. Hong, J. F. Yin, Y. L. Joo and L. A. Archer, *Sci. Adv.*, 2022, eabq4456, DOI: 10.1126/sciadv.abq4456.

147 Y. C. Hu, Z. W. Min, G. Y. Zhu, Y. W. Zhang, Y. X. Pei, C. Chen, Y. M. Sun, G. J. Liang and H. M. Cheng, *Nat. Commun.*, 2025, **16**, 3255, DOI: 10.1038/s41467-025-58473-3.

148 Q. H. Xiong, M. B. Huang, T. L. Ren, S. X. Wu, W. F. Wang, Z. P. Xiang, K. Wan, Z. Y. Fu and Z. X. Liang, *Adv. Energy Mater.*, 2024, 2403347, DOI: 10.1002/aenm.202403347.

149 M. Zhao, T. Cheng, T. Y. Li, S. Wang, Y. B. Yin and X. F. Li, *Energy Environ. Sci.*, 2025, **18**, 378–385, DOI: 10.1039/d4ee04046e.

150 N. S. Alghamdi, D. Rakov, X. Y. Peng, J. Lee, Y. X. Huang, X. C. Yang, S. B. Zhang, I. R. Gentle, L. Z. Wang and B. Luo, *Angew. Chem., Int. Ed.*, 2025, **64**, e202502739, DOI: 10.1002/anie.202502739.

151 J. Y. Ye, L. Xia, H. Y. Li, F. P. G. de Arquer and H. X. Wang, *Adv. Mater.*, 2024, **36**, 2402090, DOI: 10.1002/adma.202402090.

152 E. K. Gikunoo, D. B. Han, M. Vinothkannan and S. Shanmugam, *J. Power Sources*, 2023, **563**, 232821, DOI: 10.1016/j.jpowsour.2023.232821.

153 Y. W. Zhang, Y. C. Hu, C. X. Dong, F. Y. Xiao, J. Z. Huang, J. Chen, G. J. Liang and H. M. Cheng, *Adv. Funct. Mater.*, 2025, 2500909, DOI: 10.1002/adfm.202500909.

154 Z. B. Pei, Z. X. Zhu, D. Sun, J. Y. Cai, A. Mosallanezhad, M. H. Chen and G. M. Wang, *Mater. Res. Bull.*, 2021, **141**, 111347, DOI: 10.1016/j.materresbull.2021.111347.

155 J. Yang, H. Yan, Y. Li and A. Tang, *J. Mater. Chem. A*, 2025, **13**, 23059–23072, DOI: 10.1039/d5ta03112e.

156 C. Li, Y. L. Xin, W. Gao and Y. P. Chen, *Small*, 2025, **21**, e08359, DOI: 10.1002/smll.202508359.

157 D. R. Fan, J. Y. Gong, S. T. Deng, H. Yan, Q. Zhu and H. R. Jiang, *J. Energy Storage*, 2024, **92**, 112215, DOI: 10.1016/j.est.2024.112215.

158 I. E. Udom, Y. Yao and L. H. Zhao, *J. Mater. Chem. A*, 2025, **13**, 31623–31631, DOI: 10.1039/d5ta04678e.

159 Z. Q. Wei, Z. D. Huang, G. J. Liang, Y. Q. Wang, S. X. Wang, Y. H. Yang, T. Hu and C. Y. Zhi, *Nat. Commun.*, 2024, **15**, 3841, DOI: 10.1038/s41467-024-48263-8.

160 C. X. Wang, G. Y. Gao, Y. Q. Su, J. Xie, D. Y. He, X. M. Wang, Y. R. Wang and Y. G. Wang, *Nat. Commun.*, 2024, **15**, 6234, DOI: 10.1038/s41467-024-50543-2.

161 R. H. Zhao, K. Lu, M. Pasha, R. Q. Kuang, H. Zhang and S. T. Lu, *J. Mater. Chem. A*, 2024, **12**, 24468–24476, DOI: 10.1039/d4ta03881a.

162 J. Yang, H. Yan, Q. Zhang, Y. Li and A. Tang, *Adv. Funct. Mater.*, 2025, 2509931, DOI: 10.1002/adfm.202509931.

163 H. Zhang, T. H. Ding, R. H. Zhao, R. Q. Kuang, K. Lu and S. T. Lu, *J. Power Sources*, 2024, **612**, 234798, DOI: 10.1016/j.jpowsour.2024.234798.

164 Z. Q. Wei, G. M. Qu, Z. D. Huang, Y. Q. Wang, D. D. Li, X. R. Yang, S. C. Zhang, A. Chen, Y. B. Wang, H. Hong, Q. Li and C. Y. Zhi, *Adv. Mater.*, 2024, **36**, 2414388, DOI: 10.1002/adma.202414388.

165 Y. C. Hu, T. Hu, Y. W. Zhang, H. C. Huang, Y. X. Pei, Y. H. Yang, Y. D. Wu, H. B. Hu, G. J. Liang and H. M. Cheng, *Chem. Sci.*, 2024, **15**, 14195–14201, DOI: 10.1039/d4sc04206a.

166 F. ShakeriHosseinabad, S. R. Daemi, D. Momodu, D. J. L. Brett, P. R. Shearing and E. P. L. Roberts, *ACS Appl. Mater. Interfaces*, 2021, **13**, 41563–41572, DOI: 10.1021/acsami.1c09770.

167 F. C. Walsh, C. P. de Léon, L. Berlouis, G. Nikiforidis, L. F. Arenas-Martínez, D. Hodgson and D. Hall, *ChemPlusChem*, 2015, **80**, 288–311, DOI: 10.1002/cplu.201402103.

168 L. Zhou, Y. T. Wu, Y. Y. Xie, J. Li, X. X. Zhang, K. J. Liu, H. Zhang and T. Qi, *J. Electroanal. Chem.*, 2024, **973**, 118669, DOI: 10.1016/j.jelechem.2024.118669.

169 H. Yu, M. Pritzker and J. Gostick, *J. Electrochem. Soc.*, 2023, **170**, 020536, DOI: 10.1149/1945-7111/acb8dd.

170 K. Amini and M. D. Pritzker, *J. Power Sources*, 2021, **506**, 230237, DOI: 10.1016/j.jpowsour.2021.230237.

171 G. Nikiforidis, L. Berlouis, D. Hall and D. Hodgson, *J. Power Sources*, 2013, **243**, 691–698, DOI: 10.1016/j.jpowsour.2013.06.045.

172 K. Amini and M. D. Pritzker, *Appl. Energy*, 2019, **255**, 113894, DOI: 10.1016/j.apenergy.2019.113894.

173 X. Xie, F. Mushtaq, Q. H. Wang and W. A. Daoud, *ACS Energy Lett*, 2022, **7**, 3484–3491, DOI: 10.1021/acsenergylett.2c01646.

174 X. Y. Huang, R. Zhou, X. L. Luo, X. H. Yang, J. Cheng and J. Y. Yan, *Adv. Appl. Energy*, 2023, **12**, 100154, DOI: 10.1016/j.adapen.2023.100154.

175 L. Wang, S. G. Yao, C. Ying, H. J. Yao and J. W. Yang, *Electrochim. Acta*, 2024, **475**, 143622, DOI: 10.1016/j.electacta.2023.143622.

176 T. Otani, T. Okuma and T. Homma, *J. Electroanal. Chem.*, 2020, **878**, 114583, DOI: 10.1016/j.jelechem.2020.114583.

177 S. G. Yao, X. F. Sun, X. X. Yang, R. Zhou and J. Cheng, *J. Energy Storage*, 2021, **33**, 102120, DOI: 10.1016/j.est.2020.102120.

178 X. Y. Huang, S. G. Yao, R. Zhou, X. H. Yang, X. Kan and J. Cheng, *J. Energy Storage*, 2022, **50**, 104246, DOI: 10.1016/j.est.2022.104246.

179 S. G. Yao, R. Zhou, X. Y. Huang, D. Liu and J. Cheng, *Electrochim. Acta*, 2021, **374**, 137895, DOI: 10.1016/j.electacta.2021.137895.

180 D. L. Collins-Wildman, K. Higa and V. S. Battaglia, *J. Power Sources*, 2025, **628**, 235737, DOI: 10.1016/j.jpowsour.2024.235737.

181 Y. H. Cheng, N. Y. Zhang, Q. L. Wang, Y. J. Guo, S. Tao, Z. J. Liao, P. Jiang and Z. H. Xiang, *Nano Energy*, 2019, **63**, 103822, DOI: 10.1016/j.nanoen.2019.06.018.

182 R. Zhou, S. G. Yao, Y. H. Zhao and J. Cheng, *Ind. Eng. Chem. Res.*, 2021, **60**, 1434–1451, DOI: 10.1021/acs.iecr.0c05292.

183 X. Y. Huang, S. G. Yao, X. H. Yang, X. F. Sun, R. Zhou, X. Z. Liu and J. Cheng, *J. Energy Storage*, 2022, **55**, 105624, DOI: 10.1016/j.est.2022.105624.

184 T. Xue and H. J. Fan, *J. Energy Chem.*, 2021, **54**, 194–201, DOI: 10.1016/j.jechem.2020.05.056.

185 D. Han, H. Jang, J. Choi, J. Park, S. Kim, S. Han, W. Lee, J. H. Lee, P. Oh, Y. Han and M. Park, *Small*, 2025, **21**, 2500787, DOI: 10.1002/smll.202500787.

186 X. Liu, Z. Chen, C. Y. Zhang, C. S. Ding, H. T. Feng, Y. Y. Cui and Y. F. Gao, *Adv. Funct. Mater.*, 2025, 2509495, DOI: 10.1002/adfm.202509495.

187 J. Cui, Z. K. Liu, C. Q. Song, Z. D. Meng and P. Kang, *Small*, 2025, **21**, 2506034, DOI: 10.1002/smll.202506034.

188 X. Y. Wang, R. J. Liu, Z. J. Li, H. Gao and T. S. Zhao, *J. Colloid Interface Sci.*, 2025, **702**, 138983, DOI: 10.1016/j.jcis.2025.138983.

189 C. X. Xie, T. Y. Li, C. Z. Deng, Y. Song, H. M. Zhang and X. F. Li, *Energy Environ. Sci.*, 2020, **13**, 135–143, DOI: 10.1039/c9ee03702k.

190 Q. Wang, W. H. Zhou, Y. Y. Zhang, H. R. Jin, X. R. Li, T. S. Zhang, B. Y. Wang, R. Z. Zhao, J. W. Zhang, W. Li, Y. Qiao, C. K. Jia, D. Y. Zhao and D. L. Chao, *Natl. Sci. Rev.*, 2024, **11**, nwae230, DOI: 10.1093/nsr/nwae230.

191 Y. Q. Wang, H. Hong, Z. Q. Wei, D. D. Li, X. R. Yang, J. X. Zhu, P. Li, S. N. Wang and C. Y. Zhi, *Energy Environ. Sci.*, 2025, **18**, 1524–1532, DOI: 10.1039/d4ee03385j.

192 H. Jang, M. G. Son, D. Han, J. Choi, J. H. Lee, P. Oh, J. Kang and M. Park, *Adv. Energy Mater.*, 2025, **15**, 2500621, DOI: 10.1002/aenm.202500621.

193 M. Kim, S. Lee, J. Choi, J. Park, J. W. Park and M. Park, *Energy Storage Mater.*, 2023, **55**, 698–707, DOI: 10.1016/j.ensm.2022.12.035.

194 B. Kim, Y. S. Kim, D. Dulyawat and C. H. Chung, *J. Energy Storage*, 2023, **72**, 108337, DOI: 10.1016/j.est.2023.108337.

195 T. M. Narayanan, Y. G. Zhu, E. Gençer, G. McKinley and Y. Shao-Horn, *Joule*, 2021, **5**, 2934–2954, DOI: 10.1016/j.joule.2021.07.010.

196 W. Wei, S. B. Nan, H. R. Wang, S. C. Xu, X. X. Liu and R. H. He, *J. Membr. Sci.*, 2023, **672**, 121453, DOI: 10.1016/j.memsci.2023.121453.

197 L. P. Zhi, Z. Z. Yuan and X. F. Li, *Adv. Membr.*, 2022, **2**, 100029, DOI: 10.1016/j.advmem.2022.100029.

198 H. Zhang, C. Sun and M. Ge, *Batteries*, 2022, **8**, 202, DOI: 10.3390/batteries8110202.

199 H. L. Huang, Y. Zhu, F. J. Chu, S. C. Wang and Y. H. Cheng, *Chem Asian J*, 2023, **18**, e202300492, DOI: 10.1002/asia.202300492.

200 Z. Wang, L. H. Yu, Y. Z. Nie, A. N. Gao and J. Y. Xi, *Small*, 2025, e09008, DOI: 10.1002/smll.202509008.

201 Y. X. Wang, T. G. Guo, B. Hu, E. R. Yang, R. F. Gao, H. J. Li, X. W. Zhou, Y. Cheng, K. Geng, H. Y. Tang and N. W. Li, *J. Membr. Sci.*, 2025, **733**, 124323, DOI: 10.1016/j.memsci.2025.124323.

202 X. R. Yang, Z. Q. Wei, H. L. Hu, H. Hong, Y. Q. Wang, J. X. Zhu, P. Li, T. R. Wang, J. Fan and C. Y. Zhi, *Adv. Mater.*, 2025, e10023, DOI: 10.1002/adma.202510023.

203 Y. Q. Huang, C. Y. Liao, Q. L. Song, Z. Z. Yuan and X. F. Li, *Angew. Chem., Int. Ed.*, 2025, **64**, e202511744, DOI: 10.1002/anie.202511744.

204 J. Q. Wang, Z. X. Liu, Z. Z. Xu, M. Ding, B. Lu, C. K. Jia and G. M. Zhou, *Angew. Chem., Int. Ed.*, 2025, **64**, e202503109, DOI: 10.1002/anie.202503109.

205 Y. Lim, M. Shin, J. J. Lee, C. Kim and Y. Kwon, *Chem. Eng. J.*, 2025, **508**, 161090, DOI: 10.1016/j.cej.2025.161090.

206 J. Wu, C. G. Yuan, T. Y. Li, Z. Z. Yuan, H. M. Zhang and X. F. Li, *J. Am. Chem. Soc.*, 2021, **143**, 13135–13144, DOI: 10.1021/jacs.1c04317.

207 J. E. Wu, C. Y. Liao, T. Y. Li, W. J. Lu, W. Xu, B. J. Ye, G. H. Li, H. J. Zhang and X. F. Li, *Adv. Energy Mater.*, 2023, **13**, 2300779, DOI: 10.1002/aenm.202300779.

208 X. N. Liu, M. Q. Shi, C. Y. Liao, N. Ta, Y. W. Chen, C. Z. Deng, H. J. Zhang, W. J Lu and X. F. Li, *Nat. Chem. Eng.*, 2025, **2**, 369–378, DOI: 10.1038/s44286-025-00238-2.

209 Y. S. Xia, H. Y. Cao, F. Xu, Y. X. Chen, Y. Xia, D. Z. Zhang, L. H. Dai, K. Qu, C. Lian, K. Huang, W. H. Xing, W. Q. Jin and Z. Xu, *Nat. Sustain.*, 2022, **5**, 1080–1091, DOI: 10.1038/s41893-022-00974-w.

210 X. X. Hou, K. Huang, Y. S. Xia, F. Y. Mu, H. Y. Cao, Y. Xia, Y. L. Wu, Y. Q. Lu, Y. X. Wang, F. Xu, Y. Yu, W. H. Xing and Z. Xu, *AIChE J.*, 2022, **68**, e17738, DOI: 10.1002/aic.17738.

211 Y. S. Xia, X. X. Hou, X. Y. Chen, F. Y. Mu, Y. Wang, L. H. Dai, X. Liu, Y. Yu, K. Huang, W. H. Xing and Z. Xu, *Chem. Eng. J.*, 2023, **465**, 142912, DOI: 10.1016/j.cej.2023.142912.

212 X. Liu, K. N. Xu, J. Y. Ding, T. Chen, X. X. Hou, H. Y. Cao, Y. Xia, Y. Q. Lu, Y. X. Wang, S. Fan, K. Huang and Z. Xu, *AIChE J.*, 2025, **71**, e18728, DOI: 10.1002/aic.18728.

213 S. H. Lin, X. Liu, K. A. Xu, K. W. Wang, N. N. Chang, Y. X. Wang, K. Huang, W. H. Xing and Z. Xu, *J. Membr. Sci.*, 2025, **722**, 123909, DOI: 10.1016/j.memsci.2025.123909.

214 S. H. Lin, T. H. Yi, J. X. Wang, D. Z. Zhang, N. N. Chang, Y. Yu, K. Huang, W. H. Xing and Z. Xu, *Adv. Funct. Mater.*, 2025, e17859, DOI: 10.1002/adfm.202517859.

215 D. L. Yu, L. P. Zhi, F. F. Zhang, Y. Song, Q. Wang, Z. Z. Yuan and X. F. Li, *Adv. Mater.*, 2023, **35**, 2209390, DOI: 10.1002/adma.202209390.

216 Y. Chen, M. Y. Zhou, Y. H. Xia, X. Wang, Y. Liu, Y. Yao, H. Zhang, Y. Li, S. T. Lu, W. Qin, X. H. Wu and Q. Wang, *Joule*, 2019, **3**, 2255–2267, DOI: 10.1016/j.joule.2019.06.007.

217 L. P. Zhi, C. Y. Liao, P. C. Xu, F. S. Sun, F. T. Fan, G. H. Li, Z. Z. Yuan and X. F. Li, *Angew. Chem., Int. Ed.*, 2024, **63**, e202403607, DOI: 10.1002/anie.202403607.

218 S. Q. Huang, Z. Z. Yuan, M. Salla, X. Wang, H. Zhang, S. P. Huang, D. G. Lek, X. F. Li and Q. Wang, *Energy Environ. Sci.*, 2023, **16**, 438–445, DOI: 10.1039/d2ee02402k.

219 S. N. Wang, T. Y. Li, C. G. Yuan, J. X. Zhu, P. Li, S. C. Zhang, Z. Q. Wei, Y. Q. Wang, X. F. Li and C. Y. Zhi, *Energy Environ. Sci.*, 2024, **17**, 7155–7164, DOI: 10.1039/d4ee01015a.

220 R. E. Ling, Z. X. Zhu, K. Peng, J. K. Fang, W. H. Zou, Q. X. Li, Y. L. Liu, Q. S. Zhu, N. Lin, T. W. Xu and Z. J. Yang, *Adv. Mater.*, 2024, **36**, 2404834, DOI: 10.1002/adma.202404834.

221 L. P. Zhi, C. Y. Liao, P. C. Xu, F. S. Sun, C. G. Yuan, F. T. Fan, G. H. Li, Z. Z. Yuan and X. F. Li, *Energy Environ. Sci.*, 2024, **17**, 717–726, DOI: 10.1039/d3ee02693k.

222 F. L. Zhu, Z. C. Hu, W. Guo and Y. Z. Fu, *Adv. Funct. Mater.*, 2024, **34**, 2405815, DOI: 10.1002/adfm.202405815.

223 X. Q. Liu, H. M. Zhang, Y. Q. Duan, Z. Z. Yuan and X. F. Li, *ACS Appl. Mater. Interfaces*, 2020, **12**, 51573–51580, DOI: 10.1021/acsami.0c16743.
224 W. Zhang, R. Mu, Z. H. Chang, C. Y. Zhang, B. H. Wang, H. J. Wu and D. Gu, *J. Energy Storage*, 2025, **134**, 118214, DOI: 10.1016/j.est.2025.118214.
225 Y. L. Zhang, D. Henkensmeier, S. Kim, R. Hempelmann and R. Y. Chen, *J. Energy Storage*, 2019, **25**, 100883, DOI: 10.1016/j.est.2019.100883.
226 Y. Kim, D. Yun and J. Jeon, *Electrochim. Acta*, 2020, **354**, 136691, DOI: 10.1016/j.electacta.2020.136691.
227 Z. P. Xie, Q. Su, A. H. Shi, B. Yang, B. X. Liu, J. C. Chen, X. C. Zhou, D. J. Cai and L. Yang, *J. Energy Chem.*, 2016, **25**, 495–499, DOI: 10.1016/j.jechem.2016.02.009.
228 T. V. Arya, M. Aparnasree and M. Ulaganathan, *J. Power Sources*, 2025, **645**, 237112, DOI: 10.1016/j.jpowsour.2025.237112.
229 C. X. Xie, Y. Q. Duan, W. B. Xu, H. M. Zhang and X. F. Li, *Angew. Chem., Int. Ed.*, 2017, **56**, 14953–14957, DOI: 10.1002/anie.201708664.
230 P. Tippayamalee, C. Pattanathummasid, R. Chanajaree, P. Pienpinijtham, S. Kheawhom and R. Cheacharoen, *J. Energy Storage*, 2024, **86**, 111295, DOI: 10.1016/j.est.2024.111295.
231 M. H. Yang, Z. Z. Xu, W. Z. Xiang, H. Xu, M. Ding, L. Y. Li, A. Tang, R. H. Gao, G. M. Zhou and C. K. Jia, *Energy Storage Mater.*, 2022, **44**, 433–440, DOI: 10.1016/j.ensm.2021.10.043.
232 J. Yang, H. Yan, H. H. Hao, Y. X. Song, Y. Li, Q. H. Liu and A. Tang, *ACS Energy Lett.*, 2022, **7**, 2331–2339, DOI: 10.1021/acsenergylett.2c00560.
233 Y. Zhao, X. N. Wang, C. K. Jia and M. Ding, *J. Colloid Interface Sci*, 2024, **673**, 496–503, DOI: 10.1016/j.jcis.2024.06.078.
234 W. Li, X. Dan, Q. L. Wen, C. He, A. Hammad, F. D. Ning, Y. Y. Liu, X. Y. Zhu, W. T. Huang, S. Y. Zou, J. H. Huang and X. C. Zhou, *Small*, 2025, **21**, 2505164, DOI: 10.1002/smll.202505164.
235 Y. C. Cai, H. Zhang, T. D. Wang, S. B. Xi, Y. X. Song, S. D. Rong, J. Ma, Z. Han, C. T. J. Low, Q. Wang and Y. Ji, *Joule*, 2025, **9**, 101768, DOI: 10.1016/j.joule.2024.09.015.
236 A. S. Ramanujam, V. Singh, P. Navalpotro, N. Patil and R. Marcilla, *Electrochim. Acta*, 2025, **537**, 146825, DOI: 10.1016/j.electacta.2025.146825.
237 A. S. Ramanujam, P. Navalpotro, N. Patil and R. Marcilla, *Batteries & Supercaps*, 2025, **00**, e202500529, DOI: 10.1002/batt.202500529.
238 Y. Z. Wang, D. K. Zhu, T. C. Guo, Z. X. Shi, F. W. Ming, J. K. El-Demellawi, Y. P. Zhu and H. N. Alshareef, *Mater. Today Energy*, 2025, **53**, 101999, DOI: 10.1016/j.mtener.2025.101999.
239 E. Indhuja, K. S. I. Leka, S. S. Kumar and P. Ragupathy, *Electrochim. Acta*, 2025, **540**, 147225, DOI: 10.1016/j.electacta.2025.147225.
240 Y. F. Zhao, S. H. Si and C. Liao, *J. Power Sources*, 2013, **241**, 449–453, DOI: 10.1016/j.jpowsour.2013.04.095.
241 J. Winsberg, T. Janoschka, S. Morgenstern, T. Hagemann, S. Muench, G. Hauffman, J. F. Gohy, M. D. Hager and U. S. Schubert, *Adv. Mater.*, 2016, **28**, 2238–2243, DOI: 10.1002/adma.201505000.
242 H. Fan, J. H. Zhang, M. Ravivarma, H. B. Li, B. Hu, J. F. Lei, Y. Y. Feng, S. Z. Xiong, C. He, J. Y. Gong, T. Y. Gao and J. X. Song, *ACS Appl. Mater. Interfaces*, 2020, **12**, 43568–43575, DOI: 10.1021/acsami.0c09941.
243 L. C. Yu, Y. C. Luo, W. Feng, S. Zhang and X. A. Zhang, *J. Mater. Chem. A*, 2023, **11**, 18911–18921, DOI: 10.1039/d3ta02241b.
244 H. Fan, B. Hu, H. B. Li, M. Ravivarma, Y. Y. Feng and J. X. Song, *Angew. Chem., Int. Ed.*, 2022, **61**, e202115908, DOI: 10.1002/anie.202115908.
245 J. Luo, B. Hu, M. W. Hu, W. D. Wu and T. L. Liu, *Angew. Chem., Int. Ed.*, 2022, **61**, e202204030, DOI: 10.1002/anie.202204030.
246 L. Li, Y. H. Su, Y. L. Ji and P. Wang, *J. Am. Chem. Soc.*, 2023, **145**, 5778–5785, DOI: 10.1021/jacs.2c12683.
247 X. W. Wang, W. Tang and K. P. Loh, *ACS Appl. Energy Mater.*, 2021, **4**, 3612–3621, DOI: 10.1021/acsaem.1c00031.
248 M. Park, E. S. Beh, E. M. Fell, Y. Jing, E. F. Kerr, D. De Porcellinis, M. A. Goulet, J. Ryu, A. A. Wong, R. G. Gordon, J. Cho and M. J. Aziz, *Adv. Energy Mater.*, 2019, **9**, 1900694, DOI: 10.1002/aenm.201900694.
249 L. J. Miao, Y. J. Shen, J. Y. Cao, Y. M. Shen and J. Xu, *J. Energy Storage*, 2024, **86**, 111242, DOI: 10.1016/j.est.2024.111242.
250 S. T. Senthilkumar, S. E. Ibañez, P. Navalpotro, E. Pedraza, N. Patil, J. Palma and R. Marcilla, *J. Power Sources*, 2024, **608**, 234660, DOI: 10.1016/j.jpowsour.2024.234660.
251 P. Richtr, J. Hnát, J. Charvat, M. Bures, J. Pocedic, M. Paidar, J. Kosek and P. Mazúr, *J. Energy Storage*, 2025, **115**, 115835, DOI: 10.1016/j.est.2025.115835.
252 C. Díaz, A. Moreno-Zuria, A. Sfeir, S. Royer, L. Sierra, B. López, M. Mohamedi and R. Palacio, *J. Energy Storage*, 2025, **126**, 117099, DOI: 10.1016/j.est.2025.117099.
253 J. Strada, E. Emanuele, L. Magagnin, F. Nespoli and B. Bozzini, *J. Electroanal. Chem.*, 2025, **988**, 119136, DOI: 10.1016/j.jelechem.2025.119136.
254 X. H. Liu, X. Y. Liu and H. J. Peng, *Ind. Eng. Chem. Res.*, 2023, **62**, 20963–20978, DOI: 10.1021/acs.iecr.3c02416.
255 H. P. Pang, P. P. Sun, H. Y. Gong, N. Zhang, J. C. Cao, R. H. Zhang, M. F. Luo, Y. Li, G. L. Sun, Y. G. Li, J. L. Deng, M. Gao, M. Wang and B. A. Kong, *ACS Appl. Mater. Interfaces*, 2021, **13**, 39458–39469, DOI: 10.1021/acsami.1c10925.
256 M. F. Liu, H. X. Dong, G. L. Wang and J. Zhao, *Nano Lett.*, 2024, **24**, 12102–12110, DOI: 10.1021/acs.nanolett.4c02820.
257 M. J. Wu, G. X. Zhang, N. Chen, Y. F. Hu, T. Regier, D. Rawach and S. H. Sun, *ACS Energy Lett*, 2021, **6**, 1153–1161, DOI: 10.1021/acsenergylett.1c00037.
258 C. Z. Bao, M. W. Tong, X. L. Li and Z. H. Xiang, *J. Energy Chem.*, 2024, **92**, 8–15, DOI: 10.1016/j.jechem.2024.01.035.
259 J. L. Xue, S. P. Deng, R. Wang and Y. S. Li, *Carbon*, 2023, **205**, 422–434, DOI: 10.1016/j.carbon.2023.01.034.
260 S. Q. Huang, H. Zhang, J. H. Zhuang, M. Y. Zhou, M. Q. Gao, F. F. Zhang and Q. Wang, *Adv. Energy Mater.*, 2022, **12**, 2103622, DOI: 10.1002/aenm.202103622.

261 D. X. Guo and W. Chen, *J. Energy Storage*, 2025, **124**, 116911, DOI: 10.1016/j.est.2025.116911.

262 S. Hosseini, A. Abbasi, L. O. Uginet, N. Haustraete, S. Praserthdam, T. Yonezawa and S. Kheawhom, *Sci. Rep.*, 2019, **9**, 14958, DOI: 10.1038/s41598-019-51412-5.

263 R. Khezri, S. Hosseini, A. Lahiri, S. R. Motlagh, M. T. Nguyen, T. Yonezawa and S. Kheawhom, *Int. J. Mol. Sci.*, 2020, **21**, 7303, DOI: 10.3390/ijms21197303.

264 A. D. Modestov, V. N. Andreev, A. E. Antipov and M. M. Petrov, *Energy Technol.*, 2021, **9**, 2100233, DOI: 10.1002/ente.202100233.

265 D. Milian, Y. Rharbi and N. El Kissi, *Rheol. Acta*, 2024, **63**, 645–656, DOI: 10.1007/s00397-024-01464-w.

266 D. Milian, N. H. Choi, M. T. Tsehaye, P. Fischer, J. Tübke, C. Iojoiu, D. C. D. Roux and N. El Kissi, *J. Power Sources*, 2023, **555**, 232331, DOI: 10.1016/j.jpowsour.2022.232331.

267 M. T. Tsehaye, N. H. Choi, P. Fischer, J. Tubke, E. Planes, F. Alloin and C. Iojoiu, *ACS Appl. Energy Mater.*, 2022, **5**, 7069–7080, DOI: 10.1021/acsaem.2c00697.

268 R. Khezri, A. Parnianifard, S. R. Motlagh, M. Etesami, W. Lao-atiman, A. Abbasi, A. Arpornwichanop, A. A. Mohamad, S. Olaru and S. Kheawhom, *J. Ind. Eng. Chem.*, 2022, **115**, 570–582, DOI: 10.1016/j.jiec.2022.09.003.

269 R. Khezri, S. R. Motlagh, M. Etesami, P. Pakawanit, S. Olaru, A. Somwangthanaroj and S. Kheawhom, *Appl. Energy*, 2024, **376**, 124239, DOI: 10.1016/j.apenergy.2024.124239.

270 R. Khezri, S. R. Motlagh, M. Etesami, A. A. Mohamad, R. Pornprasertsuk, S. Olaru and S. Kheawhom, *Appl. Energy*, 2023, **348**, 121564, DOI: 10.1016/j.apenergy.2023.121564.

271 S. Hameed, D. Li, M. K. Aslam, S. Chen and J. J. Duan, *Chem. Commun.*, 2025, **61**, 13636–13639, DOI: 10.1039/d5cc03154k.

272 K. Wang, Y. Y. Wu, X. B. Cao, L. Gu and J. Hu, *Adv. Funct. Mater.*, 2020, **30**, 1908965, DOI: 10.1002/adfm.201908965.

273 M. K. Aslam, H. R. Wang, Z. H. Nie, S. Chen, Q. Li and J. J. Duan, *Mater. Horiz.*, 2024, **11**, 2657–2666, DOI: 10.1039/d4mh00219a.

274 T. T. Lei, Y. F. Xu, Y. Li, L. Y. Huang, L. Ma, D. Q. Si, K. R. Wang, F. M. Wang, J. Q. Liu, L. Lei, L. P. Cao and Y. Yang, *Curr. Opin. Electrochem.*, 2025, **52**, 101702, DOI: 10.1016/j.coelec.2025.101702.

275 J. H. Yang, C. X. Zhou, Y. Q. Xiang, Y. L. Bi, X. Y. Tan, A. W. Robertson, Y. F. Cheng and Z. Y. Sun, *ChemSusChem*, 2025, **18**, e202500384, DOI: 10.1002/cssc.202500384.

276 E. M. Groiss, M. Duranti, W. G. Morais, M. Fedel and E. G. Macchi, *Electrochim. Acta*, 2025, **530**, 146387, DOI: 10.1016/j.electacta.2025.146387.

277 Y. F. Song, Q. A. Zhang, Y. Li and A. Tang, *Chem. Eng. J.*, 2025, **522**, 167948, DOI: 10.1016/j.cej.2025.167948.

278 Y. F. Song, H. Yan, Z. X. Cong, J. Yang, Y. Li and A. Tang, *Chem. Eng. J*, 2024, **487**, 150592, DOI: 10.1016/j.cej.2024.150592.

279 E. B. Boz, A. Bondre, R. De Bruijne and A. Forner-Cuenca, *Adv. Mater.*, 2025, **37**, 2414596, DOI: 10.1002/adma.202414596.

280 Y. Shi, Z. Y. Wang, Y. X. Yao, W. W. Wang and Y. C. Lu, *Energy Environ. Sci.*, 2021, **14**, 6329–6337, DOI: 10.1039/d1ee02258j.

281 R. F. Savinell and J. S. Wainright, *Electrochem. Soc. Interface*, 2023, **32**, 61, DOI: 10.1149/2.F08233IF.

282 H. Y. Li, Z. Q. Zhang, H. J. Zhang and Y. C. Zhou, *Batteries*, 2025, **11**, 166, DOI: 10.3390/batteries11040166.

283 N. Devi, P. Singh, A. Arpornwichanop and Y. S. Chen, *Electrochim. Acta*, 2025, **511**, 145393, DOI: 10.1016/j.electacta.2024.145393.

284 R. B. Krishnappa, S. G. Subramanya, A. Deshpande and B. Chakravarthi, *Fluids*, 2023, **8**, 237, DOI: 10.3390/fluids8080237.

285 V. Tam, R. Savinell and J. Wainright, *J. Electrochem. Soc.*, 2025, **172**, 070503, DOI: 10.1149/1945-7111/ade745.

286 A. Concheso, D. Barreda, Z. González, P. Alvarez, R. Menéndez, C. Blanco, V. G. Rocha and R. Santamaría, *Battery Energy*, 2025, e20240059, DOI: 10.1002/bte2.20240059.

287 Y. X. Song, H. Yan, H. H. Hao, Z. H. Liu, C. W. Yan and A. Tang, *Small*, 2022, **18**, 2204356, DOI: 10.1002/smll.202204356.

288 J. Yang, H. Yan, Q. A. Zhang, Y. F. Song, Y. Li and A. Tang, *Small*, 2024, **20**, 2307354, DOI: 10.1002/smll.202307354.

289 Y. X. Song, K. Y. Zhang, X. R. Li, C. W. Yan, Q. H. Liu and A. Tang, *J. Mater. Chem. A*, 2021, **9**, 26354, DOI: 10.1039/d1ta07295a.

290 X. S. Cheng, T. Xuan and L. W. Wang, *Chem. Eng. J.*, 2024, **491**, 151936, DOI: 10.1016/j.cej.2024.151936.

291 N. Sinclair, M. Vasil, C. Kellamis, E. A. Nagelli, J. Wainright, R. Savinell and G. E. Wnek, *J. Electrochem. Soc.*, 2023, **170**, 050516, DOI: 10.1149/1945-7111/acced2.

292 Y. Xu, Y. H. Wen, J. Cheng, G. P. Cao and Y. S. Yang, *Electrochem. commun.*, 2009, **11**, 1422–1424, DOI: 10.1016/j.elecom.2009.05.021.

293 H. Yousofian-Varzaneh, H. R. Zare and M. Namazian, *J. Electroanal. Chem.*, 2016, **776**, 193–201, DOI: 10.1016/j.jelechem.2016.07.019.

294 E. Blumbergs, V. Serga, E. Platacis, M. Maiorov and A. Shishkin, *Metals*, 2021, **11**, 1714, DOI: 10.3390/met11111714.

295 E. Blumbergs, M. Maiorov, A. Bogachov, E. Platacis, S. Ivanov, P. Gavrilovs and V. Pankratov, *Metals*, 2025, **15**, 959, DOI: 10.3390/met15090959.

296 F. Y. Chen, Q. Sun, W. Gao, J. G. Liu, C. W. Yan and Q. Y. Liu, *J. Power Sources*, 2015, **280**, 227–230, DOI: 10.1016/j.jpowsour.2015.01.049.

297 Y. K. Zeng, Z. F. Yang, F. Lu and Y. L. Xie, *Appl. Energy*, 2019, **255**, 113756, DOI: 10.1016/j.apenergy.2019.113756.

298 S. W. Tan, D. Y. He, T. Xu, R. Fang, Y. R. Wang, G. W. Diao and C. X. Wang, *Inorg. Chem.*, 2025, **64**, 4183–4189, DOI: 10.1021/acs.inorgchem.5c00248.

299 X. L. Zhou, L. Y. Lin, Y. H. Lv, X. Y. Zhang and Q. X. Wu, *J. Power Sources*, 2018, **404**, 89–95, DOI: 10.1016/j.jpowsour.2018.10.011.

300 X. L. Zhou, L. Y. Lin, Y. H. Lv, X. Y. Zhang, L. D. Fan and Q. X. Wu, *J. Power Sources*, 2020, **450**, 227613, DOI: 10.1016/j.jpowsour.2019.227613.

301 X. L. Ye, N. X. Xiong, S. P. Huang, Q. X. Wu, H. N. Chen and X. L. Zhou, *Small Methods*, 2024, **8**, 2301233, DOI: 10.1002/smtd.202301233.

302 Y. Yang, Y. Xiang, Y. W. Yang, X. Xie, F. Mushtaq, R. Q. Zhang and W. A. Daoud, *Adv. Funct. Mater.*, 2024, **35**, 2413685, DOI: 10.1002/adfm.202413685.

303 M. D'Adamo, W. Badenhorst, L. Murtomaeki, P. Cordoba, M. Derbeli, J. A. Saez-Zamora and L. Trilla, *Energies*, 2025, **18**, 2084, DOI: 10.3390/en18082084.

304 P. Leung, J. Palma, E. Garcia-Quismondo, L. Sanz, M. R. Mohamed and M. Anderson, *J. Power Sources*, 2016, **310**, 1–11, DOI: 10.1016/j.jpowsour.2015.12.069.

305 L. Faggiano, G. Lacarbonara, W. D. Badenhorst, L. Murtomäki, L. Sanz and C. Arbizzani, *J. Power Sources*, 2022, **520**, 230846, DOI: 10.1016/j.jpowsour.2021.230846.

306 L. Sanz, J. Palma, E. García-Quismondo and M. Anderson, *J. Power Sources*, 2013, **224**, 278–284, DOI: 10.1016/j.jpowsour.2012.10.005.

307 E. A. Stricker, K. W. Krueger, R. F. Savinell and J. S. Wainright, *J. Electrochem. Soc.*, 2018, **165**, A1797–A1804, DOI: 10.1149/2.1031809jes.

308 Y. Li, J. Sniekers, J. Malaquias, X. F. Li, S. Schaltin, L. Stappers, K. Binnemans, J. Fransaer and I. F. J. Vankelecom, *Electrochim. Acta*, 2017, **236**, 116–121, DOI: 10.1016/j.electacta.2017.03.039.

309 S. Maye, H. H. Girault and P. Peljo, *Energy Environ. Sci.*, 2020, **13**, 2191–2199, DOI: 10.1039/d0ee01590c.

310 V. M. Palakkal, T. Nguyen, P. Nguyen, M. Chernova, J. E. Rubio, G. Venugopalan, M. Hatzell, X. P. Zhu and C. G. Arges, *ACS Appl. Energy Mater.*, 2020, **3**, 4787–4798, DOI: 10.1021/acsaem.0c00400.

311 D. Li, Y. S. Zhang, Y. Shi, L. Zhang, J. Li, Q. Fu, X. Zhu and Q. Liao, *Ind. Eng. Chem. Res.*, 2023, **62**, 12855–12863, DOI: 10.1021/acs.iecr.3c01225.

312 J. B. Yang, Q. H. Yu, S. Chen, F. W. Yan and Y. Yu, *Energy Convers. Manage.*, 2024, **311**, 118523, DOI: 10.1016/j.enconman.2024.118523.

313 N. Jaiswal, H. Khan and R. Kothandaraman, *J. Electrochem. Soc.*, 2022, **169**, 040543, DOI: 10.1149/1945-7111/ac662a.

314 M. Krishna, E. J. Fraser, R. G. A. Wills and F. C. Walsh, *J. Energy Storage*, 2018, **15**, 69–90, DOI: 10.1016/j.est.2017.10.020.

315 M. E. Joy, R. G. A. Vivekanand, R. G. A. Wills and M. Neergat, *J. Electrochem. Soc.*, 2024, **171**, 120505, DOI: 10.1149/1945-7111/ad9a04.

316 X. F. Luo, Z. Liu, B. L. Jiang, D. D. Ji and C. M. Huang, *J. Energy Storage*, 2020, **30**, 101475, DOI: 10.1016/j.est.2020.101475.

317 C. Y. Lee, Y. H. Lai, K. R. Pan, H. L. Tan and H. Y. Chen, *ACS Appl. Energy Mater.*, 2020, **3**, 9576–9584, DOI: 10.1021/acsaem.0c00940.

318 Y. T. Lin, H. L. Tan, C. Y. Lee and H. Y. Chen, *Electrochim. Acta*, 2018, **263**, 60–67, DOI: 10.1016/j.electacta.2018.01.013.

319 Y. S. Hu, Z. Liu, B. L. Jiang, F. Zhao, Z. Y. Yan, X. Y. Wang and B. Ma, *J. Energy Storage*, 2023, **73**, 108874, DOI: 10.1016/j.est.2023.108874.

320 Y. S. Hu, Z. Liu, F. Zhao, D. D. Ji, B. L. Jiang, M. Y. Hu, B. Ma and Z. Y. Yan, *J. Energy Storage*, 2024, **88**, 111550, DOI: 10.1016/j.est.2024.111550.

321 K. Ghasemi, M. S. Rahmanifar and S. M. M. Khoshdel, *J. Energy Storage*, 2022, **55**, 105631, DOI: 10.1016/j.est.2022.105631.

322 X. F. Luo, Z. Liu, B. L. Jiang and D. D. Ji, *J. Energy Storage*, 2019, **24**, 100771, DOI: 10.1016/j.est.2019.100771.

323 D. D. Ji, Z. Liu, B. L. Jiang, B. Sun and X. Zhang, *J. Energy Storage*, 2022, **47**, 103549, DOI: 10.1016/j.est.2021.103549.

324 Z. Liu, X. F. Luo and D. D. Ji, *J. Energy Storage*, 2021, **38**, 102524, DOI: 10.1016/j.est.2021.102524.

325 Z. L. Na, F. Liang, D. M. Yin and L. M. Wang, *RSC Adv*, 2016, **6**, 56399–56405, DOI: 10.1039/c6ra09969f.

326 Z. Liu, J. Shi, D. D. Ji, X. Zhang and B. Sun, *J. Electrochem. Soc.*, 2021, **168**, 070545, DOI: 10.1149/1945-7111/ac132c.

327 S. Rathod, S. P. Yadav, M. K. Ravikumar, N. Jaiswal, S. Patil and A. K. Shukla, *Electrochim. Acta*, 2023, **441**, 141767, DOI: 10.1016/j.electacta.2022.141767.

328 K. K. Sarigamala, Y. H. Lin, K. R. Pan and H. Y. Chen, *J. Energy Storage*, 2023, **70**, 107957, DOI: 10.1016/j.est.2023.107957.

329 D. D. Ji, Z. Liu, L. W. Li, L. Jiang, L. Li and X. X. Liu, *J. Energy Storage*, 2024, **78**, 109978, DOI: 10.1016/j.est.2023.109978.

330 W. L. Jiang, F. J. Jiang, J. X. Zhang, F. Yang, L. Y. Liu and M. R. Hu, *J. Energy Storage*, 2024, **80**, 110274, DOI: 10.1016/j.est.2023.110274.

331 Z. C. Xu, Q. Fan, Y. Li, J. Wang and P. D. Lund, *Renew. Sust. Energ. Rev.*, 2020, **127**, 109838, DOI: 10.1016/j.rser.2020.109838.

332 J. Wei, P. B. Zhang, J. J. Sun, Y. Z. Liu, F. J. Li, H. F. Xu, R. Q. Ye, Z. X. Tie, L. Sun and Z. Jin, *Chem. Soc. Rev.*, 2024, **53**, 10335–10369, DOI: 10.1039/d4cs00584h.

333 Z. Z. Yuan, Y. B. Yin, C. X. Xie, H. M. Zhang, Y. Yao and X. F. Li, *Adv. Mater.*, 2019, **31**, 1902025, DOI: 10.1002/adma.201902025.

334 L. H. Dai, K. Huang, F. Xu, S. H. Lin and Z. Xu, *Angew. Chem., Int. Ed.*, 2025, **64**, e202504134, DOI: 10.1002/anie.202504134.

335 G. Leverick and Y. Shao-Horn, *Adv. Energy Mater.*, 2023, **13**, 2204094, DOI: 10.1002/aenm.202204094.

336 Y. X. Zhu, M. Y. Ge, F. C. Ma, Q. H. Wang, P. Huang and C. Lai, *Adv. Funct. Mater.*, 2024, **34**, 2301964, DOI: 10.1002/adfm.202301964.

337 J. Wei, P. B. Zhang, T. Y. Shen, Y. Z. Liu, T. F. Dai, Z. X. Tie and Z. Jin, *ACS Energy Lett*, 2023, **8**, 762–771, DOI: 10.1021/acsenergylett.2c02646.

338 X. Y. Yu, Y. T. Feng, J. Z. Tian, X. Liu, B. Y. Wang, Y. Y. Zhang, T. S. Zhang, G. Y. Li, X. R. Li, H. R. Jin, W. H. Li, W. Zhou, Z. Y. Zeng, L. Q. Li, D. Y. Zhao and D. L. Chao, *Angew. Chem., Int. Ed.*, 2025, **64**, e202503138, DOI: 10.1002/anie.202503138.

339 A. Bayaguud, X. Luo, Y. P. Fu and C. B. Zhu, *ACS Energy Lett*, 2020, **5**, 3012–3020, DOI: 10.1021/acsenergylett.0c01792.

340 S. Lee, C. H. Chen and A. H. Flood, *Nat. Chem.*, 2013, **5**, 704–710, DOI: 10.1038/NCHEM.1668.

341 W. L. Zhang, Y. Lu, Q. Q. Feng, H. Wang, G. Y. Liu, H. Cheng, Q. B. Cao, Z. J. Luo, P. Zhou, Y. C. Xia, W. H. Hou, K. Zhao, C. Y. Du and K. Liu, *Nat. Commun.*, 2025, **16**, 3344, DOI: 10.1038/s41467-025-58627-3.

342 M. J. Li, R. P. Hicks, Z. F. Chen, C. Luo, J. C. Guo, C. S. Wang and Y. H. Xu, *Chem. Rev.*, 2023, **123**, 1712–1773, DOI: 10.1021/acs.chemrev.2c00374.

343 L. Y. Zhang and G. H. Yu, *Angew. Chem., Int. Ed.*, 2021, **60**, 15028–15035, DOI: 10.1002/anie.202102516.

344 K. Q. Qu, X. J. Lu, N. Jiang, J. K. Wang, Z. Tao, G. J. He, Q. Yang and J. S. Qiu, *ACS Energy Lett.*, 2024, **9**, 1192–1209, DOI: 10.1021/acsenergylett.4c00113.

345 Z. Liu, F. Feng, W. C. Feng, G. W. Wang, B. Qi, M. Gong, F. Zhang and H. Pang, *Energy Environ. Sci.*, 2025, **18**, 3568–3613, DOI: 10.1039/d4ee05298f.

346 T. Wong, Y. J. Yang, R. Tan, A. Q. Wang, Z. Zhou, Z. Z. Yuan, J. X. Li, D. Z. Liu, A. Alvarez-Fernandez, C. C. Ye, M. Sankey, D. Ainsworth, S. Guldin, F. Foglia, N. B. McKeown, K. E. Jelfs, X. F. Li and Q. L. Song, *Joule*, 2025, **9**, 101795, DOI: 10.1016/j.joule.2024.11.012.

347 B. Jiang, L. T. Wu, L. H. Yu, X. P. Qiu and J. Y. Xi, *J. Membr. Sci.*, 2016, **510**, 18–26, DOI: 10.1016/j.memsci.2016.03.007.

348 V. Duraisamy, D. B. Han and S. Shanmugam, *J. Power Sources*, 2024, **611**, 234762, DOI: 10.1016/j.jpowsour.2024.234762.

349 M. R. Kraglund, M. Carmo, G. Schiller, S. A. Ansar, D. Aili, E. Christensen and J. O. Jensen, *Energy Environ. Sci.*, 2019, **12**, 3313–3318, DOI: 10.1039/c9ee00832b.

350 Q. Dai, F. Xing, X. N. Liu, D. Q. Shi, C. Z. Deng, Z. M. Zhao and X. F. Li, *Energy Environ. Sci.*, 2022, **15**, 1594–1600, DOI: 10.1039/d2ee00267a.

351 P. P. Zuo, C. C. Ye, Z. R. Jiao, J. Luo, J. K. Fang, U. S. Schubert, N. B. McKeown, T. L. Liu, Z. J. Yang and T. W. Xu, *Nature*, 2023, **617**, 299–305, DOI: 10.1038/s41586-023-05888-x.

352 R. Tan, A. Q. Wang, R. Malpass-Evans, R. Williams, E. W. Zhao, T. Liu, C. C. Ye, X. Q. Zhou, B. P. Darwich, Z. Y. Fan, L. Turcani, E. Jackson, L. J. Chen, S. M. Y. Chong, T. Li, K. E. Jelfs, A. I. Cooper, N. P. Brandon, C. P. Grey, N. B. McKeown and Q. L. Song, *Nat. Mater.*, 2020, **19**, 195–202, DOI: 10.1038/s41563-019-0536-8.

353 A. Q. Wang, C. Breakwell, F. Foglia, R. Tan, L. Lovell, X. C. Wei, T. Wong, N. Q. Meng, H. D. Li, A. Seel, M. Sarter, K. Smith, A. Alvarez-Fernandez, M. Furedi, S. Guldin, M. M. Britton, N. B. McKeown, K. E. Jelfs and Q. L. Song, *Nature*, 2024, **635**, 353–358, DOI: 10.1038/s41586-024-08140-2.

354 N. N. Chang, Y. B. Yin, M. Yue, Z. Z. Yuan, H. M. Zhang, Q. Z. Lai and X. F. Li, *Adv. Funct. Mater.*, 2019, **29**, 1901674, DOI: 10.1002/adfm.201901674.

355 G. N. Chen, C. L. Chen, Y. N. Guo, Z. Y. Chu, Y. Pan, G. Z. Liu, G. P. Liu, Y. Han, W. Q. Jin and N. P. Xu, *Science*, 2023, **381**, 1350–1356, DOI: 10.1126/science.adi1545.

356 J. E. Wu, Q. Dai, H. M. Zhang and X. F. Li, *ChemSusChem*, 2020, **13**, 3805–3819, DOI: 10.1002/cssc.202000633.

357 K. Huang, F. Y. Mu, X. X. Hou, H. Y. Cao, X. Liu, T. Chen, Y. Xia and Z. Xu, *Angew. Chem., Int. Ed.*, 2024, **63**, e20240155, DOI: 10.1002/anie.202401558.

358 J. Y. Ding, Y. L. Wu, Y. X. Wang, J. Wei, X. X. Hou, K. Huang and Z. Xu, *Chin. Sci. Bull.*, 2026, **71**, 339–354, DOI: 10.1360/CSB-2025-0500.

359 D. Z. Zhang, K. Huang, Y. S. Xia, H. Y. Cao, L. H. Dai, K. Qu, L. Xiao, Y. Q. Fan and Z. Xu, *Angew. Chem., Int. Ed.*, 2023, **62**, e20231094, DOI: 10.1002/anie.202310945.

360 Y. L. Wu, Y. X. Wang, D. Z. Zhang, F. Xu, L. H. Dai, K. Qu, H. Y. Cao, Y. Xia, S. Y. Li, K. Huang and Z. Xu, *Angew. Chem., Int. Ed.*, 2023, **62**, e20231357, DOI: 10.1002/anie.202313571.

361 T. V. Sawant and J. R. McKone, *J. Phys. Chem. C*, 2019, **123**, 144–152, DOI: 10.1021/acs.jpcc.8b09607.

362 K. V. Greco, A. Forney-Cuenca, A. Mularczyk, J. Eller and F. R. Brushett, *ACS Appl. Mater. Interfaces*, 2018, **10**, 44430–44442, DOI: 10.1021/acsami.8b15793.

363 Y. Z. Nie, J. J. Wu, H. Chen, L. H. Yu, L. Liu and J. Y. Xi, *ACS Mater. Lett.*, 2024, **6**, 4028–4035, DOI: 10.1021/acsmaterialslett.4c01340.

364 P. F. Wang, T. Peng, Y. H. Ban and M. L. Zheng, *Adv. Funct. Mater.*, 2024, **34**, 2409036, DOI: 10.1002/adfm.202409036.

365 Z. N. Duan, Z. G. Qu, Q. L. Ren and J. F. Zhang, *Electrochem. Energy Rev.*, 2021, **4**, 718–756, DOI: 10.1007/s41918-021-00108-4.

366 R. K. K. Gautam and A. Kumar, *J. Energy Storage*, 2022, **48**, 104003, DOI: 10.1016/j.est.2022.104003.

367 L. M. Pan, J. Sun, H. H. Qi, M. S. Han, Q. X. Dai, J. H. Xu, S. X. Yao, Q. L. Li, L. Wei and T. S. Zhao, *Proc. Natl. Acad. Sci. U. S. A.*, 2023, **120**, e2305572120, DOI: 10.1073/pnas.2305572120.

368 X. Y. Ke, J. M. Prahl, J. I. D. Alexander, J. S. Wainright, T. A. Zawodzinski and R. F. Savinell, *Chem. Soc. Rev.*, 2018, **47**, 8721–8743, DOI: 10.1039/c8cs00072g.

369 K. Peng, C. X. Jiang, Z. R. Zhang, C. Zhang, J. Wang, W. J. Song, Y. X. Ma, G. G. Tang, P. P. Zuo, Z. J. Yang and T. W. Xu, *Proc. Natl. Acad. Sci. U. S. A.*, 2024, **121**, e2406182121, DOI: 10.1073/pnas.2406182121.

370 H. F. Bian, C. C. Li, G. Xue, H. Wu, B. Wang, F. Q. Li, D. Bin, H. B. Lu and X. K. Meng, *Adv. Mater.*, 2025, **37**, 2505982, DOI: 10.1002/adma.202505982.

371 T. Y. Li, C. K. Zhang and X. F. Li, *Chem. Sci.*, 2022, **13**, 4740–4752, DOI: 10.1039/d2sc00291d.

372 L. N. Tang, P. Leung, Q. Xu and C. Flox, *ChemElectroChem*, 2024, **11**, e202400024, DOI: 10.1002/celc.202400024.

373 F. Wang, Z. B. Ma and J. Cheng, *J. Am. Chem. Soc.*, 2024, **146**, 14566–14575, DOI: 10.1021/jacs.4c01221.

374 F. Mushtaq, Y. Xiang, M. Fahim, X. Xie, H. Zhao and W. A. Daoud, *Energy Storage Mater.*, 2024, **73**, 103864, DOI: 10.1016/j.ensm.2024.103864.

375 Z. H. Sun, Y. K. Wang, S. Y. Shen, X. Y. Li, X. F. Hu, M. Y. Hu, Y. Q. Su, S. J. Ding and C. H. Xiao, *Angew. Chem., Int. Ed.*, 2023, **62**, e202309622, DOI: 10.1002/anie.202309622.

376 L. Geng, C. Zhao, J. T. Yan, C. R. Fu, X. D. Zhang, J. M. Yao, H. M. Sun, Y. Su, Q. N. Liu, L. Q. Zhang, Y. F. Tang, F. Ding and J. Y. Huang, *J. Mater. Chem. A*, 2022, **10**, 14875–14883, DOI: 10.1039/d2ta02513b.

377 Y. P. Han, P. He and Y. Xu, *Joule*, 2025, **9**, 102053, DOI: 10.1016/j.joule.2025.102053.

378 W. L. Wu, X. P. Yang, K. Wang, C. C. Li, X. Zhang, H. Y. Shi, X. X. Liu and X. Q. Sun, *Chem. Eng. J.*, 2022, **432**, 134389, DOI: 10.1016/j.cej.2021.134389.

379 M. Zhou, S. Guo, J. L. Li, X. B. Luo, Z. X. Liu, T. S. Zhang, X. X. Cao, M. Q. Long, B. G. Lu, A. Q. Pan, G. Z. Fang,

J. Zhou and S. Q. Liang, *Adv. Mater.*, 2021, **33**, 2100187, DOI: 10.1002/adma.202100187.

380 J. X. Bi, Z. K. Zhou, J. H. Li, B. X. Li, X. J. Sun, Y. H. Liu, K. Wang, G. W. Gao, Z. Z. Du, W. Ai and W. Huang, *Angew. Chem., Int. Ed.*, 2024, **63**, e202407770, DOI: 10.1002/anie.202407770.

381 H. X. Cai, S. S. Bi, R. Wang, L. L. Liu and Z. Q. Niu, *Angew. Chem., Int. Ed.*, 2022, **61**, e202205472, DOI: 10.1002/anie.202205472.

382 S. X. Wang, Y. Guo, X. F. Du, L. L. Xiong, Z. S. Liang, M. B. Ma, Y. H. Xie, W. Z. You, Y. Meng, Y. F. Liu and M. X. Liu, *Nat. Commun.*, 2024, **15**, 6476, DOI: 10.1038/s41467-024-50723-0.

383 H. Z. Zhang, Y. X. Yu, D. Y. Xu, M. H. Zhang, C. J. Huang, J. X. Wang, H. Liu, F. Yang, M. Q. Li, D. J. Liu, X. H. Lu, K. Xu and Y. S. Meng, *J. Am. Chem. Soc.*, 2025, **147**, 19829–19840, DOI: 10.1021/jacs.5c03861.

384 A. Alem, P. Poormehrabi, J. Lins, L. Pachernegg-Mair, C. Bandl, V. Ruiz, E. Ventosa, S. Spirk and T. Gutmann, *Energy Environ. Sci.*, 2025, **18**, 7373–7401, DOI: 10.1039/d5ee01311a.

385 E. W. Zhao, T. Liu, E. Jónsson, J. Lee, I. Temprano, R. B. Jethwa, A. Q. Wang, H. Smith, J. Carretero-Gonzalez, Q. L. Song and C. P. Grey, *Nature*, 2020, **579**, 224–228, DOI: 10.1038/s41586-020-2081-7.

386 M. E. Carrington, L. M. Yi, E. Jónsson and C. P. Grey, *Chem*, 2025, **11**, 102543, DOI: 10.1016/j.chempr.2025.102543.

387 P. B. Zhang, Y. Z. Liu, J. Wei, Z. A. Wu, X. M. Song, G. C. Ding, H. Z. Wang, J. C. Liang, Z. X. Tie and Z. Jin, *Nat. Commun.*, 2025, **16**, 4727, DOI: 10.1038/s41467-025-59962-1.

388 J. F. Lei, Y. Q. Zhang, Y. X. Yao, Y. Shi, K. L. Leung, J. Fan and Y. C. Lu, *Nat. Energy*, 2023, **8**, 1355–1364, DOI: 10.1038/s41560-023-01370-0.

389 X. X. Hou, X. Y. Chen, X. Liu, Y. Q. Lu, J. Zou, J. Y. Ding, K. Huang, W. H. Xing and Z. Xu, *J. Membr. Sci.*, 2024, **701**, 122730, DOI: 10.1016/j.memsci.2024.122730.

390 L. Nie, Y. Li, X. Y. Wu, M. T. Zhang, X. R. Wu, X. Xiao, R. H. Gao, Z. H. Piao, X. Wu, Y. Song, S. J. Chen, Y. F. Zhu, Y. Yu, S. J. Ling, K. Zheng and G. M. Zhou, *eScience*, 2025, **5**, 100395, DOI: 10.1016/j.esci.2025.100395.

391 Y. J. Zhao and M. L. Zheng, *Renew. Sust. Energ. Rev.*, 2025, **215**, 115604, DOI: 10.1016/j.rser.2025.115604.

392 H. Wang, S. A. Pourmousavi, W. L. Soong, X. A. Zhang and N. Ertugrul, *J. Energy Storage*, 2023, **58**, 106384, DOI: 10.1016/j.est.2022.106384.

393 S. Li, K. Li, E. Xiao and C. K. Wong, *IEEE Trans. Ind. Electron.*, 2020, **67**, 8484–8494, DOI: 10.1109/TIE.2019.2949534.

394 D. Reber, *Nat. Energy*, 2025, **10**, 23–27, DOI: 10.1038/s41560-024-01677-6.

395 Y. Zhang, P. P. Wu, C. X. Chen, Y. J. Liu, X. Q. Cai, W. L. Liang, M. H. Li, X. Y. Zhuang, Y. J. Li, X. P. Chen, M. Y. Sun, L. Wei, X. Hu and Z. H. Wen, *Chem. Soc. Rev.*, 2025, **54**, 9685–9806, DOI: 10.1039/d5cs00785b.

396 W. Deng, B. Qiu, J. H. Chen, Z. Li, Y. B. Tang, Z. P. Liu and Y. S. Meng, *Nat. Rev. Chem.*, 2026, DOI: 10.1038/s41570-026-00801-2.

397 D. Reber, Z. Y. Wang, K. Amini, Y. Jing, J. Lorenzetti, K. Xu, A. Khetan and Q. Wang, *Chem. Rev.*, 2025, **125**, 11216–11259, DOI: 10.1021/acs.chemrev.5c00332.

398 S. Chaudhuri and R. J. Maurer, *ACS Electrochem.*, 2025, **1**, 1014–1032, DOI: 10.1021/acselectrochem.4c00102.

399 R. Garg, V. Majhi, V. Chamola, A. Elhence and J. Pandey, *ACS Omega*, 2026, **11**, 12565–12584, DOI: 10.1021/acsomega.5c12654.

400 R. Ahmed, S. Sharma, S. Dhandapani, A. Thumar, R. Kamalanathan, A. Iranzo, P. Kauranen, C. Chinnasamy and A. M. Kannan, *J. Power Sources*, 2026, **665**, 239101, DOI: 10.1016/j.jpowsour.2025.239101.